Microstructures and deformation history of mantle xenoliths of the Northern Cordillera.

Arvid Cesar Gonzalez Gonzalez.

Earth and Planetary Sciences.

McGill University, Montreal.

September 2022.

A thesis submitted to McGill University in partial fulfillment of the requirements of the degree of Master of Science.

ACKNOWLEDGMENTS

First, I would like to thank my supervisors Jamie Kirkpatrick and William Minarik for their excellent guidance and support throughout my research project. Without their knowledge, patience, and encouragement this thesis would not be possible. Thanks to Caroline Seyler for training me in the EBSD and for her detailed user's manual. Special thanks to my supervisory committee member Fiona Darbyshire for providing valuable insight and interesting scientific discussions. Thanks to Lang Shi for his collaboration and availability in all EBSD-related matters and to Kristy Thornton for not letting me miss a deadline during these two years. I would like to take the time to thank Clément Estève for his advice during conferences and discussions on the tectonics of the Cordillera. I'd like to thank Geotop for the much-needed funding of this project.

Finally, my gratitude to Yuli for her unconditional support.

CONTRIBUTION OF AUTHORS

I, Arvid Cesar Gonzalez Gonzalez, assume full authorship for all written content in this thesis. This project was designed by my supervisor James Kirkpatrick who provided financial support for data acquisition, and extensive help in the development of Matlab scripts. I also care to acknowledge insightful contribution from my co-supervisor William Minarik, who provided access to a vast collection of Cordilleran mantle xenoliths. His contribution was instrumental in our understanding of the petrology and geochemistry of our samples.

The much-appreciated review process of this document was largely conducted by James Kirkpatrick, William Minarik and Fiona Darbyshire.

We also care to thank Caroline Seyler, who served as a consultant in this work and was responsible for my early training in EBSD and Mtex.

Finally, we thank Lang Shi for his diligence, availability, and patience in all EBSD-related procedures.

ABSTRACT

To investigate the possible role of the mantle during tectonic assembly of the Canadian Cordillera and constrain the seismic properties of the mantle lithosphere, we analyzed microstructures of mantle xenoliths sampled at 12 sites across the Cordillera. The xenoliths were sourced from the shallow mantle lithosphere at ambient temperatures of 850 to 1100 °C. Sample sites are Tertiary to Recent volcanic centers that are situated on predominantly Peri-Laurentian terranes, with a few on Laurentian terranes. We surveyed 195 xenoliths, which exhibit equigranular, protogranular, porphyroclastic and mylonitic textures, as well as transitional textures and some evidence for static annealing. This progression is marked by an increasingly defined grain shape preferred orientation, increased elongation of olivine grains and an overall reduction in grainsize. All sample suites exhibited a range of textures. Equigranular and protogranular textures were the most common, with relatively few porphyroclastic and mylonitic textures. We selected a subset of samples for electron backscattered diffraction (EBSD) mapping to analyse fabric, texture, lattice-preferred orientation, and grain size. Crystallographic preferred orientations (CPOs) are weak to moderate, with the weakest measured CPOs corresponding to the Laurentian sites. Our xenoliths exhibit 3 different fabrics: A-type fabrics, corresponding to the [100](010) slip system in olivine and indicative of low water content and low to intermediate stress; D-type fabrics, corresponding to the [100](0kl) slip system and AG, defined by (010)[100] and (010)[001]. Calculated seismic properties show moderate seismic anisotropy of 1.7 – 12.7% for Vp and 1.5 – 9.2% for Vs, which agree with previously published data. Overall, these results qualitatively suggest low strain throughout the Cordilleran mantle, despite the large crustal shortening during assembly of the Cordillera. They may also indicate that the mantle underlying the Peri-Laurentian terranes experienced a distinct deformation history relative to the cratonic mantle.

RÉSUMÉ

Afin d'étudier le rôle du manteau pendant l'assemblage tectonique de la Cordillère canadienne et de d'apporter des contraintes sur les propriétés sismiques de la lithosphère mantellique, nous avons analysé les microstructures de 195 xénolites échantillonnés sur 12 sites de la Cordillère. Les xénolites proviennent du manteau lithosphérique à des températures de 850 à 1100°C. Les sites d'échantillonnage sont des centres volcaniques Tertiaires à récents, sur des terranes principalement péri-laurentiens, avec quelques-uns sur des terranes laurentiens. Nous avons recensé 151 xénolites, avec des textures équigranulaires, protogranulaires, porphyroclastiques et mylonitiques, ainsi que des textures transitionnelles. Cette progression est marquée par une foliation de plus en plus définie, un allongement des grains d'olivine et une réduction de la taille des grains. Les textures équigranulaires et protogranulaires étaient les plus courantes, avec relativement peu de textures porphyroclastiques et mylonitiques. Nous avons sélectionné un sous-ensemble d'échantillons pour la cartographie par diffraction des électrons rétrodiffusés (EBSD) afin d'analyser la fabrique de la roche, la texture, les orientations préférentielles cristallographiques des grains et la taille des grains. Les orientations préférentielles cristallographiques des grains (OPCs) sont faibles à modérées. Les OPCs les plus faibles correspondent aux sites d'échantillonnage laurentiens. Les xénolites présentent trois fabriques minérales: type A, correspondant au système de glissement [100] (010) dans l'olivine et indiquant une faible teneur en eau et une contrainte faible à intermédiaire, type D, correspondant au système de glissement [100] (0kl) et type AG définie par (010)[100] et (010)[001]. Les propriétés sismiques calculées montrent une anisotropie sismique modérée. Les anisotropies de 1.7 – 12.7% pour Vp et 1.5 – 9.2% pour Vs sont en accord avec des données publiées. Nos résultats suggèrent une faible déformation du manteau, malgré le raccourcissement de la croûte pendant l'assemblage de la Cordillère. Ils peuvent également indiquer une histoire de déformation distincte du manteau sous-jacent aux terranes péri-laurentiens par rapport au manteau cratonique.

LIST OF FIGURES

LIST OF TABLES

TABLE OF CONTENTS

CHAPTER 1

Introduction

1.1 Context

Spinel peridotite xenoliths commonly occur in many alkali basalt centers of the northern North American Cordillera. Such xenoliths, when unaltered, represent a unique opportunity to directly study the properties of otherwise inaccessible mantle rocks. In the last 40 years, a wealth of studies has characterized the geochemistry, model ages, temperatures, etcetera of mantle xenoliths in many Cordilleran volcanic suites (e.g., Canil and Russel., 2022; Francis et al., 2010; Peslier et al., 2000a; Peslier et al., 2002) However, the analysis of deformation microstructures such as crystallographic preferred orientations (CPOs) of olivine and/or other mantle minerals in the Cordillera, which can inform tectonic history is limited to a few studies, mostly characterizing the mantle under individual locations (Ji et al., 1994; Morales & Tommasi, 2011). The development of olivine CPO fabrics through laboratory experiments that replicate conditions of the upper mantle, allows for the classification of six olivine fabric-types (A, B, C, D, E and AG) as a function of temperature, stress, strain geometry and water content (Holtzman et al., 2003; Karato et al., 2008; Skemer & Hansen, 2016). Therefore, the characterization of microstructures provides key insights into tectonic setting, strain geometry, geochemical processes (e.g., melt-rock reactions and partial melting), mantle flow and seismic anisotropy of the lithospheric mantle (Cao et al., 2017; Karato, 2008; Karato et al., 2008; Skemer & Hansen, 2016).

In the last two decades, the electron backscattered diffraction (EBSD) method has become the main choice in microstructure studies as it allows for fast acquisition of data at sub-micron resolutions from standard polished thin sections. Backscattered electrons (BSE) refracted from a specimen tilted 70° to the incident electron beam in a scanning electron microscope (SEM), form a pattern that is imaged on a phosphor screen. Analysis of the diffraction pattern allows the identification of the mineral phase and its crystal lattice orientation by comparing the positions, profile shapes and band intensities of the captured diffraction pattern, known as Kikuchi bands, with the known crystallographic structure of minerals in a database. Data post-processing using the Mtex toolbox package (https://mtex-toolbox.github.io/index) permits multiple analysis including grain geometry, misorientation angles and axes, modal contents, CPO, and seismic

anisotropy. This, in turn, helps to interpret processes and deformation mechanisms including mantle flow, subgrain formation, and deformation mechanism (e.g., diffusion creep, grain boundary sliding (GBS) or dislocation creep). In this study, we use this approach to characterize the lithospheric mantle underlying 12 volcanic suites along the whole latitude range of the Canadian Cordillera and better understand its origin, evolution, and spatial variations.

1.2 Tectonic context on the Northern Cordillera

The Canadian Cordillera consists of an amalgamation of terranes with disparate tectonic histories that were assembled through collision and accretion of terranes to the western margin of North America, as well as forearc rifting and coastwise transport (Monger & Price, 2002; Price, 1994). The architecture of the Cordilleran crust is well resolved by geophysical imaging and geological mapping. Surface geology and reflection seismology shows large crustal shortening, with some tectonic slivers thrust tens to hundreds of km onto the pre-Cordillera Laurentian basement (Cook et al., 2004). Notably, seismic reflection studies showed reflections corresponding to pre-Cordilleran layered sedimentary rocks beneath some of the allochthonous terranes (Cook et al., 2004). The average Moho depth throughout the Cordillera is 30 – 35 km, which contrasts with the western margin of cratonic North America where the depth is 40 – 45 km (Cook et al., 2004; Hyndman et al., 2005; Tarayoun et al., 2017). The absence of a thick crustal root to support the high average Cordilleran elevation has been established by accumulating seismic structure data showing a thin, hot crust (Tarayoun et al., 2017). This requires thermal expansion of the uppermost mantle caused by steep geotherms (Currie & Hyndman, 2006; Hyndman et al., 2005; Mazzotti & Hyndman, 2002), which is consistent with high regional heat flow (Lewis et al., 2003), low elastic thickness (< 10 km) (Audet & Mareschal, 2007) and low mantle-refracted P-wave (Pn) velocities (Hyndman & Lewis, 1999; Lewis et al., 2003).

Seismic studies (e.g., Audet et al., 2019; Tarayoun et al., 2017) have interpreted a relatively flat, shallow lithosphere-asthenosphere boundary (LAB) at ~50 km for the northern Cordillera based on the presence of a sub-Moho, high-velocity layer followed by a pronounced downward decrease in seismic wave speed in receiver function phase conversions. This low-velocity zone underlying the LAB with shear-wave velocities as low as 3:0 km/s, has been attributed to 1.5–2.5% partial melting (Smale, 2020). Such a shallow LAB has been proposed as the mechanism

that explains the thermal state supporting the Cordillera (Hyndman & Canil, 2021; Hyndman & Currie, 2011). The ~50km LAB depth imaged in seismic studies contrasts with geochemical estimations of ~65km, based on the equilibration of basaltic lavas derived near or below the LAB (Canil et al., 2021). Despite the differences resulting from the use of different approaches and/or study areas, it generally agreed that the LAB under the Cordillera, like the Moho, is anomalously flat and shallow for its respective surface topography.

Two main models attempt to describe the formation of the Cordillera: (1) an accretionary orogen formed by successive addition of thin-skinned terranes to the continental margin, (2) a late-Cretaceous collision between an exotic ribbon microcontinent and cratonic North America. The prevailing view of an accretionary orogen predicts an east-dipping LAB at the Cordillera-craton boundary (Chen et al., 2019). It invokes three mechanisms to explain the shallow LAB: (1) upwelling of dry asthenosphere conditioned by slab window opening (Madsen et al., 2006; Thorkelson et al., 2011), (2) the presence of small-scale convection cells in a hydrated sub-lithospheric mantle (Currie & Hyndman, 2006), and (3) delamination of the lithospheric mantle (Bao et al., 2014). However, due to insufficient geological and geophysical data it is difficult to corroborate the dominance of one of these mechanisms (Audet et al., 2019). A less-accepted collisional model assumes the Triassic-Jurassic assembly of multiple terranes as a composite ribbon continent and its collision with Laurentia ~100 Ma (Johnston, 2008). The allochthonous character of the pre-formed ribbon is in agreement with Re-Os model ages of ~1.1 Ga obtained from mantle xenoliths in the Cordillera (Peslier et al., 2000a). These are interpreted as the age of melt extraction and lithospheric mantle formation and contrast with a much older (~2.5 Ga) estimations for the age of the cratonic Laurentian mantle beneath North America (LeCheminant, 1996). However, lithospheric removal processes could also have rejuvenated an older lithospheric mantle of either exotic or North American origin. This model predicts a west-dipping LAB at the cordillera-craton boundary, which is consistent with seismic observations (Chen et al., 2019; Estève et al., 2021).

The origin and dynamics of the mantle underlying the Canadian Cordillera remains a controversial subject. While some models propose a uniform, homogeneous continental mantle underlying the accreted terranes, others consider that certain terranes may have imported their own

mantle (Chen et al., 2019). Three main hypotheses have been proposed to explain the nature of the lithosphere beneath the NCC (Audet et al., 2019): (1) most of lithosphere under the Cordillera is of ancestral North American origin. (2) the lithosphere has an exotic origin as it was accreted with the terranes, and (3) recent lithospheric removal processes have rejuvenated the cordilleran lithosphere. The first two models imply long-lived thin lithosphere despite the different origins, whereas in the third, the lithosphere is juvenile.

Testing these hypotheses is necessary to understand the structure and active deformation of the modern Cordillera. For example, the "orogenic float" concept (Oldow et al., 1990) for continental-collision systems was adopted by Mazzotti and Hyndman (2002) to integrate observations of high heat flow and thin mechanical lithosphere in the Canadian Cordillera. In this model, displacement of a thin and rigid Cordilleran upper crust is accommodated by a weak lower crust acting as a detachment (shear) zone due to the elevated geotherm. This decoupling level then joins the basal detachment of thrusting in the foreland as the compressive stresses reactivate the Mesozoic fold-and-thrust belt at the Cordilleran Deformation Front, which generates seismic activity far from the plate collision of the Yakutat block in the corner of the Gulf of Alaska (Mazzotti and Hyndman, 2002; Hyndman et al., 2005). This model is consistent with many other geophysical observations for the Cordillera including a flat, shallow Moho at ~30-35 km depth, elevated upper mantle temperatures, and low effective elastic thickness (Tarayoun et al., 2017 and references therein), but has yet to be reconciled with observations of the deformation history of the mantle.

1.3 Cordilleran xenoliths

Small Tertiary to Recent alkaline volcanic centres distributed along the Cordillera provide a regional sampling of the upper mantle underlying many of the Cordilleran terranes. The locations of these volcanic centers are determined by the current tectonic configuration between the North American, Pacific, and Juan de Fuca plates. Calc-alkaline stratovolcanoes prevail where plate boundaries are convergent, whereas extensional and/or transtensional plate boundaries are associated with mafic alkaline magmatism. Lava flows throughout the Cordillera have oxidized flow tops, indicating that they were erupted subaerially (Eiché et al., 1987). In many of these centers, erupted alkaline basalts entrained mantle xenoliths with no apparent crustal contamination

(Peslier et al., 2002). These mantle xenoliths provide an opportunity to characterize the compositional characteristic of the mantle and represent a window into its deformation history as they potentially retain evidence of previous geochemical and tectonic events/processes within the lithosphere. Mantle xenoliths were sourced from depths of ~30–80 km (Edwards & Russell, 2000; Francis et al., 2010; Peslier et al., 2002; Peslier et al., 2000a; Peslier et al., 2000b; Shi et al., 1998) The xenoliths occur as inclusions in lava flows or in bombs in cinder cones, with minor alteration.

Detailed petrological descriptions can be found in Francis et al. (2010) and Peslier et al. (2002). The samples show little to no indication of deformation during entrainment or eruption as no reaction rims were observed around orthopyroxene and spinel and no diffusion zones around olivine. Lherzolites in contact with basalts, however, exhibit moderate redistribution of oxides by percolation of fluids along grain boundaries in a 1-2 cm-thick zone that is parallel to the contact.

Geochemical analyses of mantle xenoliths indicate that the mantle lithosphere of the Cordillera is relatively homogeneous in composition (Peslier et al., 2002). For most suites, relatively fertile spinel lherzolites are largely predominant in the lithospheric mantle. This is indicative of a melting event(s) during mid-Proterozoic production of mid-ocean ridge basalt (Francis et al., 2010). However, changes in isotopic signatures of Sr and Nd from mantle xenoliths across both sides of the Tintina fault have been interpreted to reflect different lithospheric mantles (Abraham et al., 2001). A clear distinction can also be made between suites of unimodal or bimodal xenolith populations (Shi et al., 1998). Unimodal volcanic centers are dominated by fertile lherzolite xenoliths, whereas in bimodal suites (Alligator Lake, Hirschfield Creek and Llangorse Mountain), refractory harzburgite with higher MgO and lower Al_2O_3 contents in addition to lherzolites are interpreted to have formed at higher temperatures and greater depth (Shi et al., 1998). Metasomatic enrichment and partial melting associated with the ingress of ~15 % volatiles (Francis et al., 2010) are interpreted as the processes responsible for producing a basal harzburgite layer at higher temperatures (Shi et al., 1998), possibly related to subduction or magmatism of the Late Cretaceous Carmacks Group (Francis et al., 2010; Peslier et al., 2000b). The bimodal suites overlie a zone of low seismic velocity that is attributed to anomalously hot mantle (Frederiksen et al., 1998) and broadly correlates with a zone of high resistivity interpreted from magnetotelluric models (Ledo et al., 2004).

The presence of a significant number of the aluminous augite-bearing xenoliths in Kostal Lake and Summit Lake has been well documented in numerous studies (Brearley et al., 1984; Francis et al., 2010; Morales & Tommasi, 2011; Peslier et al., 2002). Clinopyroxene appears as interstitial grains in triple junctions and/or film-like along grain boundaries, often engulfing olivine grains. This has been interpreted to reflect a secondary origin of clinopyroxene, related to "melt percolation in static conditions" (Morales and Tommasi, 2011). Peslier et al. (2002) interpreted that the aluminous augite in KL and SL represents cumulates formed by the reaction of alkaline melts with a peridotitic wall rock of the lithospheric mantle and proposed veins of discordant dunite, wehrlite, pyroxenite and opx-poor lherzolites crosscutting a lithospheric mantle characterized by Cr-diopside peridotite. From the presence of phlogopite crystallized from ingressing melt in wehrlites, Canil and Scarfe (1989) suggest that metasomatism of the upper mantle beneath Kostal Lake post-dates the initial phase of volcanism in this region (3-5 Ma) and was prior to the minimum post-glacial age of entrainment (~400 B.P.)

The higher modal contents of clinopyroxene (cpx), resulting in opx-poor lherzolites and wehrlites in SL and KL, have been attributed to reactions between host peridotite and alkaline melts under several possible scenarios. At static conditions olivine + cpx first crystallize when peridotite starts to react with the melt followed by crystallization of olivine $\pm$ cpx $\pm$ opx at lower temperatures, still in excess of 1200°C (Morales and Tommasi, 2011; Peslier et al., 2002). A scenario based on studying exposed ophiolites proposes that as basaltic melts formed at high pressures infiltrate the shallow lithospheric mantle, olivine crystallizes at the expense of pyroxenes forming dunites as such melts are saturated only in olivine at low pressures. In these replacive dunites, the increase in liquid fraction and respective increase in porosity, coupled with the higher permeability of dunite compared to pyroxene-bearing rocks, form high-permeability channels favoring the flow of ascending melt (Kelemen et al., 1995). The migrating melts become increasingly richer in orthopyroxene (opx) component as they continue to react with peridotites, thus forming harzburgites. As the reaction progresses, melts are then enriched in clinopyroxene (cpx) component, resulting in the formation of lherzolites, websterites, and clinopyroxenite. (Chin et al., 2020; Kelemen et al., 1992). Alternatively, Peslier et al. (2002) proposed a cumulate origin

for the lithospheric mantle beneath SL and KL where "Cr-diopside peridotite is crosscut by veins of discordant dunite, wehrlite, pyroxenite and opx-poor lherzolites".

In their 2011 study of Summit Lake xenoliths, Morales and Tommasi suggest the development of a 'ghost lithosphere' (Vauchez & Garrido, 2001) induced by reactive melt percolation, defined as a transitional zone between the lithosphere and the asthenosphere which retains the fossil lithospheric seismic anisotropy but has lower seismic velocities.

Peslier et al. (2002) remark that Summit Lake and Kostal Lake are the most proximal to the craton and hypothesised that the contact between the craton and the Cordillera facilitates the circulation and entrapment of melts at lithospheric mantle depths through ductile shear zones as a mechanism that explains this melt-host rock interaction. Canil and Russell (2022) compared Summit Lake xenoliths located ~20km from the Cordillera-craton boundary to xenoliths in Mount Timothy, ~160 km further west. From their thermobarometry results, they propose a thinner lithosphere by 20 km and a hotter Moho by 200 °C for Summit Lake at least at the time of xenolith entrainment ~28 Ma., possibly due to focused heat during convection favored by the vertical step in crustal depth at the Cordillera-craton boundary, referred to as edge convection.

Osmium isotopic analyses of mantle xenoliths from different volcanic localities along the southern Canadian Cordillera revealed middle Proterozoic model formation ages (1.12 ± 0.26 Ga) (Peslier et al., 2000a) for the mantle lithosphere of the northern Canadian Cordillera in contrast with older, early Proterozoic basement of cratonic North America (~1.8 to 2.3 Ga) (Nelson et al., 2013) and the younger rocks (0.5 Ga) that make up the overlying terranes (Peslier et al., 2002). This temporal gap suggests that there is no direct genetic relationship between the accreted terranes and mantle lithosphere beneath the Canadian Cordillera (Cook et al., 2004; Peslier et al., 2000a; Snyder et al., 2002). The model age of the mantle lithosphere is also discordant with those of generally accepted rifting events that affected the western North American margin at ~1.4 Ga (Höy, 1989), ~0.70–0.76 Ga (Powell et al., 1993; Wingate & Giddings, 2000) and ~0.57 Ga (Colpron et al., 2002).

Suite	Lat (°N)	Lon (°W)	Mantle Age (Ga)[1]	Eruption Age	Ave. T (°C)	Terrane	Realm
Prindle Volcano (PV)	63.400	141.400	1.1 ± 0.26	6.26 and 3.57 Ma[3]	908[5]	Yukon-Tanana	Peri-Laurentian
Fort Selkirk (FS)	62.783	137.400	1.1 + 0.26	1.08 Ma[3]	962[5]	Quesnellia	Peri-Laurentian
Alligator Lake (AL)	60.416	135.426	1.1 + 0.26	3.3-3.1 Ma[3]	998[6]	Stikinia	Peri-Laurentian
Hirchfield Creek (HC)	59.537	132.942	1.1 + 0.26	Tertiary to recent[2]	910[7]	Cache Creek	Peri-Laurentian oceanic
Llangorse Mountain (LG)	59.367	132.792	1.1 + 0.26	Tertiary to recent[2]	905[7]	Cache Creek	Peri-Laurentian oceanic
Castle Rock (CR)	57.617	130.667	1.1 ± 0.26	Tertiary to recent[2]	981[5]	Stikinia	Peri-Laurentian
Summit Lake (SL)	54.307	122.367	1.1 + 0.26	26 Ma[4]	1090[8]	Slide Mountain	Peri-Laurentian
Jacques Lake (JL)	52.580	121.050	1.1 + 0.26	Tertiary to recent[2]	988[5]	Quesnellia	Peri-Laurentian
Big Timothy (BT)	52.105	120.930	1.1 + 0.26	0.4 Ma[4]	959[9]	Quesnellia	Peri-Laurentian
Kostal Lake (KL)	52.173	119.947	1.1 + 0.26	7750 BP[4]	1002[10]	North American Strata	Laurentian
Rayfield River (RR)	51.327	121.108	1.1 ± 0.26	6-10 Ma[4]	912[9]	Quesnellia	Peri-Laurentian
Lightning Peak (LP)	48.879	118.530	1.1 + 0.26	2.5 Ma[4]	1000*	Quesnellia	Peri-Laurentian

Table 1-1. Location, temperature, and surface tectonic units of the twelve xenolith suites in this study. (1) Peslier et al. (2000a). (2) Francis et al. (2010). (3) Edwards and Russell (2000). (4) Peslier et al., (2002). (5) Prescott (1983). (6) Francis (1987). (8) Brearly et al. (1984). (9) Greenfield et al. (2013). (10) Canil and Scarfe, (1989). (*) average estimation for the cordillera, data not available.

1.4 Xenolith Textures

The peridotite deformation cycle proposed by Mercier and Nicholas (1975) and revisited in Chin et al. (2021) describes the evolution of microtextures as a result of increasing strain (Figure 1-1). Here, a coarse protogranular texture is interpreted to correspond to undeformed (low strain) peridotites. As strain progressively increases, a porphyroclastic texture develops. Further strain increase causes a mylonitic texture to develop. Under static conditions, grains progressively anneal to minimize the internal stored strain energy, and olivine grains are reconfigured in an equigranular texture (deformation cycle I, Figure 1-1). A "transitional" texture, where strain-free olivine tablets partially overprint the previous porphyroclastic or mylonitic texture, develops as a consequence of the stored strain energy as post-deformation annealing begins. Since the stored strain energy required for tablet formation was acquired in a previous deformation event leading to the precedent porphyroclastic to mylonitic texture, the transitional-tablet texture represents an interruption, or "sub-cycle", relative to the main deformation cycle (Chin et al., 2021). This transitional texture between either porphyroclastic or mylonitic textures and equigranular textures has almost exclusively been observed in cratonic kimberlites prior to this study (Chin et al., 2021 and references therein).

The textures are classified according to a combination of grain and meso-scale fabric characteristics. Coarse, undeformed protogranular samples generally lack foliation. The gradation from protogranular to porphyroclastic includes the development of a bimodal grain size

distribution and a foliation defined by compositional banding and/or grain shape preferred orientation. Relative to porphyroclastic, mylonitic textures contain a greater proportion of subgrains mantling fewer porphyroclasts, indicative of dynamic recrystallization. The transition to the equigranular texture corresponds to the peak strain imposed on the rock and is marked by a rapid deformation "sub-cycle" corresponding to the enigmatic "transitional" texture followed by an increase in grain size and a decrease in aspect ratio, with the exception of the marked shape preferred orientation observed in the equigranular tabular texture. Peridotite melt depletion and recrystallization via metamorphic processes are thought be the processes responsible for the transition from equigranular to protogranular (Chin et al., 2021) thus finalizing the completion of the cycle.

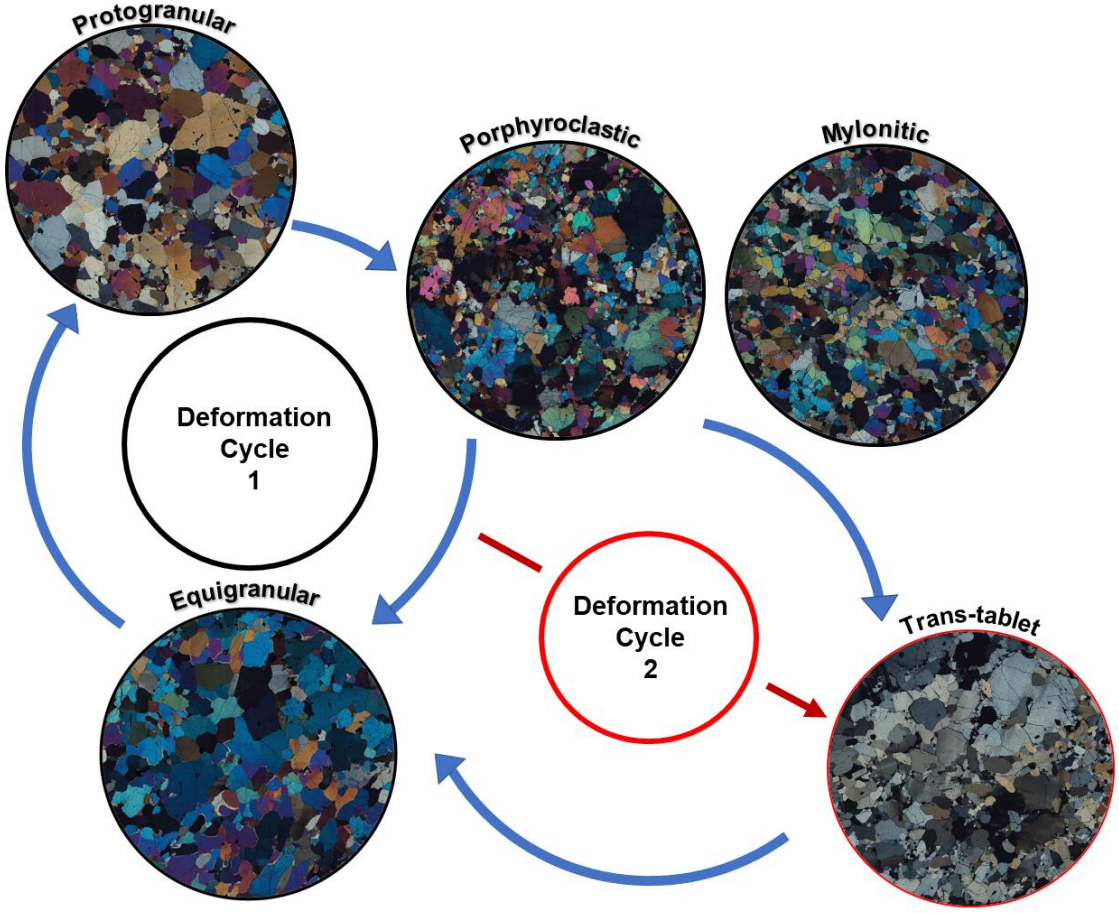

Figure 1-1. Peridotite deformation cycle. Modified after Chin et al., (2021) using photomicrographs from Kostal Lake samples in this study. The scale is approximately the same in all photomicrographs.

We base our definitions of these textures on the definitions proposed by Mercier and Nicholas (1975); Chin et al. (2021); Behr and Hirth (2014) and Bernard and Behr (2017), as well as some of our own petrographic observations and EBSD results.

1.4.1 Protogranular texture

Protogranular represents the initial texture in the deformation sequence of mantle xenoliths and is indicative of an undeformed lithosphere (Chin et al., 2021; Mercier & Nicolas, 1975). Although its genesis is not fully understood, Mercier and Nicholas (1975) suggest that it results from recrystallization during partial melting and that "it may develop first in a harzburgitic paragenesis with high Al-Ca enstatite or alternatively in a high-Al pigeonite-bearing peridotite". Samples with protogranular texture exhibit moderate variation in olivine grain size (1-3mm). Olivine grains are generally equant and subhedral. Grain boundaries are notably curved and irregular and 120 triple junctions are generally absent. Foliation is generally absent or weak. When present, it is defined by weak elongation of few olivine grains with aspect ratios of 2:1 and/or the presence of bands defined by composition and/or grain size. Orthopyroxene is generally coarse (1-5mm), equant and anhedral with many grains showing exsolution lamellae. Clinopyroxene is relatively less abundant and finer-grained as cpx crystals develop in interstitial spaces. Spinel grains appear as interstitial and occasionally as inclusions in opx and olivine. They lack a preferred shape orientation and are not organized in bands or strings of grains.

1.4.2 Porphyroclastic texture

Porphyroclastic samples are defined by the presence of elongate, anhedral olivine and orthopyroxene porphyroclasts with curved boundaries mantled by a finer-grained groundmass resulting from dynamic recrystallization (Bernard & Behr, 2017; Chin et al., 2021; Mercier & Nicolas, 1975). Foliation is more pronounced than in protogranular textures and defined by bands of dynamically recrystallized neoblasts and the parallel long axes of elongated porphyroclasts with aspect ratios of up to 5:1 defining a grain shape preferred orientation. The grain shape fabric is generally parallel to the orientation of compositional banding. Roughly equant, strain-free, fine-grained olivine neoblasts (150μm -1mm) account for up to 90% of nearly pure olivine bands and can also occur as clusters around olivine porphyroclasts. Planar kink bands at high angle to the

longitudinal axis of elongation result from progressive rotations within olivine porphyroclast interiors, indicative of crystal-plastic deformation.

1.4.3 Mylonitic texture

Mylonitic samples are strongly foliated. They display parallel, 5-10 mm-thick compositional bands. Olivine grains are mostly fine-grained (< 1mm) and vary from equant to elongate. Olivine and orthopyroxene porphyroclasts are smaller than in the protogranular and porphyroclastic samples and have smaller aspect ratios up to 3:1. Long axes of aligned elongate grains are parallel to the compositional banding foliation, defining a grain shape preferred orientation. Reduction in grain size, presence of a strong foliation, and the development of a strong crystallographic preferred orientation (CPO) are evidence for pervasive dynamic recrystallization during dislocation creep. Both equant and tabular subgrains occur much more frequently than in porphyroclastic samples, to the extent that relict and recrystallized grains may be difficult to distinguish. Spinel grains have an elongated film-like appearance, concordant with the overall foliation.

1.4.4 Transitional texture

This texture has been interpreted as an intermediate stage from a strongly porphyroclastic or mylonitic texture to annealed mosaic equigranular or tabular equigranular texture (Boullier & Nicolas, 1975; Chin et al., 2021; Mercier & Nicolas, 1975). Here, strain-free olivine tablets with straight grain boundaries develop as a consequence of reduction in stored strain energy from the previous deformation stage and are superimposed on the pre-existing fabric. Due to these characteristics, the tablets lack subgrains and undulose extinction and present a low internal distortion and low aspect ratios. The average grain size of these newly developed tablets is intermediate between those of neoblasts and porphyroclasts.

Xenoliths exhibiting this transitional texture are most mostly found in cratonic kimberlites (Chin et al., 2021). Their formation has been attributed to annealing in the presence of a grain-boundary fluid during kimberlite ascent (Arndt et al., 2010; Chin et al., 2021; Drury & Roermund, 1989). However, post-deformation annealing experiments indicate that annealing at high temperatures under dry conditions could also promote the development of this texture (Boneh et al., 2021; Boneh et al., 2017). Coarse, elongated porphyroclasts are mantled by sub-500-micron

neoblasts. The presence of strain-free tablets mostly bordering the porphyroclasts is pervasive. It is worth noting that the orientation in the tablets generally conforms to the overall foliation, but some tablets are oriented at a high angle to the foliation.

1.4.5 Equigranular textures

Samples with equigranular textures are interpreted to be fully annealed and exhibit typically straight grain boundaries resulting in abundant 120^{o} triple junctions. Based on our observations of fabric development and aspect ratios and following the classification in Mercier and Nicolas (1975), these can be divided into two sub-categories: mosaic equigranular and tabular equigranular. There are currently few experimental insights into the processes and conditions of recrystallization that will determine which of these annealed sub-categories prevails, as multiple combinations could result in the same texture.

Equigranular samples range from 1 to 3 mm in olivine grain size. Typically, 85 percent of olivine grains are equant and euhedral to subhedral. Pyroxenes are less abundant in samples with equigranular texture than in other textures. Foliation is absent in most cases, but a weak foliation may be present in few samples, defined by compositional banding and/or the elongation of few olivine grains with aspect ratios of 2:1. The bands are 3 to 6 mm thick and consist of coarse-grained (1-3 mm) olivine layers alternating with bands containing predominantly orthopyroxene and smaller percentages of fine-grained olivine and clinopyroxene. Within the pure olivine bands, grains are euhedral and present abundant 120° triple-junctions, whereas olivine in contact with pyroxenes exhibit strongly curved grain boundaries.

1.4.5.1 The mosaic equigranular subtype

This subtype of the equigranular texture is characterized by mostly equant, euhedral grains of olivine, enstatite and diopside arranged in a mosaic pattern with frequent 120° triple-junctions. There is little variation from the average grain size. Olivine subgrains are rare and wider than in the rest of the textures. Foliation is absent in most cases, but some samples may present a very weak foliation defined by compositional banding and/or the elongation of few olivine grains with aspect ratios of 2:1 that conforms to the overall sense of foliation. The bands are 3 to 6 mm thick

and consist of coarse-grained (1-3 mm) olivine layers alternating with bands containing predominantly orthopyroxene and smaller percentages of fine-grained olivine and clinopyroxene.

1.4.5.2 The tabular equigranular subtype

Olivine grains in this equigranular subtype are also characterized by a rather uniform grain size, straight grain boundaries and abundant triple junctions. They differ from the mosaic type in aspect ratio. Here, olivine presents parallel elongated axes with aspect ratios of up to 4:1, which results in a well-defined foliation. Unlike the "transitional texture", tablets in this texture are not strain-free and present multiple subgrains and undulose extinction. Orthopyroxenes are euhedral to subhedral and less elongated than olivine, with aspect ratios of up to 2:1. Clinopyroxenes are mostly subhedral and interstitial.

1.5 Olivine Crystallographic Preferred Orientations

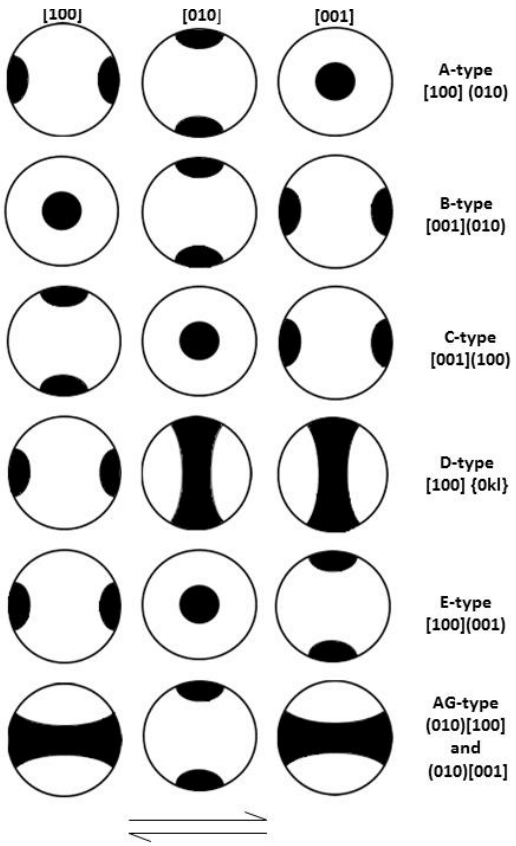

As a result of different configurations of stress, temperature, strain geometry and water content; olivine in mantle peridotites can develop different crystallographic preferred orientations (CPOs), each resulting from deformation accommodated by a different slip system. These CPOs have been observed in nature and thoroughly studied in the laboratory (Jung et al., 2006; Karato et al., 2008; Skemer & Hansen, 2016). Based on the constrains for these variables for each of these fabrics and the changes that trigger the transitions between them, several models have been proposed to predict the presence of these fabrics depending on the tectonic frame (Cao et al., 2015).

Figure 1-2. Schematic representation of six types of olivine fabric (CPOs) and their corresponding slip systems in a simple shear regime following Karato et al., (2008); Skemer and Hansen, (2016) and Michibayashi et al., (2016). Horizontal arrows represent the shear direction or lineation while the vertical direction represents the direction normal to the shear plane or foliation.

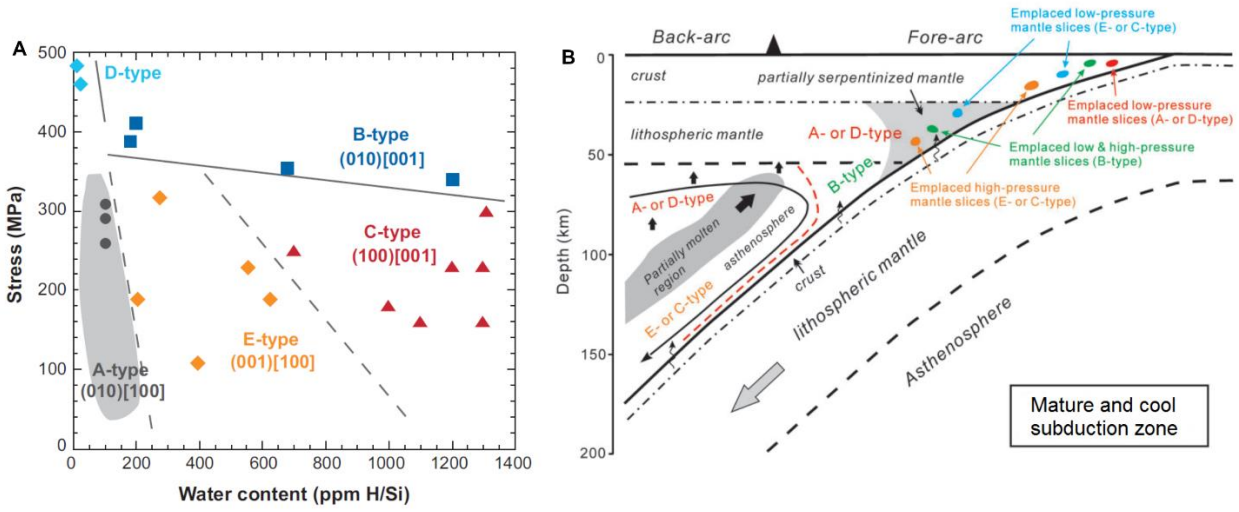

Figure 1-3. (A) constraints on water content and stress in olivine fabric development (taken from Karato et al., 2008) and (B) Schematic illustration showing olivine fabric distributions in mature and cool mantle wedges. Red dashed line in (B) denotes the boundary between olivine B-type and C- or E-type fabrics (taken from Cao et al., 2015).

1.5.1 "Wet" CPO types

The [001](010) slip system of B-type fabric is most commonly found in high water content, low-stress and low-temperature conditions typical of relatively cold lithospheric mantle in subduction zones (Figure 1-3) , despite resulting from high temperature, high stress conditions in the laboratory (Karato et al., 2008). The fast shear wave splitting polarization in olivine B-type fabric aligns horizontally, sub-perpendicularly to the flow direction in the shear plane (trench parallel).

C-type fabric involves slip on [001](100) as is associated with water-rich, high-temperature and relatively high-stress conditions. This fabric has been observed at convergent tectonic settings, preferentially in xenoliths sourced from the deeper back-arc mantle immediately atop the descending slab and in the deep-mantle (Cao et al., 2015; Karato et al., 2008; Katayama et al., 2005) (See Figure 1-3).

The [100] (001) E-type fabric is only rarely observed (Karato et al., 2008; Katayama et al., 2004). Due to the increased water content relative to the A-type fabric at the same low-stress and high-temperature conditions, this fabric has been interpreted to occur in fore-arc peridotites (Tommasi et al., 2006) and the asthenospheric mantle (Figure 1-3). Furthermore, if E-type fabric is indeed dominant in the asthenosphere, olivine [001] axes will be vertical, resulting in stronger

azimuthal anisotropy (e.g., amplitude of shear wave splitting) and weaker radial anisotropy ($V_{SHorizontal}/V_{SVertical}$) relative to the A-type fabric in the lithosphere (Karato et al., 2008).

1.5.2 "Dry" CPO-types

Olivine A-type fabric is by far the most commonly observed in upper mantle xenoliths. This is likely due to the fact that the (010)[100] is the preferred, easy-slip system in olivine. The A-type fabric in olivine corresponds to "dry", low-stress and low-temperature conditions (Karato et al., 2008). The removal of water by partial melting in the shallow asthenosphere, explains the transition from "wet" C- or E-type to A-fabrics (Karato et al., 2008), thus explaining in the preponderance of this fabric in the lithosphere (Figure 1-3).

D-type fabric similarly reflects anhydrous conditions of recrystallization, but the [100]{0kl} slip system is activated at higher stress conditions (Karato et al., 2008). Tectonic models mostly place this fabric in coexistence with A-type with localized values of stress determining the presence of one or the other (Figure 1-3).

The origin of the AG-type fabric is controversial despite being the second most common fabric in mantle peridotites (Michibayashi et al., 2016). It requires at least two slip systems, (010)[100] and (010)[001] in simple shear but may result simply from [100](010) slip in axially symmetric shortening (Michibayashi et al., 2016; Skemer and Hansen, 2016). Aside from these complex slip and strain geometry conditions, the presence of melt during plastic flow can also induce the formation of this fabric (Chin et al., 2020). Alternatively, the AG-fabric has been proposed to be induced by a shape preferred orientation (SPO) of olivine grains in composite mantle xenoliths correlated with increased melt-rock interactions (Chin et al., 2020; Qi et al., 2018).

1.6 Previous characterizations of microstructures and CPOs in Cordilleran xenoliths

To understand the deformational history, thermal conditions and the processes leading to the spatial distribution of seismic anisotropy of the lithospheric mantle, previous studies have

characterized the microstructures and CPOs in mantle xenoliths of a few locations in the Canadian Cordillera and Alaska. Littlejohn and Greenwood (1974) characterized a rather limited set of xenoliths from Nicola Lake (not in this study), Jacques Lake and Castle Rock in terms of their CPOs. Ji et al. (1994) studied xenoliths from three suites in the central and northern part of the Cordillera: Nunivak Island (NI, not included in this study), Alligator Lake (AL) and Castle Rock (CR). They found a predominance of protogranular and granuloblastic textures. Based on U-stage measurements of crystallographic orientations combined with visual analysis of CPO types, the olivine CPO patterns for CR correspond to D-type fabric. In the case of AL, samples exhibit both AG- and A-type fabrics, and for NI, AG-type fabrics dominate. Using a similar approach, Saruwatari et al. (2001) characterized xenoliths from three suites located in the southern half portion of the Canadian Cordillera: Summit Lake (SL), Jacques Lake (JL) and West Kettle River (not in this study). In these suites, the protogranular texture is dominant. The olivine CPO types in SL appear to be A- and D-type. In JL, their results resemble A- and AG-types. It is worth reiterating that although the CPO patterns are clearly discernible, these studies lack calculations of metrics that can help confirm the CPO type (e.g., BA-index) or its strength (e.g., J-index and/or M-index). Furthermore, the number of plotted olivine grains is generally low (<200), which can affect the confidence in the representation of the CPO pattern. Morales and Tomassi, (2011) studied xenoliths from SL and reported evidence of thermal annealing and reactive melt percolation. The olivine CPO patterns of 22 xenoliths indicate almost exclusively D-type fabrics. The J-index, quantifying the strength of the CPO, varies from 4.5 to 10.8, with the lowest values corresponding to wehrlites and the highest to lherzolites.

1.7 Seismic anisotropy in the Northern Cordillera

Understanding the anisotropic properties of the upper mantle has become an increasingly important tool in tectonic studies as a means to characterize mantle flow and deformation processes (Ben Ismail & Mainprice, 1998). Seismic anisotropy in the upper mantle results from to the tendency of the minerals in the mantle lithosphere peridotites to develop aligned crystallographic axes, thus developing crystallographic preferred orientations (CPOs) (Skemer and Hansen, 2016). Olivine constitutes the dominant mineral phase in the upper mantle (>60%) and it is the most inherently anisotropic mineral in mantle peridotites. In most types of LPO, the olivine fast a-axis

([100]) aligns with the direction of mantle flow. Development of LPO in olivine typically results from dislocation creep (e.g., Karato et al., 2008). A shear wave splits into two quasi-orthogonal shear waves upon entering an anisotropic medium. As they travel through the fast and slow direction of propagation in the anisotropic medium, a delay time accumulates between the two. Shear wave splitting is therefore defined by two parameters, the fast direction of wave propagation and the accumulated delay time between the fast and slow components. These parameters reflect an integrated measurement along the nearly vertical receiver-side ray path and therefore have poor vertical resolution. Shear wave splitting is analogous to the optical birefringence of minerals under polarized light.

Seismic anisotropy of the lithospheric mantle is generally quantified using two different approaches: (1) geophysical studies (seismic tomography, SKS splitting analysis and receiver functions), and (2) direct characterization of anisotropic properties of mantle xenoliths. The first one allows to cover large areas, depending on the seismic station coverage; and identifies the fast direction of wave propagation and its magnitude. This is very useful in comparisons of mantle flow to apparent plate motion or relative to tectonic units. Seismic anisotropy derived from seismic tomography is the product of an inversion that allows to quantify seismic anisotropy at a given depth range. Resolution of seismic tomography models vary depending on the types of seismic data (surface waves vs body waves) and the seismic station coverage. However, SKS splitting analysis records an integrated measurement along the nearly vertical ray path on the receiver side, resulting in poor vertical resolution. The second approach involves a direct characterization of the seismic properties of the rock but the original orientation of the xenolith in the mantle is unknown. In addition to this, the characterization of anisotropy at a certain location assumes that the studied xenoliths are representative of properties of the mantle lithosphere (hence the tendency to publish the average seismic properties of all samples).

At crustal depths, anisotropy studies of the Cordillera using seismic data show a general NW-SE alignment of the fast polarization direction matching the orientation of the major faults and terrane boundaries, followed by a counterclockwise rotation south of the McKenzie Mountains resulting in a SW-NE orientation (Estève et al., 2021; McLellan et al., 2018). In the proximity of the Cordilleran deformation front (CDF), the alignment of the fast axes roughly follows the contours of the CDF.

At upper mantle depths, a sharp contrast in azimuth is observed between measurements north and south of the Liard transfer zone (LTZ), the inferred westward extension of a Late Cretaceous rifted margin boundary. North of the LTZ, fault-parallel alignment of the fast axis near the 3 main strike-slip faults in the Cordillera (Teslin, Denali and Tintina) suggests mechanical coupling between the crust and lithospheric mantle during at least part of the Paleogene to mid-Neogene, when dextral strike-slip displacement occurred (Audet et al., 2016; McLellan et al., 2018; Rasendra et al., 2014). Estève et al. (2020) proposed that the Tintina fault chiseled off fragments of the Laurentian craton and displaced them over hundreds of kilometers between the Late Cretaceous and the Eocene. These fast-axis orientations contrast with the results of Tarayoun et al. (2017), where sub-Moho azimuths (30-60 km in depth) vary between NE-SW and NW-SE orientations.

South of the LTZ, fast axis directions are subparallel to the general trend of fast axes observed in the Canadian Shield. This observation implies that the two regions have preserved similar fabrics. Audet et al. (2016) suggest that this reflects the extent of the North American craton west of the CDF. Magnitudes of anisotropy are largest in stations near strike-slip faults (Audet et al., 2016).

Few studies have characterized the seismic anisotropy of mantle xenoliths in the Canadian Cordillera. Ji et al. (1994) found very similar average seismic anisotropy patterns for *Vp*, *A(Vs)*, fast polarization direction (Φ) and delay time (δt) in xenoliths from Castle Rock (CR), Alligator Lake (AL) and Nunivak Island (NI). Averages per suite of maximum *Vp* ranged between 8.1 and 8.3 km/s, and maximum *A(Vs)* ranged between 3.0 and 5.5 %. This relative homogeneity is more notable in Castle Rock and Nunivak Island, where the LPOs are consistently similar, irrespective of microstructure and temperature. Exceptionally, Alligator Lake samples showing granuloblastic equant texture (equigranular mosaic in this study) or tabular texture (equigranular tabular in this study) recorded weaker LPOs and consequently lower anisotropic values, possibly indicating that the mantle at AL is heterogeneous in seismic anisotropy in the depth range of the lithospheric mantle.

Saruwatari et al., (2001), similarly described three southern suites: Summit Lake, Jacques Lake and West Kettle River. The average anisotropy calculated from petrofabrics is 7.5% for

V_p and 4.8% for V_s. Consistently with these results, Morales and Tommasi (2011) studied 22 mantle xenoliths from Summit Lake and calculated P- and S-waves anisotropy values for lherzolites of 8 and 5% respectively for spinel lherzolites. In wehrlites, however, these values were lower (6.5 and 3.5%, respectively) due to a recrystallization of olivine resulting in a weaker CPO.

These previous characterizations of anisotropic properties in xenoliths of the Canadian Cordillera suggest a very homogeneous mantle. However, they only cover a limited area defined by a cluster of northern suites (Ji et al., 1994) and a cluster of southern suites (Morales & Tommasi, 2011; Saruwatari et al., 2001). Furthermore, all these suites are located on Peri-Laurentian terranes. In this study, we will analyse the seismic anisotropy of mantle xenoliths distributed along the entire latitudinal range of the Canadian Cordillera and will include one suite located on the Laurentian realm.

1.8 Objectives

We surveyed thin sections of 195 xenoliths sourced from twelve volcanic centers that are distributed across a broad latitudinal range: Prindle Volcano (PV), Fort Selkirk (FS), Alligator Lake (AL), Hirschfeld Creek (HC), Langorse Mountain (LM), Castle Rock (CR), Summit Lake (SL), Jacques Lake (JL), Kostal Lake (KL), Big Timothy (BT), Rayfield River (RR) and Lightning Peak (LP). The volcanic centers are located on five terranes that are of Laurentian or Peri-Laurentian affinity (summarized in Table 1-1). The criteria used in collecting the samples are well described in Eiché et al. (1987), Francis et al. (1987), and Peslier et al. (2002), and collection was biased toward fresh samples and was based on visual estimates of the modal proportion of pyroxene.

In this study we present a characterization of textures, deformation and estimated seismic properties in mantle xenoliths of twelve localities in the Canadian Cordillera. The goals of the study are to address the following questions:

1. Do the mantle xenoliths reflect the disparate tectonic histories of pre-orogenic cratonic mantle and the mantle underlying the modern Cordilleran orogen?
2. Can the EBSD data shed light on the processes at work in the Cordilleran lithospheric mantle during assembly of the orogen and subsequently?

3. Finally, how do the properties of the mantle inform the interpretations of geophysical imaging of the Cordillera, particularly in light of variations in seismic velocities in proximity to crustal and lithospheric-scale transform faults?

Our analysis of microstructures and seismic properties of mantle xenoliths indicates that the mantle underlying the Northern cordillera is weakly deformed, with a preponderance of coarse equigranular and protogranular textures; thus suggesting that the mantle was decoupled from the shortening stresses experienced by the crust during the assembly of the Cordillera.

CHAPTER 2

Study area

2.1 Tectonic units

The Canadian/Northern Cordillera is part of the North American Cordillera, a classic accretionary orogen which extends for 6400 km roughly parallel to the west coast of the continent with a width of approximately 800 km. This orogenic belt formed by consecutive accretion of terranes of different ages and origins to the stable margin of ancestral North America (Laurentia) during the Mesozoic before the mid-Cretaceous (Irving et al., 1996; Monger et al., 1982). These terranes are composed mostly of volcanic arc sedimentary deposits, volcanic intrusive rocks, oceanic sedimentary rocks and slivers of oceanic crust. The accretionary stages were followed by northward, orogen-parallel displacement along large dextral strike-slip faults due to the motion between the Pacific Ocean basin and the North American continent (Gabrielse, 1985). Most of the dextral displacement occurred along the Denali and Tintina faults with the latter being mostly inactive today due to unfavorable contemporary stress conditions for strike-slip faulting and, therefore, low-magnitude seismicity (Marechal et al., 2015).

From east to west across the orogen, the character of the terranes transitions from autochthonous to allochthonous. The Yukon-Tanana terrane comprises displaced, autochthonous sedimentary and metamorphic rocks of North American origin (Edwards and Russell, 2000 and references therein). The Slide Mountain terrane comprises Late Paleozoic sequences of mafic volcanic rocks interbedded with clastic rocks and chert that separate the North American craton from terranes with island arc affinities (Roback et al., 1994). These rocks are interpreted to have formed in the Slide Mountain Ocean, which was subducted under the North American plate (Roback et al., 1994 and references therein). Quesnellia and Stikinia are allochthonous terranes which are separated intermittently by the Cache Creek terrane and the dextral-transcurrent, north-northwest trending Findlay fault (Minehan, 1989). These terranes have been interpreted to have formed in oceanic island or volcanic arc tectonic settings separate from North America, based on the abundance of volcanoclastic and volcanic rocks of calc-alkaline signature, their crustal thicknesses in the range of typical island arcs and their position next to ocean floor complexes (Monger et al., 1982). Cook et al. (2004) observed the presence of the lower crustal layered

sequence (LCLS) beneath accreted rocks of the Quesnellia terrane and interpreted this terrane as a detached, thin flake that was emplaced over North American strata from hundreds of kilometers to the west. The eastern edge of Stikinia has been interpreted as a tectonic wedge that was driven into the western margin of ancient North America (Cook et al., 2004). According to the reflection seismology sections, Stikinia occupies the entire crust to the Moho, whereas Cache Creek, Quesnellia and Slide Mountain are thin crustal slivers trusted over west dipping North American strata during accretion (Cook et al., 2004).

2.2 Realms of the northern Cordillera

As a way of building a comprehensive, but simplified framework of the tectonic history, Nelson et al. (2013) divided the northern Cordillera into four large-scale paleogeographic realms, each containing several related terranes based on their region of origin as follows:

The Laurentian realm constitutes the innermost realm of western North America. It represents the western flank of present-day cratonic North America. Its rocks are related to the ancient cratonic core and include overlying strata that were deposited along its margin. The stratigraphy of the Laurentian realm comprises 2.3 to 1.8 Ga cratonic basement overlain by Paleoproterozoic through Triassic cover successions and topped by younger synorogenic clastic deposits. The autochthonous and parautochthonous character of this realm contrast with the more distant origin and /or evolution of the other three realms.

The peri-Laurentian realm lies immediately west of the Laurentian realm. Their contact is marked by intermittent fragments of the Slide Mountain terrane. Aside from the Slide Mountain terrane, the peri-Laurentian realm includes the Yukon-Tanana, Quesnel, Stikine, Cache Creek, and Bridge River allochthonous terranes. These presently pericratonic terranes including continental fragments, accretionary complexes, back-arc marginal ocean basins and fore-arc accretionary complexes were originally part of the western Laurentian margin. It wasn't until the establishment of a continental arc on the western margin of Ancestral North America in Devonian time, followed by the Late Devonian to Permian opening of the Slide Mountain Ocean in the back arc and oceanward migration of the frontal arcs that these terranes began to evolve as a distinct realm.

Closure of the Slide Mountain Ocean eventually led to collision and suturing of the peri-Laurentian terranes to the Laurentian margin in the Mesozoic

The Arctic northeastern Pacific realm includes the Arctic Alaska, Farewell, Kilbuck, and Alexander terranes. These pre-Devonian terranes of peri-Baltican-Caledonian or peri-Siberian origin migrated westward into the northeastern paleo-Pacific region during the Silurian-Devonian. This was followed by multiple arc-development events leading to local mountain-building events in the Devonian-Jurassic and an unusual episode of Triassic large igneous provinces. These terranes include early Jurassic arc, back-arc, and accretionary terranes transported together with the northeastern paleo-Pacific basin.

The Coastal realm is the westernmost realm and comprises the Crescent, Chugach, Prince William, Pacific Rim, and Yakutat terranes. These accretionary complexes are the youngest terranes of the Cordillera, having originated in the Mesozoic to Paleogene, proximal to or on the eastern side of the Pacific basin. These terranes have been the last to accrete with some still accreting along the present North American-Pacific plate boundary. They consist of later Mesozoic to Cenozoic accretionary prisms and seamounts detached from Pacific oceanic plates during subduction beneath the North American margin.

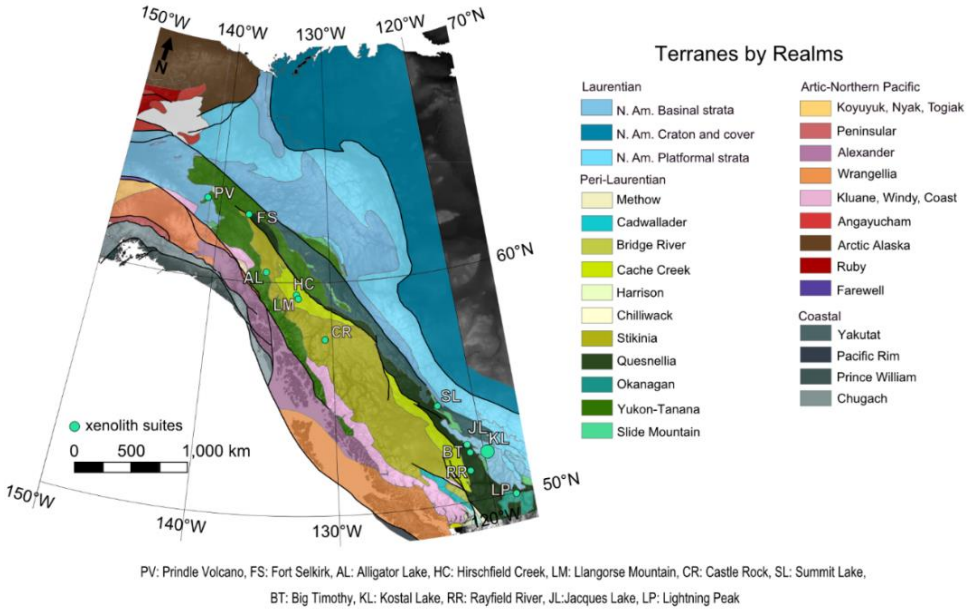

Figure 2-1. Map of the study area showing the location of mantle xenolith suites investigated and the tectonic terranes grouped by realms (Nelson et al). Access to terranes shapefile through McGill's GIC licence.

CHAPTER 3

Methods

3.1 Sample preparation and selection for EBSD analysis

Correct preparation of thin sections is an essential step in the collection of EBSD data. Poorly prepared samples can result in poor EBSD patterns and inconsistent results. Two aspects are crucial in this regard: (i) the orientation in which the rock is cut with respect to the foliation and lineation and (ii) the "smoothness" of the thin section after polishing.

The vast majority of thin sections in this study are from a previously collected sample set and were cut in an arbitrary orientation. The arbitrary thin section orientation means that the apparent absence of a grain shape preferred orientation cannot be considered diagnostic as the section might be cut at a high angle to elongate grains. For a more straightforward interpretation of CPO results, thin sections would be ideally cut perpendicularly to foliation and parallel to lineation. In this study, the orientation of the thin sections with respect to the deformation foliation was unknown. This is commonly the case for most mantle xenoliths. To correct for this limitation, the EBSD data was rotated to a common framework during the post-acquisition stage. Note, however, that the arbitrary thin section orientation does inhibit interpretation of the crystallographic orientation results (see section 5.1.4).

Poor polish of thin sections leads to weak diffraction patterns and potential mis-indexing. Since many of the thin sections used in this study were made approximately 20 years ago, they required a preliminary stage of hand polishing before the final polishing stage using colloidal silica at 0.3 microns. These samples underwent manual polishing for 15 minutes using a polishing pad and 10-micron silicon carbide powder, followed by 15 minutes at 5 microns using alumina powder and 15 minutes at 1 micron using alumina powder. Polishing of most (old and new) thin sections was finalized using 0.02-micron colloidal silica suspension in a rotatory device (MR Semicon Lab One) for two to three hours. However, a smaller subset of samples that were recently made specifically for this study was polished using colloidal silica in a Fisher Vibromatic polisher for 6 to 12 hours.

Prior to EBSD analysis all thin sections were characterized with the use of a petrographic microscope and/or photomicrographs showing the full thin section for a better visualization of

existing microstructures. A subset of samples was chosen for EBSD analysis based on the following criteria:

1. We prioritized the apparently most deformed sample(s) per suite.
2. We included at least one sample per observed texture per suite, as long as the samples were suitable for scanning.
3. We favored samples with sufficient olivine (>40%) content for CPO characterization.
4. We favored "larger samples", where the rock covers most of the thin section to maximize collected EBSD data.

3.2 Electron-backscattered diffraction (EBSD) data acquisition and treatment

Crystallographic orientations of olivine, diopside, enstatite, and spinel were measured by indexing electron-backscattered diffraction patterns in the SEM-EBSD. For all samples, crystal orientations were determined by the Aztec software from Oxford Instruments HKL. SEM/EBSD work used a Hitachi SU-5000 Variable Pressure-SEM equipped with a field emission source and Oxford SDD EDS and EBSD detectors at McGill University. Beam acceleration voltage was set to 20 kV and current was set to spot intensity 60 at a working distance of 18 mm under low vacuum operating conditions. EBSD maps were collected with step sizes between 12 µm and 47 µm depending on grain size. Samples were tilted to 70° in the sample chamber. Due to the geometry of the stage and sample holder, large area scans could only cover around 1/3 of the area of a thin section. To compensate for this, we performed two large area scans per thin section and rotated the second scan 180° around a rotation axis perpendicular to the thin section to bring the two scans into the same sample reference frame. Grain reconstruction was conducted for the two scans independently (see below), but characteristics of complete grains from the two scans were aggregated to generate a representative number of grains. Indexing rates in the raw maps exceed 75%.

Full thin section EBSD scans for a smaller subset of samples (AL45, RR10, KL04, KL37, KL44, KL51, KL55 and KL59) were performed with a Thermo Scientific Apreo scanning electron microscope (SEM), equipped with an Oxford Instruments Symmetry detector at the University of California, Santa Cruz. Beam acceleration was set to 20kV with a current of 13nA. Samples were

coated with a 5 nm-thick carbon coat and scans were collected under a high vacuum from samples tilted to 70° in the sample chamber. Step sizes ranged from 8 to 10 microns.

Post-acquisition data processing was carried out with the with MTEX v. 5.7.0 in Matlab (http://mtex-toolbox.github.io/) (Bachmann et al., 2010; Bachmann et al., 2011; Hielscher & Schaeben, 2008). Some EBSD scans contained areas of particularly poor indexing around the edges due to heterogeneous polish quality. Areas of low-quality indexing were removed by defining polygons that included high quality data and eliminated such poorly indexed areas. After this, indexation rates exceeded 85%. Wild spikes and inaccurately indexed points (MAD > 0.9°) were removed, and rare cases of mis-indexing due to the olivine hexagonal pseudosymmetry were identified and corrected. Grains were reconstructed using a threshold of ≥ 10° for grain boundaries, with grains containing < 10 pixels removed from the analysis. Grain sizes of olivine grains were estimated from the diameter of a circle with the equivalent area measured by the number of pixels within the continuous grain domain. Crystallographic preferred orientation (CPO) of olivine and pyroxenes was assessed by calculating the orientation distribution functions using a de la Vallée Poussin kernel function with a half-width of 10°. The CPO is presented as pole figures based on one crystallographic orientation per grain (lower hemisphere stereographic projection). To evaluate the textures and facilitate inter-sample comparison and comparison with previous studies, the CPO data were rotated to a common reference frame in which the maximum concentration of olivine [100] is aligned with the positive x-direction (east) on the projection and the maximum in the [010] axes is near the y-direction (north-south).

Strength of the CPOs was quantified using the dimensionless J-index (Bunge, 1982), here using one orientation per grain. We also calculated the dimensionless BA-index of the olivine CPOs, which is a function of the eigenvalues of the [100] and [010] axis orientation distribution and is a measure of the symmetry of the CPO (Mainprice et al., 2014). Following Mainprice et al. (2014), we classified the olivine CPOs into three types: 1.) BA-index < 0.35 corresponds to a fiber-[010] with point maxima in [010] and girdle distributions in [100] and [001], 2.) 0.35 < BA-index < 0.65 corresponds to an orthorhombic symmetry characterized by point maxima of all three crystallographic axes, and 3.) BA-index > 0.65, corresponds to a fiber-[100], with point maxima in [100] and girdle distributions in [010] and [001]. In addition, we evaluated intracrystalline

deformation from the intra-granular misorientations, that is the misorientation of each pixel with respect to the average for the grain.

In samples with a distinctive bimodal grain size distribution resulting from dynamic recrystallization we characterized olivine grains as relict or recrystallized following the methodology in Cross et al. (2017). Their method uses the internal distortion of each grain, quantified as the grain orientation spread (GOS, see below), to separate relict and recrystallized grain populations as relict grains are expected to have greater internal distortion than recrystallized grains. The threshold between recrystallized and relict grains is calculated as the knee (furthest point from a line connecting the ends of the trade-off curve) in a cumulative plot of the number of grains versus the grain orientation spread (GOS) for the grains in an individual scan. Once the relict and recrystallized grain populations were identified, we calculated the average grain size, average grain shape factor, average aspect ratio, J-index, M-index and BA-index for each population separately (Table 7-2). Unlike recrystallized grain size paleopiezometry, this method is independent of the grain size measurement and avoids overlapping of different grain populations.

3.3 Definitions of some metrics obtained from EBSD analysis

Orientation distribution functions (ODF): is a function on the orientation space that associates to each orientation *g* the volume percentage of crystals in a polycrystalline specimen that are in this specific orientation (Mtex documentation: https://mtex-toolbox.github.io/ODFTutorial.html). It contains all the crystal orientation information. Its total volume is defined by the crystal symmetry and specimen symmetry (Mainprice et al., 2014). It considers only the orientation of crystals disregarding their shape, position and size. Bunge (1982) defines the crystal orientation by three Euler rotation angles φ_1, Φ, and φ_2 relative to successive rotations about *z*, *x*, *z*.

Misorientation distribution function (MDF): similarly, the MDF is the difference between two orientations $g1$ and $g2$.

Mean angular deviation (MAD): A number in degrees that expresses how well the detected electron backscatter patterns correspond to the actual electron backscatter patterns as estimated by

the Aztex software. It represents the averaged angular misfit between detected and simulated Kikuchi bands (Maitland & Sitzman, 2007).

J-index: This dimensionless index characterizes the strength of the CPO. It is computed as the integral of the square of the orientation distribution function (Bunge, 1982) and ranges from 1 in a random fabric to infinity in a single crystal. Here, it is calculated using one point per grain, representing the average orientation of the grain. This avoids overestimations in the contribution of porphyroclasts in samples with bimodal grain size distributions. It is worth mentioning that other studies use one orientation data per pixel in their computations, which yields higher values for samples with variable grain sizes than using one point per grain (Bernard et al., 2019). We used one point per grain based on the fact that only a small percentage of our samples presents a strongly bimodal grain size distribution.

M-index: Also used to quantify the CPO strength (Skemer et al., 2005), it varies from 0 (for a perfectly random texture) to 1 (for perfect crystallographic alignment). It is the difference between uniform and measured misorientation angles, and hence, a partial measure of the MDF (Ben Ismail & Mainprice, 1998).

BA-index: Quantifies the symmetry of the CPO as a function of the eigenvalues of the [100] and [010] axis orientation distribution (Mainprice et al., 2014). It varies from 0 to 1 and it's defined by the expression:

$$BA = 0.5\,[2 - \left(\frac{P010}{G010 + P010}\right) - \left(\frac{G100}{G100 + P100}\right)]$$

where point (P) and girdle (G) components are compared to the point and girdle sum in order to minimize the dependence of the texture symmetry on the random component (Boneh et al., 2015; Mainprice et al., 2014).

Shape factor: the ratio of the perimeter of the grain over the perimeter of a circle with the same area. It reflects the degree of sinuosity of grain boundaries.

Aspect ratio: the ratio between the two components of a best-fit ellipse approximating a grain with the same area (https://mtex-toolbox.github.io/grain2d.aspectRatio.html).

Aspect ratio = length / width

Misorientation to mean orientation (M2M): the misorientation angles (in degrees) at the indexed positions within a grain relative to the grain mean orientation (Grain Orientation Parameters | MTEX (mtex-toolbox.github.io)).

Grain Orientation Spread (GOS): The average of the misorientation angles to the grain mean orientation Grain Orientation Parameters | MTEX (mtex-toolbox.github.io).

3.4 Seismic properties

Seismic properties of the xenolith samples were calculated from the CPOs of olivine, enstatite, and diopside and their respective modal contents as represented in the EBSD data following Mainprice et al. (2014) and using the MTEX toolbox (Mainprice et al., 2011). Modal abundances of olivine, orthopyroxene and clinopyroxene were normalized as some samples reach up to ~10% of not-indexed areas (Tables 7-2 and 7-3). Unlike the CPO calculations, where we used one point per grain to avoid over-representation of large grains, we used all data points within the polygon showing a well-indexed region in each scan for our computations of seismic anisotropy. The reason behind this is that bigger grains are volumetrically most significant and hence will have a greater impact on seismic waves passing through them. A Voigt-Reuss-Hill averaging (which assumes uniform strain and stress) was applied in all calculations. The effective elastic stiffness tensor C is a fourth-order tensor that allows to relate strain to stress for a given material (Bernard et al., 2021). We calculated the elastic stiffness tensors C_{ij} for all samples at the estimated conditions in the mantle at which the samples crystallized. In situ mineral elastic constants were calculated using the room-temperature values in addition to the temperature- and pressure-derivatives for olivine, enstatite, and diopside (Abramson et al., 1997). We used the average temperature per suite in our calculations, since data for each individual xenolith was not readily available (Table 1-1) and, due to the absence of garnet in the samples and consequent lack of barometry, assumed a uniform pressure of 1 GPa (Peslier et al., 2002). We show the results for representative samples in the same rotated reference frame used for CPO comparison and report

the magnitudes and anisotropies of the seismic velocity parameters in Table 7-3 for comparison to geophysical data. We have not averaged seismic properties of samples from the same sample suites as there are only one to three EBSD datasets for each suite. However, we collected EBSD data for the sample that we judged exhibited the strongest deformation fabric from each sample suite to constrain the upper bound on the mantle anisotropy at each sample location. The anisotropy values produced by MTEX are defined and calculated as follows (Bernard et al., 2021; Mainprice & Silver, 1993):

- **AVp** (Compressional P-wave anisotropy percentage) characterizes difference between minimum and maximum P-wave velocities (Vp) as a percentage of the mean.

$$AVp = 2 * \frac{(Vpmax - Vpmin)}{(Vpmax + Vpmin)} * 100$$

- **Avs (**Compressional P-wave anisotropy percentage). This measurement is relevant for anisotropic studies of shear wave splitting. It is directionally dependent and characterizes the delay time between the fast and slow shear waves.

$$AVs = 2 * \frac{(Vsmax - Vsmin)}{(Vsmax + Vsmin)} * 100$$

- **AVs1** (Shear wave anisotropy percentage of the fast shear wave). This measurement characterizes the azimuthal variations of the fast shear wave.

$$AVs1 = 2 * \frac{(Vs1max - Vs1min)}{(Vs1max + Vs1min)} * 100$$

- **AVs2** (Shear wave anisotropy percentage of the slow shear wave). This measurement characterizes the azimuthal variations of the slow shear wave.

$$AVs1 = 2 * \frac{(Vs2max - Vs2min)}{(Vs2max + Vs2min)} * 100$$

where Vs1 and Vs2 are the fast and slow shear wave velocities, respectively.

CHAPTER 4

Results

4.1 Modal abundances

As in previous studies on Cordilleran xenoliths (e.g., Peslier et al., 2000; Francis et al., 2010), spinel lherzolites are dominant in our studied samples representing 79% of all samples. Harzburgites represent ~6% and are present in JL (1), CR (1), LG (4), AL (2) and KL (3). Wehrlites, representing ~10% are only present in the southern portion of the Cordillera, more specifically in SL and KL. Similarly, KL is the only suite hosting dunites (~3%). The remaining ~2% corresponds to orthopyroxenites (2) and clinopyroxenites (2).

Visual estimates and EBSD data of the mineral composition of xenoliths yield mineral modes ranging from 50 to 99% olivine, 10–30 % orthopyroxene, 3–20% clinopyroxene, 2–5% oxides and 2–10% spinel. The modal abundances resulting from the EBSD analyses are plotted in figure 4-1. The relative abundance of wehrlites in this sample subset is higher, as samples with a higher content of clinopyroxene were selected in order to study the influence of melt in SL and KL.

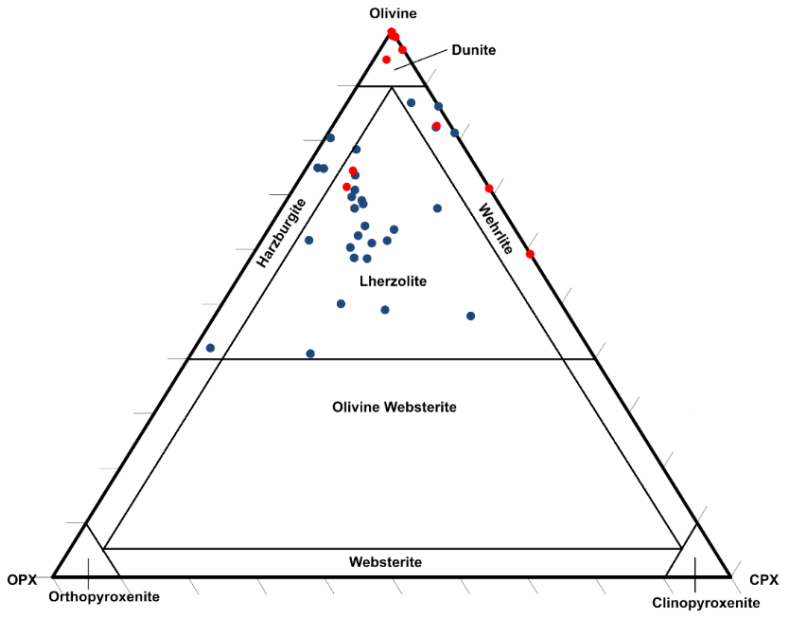

Figure 4- 1. Peridotite ternary diagram of sample subset chosen for EBSD analysis. Red dots represent samples from the Laurentian Realm. Blue dots are Peri-Laurentian samples.

4.2 Grain Size Distributions

Samples with porphyroclastic, transitional and mylonitc textures are generally fine-grained ($\tilde{x}$<400µm). The average grain size in these textures depends on the relative proportion of recrystallized grains as the average grain size for recrystallized grains in these textures is 206 µm. On the other hand, samples with protogranular and equigranular textures, generally exhibit grain sizes exceeding 400 µm (Table 7-2, Figures 7-1 and 7-2).

4.3 Microtextures

Mantle xenoliths in volcanic centers along the Canadian Cordillera include all textures described in the peridotite deformation cycle, with many xenoliths displaying intermediate textures between these (evaluated from petrographic microscope observations). All samples preserve clear evidence for deformation by dislocation creep including undulose extinction and subgrain boundaries. Some locations (e.g., Llangorse Mountain, equigranular) exhibited exclusively one texture, suggesting a rather homogenous stage/process of mantle deformation. Most suites, however, present more than one texture, indicating either relict textures sourced from a heterogeneous mantle or transient stages of deformation at the time of eruption.

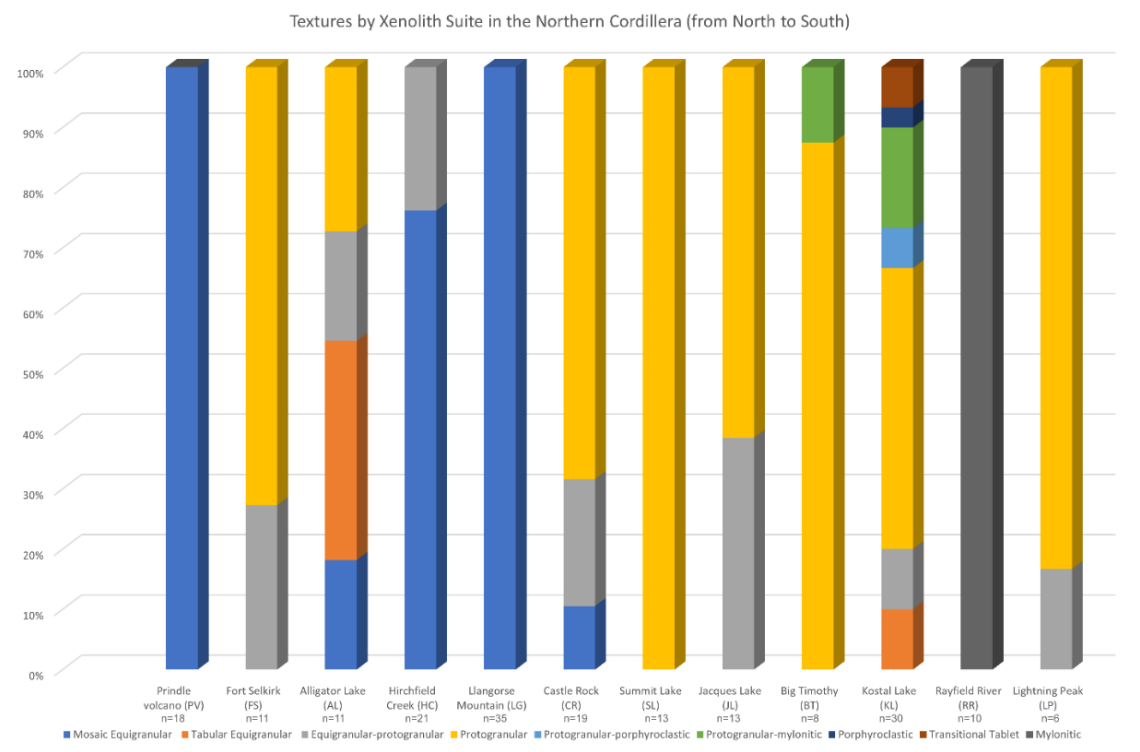

Figure 4-2. Relative abundance of textures suite in the Canadian Cordillera. N indicates number of samples.

Coarse equigranular and protogranular textures are dominant in most Cordilleran suites (Figure 4-2). These textures represent more than 90% of the studied samples. Xenoliths exhibiting the less common porphyroclastic, mylonitic and transitional textures are limited to southern suites, in particular KL and RR. In this section we present a series of figures and plots that illustrate the main characteristics of the textures in the deformation cycle in mantle xenoliths from the Cordillera. Note that M2M maps of samples with a substantial portion of small grains show olivine grain boundaries in two colors: blue for dynamically recrystallized grains (neoblasts) and black for relict grains (porphyroclasts).

The protogranular texture is the most abundant in Cordilleran xenoliths as it represents the largest number of xenoliths (n=63) and is found in seven suites. Summit Lake (SL) xenoliths in this study displays this texture exclusively. However, previous studies have reported equigranular and porphyroclastic textures for this suite using different criteria in their microtexture classification (Ji et al., 1994; Morales and Tommasi, 2011). While the protogranular texture is absent in Fort Selkirk (FS) and Hirschfield Creek, intermediate textures display some of the characteristics of this texture. Figure 4-3 shows a typical protogranular sample (SL39) with an overall coarse grain size and relatively little variation in grain size, highly irregular grain boundaries, absent foliation and rare subgrains. The aspect ratio of olivine grains shows no clear trend with grain size and EBSD analysis shows that olivine grains of all sizes exhibit low GOS. Furthermore, shape factors of grains identified as relict and recrystallized based on the GOS value show no difference in grain shape or grain boundary tortuosity. While there are no significant differences in grain size, aspect ratios and observable foliation between mosaic equigranular and protogranular samples, the latter present slightly higher GOS and shape factors on average (Table 7-2). Orthopyroxene grains lack a shape preferred orientation. They are equant, subhedral to euhedral and equal or larger in grain size than olivine. Spinel and clinopyroxene frequently appear as inclusions within olivine grains. Clinopyroxene is interstitial, fine-grained (<1mm) and lacks a shape preferred orientation. Both pyroxenes frequently display exsolution lamellae in all suites and alteration reaction textures in southern suites (e.g., Lightning Peak). Spinel is holly-leaf-shaped and occasionally forms string of grains that conform to a weak foliation.

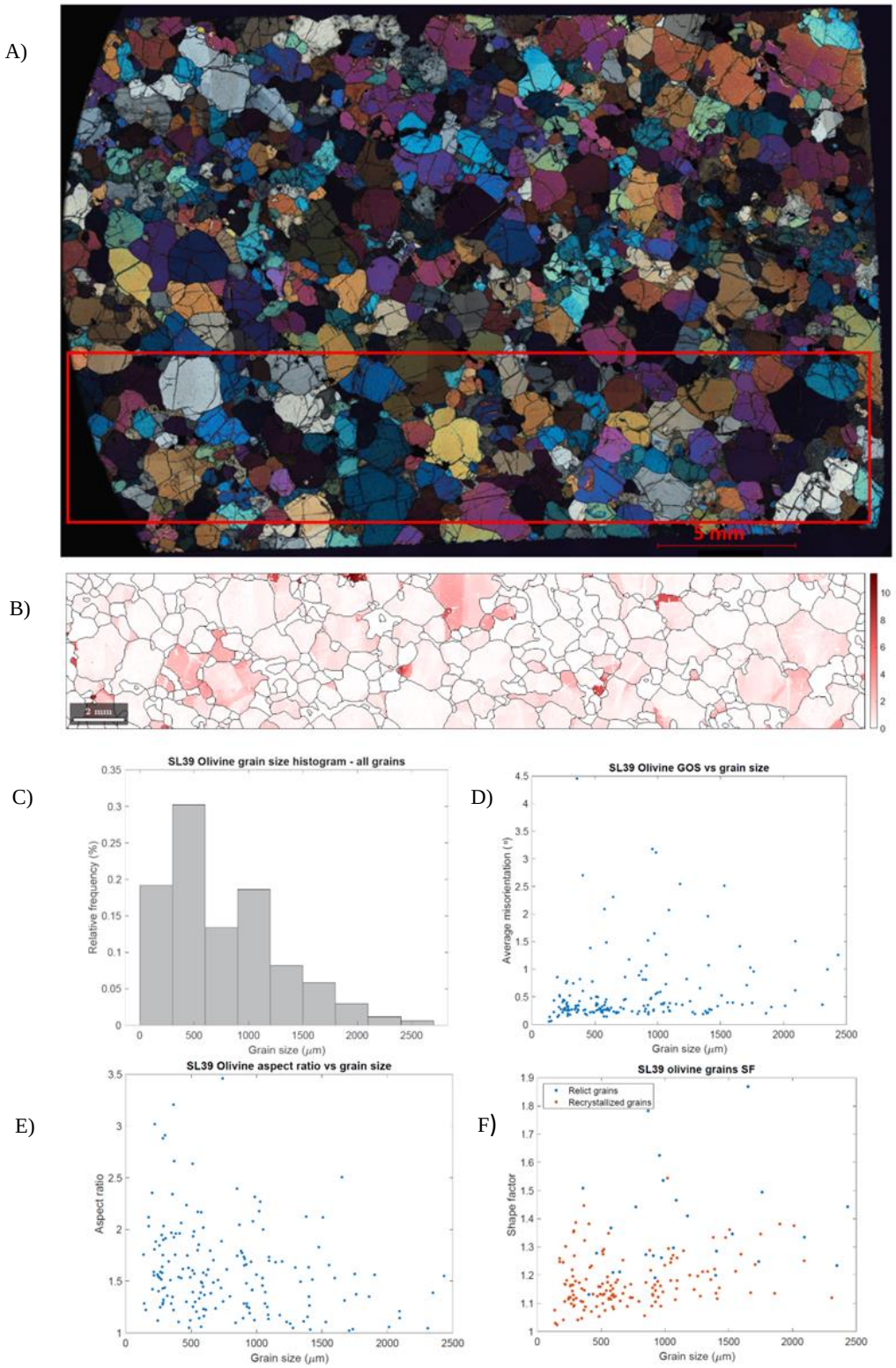

Figure 4-3. Key characteristics of protogranular texture from sample SL39. (A) photomicrograph of thin section in crossed polarized light (XPL) showing scanned area in red polygon. (B) Misorientation to mean (M2M) map of olivine grains. (C) Olivine grain size histogram for all grains in the EBSD map. (D) Average misorientation (GOS) vs grain size plot. (E) Aspect ratio vs grain size plot. (F) Shape factor vs grain size plot.

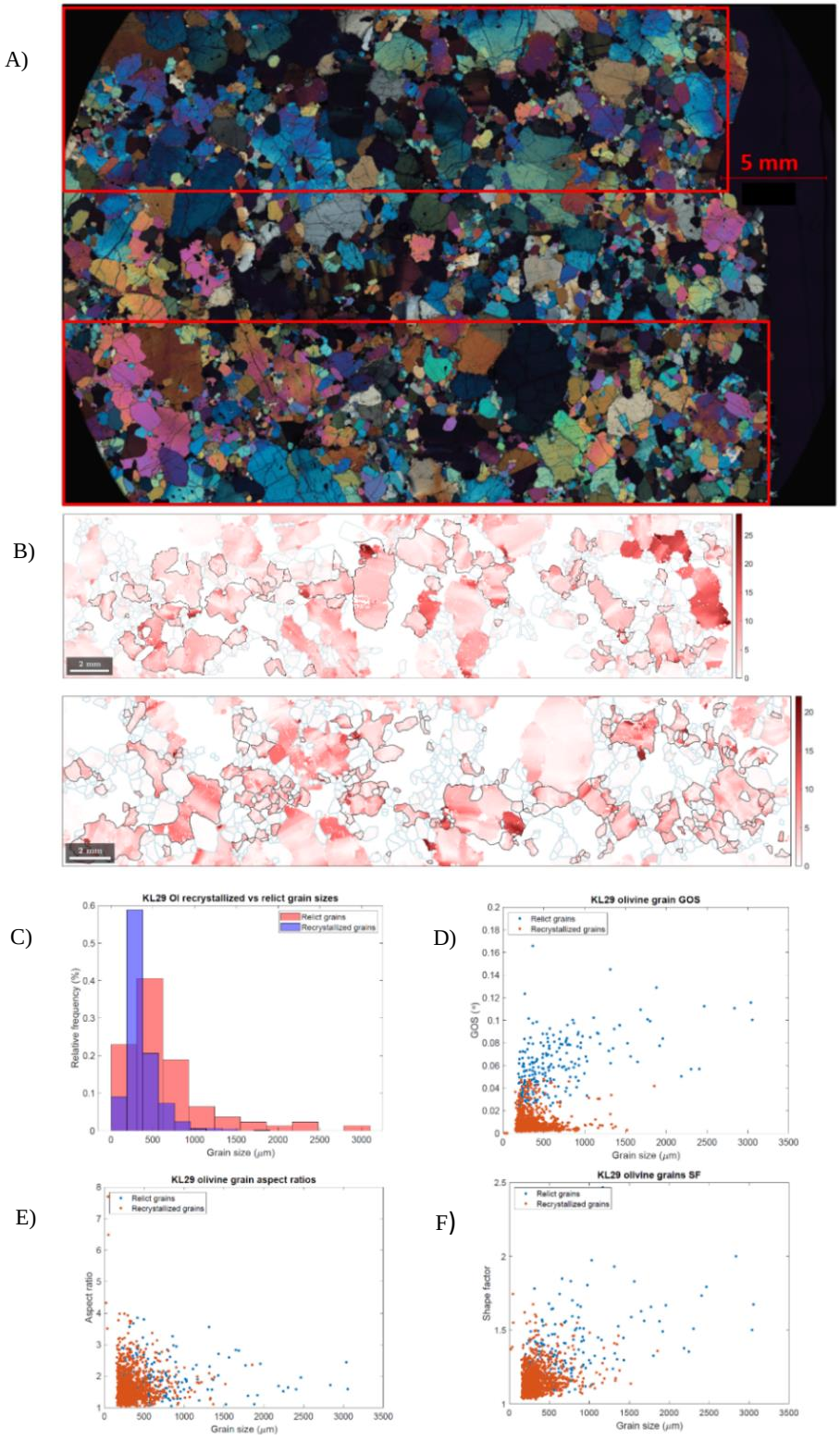

Figure 4-4. Key characteristics of porphyroclastic texture from sample KL29. (A) Photomicrograph of thin section in crossed polarized light (XPL) showing scanned areas in red polygons. (B) Misorientation to mean (M2M) map of olivine grains. (C) Olivine grain size histogram. (D) Average misorientation (GOS) vs grain size plot. (E) Aspect ratio vs grain size plot. (F) Shape factor vs grain size plot.

KL29 was the only sample classified as porphyroclastic. Figure 4-4 shows the main features of this texture. Relative to the protogranular texture, the porphyroclastic texture contains abundant small grains (e.g., with an equivalent diameter of less than 500 μm). Elongated olivine porphyroclasts with aspect ratios of up to 4:1 and abundant subgrains are mantled by sub-500-micron equant recrystallized grains showing no internal dislocations. Clinopyroxene grains are anhedral, randomly distributed and range in size from sub-500 μm to 6 mm. Spinel is scarce, interstitial and very fine-grained. The M2M map and the olivine grain size histogram illustrate the differences in grain size distribution between the populations of relict and recrystallized grains. Olivine grains exceeding 1.5 mm in size are predominantly classified as relict (Figure 4-4-d, e and f). There is no clearly defined difference in aspect ratios between the 2 populations as many porphyroclasts lack elongation in the reference frame of the thin section. Porphyroclasts exhibit strongly irregular grain boundaries as evidenced by the high proportion of porphyroclasts with shape factors exceeding 1.5, whereas recrystallized olivine grains present gently curved grain boundaries with shape factors predominantly under 1.5 (Figure 4-4-f).

All samples displaying a purely mylonitic texture are found in Rayfield River. They show a strong foliation marked by a significant reduction in olivine grain size, a well-defined shape preferred orientation of olivine porphyroclasts and the occurrence of ~5mm bands of similar composition and grain size (Figure 4-5). Spinel forms interrupted strings of elongated grains in the same orientation as the overall foliation. Here, olivine porphyroclasts are less frequent, relatively small (1-2 mm) and their aspect ratios rarely exceed 3:1. Orthopyroxene porphyroclasts are coarse (2-4 mm) and are often elongated at a high angle to the overall foliation (e.g., RR10, Figure 7-1). Clinopyroxene is fine-grained, subhedral and mostly distributed along ~3mm bands where olivine is very fine-grained. Spinel appears as elongated, film-like and/or holly leaf-shaped interstitial grains that form interrupted strings conforming to the direction of the overall foliation. Since grain size reduction is pervasive, the populations identified as relict and recrystallized grains exhibit the same grain size range. There are, therefore, relatively large, low GOS recrystallized grains or, equivalently, small porphyroclasts with large GOS. Similarly, there are no observable differences in aspect ratio and shape factor as both relict and recrystallized grains are equant to sub-equant with very irregular grain boundaries.

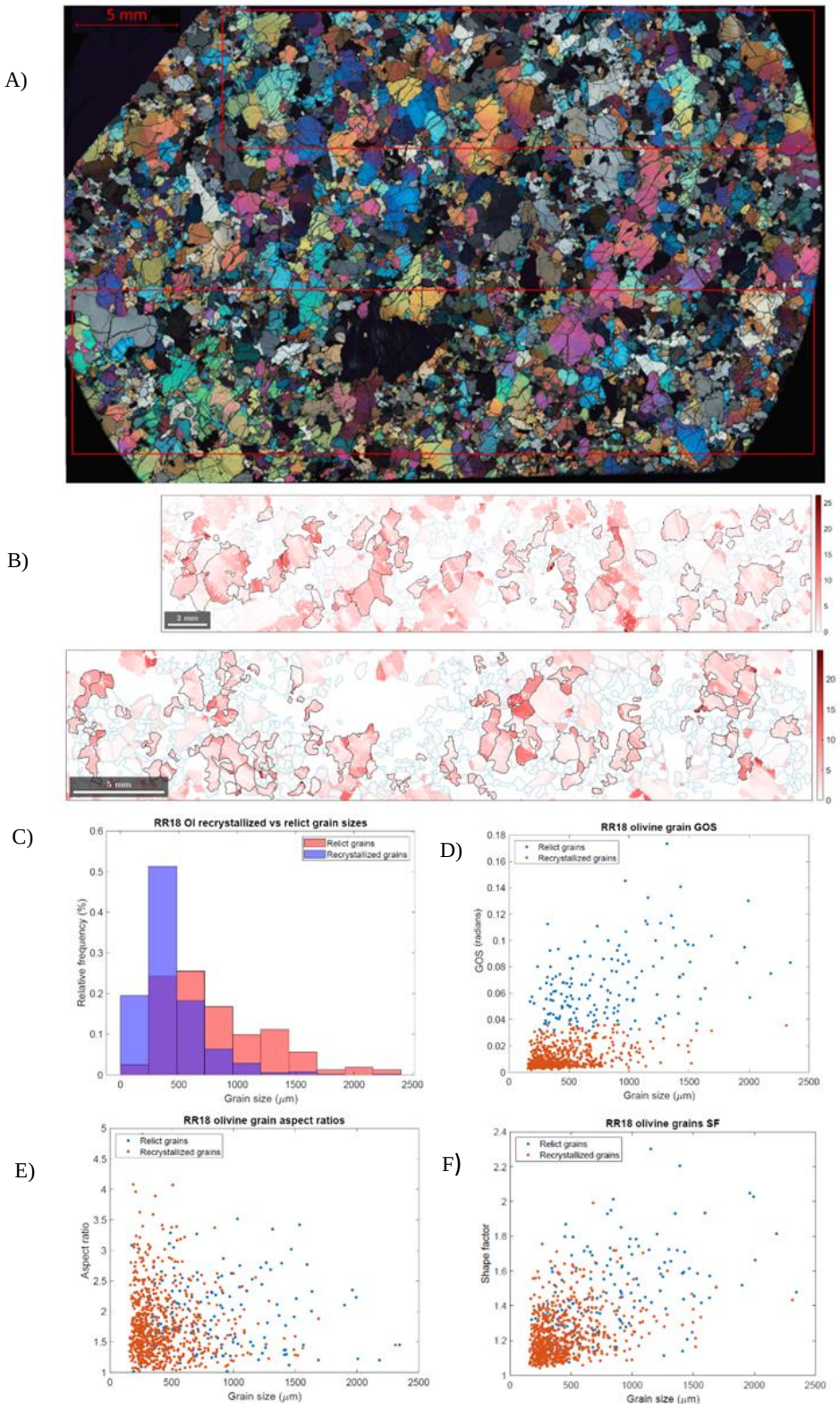

Figure 4-5. Key characteristics of mylonitic texture from sample RR18. (A) Photomicrograph of thin section in crossed polarized light (XPL) showing scanned area in red polygon. (B) Misorientation to mean (M2M) map of olivine grains. (C) Olivine grain size histogram. (D) Average misorientation (GOS) vs grain size plot. (E) Aspect ratio vs grain size plot. (F) Shape factor vs grain size plot

The transitional tabular texture has only been observed in two samples from Kostal Lake. Samples KL51 and KL53 display coarse, elongated olivine porpyroclasts mantled by neoblasts and euhedral olivine tablets. The dynamically recrystallized olivine neoblasts are sub-500-micron equant grains with gently curved boundaries that lack internal misorientations. They are grouped as small clusters and/or bands that define the foliation together with the shape preferred orientation of porphyroclasts. The tablets, on the other hand, present grain sizes between ~700 and 1500 microns, straight grain boundaries and aspect ratios ranging from 2:1 to 3:1. The tablets lack internal deformation as evidenced from the lack of undulose extension in cross-polar photomicrographs and the M2M maps. Sample KL53 (Figure 4-6) is a dunite where the modal content of pyroxenes is less than 1%. Multiple olivine tablets with parallel elongated boundaries are visible in figure 4-6a, mostly oriented in the direction of the foliation although fewer tablets develop in a quasi-perpendicular orientation to the foliation. In figure 4-6, tablets plot as 700-1500 μm recrystallized grains with low GOS (<0.03 radians) and aspect ratios >2. However, there are no distinct populations in terms of aspect ratio and shape factor between relict and recrystallized grains as porphyroclasts appear as both equant and elongated grains with relatively gently curved grain boundaries.

Sample KL51 shows a higher modal presence of pyroxenes (cpx=15.37 %, opx=2.01%). Olivine porphyroclasts are smaller than in sample KL53 reaching up to 2.5 mm and aspect ratios of up to 5:1. Clinopyroxene shows a great variation in grain size from ~200 μm to 4 mm. Fine-grained clinopyroxene is mostly sub-equant and interstitial, whereas coarse grains are anhedral and appear to have crystallized from film-like higher concentrations of melt along grain boundaries as evidenced by protrusions that propagate along grain boundaries of neighbouring olivine grains (Figure 7-1). In all cases, olivine grain size is greatly reduced due to recrystallization when in contact with clinopyroxene. Orthopyroxene grew as exsolution lamellae at the expense of clinopyroxene. Spinel is absent from both samples.

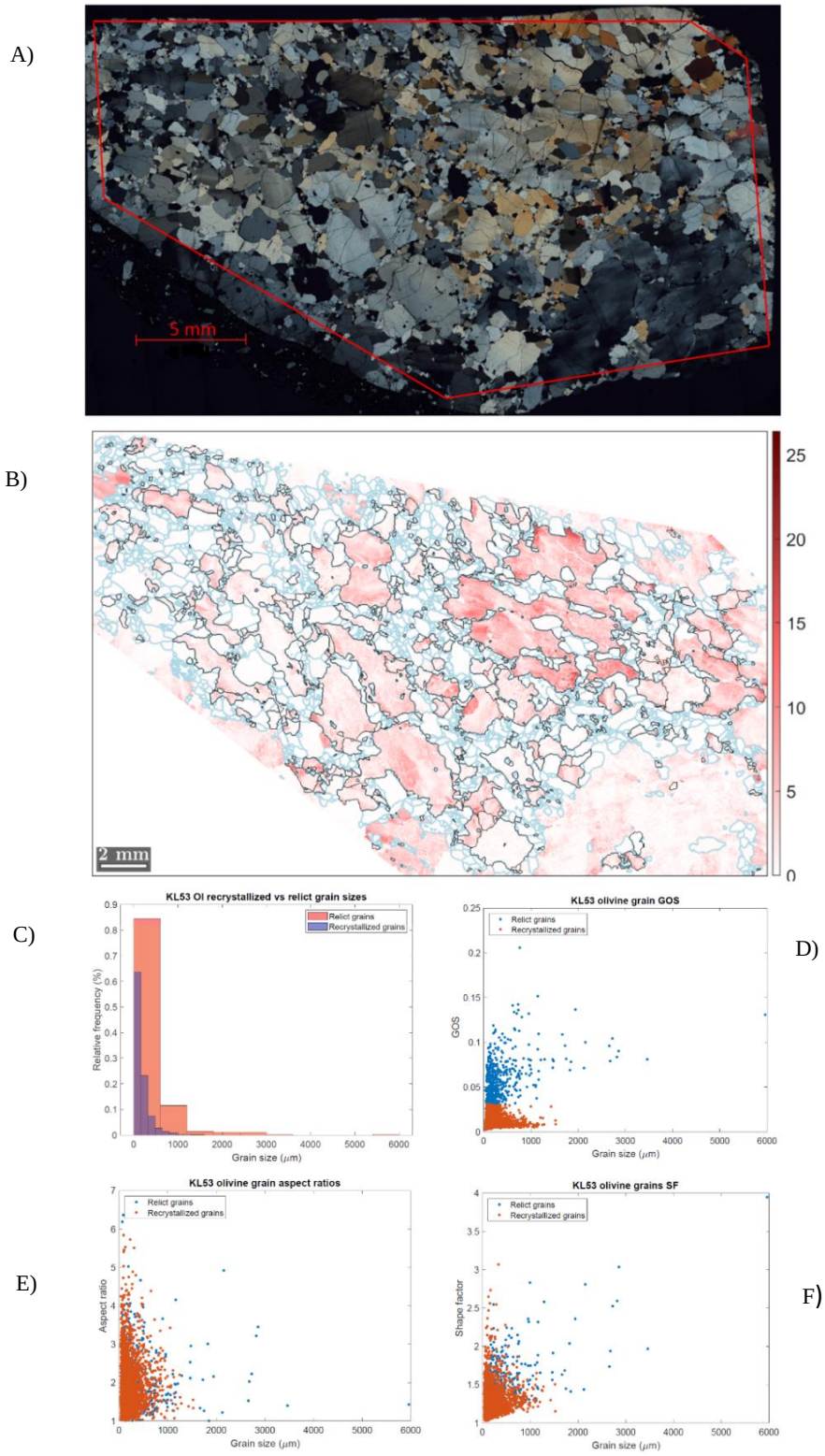

Figure 4-6. Figure 4-6. Key characteristics of transitional tablet texture from sample KL53. (A) Photomicrograph of thin section in crossed polarized light (XPL) showing scanned area in red polygon. (B) Misorientation to mean (M2M) map of olivine grains. (C) Olivine grain size histogram. (D) Average misorientation (GOS) vs grain size plot. (E) Aspect ratio vs grain size plot. (F) Shape factor vs grain size plot.

Figure 4-7 shows the main characteristics of a typical mosaic equigranular texture including straight grain boundaries, abundant triple junctions at 120 degrees, low aspect ratios, few subgrains (low GOS) and little variation in grain size. Samples exhibiting this texture generally lack a foliation. However, in a few cases, individual grains with a weak to moderate shape preferred orientation (e.g., PV08) define a weak foliation. Figure 4-7a shows some tablets in sample AL57 dominated by equant grains. The higher aspect ratios in figure 4-7e correspond to these short tabular grains. Compositional bands ~5mm-wide with distinct grain sizes (e.g., LG14, Figure 7-1) define a weak foliation. The mosaic equigranular texture is the most abundant in northern volcanic suites and absent in suites south of Summit Lake (Figure 4-2). All xenoliths in Prindle Volcano and Llangorse Mountain were classified texturally as mosaic equigranular. However, xenolith PV08 displays some characteristics that are intermediate between mosaic and tabular equigranular. The rest of the northern suites exhibit varying percentages of this textures and/or an intermediate texture between equigranular and protogranular.

In the suites where the mosaic equigranular texture is predominant (Prindle Volcano, Llangorse Mountain and Hirschfield Creek), xenoliths are mostly pyroxene-rich lherzolites with minor abundance of xenoliths displaying a cumulate igneous crystallization texture. Orthopyroxene is marginally coarser than olivine, euhedral and lacks a shape preferred orientation. Clinopyroxene is fine-grained, euhedral and mostly interstitial in lherzolites; occasionally forming interrupted strings of grains in samples where a weak foliation is present. In xenoliths displaying a cumulate texture, coarse clinopyroxene grains (1-2 mm) form monomineralic bands varying in width from 2 to 20 mm. In most mosaic equigranular samples, there are discontinuous, parallel strings of elongated spinel grains. In samples where a weak foliation is present, these spinel strings of grains conform to the orientation of the foliation. However, such strings of spinel grains are also present in samples with no discernible foliation or shape preferred orientation in other mineral phases.

Grain shape preferred orientation is most pronounced in the tabular equigranular texture (Figure 4-8). Samples exhibiting this texture show elongated euhedral olivine grains with straight boundaries, multiple subgrains at high angle to the foliation and aspect ratios of up to 5:1. Triple junctions at 120 degrees are abundant. Xenoliths exhibiting this texture were exclusively identified

in Prindle Volcano (n=1) Alligator Lake (n=4) and Kostal Lake (n=3). Long aspect ratios are exclusive to olivine as pyroxenes, where present, are equant. Spinel is minor, interstitial and shows no defined distribution pattern in samples with this texture.

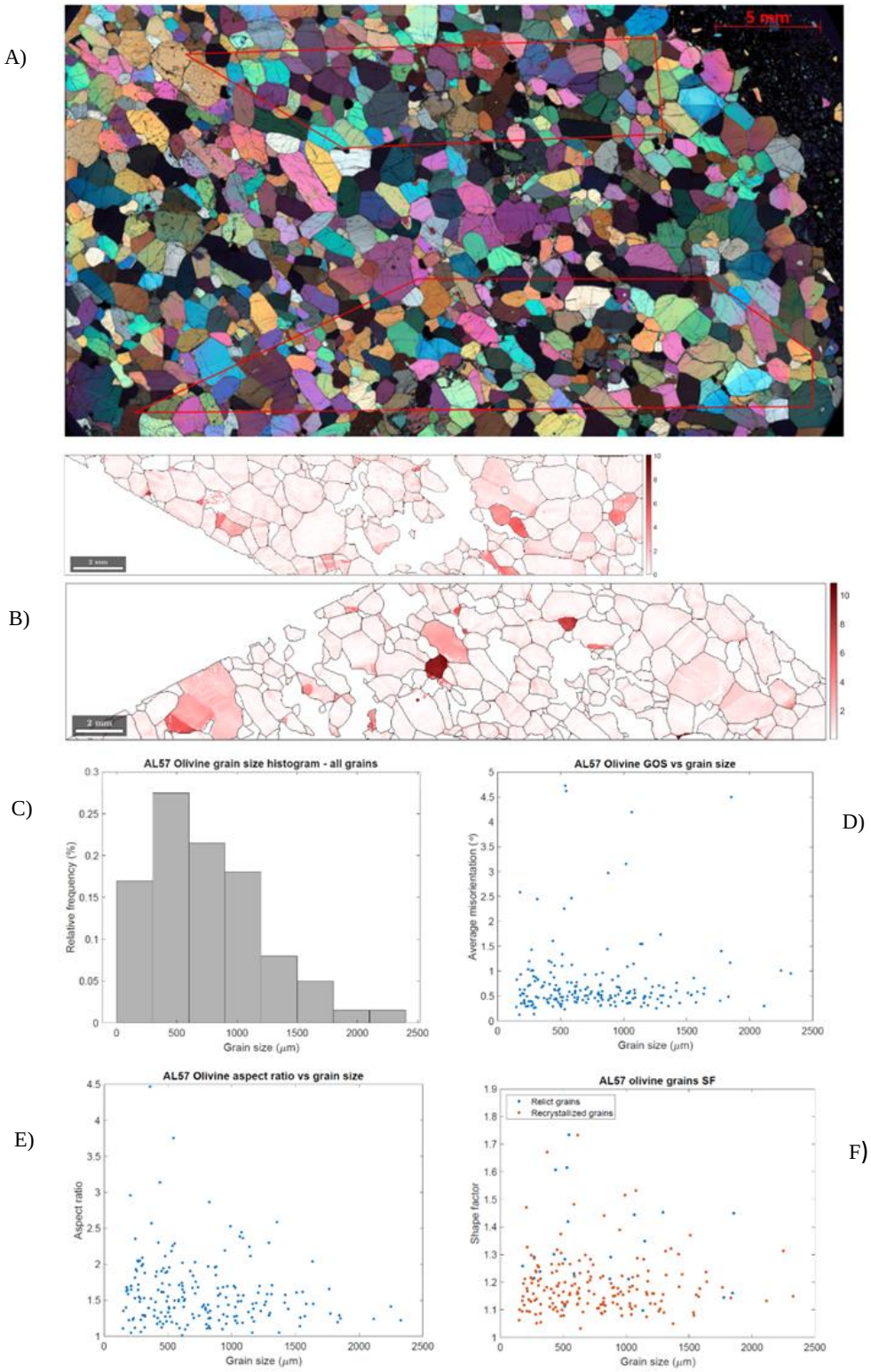

Figure 4-7. Key characteristics of mosaic equigranular texture from sample AL57. (A) Photomicrograph of thin section in crossed polarized light (XPL) showing scanned area in red polygon. (B) Misorientation to mean (M2M) map of olivine grains. (C) Olivine grain size histogram. (D) Average misorientation (GOS) vs grain size plot. (E) Aspect ratio vs grain size plot. (F) Shape factor vs grain size plot.

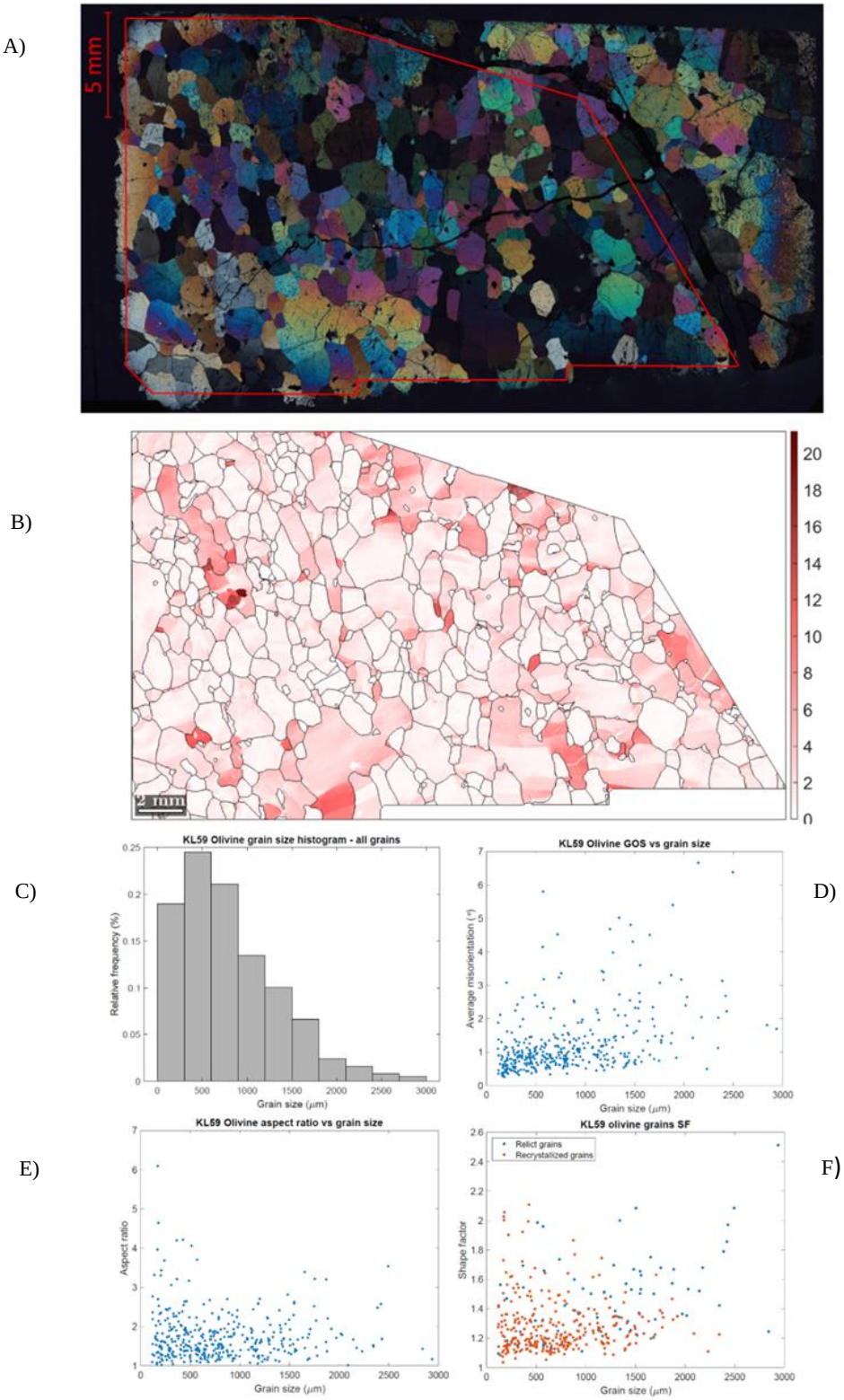

Figure 4-8. Key characteristics of tabular equigranular texture from sample KL59. (A) Photomicrograph of thin section in crossed polarized light (XPL) showing scanned area in red polygon. (B) Misorientation to mean (M2M) map of olivine grains. (C) Olivine grain size histogram. (D) Average misorientation (GOS) vs grain size plot. (E) Aspect ratio vs grain size plot. (F) Shape factor vs grain size plot.

Intermediate textures

A few samples in this study displayed intermediate characteristics between 2 textures. These include:

Equigranular-protogranular samples: In this intermediate texture, there is little variation in grain size. While olivine grains are mostly equant, grain boundaries are more irregular than in purely equigranular samples varying from straight to gently curved. There are more elongated grains scattered within the sample and 120-degree triple junctions are scarce, but still present. Foliation is either absent or weak. Elongated grains, if present, have parallel long axes defining a grain shape preferred orientation foliation that may also be parallel to compositional bands. This intermediate texture is common in both northern and southern suites and only absent in suites where xenoliths display only one texture.

Protogranular-porphyroclastic: In this intermediate texture, samples contain a substantial proportion of small grains, but lack the elongated aspect ratios seen in porphyroclasts in the porphyroclastic texture (e.g., KL65) and no defined foliation is observed as porphyroclasts and neoblasts are randomly oriented.

Protogranular-mylonitic: Here, the foliation is well defined like in mylonitic samples. However, grain size reduction of porphyroclasts is not as pervasive as in mylonitic samples (e.g., KL37, KL44).

Mosaic-tabular equigranular: Some samples in the mosaic equigranular texture show areas and/or bands where a few olivine tablets can be seen (e.g., PV08). Similarly, in tabular equigranular samples, there are small clusters (~5mm in diameter) where olivine grains are equant (e.g., KL62). In these cases, we classified the sample based on the predominance of either equant or tabular grains.

4.4 Olivine CPO Types

Table 7-2 summarizes the results from the EBSD analyses. The EBSD analyses of Cordilleran samples consistently yielded three olivine fabric types: A-, D- and AG-type (Figures 4-9 and 7-3). Nine samples exhibit the AG-type fabric (fiber-[010], BA<0.35), eighteen display the most-abundant A-type fabric (orthorhombic, 0.35<BA<0.65), while twelve display D-type fabric (fiber-[100], BA>0.65).

In all the xenolith suites where the AG-type occurs (PV, AL, JL, KL), the A-type fabric is also present, suggesting an evolution of the AG-type from a pre-existing A-type fabric. On the other hand, suites with xenoliths exhibiting D-type fabric, are almost exclusively restricted to this fabric type. The only exception is sample LG14 which displays a A-type fabric, thus differing from the other two samples in that suite (LG33 and LG33), both D-type fabrics.

For most samples, the olivine CPO observed in the pole figures matches the pattern predicted by the BA-index. However, in a few samples, the pattern is slightly ambiguous, resembling the characteristics of either two CPOs or another CPO (Table 4-2). This happens when the BA-index of either the bulk sample or grains identified as recrystallized approaches 0.35 (threshold between fiber-[010] and orthorhombic). However, it doesn't occur when the BA-index is close to 0.65 (threshold between orthorhombic and fiber-[100]). In addition to this, samples with a very weak CPO display a rather diffused, inconclusive CPO pattern. These include KL04 (J=2.56) and KL29 (J=1.30). Finally, sample BT26 also produced a poorly defined pattern. This sample presents very coarse orthopyroxene grains, which resulted in the lowest number of scanned olivine grains.

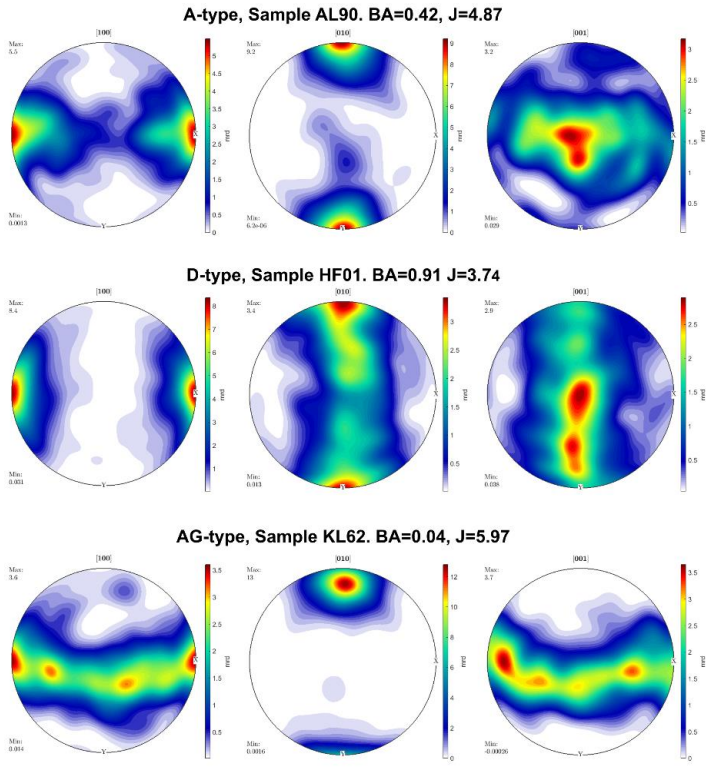

Figure 4-9. Examples of each of the CPO types found in this study.

A-type fabric corresponds to the (010)[100] slip system and shows point maxima in [100], [010] and [001].

D-type fabric corresponds to the (0kl)[100] slip system and shows point maxima in [100], and girdle distributions in [010] and [001].

AG-type corresponds to the (010)[100] and (010)[001] slip system and shows point maxima in [010] and girdle distributions in [100] and [001].

Table 4-1. Samples with bulk orthorhombic BA-index and CPO pattern resembling fiber-[010]

Sample	BA	J	CPO	Comment
AL45 Relict Rex(93%)	0.43 0.31 0.29	3.74 12.22 3.69	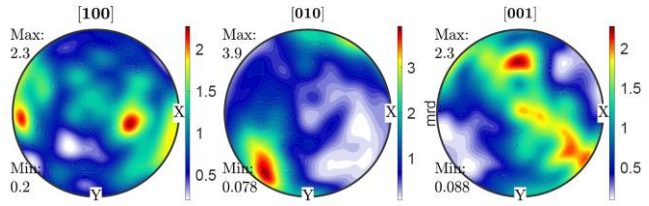	BA is indicative of A-type fabric, pattern resembles AG-type
BT22 Relict Rex(42%)	0.52 0.55 0.38	2.23 3.04 2.34	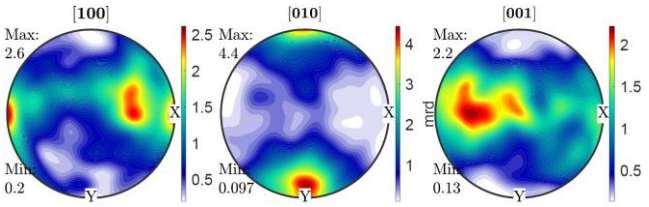	BA is indicative of A-type fabric, pattern is intermediate between A- and AG-type
BT23 Relict Rex(57%)	0.40 0.47 0.24	3.27 7.78 3.89	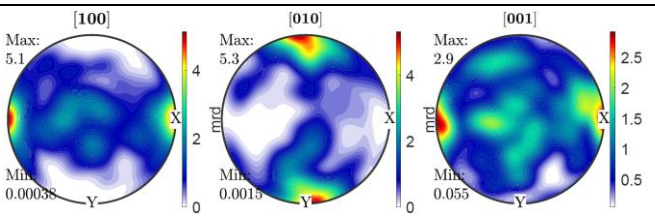	BA is indicative of A-type fabric, pattern resembles AG-type
JL12 Relict Rex(48%)	0.55 0.62 0.38	3.52 7.09 3.43	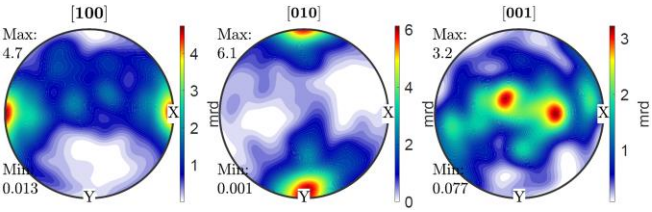	BA is indicative of A-type fabric, pattern is intermediate between A- and AG-type
KL53 Relict Rex(54%)	0.41 0.59 0.37	2.23 3.17 2.22	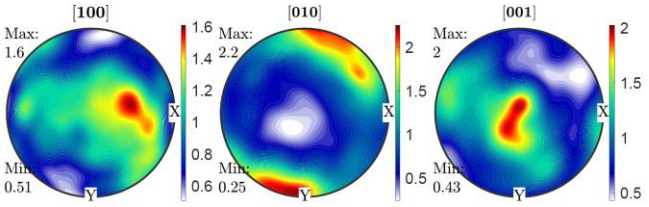	BA is indicative of A-type fabric, pattern is intermediate between A- and AG-type

4.5 Pyroxene CPOs

Most pyroxene CPOs in our samples are very dispersed and therefore weak. Samples where the J-index for either clinopyroxene or orthopyroxene is anomalously high (J>15) contain very

few grains of either phase (modal %<3) (Table 7-2). Pyroxene CPOs correlated with that of olivine are characterized by [001]px maxima parallel or subparallel to the [100]ol maximum and by [100]opx and [010]cpx maxima aligned with the [010]ol maximum (Liu et al., 2019). In 22 out of our 39 scanned samples, the pyroxene CPOs are uncorrelated with the olivine CPO, while in 17 samples at least one pyroxene CPO is correlated with that of olivine. Pyroxene CPOs that are strongly correlated with that of olivine are indicated with black arrows in Figure 7-3 while those that are partially correlated are indicated with grey arrows.

4.6 Fabric Strength

Fabric strength, here quantified as dimensionless J- and M-indexes, can be used as a proxy indicating the degree to which grains are aligned. J-indexes in our samples range from 1.30 to 8.04 while M-indexes range from 0.02 to 0.29. We found a strong correlation between J- and M-indices (R^2=0.82). The J-index is moderately correlated with the GOS (Figure 4-10b), with sample AL45 displaying unusually high GOS. As a result of this correlation, we observed a relationship between the J-index and the microtextures, with the exceptions of sample KL37 and KL44. Unlike proto-mylonitic samples in RR, these samples present a relatively high CPO strength.

Samples exhibiting porphyroclastic texture or an intermediate texture between protogranular and porphyroclastic have the lowest J-index ranging from 1.30 to 1.44. As the J-index increases we see a succession in microtextures as follows: equigranular-mosaic (J=1.53-3.39), transitional (J=2.09-2.23), protogranular (J=1.88-4.64), protomylonic (J=2.39-6.88), intermediate texture equigranular-protogranular (J=3.10-3.93) and equigranular- tablet (J=4.87-8.03). Two main factors explain why the J-index-intervals for the different textures overlap: (1) the samples are from 12 different suites with different local processes and conditions potentially influencing the development of textures and CPOs (temperature, pressure, presence of melt, etc.) and (2) many xenoliths exhibit features of intermediate textures (e.g equigranular-protogranular).

In general, our samples yielded low to moderate J-index. The average J-index of the 39 Cordilleran samples was 3.26. The average J-index for the northern suites (PV, FS, AL, HF, LG

and CR) is 3.00 whereas for the southern suites (SL, JL, KL, BT, RR and LP) it is 3.48. Natural peridotites can reach J-indexes up to 20 and peak at 3-5 (Tommasi & Vauchez, 2015).

a)

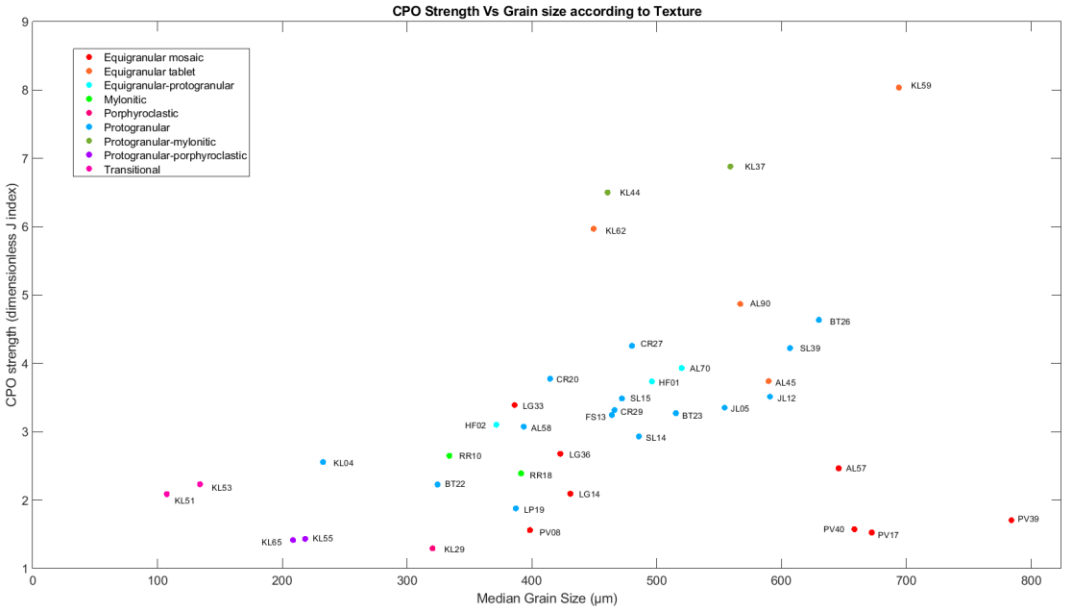

b)

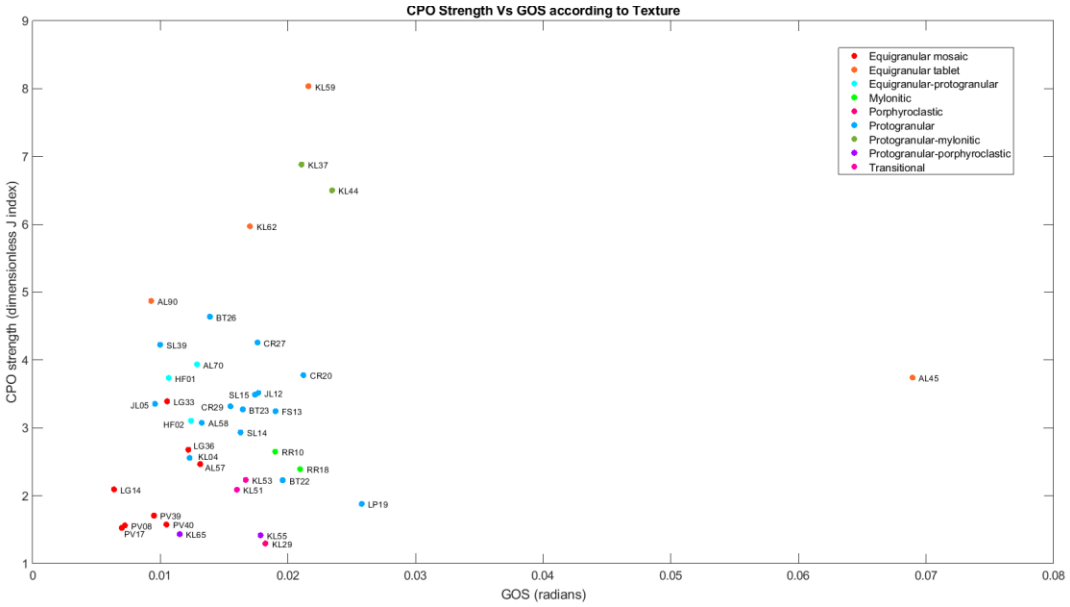

Figure 4-10. Microstructural factors affecting CPO strength. (a) plot of J-index vs olivine median grain size. (b) plot of J-index vs olivine intragrain misorientations (GOS).

4.7 Seismic anisotropy

The ultramafic xenoliths directly sample the Cordilleran lithospheric mantle. However, they represent only accidental fragments, which limits their usefulness as reliable proxy of the upper

mantle beneath each locality. Furthermore, the vertical distribution and orientation of the foliation and lineation of these xenoliths within the ~15 km of lithospheric mantle is unknown.

The seismic properties for the scanned lherzolites, harzburgites and wehrlites, calculated using in situ mantle temperature conditions listed in table 1-1 and an assumed uniform pressure of 1 GPa representative of the shallow mantle are presented in figure 7-4 as a series of contour diagrams. For consistency, results are presented in the same reference frame as the CPOs in figure 7-3. Vp values range from 2.0 to 13.0 km/h. A(Vp) values range from 1.5 – 12.7 % and its distribution (concentration of maxima) resembles that of the olivine CPO pattern. Therefore, the maximum and minimum Vp are correlated with the preferred orientation of the olivine fast a-axis and the slow b-axis respectively. Vs1 values vary from 1.0 to 6.4 km/s, while Vs2 varies from 1.1 to 7.8 km/s. A(Vs) ranges from 1.5 – 9.2%. A(Vs) distribution, while also dependent on the olivine LPO, is more complex geometrically. This is because there is an important distinction between the angles for maximum and minimum for Vp and Vs. While the angle between the Vp, maximum and minimum is orthogonal, that between the Vs maximum and minimum is approximately 45 degrees. This inherent property of Vs hinders tectonic interpretations of observed S-wave splitting (Ji et al., 1994 and references therein).

As a result of the common reference frame in our data processing methods, S1 is generally polarized parallel or subparallel to the olivine [100] maximum. Birefringence of S-waves is lowest for propagation directions at low angle to the [100] maximum (Morales and Tommasi, 2011). Minimal differences between the two polarization directions Vs1 and Vs2 were observed for A-type fabrics with moderate to high J-index as S_2 in A-type fabrics is generally parallel or subparallel to the [100] maxima. The average difference between Vs2 and Vs1 in A-type fabrics is 8.6%. Also in agreement with Morales and Tommasi (2011), the highest birefringences for S-waves are observed where propagation directions of S are at high angles to the [100] maximum, namely in AG-type and D-type fabrics. In AG-type samples with moderate to well-defined CPO, Vs2 is lower than Vs1. In average Vs2 is 35% slower than Vs1 in AG-type samples. Contrarily, Vs2 is faster than Vs1 in D-type fabric by a factor of ~2. The differences between Vs1 and Vs2 in AG and D-type fabrics are generally lower in samples with weak CPOs.

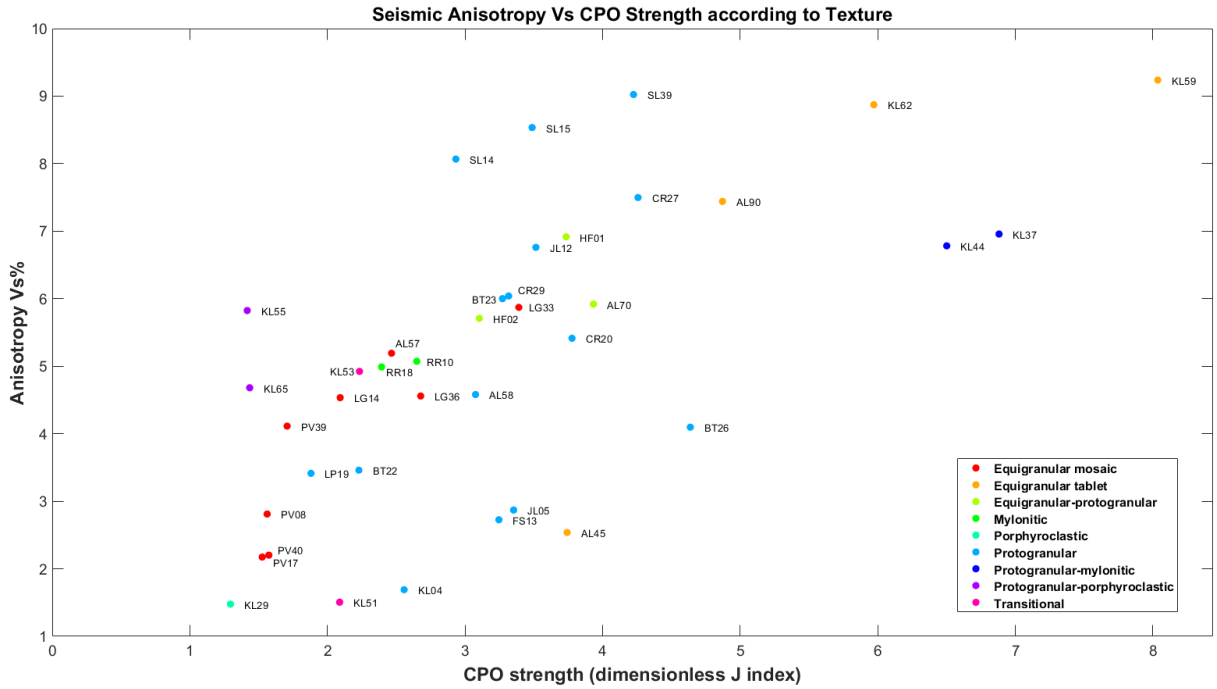

Figure 4-11. Incidence of CPO strength in seismic anisotropy.

As expected, the strength of the olivine CPO influences the magnitude of seismic anisotropy. We found similar correlations between J-index and A(Vp) (R^2 =0.37) and J-index and A(Vs) (R^2 =0.43) based on a linear fit. Figures 4-11 and 4-12 show the incidence of variables that affect the magnitude of the anisotropy. A higher pyroxene content weakens the bulk anisotropy in mantle peridotites as it reduces the modal content of olivine as the most anisotropic mineral and may correspond to melt rock interaction that disperses the olivine CPO. This effect is evident for samples with approximately the same strength of olivine CPO, but with significantly different pyroxene content (CR20 vs SL15 or LG33 vs SL39). Another factor that may explain a distinctly higher anisotropy for some samples is the coeval deformation of olivine and pyroxenes, where the olivine LPO pattern in [100] matches that of opx and/or cpx in [001]. This simultaneous deformation under the same strain geometry reinforces the anisotropy of the rock as the resulting orientation is the same for the phases involved. This is particularly the case for the three scanned SL wehrlites where Ol [100] has the same pattern as cpx [001] and for lherzolites JL12 and CR27, where deformation of both opx and cpx was coeval with olivine. A simple comparison between SL14, where both opx and cpx CPOs are strongly correlated to that of olivine, and AL70, where the deformation of pyroxenes is not coeval, shows a higher anisotropy for the former, despite similar olivine contents and a higher J-index for AL70.

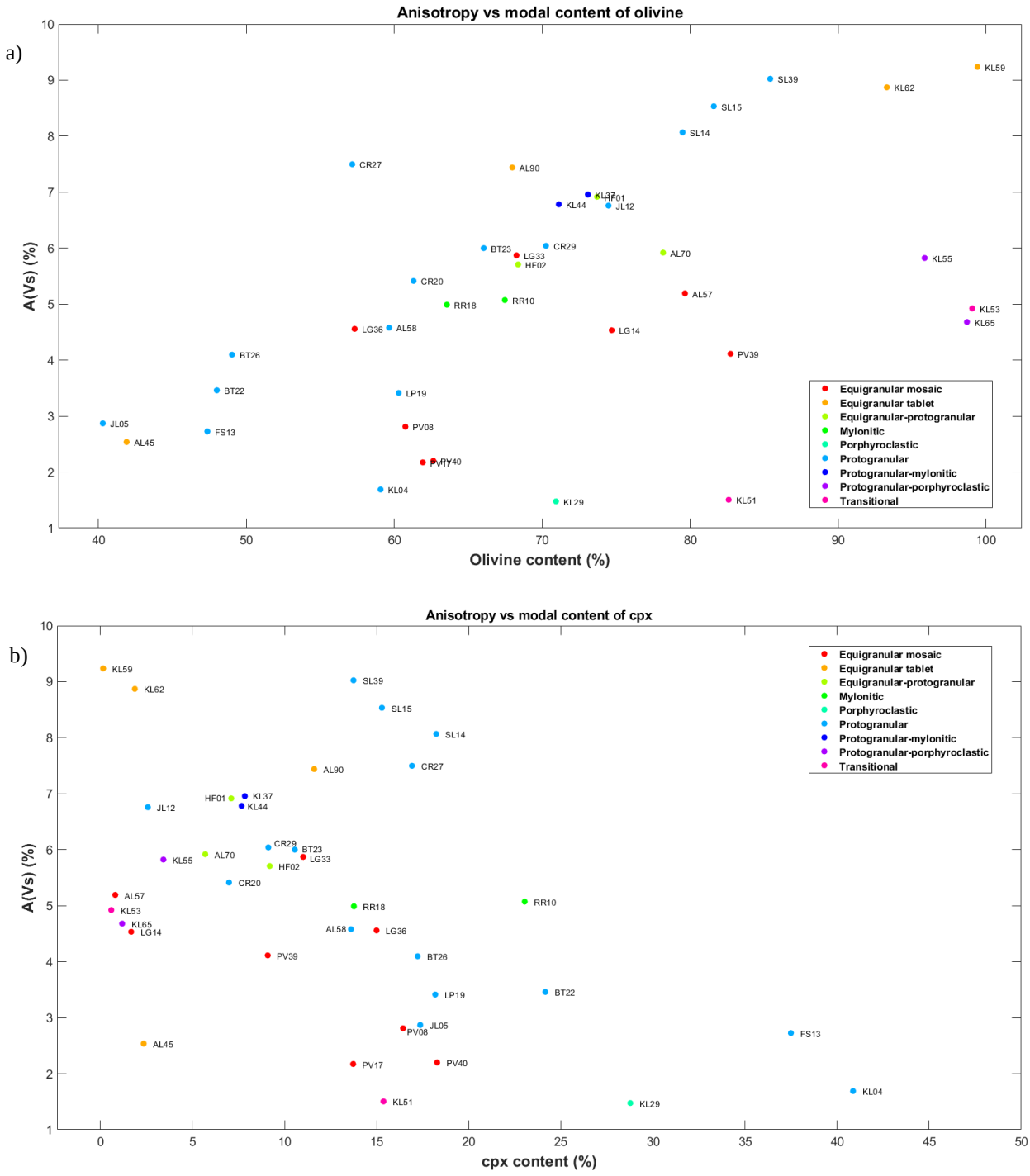

Figure 4-12. Effect of modal compositions on seismic anisotropy. (a) Plot of seismic anisotropy (AVs) vs olivine content. (b) Plot of seismic anisotropy (AVs) vs cpx content.

4.8 Evidence of melt-rock interaction in SL and KL

The increased cpx content in Summit Lake and Kostal Lake xenoliths, particularly augite, is observed in the form of pyroxenitic veins, composite peridotite-pyroxenite xenoliths, and large, anhedral clinopyroxene grains. Both localities also contain dunite, harzburgite and opx-poor lherzolite xenoliths resulting from earlier reactions between basaltic melts and peridotitic wall rock (Ji et al., 1994; Morales and Tommasi, 2011; Peslier et al., 2002).

Melt-rock interactions preserved in mantle xenoliths are inferred to produce microtextural changes in olivine. Curvilinear olivine grain boundaries described in Chin et al. (2020) and Le Roux et al. (2008) are inferred to result from melt percolation. Therefore, melt-peridotite interaction has been proposed as a mechanism that explains the transition from equigranular to protogranular textures (Chin et al., 2021). This process is accompanied by a significant reduction in overall grain size as fine-grained neoblasts are formed along olivine grain boundaries in contact with melt/cpx. In KL samples, this reduction in grain size along coarse olivine grains induces a transition from either equigranular or protogranular textures to porphyroclastic.

4.9 One sample, two textures. A case study on the effects of melt

To further characterize the effects of melt, we used sample KL55 which shows two differentiated areas in the same thin section: one affected by melt percolation where olivine has more curved grain boundaries and a bimodal grain size distribution and one “dry” section with straight grain boundaries, abundant triple junctions at 120 degrees and little variation in grain size (Figure 4-13).

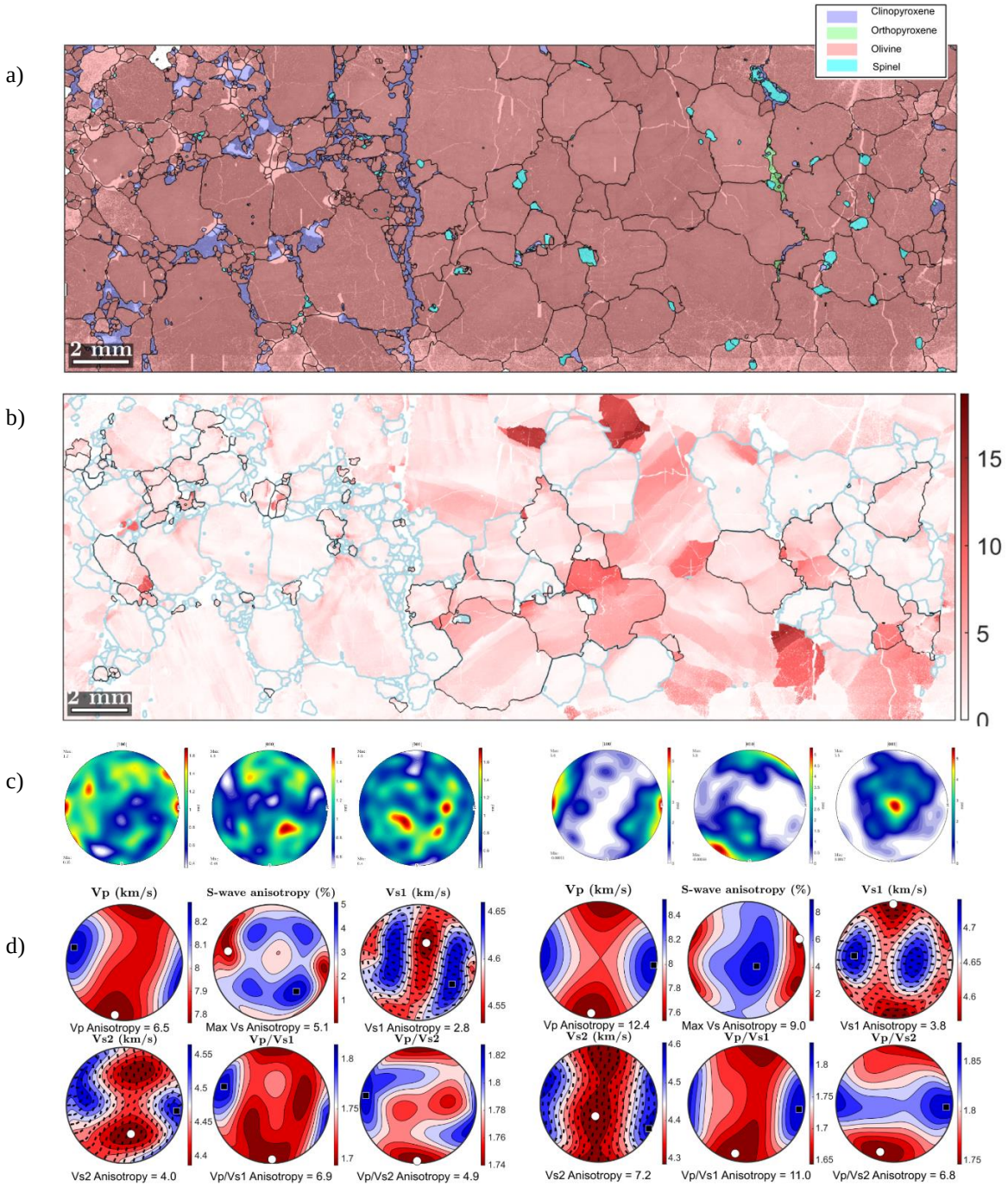

Figure 4-13. Effects of melt in 2 sections of sample KL55. (a) Phase map showing incidence of melt in left portion of the sample. (b) M2M map showing intragranular misorientations, (c) Olivine CPOs of left and right side. (d) Anisotropic properties of left and right side.

KL55	Ol (%)	cpx (%)	n	Median Grain size (μm)	Shape Factor	Ave. GOS (°)	J_Ol	M_Ol	BA	J_CPX	M_CPX
Bulk	96.10	3.90	579	208.54	1.25	1.023	1.42	0.013	0.43	2.77	0.015
Left Side	91.69	8.31	460	186.68	1.23	0.985	1.39	0.004	0.59	4.40	0.030
Right Side	98.89	1.11	129	398.01	1.36	1.193	4.98	0.230	0.61	3.04	0.021

Table 4-3. EBSD metrics of bulk sample and left and right sides of sample KL55.

Figure 4-13 and table 4-3 illustrate the effects of melt in mantle peridotites. The left side of the sample contains abundant interstitial diopside, which corresponds to locations where melt was present. The pervasive distribution of melt caused a significant reduction in grain size when olivine was in contact with melt, resulting in development of numerous neoblasts along grain boundaries and a porphyroclastic texture. The right side, where melt is almost non-existent, shows little variation in grain size and a protogranular texture. From the M2M map (Figure 4-13-b), we can infer that both the porphyroclasts and neoblasts on the left side are weakly deformed internally, resulting in a low average GOS of 0.99 degrees. In contrasts, coarse grains on the right-side display multiple subgrains and hence a higher GOS of 1.19 degrees. The CPO pattern in the left side is reminiscent of the AG-type fabric, with [100] exhibiting a girdle distribution. This is mostly due to a significant reduction in BA-index for recrystallized grains (BA=0.43) relative to relict grains (BA=0.53) on the left side. Additionally, the strength of the CPO in the left side of the sample is very low (J-index=1.39). The right side displays a CPO corresponding to the A-type fabric and consistent with a BA-index of 0.61. Furthermore, the CPO on this side is much stronger (J=4.99). Finally, a comparison of the anisotropic properties shows a moderate anisotropy for the left side (Max Avs=5.1%) in contrast with high anisotropy for the right side (Max Avs=9.0%).

In addition to the single sample case described above, samples from the KL suite show systematic changes with pyroxene content that indicate prevalent melt-rock interactions. Morales and Tommasi (2011) describe a progressive reduction in CPO strength with increasing cpx content in SL. In our analysis of KL samples, we observe a similar trend for samples where cpx content is higher than 5% (Figure 4-14-a). Here, an increase in cpx content reduces the overall olivine grain size where olivine is in contact with melt. Figure 4-14-d illustrates the relationship between olivine grain size and strength of the CPO. Sample KL 29 appears as an outlier from the overall trend as the size of porphyroclasts increases the olivine median grain size. In samples where clinopyroxene content is lower than 5% (KL65, KL53, KL55R, KL62 and KL59), the strength of the CPO appears to be a consequence of the prevalence of dislocation creep and hence subgrain formation and overall grain size (Figure 4-14-b and c).

Kostal Lake xenoliths anomalously display a wide range of textures in the peridotite deformation cycle. The only texture that was not observed in our sample set is mosaic equigranular. However, samples with tabular equigranular texture show relatively small areas where olivine

grain shapes resemble the mosaic texture. Despite not finding purely mylonitic samples, five samples display an intermediate texture between protogranular and mylonitic (Table 7-1).

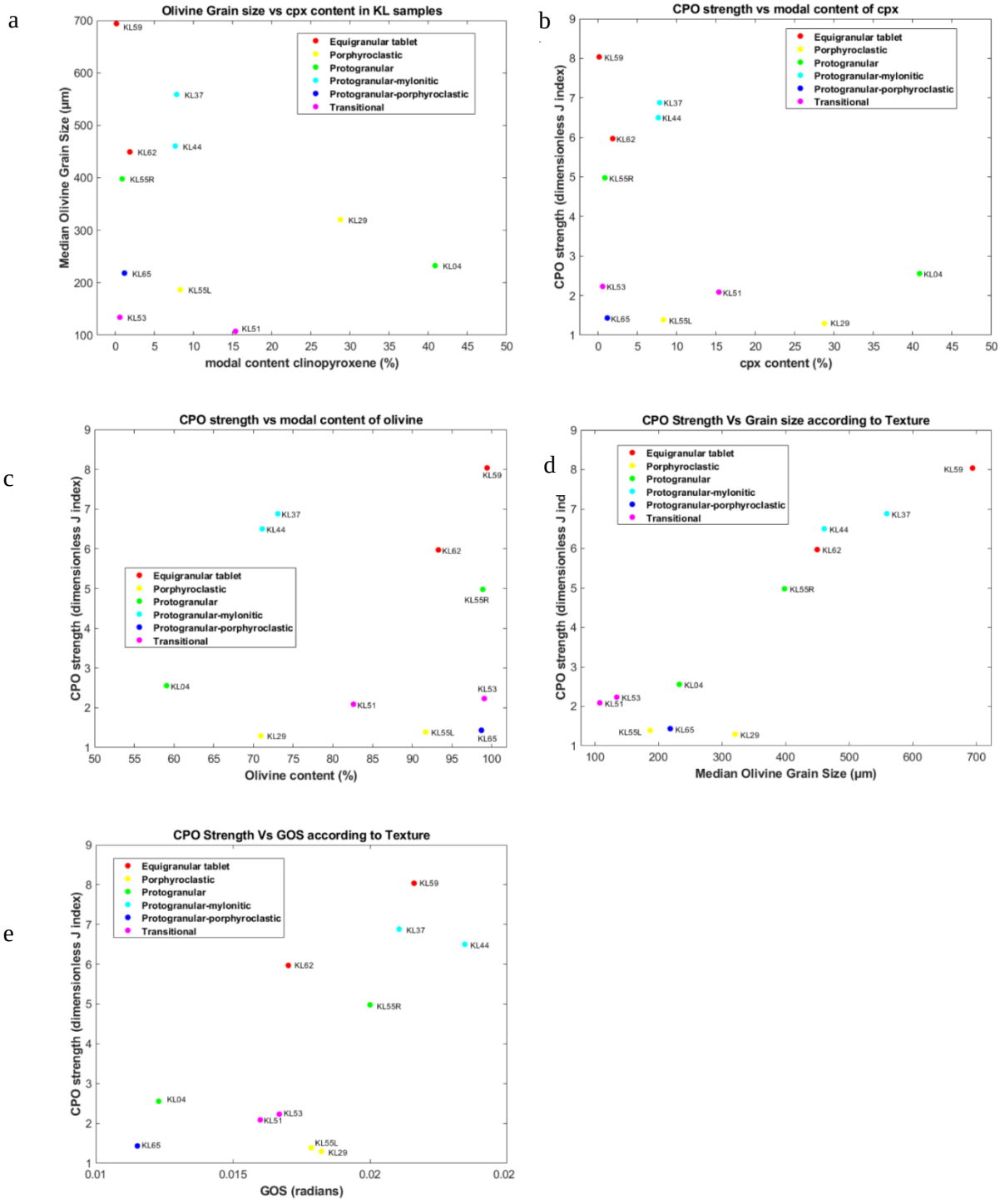

Figure 4- 14. Influence of modal contents of olivine and clinopyroxene/melt in olivine median grain size and strength of the CPO (J-index) grouped by texture. The two textures present in sample KL55 were represented as individual samples (KL55L for left side and KL55R for right side).

In addition to weakening the strength of the CPO (Holtzman et al., 2003; Le Roux et al., 2008), a high melt fraction environment can induce the development of AG-type fabrics from a pre-existing A-type fabric (Chin et al., 2020; Higgie & Tommasi, 2012). Despite a considerable number of studies reporting this fabric transition (Baptiste & Tommasi, 2014; Chin et al., 2016; Chin et al., 2020; Dijkstra et al., 2002; Soustelle et al., 2010), the physical-chemical mechanisms/processes involved in this fabric transition remain poorly understood. Kostal Lake samples are characterized by orthorhombic A-type fabric and axial-[010] or AG-type fabric. While there is no linear relationship between the cpx content and the BA-index, the samples exhibiting AG-type CPO show more textural evidence of rock-melt interaction. Both KL62 and KL65 are dunites resulting from early crystallization of olivine from the transient melt, while KL29 and KL04 are wehrlites with the highest clinopyroxene content, representing a later stage of cpx crystallization from the melt. Figure 4-15 shows an overall decrease of BA-index with increasing cpx context for samples with cpx modal content >5%. Finally, an increase in clinopyroxene content leads to a reduction in the modal abundance of olivine, the most anisotropic mineral in mantle peridotites. This, combined with a decrease in the strength of the olivine CPO, leads to a reduction of anisotropy in A(Vp) and A(Vs). (Figure 4-16).

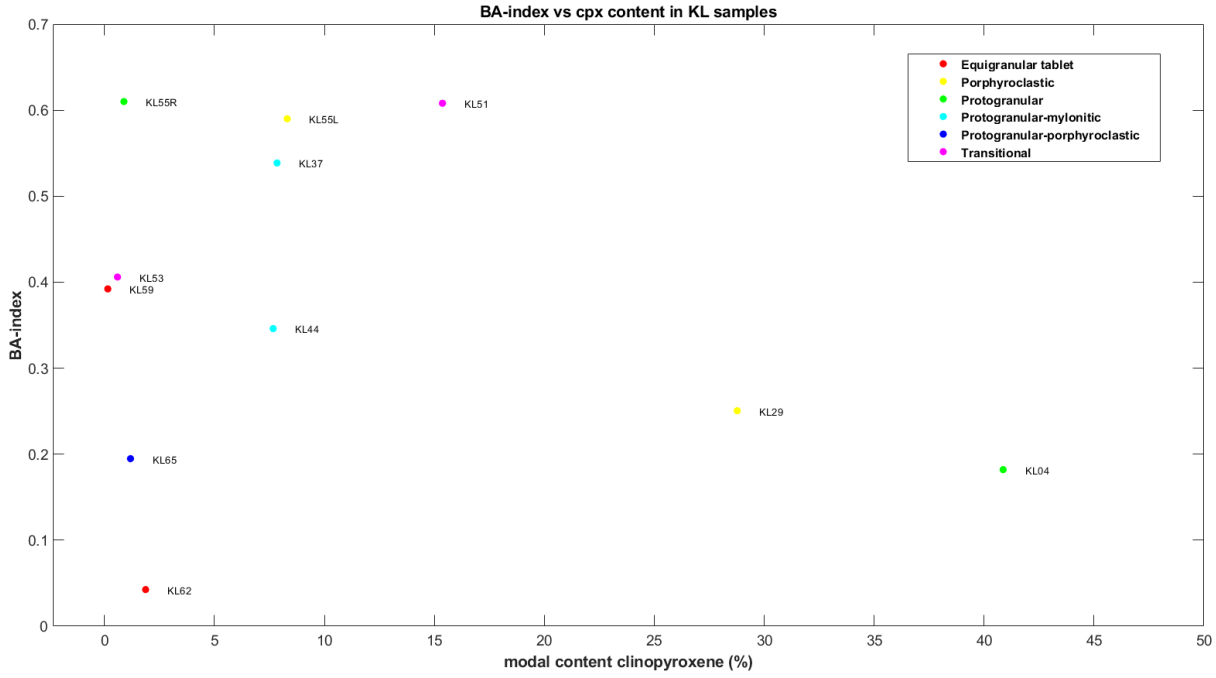

Figure 4-15. Changes in BA-index as a response to increased melt content in Kostal Lake grouped by texture. The two textures present in sample KL55 were represented as individual samples (KL55L for left side and KL55R for right side).

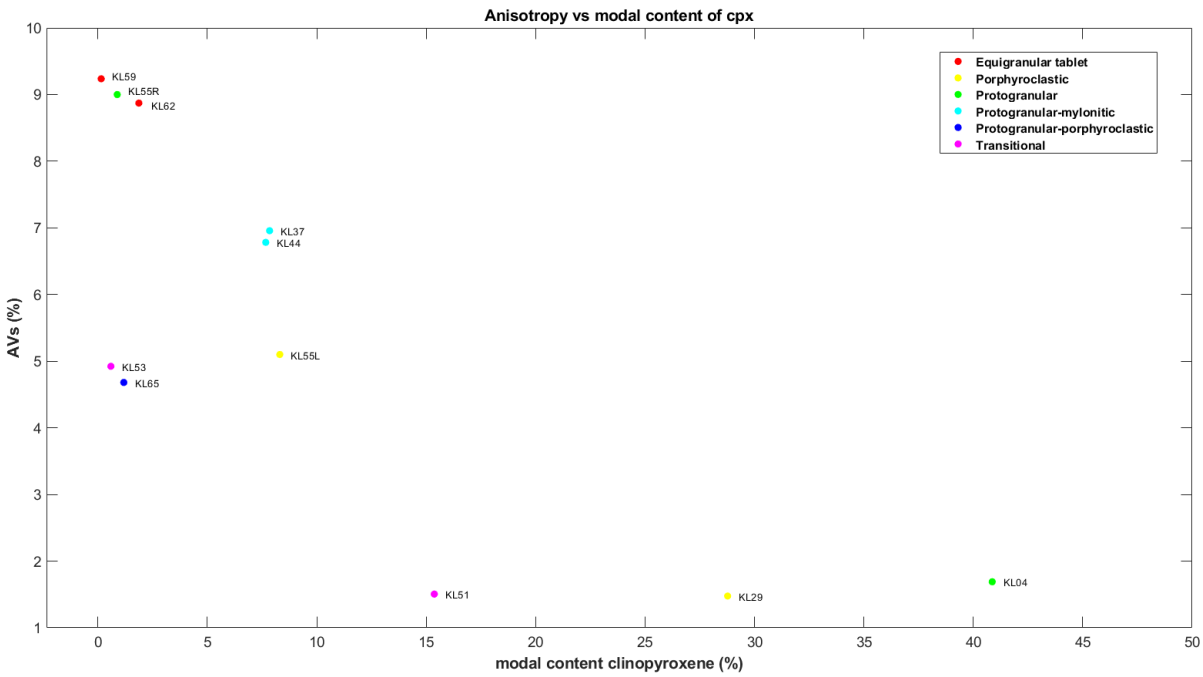

Figure 4-16. Changes in anisotropic properties (maximum A(Vs)) as a response to increased melt content in Kostal Lake grouped by texture. The two textures present in sample KL55 were represented as individual samples (KL55L for left side and KL55R for right side).

CHAPTER 5

Discussion

5.1 Discussion of data

Mantle xenoliths represent a direct window to study the lithospheric mantle. In this work we characterize for the first time the deformation microstructures of 195 xenoliths from eleven volcanic centers covering the entire latitudinal range of the Canadian Cordillera and one on the Alaskan side of the Canada/USA border (Prindle volcano). A sample subset was selected for EBSD analysis based on petrological characterizations of microtextures for each suite. Based on these criteria, the quality of the EBSD scans, and the comparison of our results to previously published work, we are confident in the validity of the data presented in this study as a means to describe the deformation mechanisms at work in the Cordilleran mantle as well as emerging spatial patterns for the Cordilleran mantle. A characterization of subcontinental mantle from mantle xenoliths, however, is based on the assumption that the entrained xenoliths are representative of the lithospheric mantle. Alteration of the xenoliths during ascent and eruption is minor (Peslier et al., 2002). Despite the Cordilleran mantle being relatively thin (10-15 km), and relatively homogeneous in temperature, model ages and prevalence of annealed and weakly deformed textures; we don't have direct means to test the validity of this assumption. To avoid any implication about the volume of mantle associated with each texture, we did not average any of the deformation textures or rock seismic properties.

To compare and contrast our results to previously published data and proceed to discuss the implications of our results in the tectonic context of the Cordillera, we first evaluate the various sources of uncertainty in our work. Following the discussion in Bernard et al. (2019), uncertainties originate from three primary sources: (1) calibration-related, (2) analytical, and (3) uncertainties regarding whether the measurements are representative of deformation conditions.

5.1.1 Instrumentation-related uncertainties

The EBSD detector used in McGill University has been calibrated by Hitachi so that the diffraction pattern that is recorded by the phosphor screen can match the index files (database of patterns for each phase). We used working distance of 18 mm, which has been optimized to make sure of this.

However, even after calibration, measurements of crystallographic orientation are typically said to have a ±1° misfit between the index file and the diffraction pattern due to the blurred edges of the Kikuchi bands. This may have repercussions in the generation and interpretation of M2M maps, but any change in orientation over 2° can be interpreted confidently. The spatial position of the beam on the sample can also induce error in the scans as it is dependent on the motors driving the stage and can drift with time. Furthermore, thermal effects or vacuum stability in the chamber can change the beam conditions, therefore having the potential to affect indexing performance. Overall, these effects are small compared to the strength of the patterns produced. In all cases, the grain reconstructions matched expectations from petrographic microscope and in comparisons between scans collected from the two different SEMs.

5.1.2 Non-scanned areas

Each scan performed at McGill University covers an area of one-third of the thin section corresponding to the top lengthwise portion of the thin section. This is because scanning a larger area increases the risk of collision between the backscatter detector (BSE) and the sample holder. For most thin sections, two scans were performed by rotating the thin section 180^{o}, thus covering approximately 2/3 of the total thin section area and excluding the central 1/3 lengthwise portion (Fig. 4-5A). This may, therefore, miss important textural and/or modal features in our samples, especially those that are banded or foliated parallel or subparallel to the length of the thin section. However, by combining two scans per sample, the EBSD data capture hundreds of grains for each sample, so represent a statistically robust measure of the deformation textures.

5.1.3 Areas of relatively poorer indexing and grain reconstruction during post-processing

In scanned areas or individual fields where the indexing is poorer due to multiple factors (polishing, irregularities in electron beam, cracks in the sample, etc.), and indexed pixels are therefore separated, the grain reconstruction routine we developed in Mtex may reconstruct grains incorrectly. For example, a large grain may be reconstructed as multiple smaller grains with very irregular boundaries if there are patches of indexed pixels separated by non indexed pixels.

Similarly, in samples where olivine reacts and breaks down along its boundaries, the script may identify olivine fragments as individual grains, thus affecting metrics such as grain size, GOS and CPOS. Where this occurred, we corrected by changing the threshold for minimum grain size, based on a comparison with photomicrographs. The impact of this issue in our samples is reduced to a very small number of small grains or grain boundaries of individual grains in a few samples. In such cases, we decided if it was preferable to still maintain the poorly indexed area in order to keep a larger well-indexed portion of the scan or simply eliminate the poorly indexed area from the analyzed polygon (Figure 5-1).

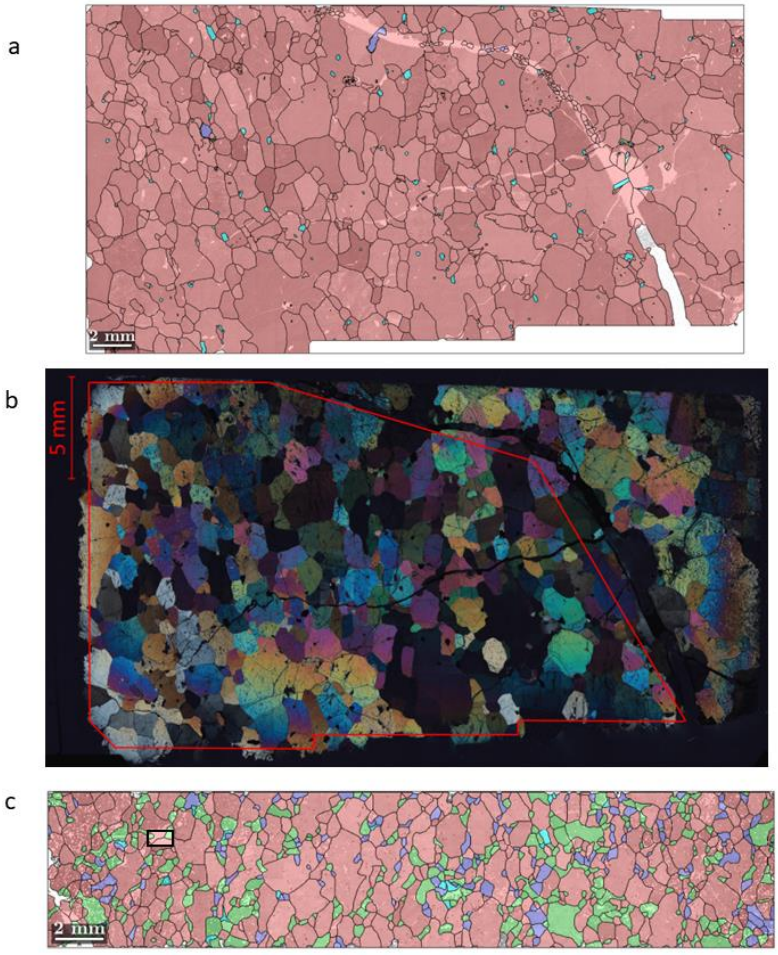

Figure 5-1. Problems in EBSD indexing leading to poor grain reconstruction. (a) phase map of scanned area in sample KL59. Mtex identifies olivine fragments in the thin section crack as small grains. (b) Photomicrograph showing thin section cracks and polygon used for analysis. (c) Phase map of sample HF01. Black rectangle shows poorly indexed field denoted by clearer pink color. In cases where the reconstructed grains were similar or identical to what was observed in the photomicrograph, we kept the data. Eliminating this field implied eliminating all data to the left or above.

5.1.4 Step sizes

Step sizes of EBSD were determined prior to scans based on the overall grain size in the sample as evaluated from petrographic microscope observations. This can lead to small errors in

grain area and boundary complexity (shape factor) as the distance between indexed pixels is larger. After close examination, based on comparison to photomicrographs, the grain reconstruction in samples where larger step sizes were used was satisfactory and no errors were found resulting from our choice in step size.

5.1.5 Sample edges peeling off during polishing

The edges of sample AL45 slightly peeled off during the polishing process, mainly at the manual stages. The peeling is most likely caused by old epoxy and perhaps poorly prepared glass surfaces. The bathing colloidal fluid will transport any frictional heating away. The colloidal silica is corrosive, so it can exploit any interfaces and perhaps infiltrate into the epoxy-glass contact via capillary action and some dissolution. While the scan was performed in the central part of the sample, we suspect this problem may have induced errors in the GOS of this sample, which is anomalously high. Other parameters for this sample fell within the range of average values for Cordilleran xenoliths and more specifically for Alligator Lake samples.

5.1.6 Approach to CPO representation

In this work we used one point per grain when plotting pole figures, as it minimizes weighting toward individual large grains, so is a better approach for most samples showing porphyroclastic and mylonitic textures.

The common reference frame used by rotating the maxima in [100] to the E-W direction may lead to the omission of B-, C- and E-type fabrics for samples with orthogonal CPO ($0.35<BA<0.65$). A rotation of 90° around the [010] cluster in B-types fabrics results in the A-type pattern. Similarly, rotating 90° around the vertical [010] cluster and then 90° around the [100] cluster in C-type results in A-type. If the [100] cluster in E-type fabric is rotated 90°, the apparent pattern is that of A-type fabrics. Therefore, visual inspections of fabric types can be problematic if the thin section orientation with respect to foliation and lineation is unknown. Extra work is needed to evaluate specific slip systems to differentiate A-, B-, C- and E-type fabrics. To partially correct for this, the [100] maxima was rotated in a N-S orientation to check for C-type fabric in

cases where the A-type fabric pattern wasn't well defined, but the observed pattern didn't correspond.

Another limitation in the CPO fabric classification in this study comes from the assumption of a simple shear regime. However, different stress configurations result in different CPO patterns for the same slip system (Skemer and Hansen, 2016). Namely, in triaxial compression, the pattern for A- and B-type fabrics is the same as the AG-type fabric in simple shear. (Figure 5-2)

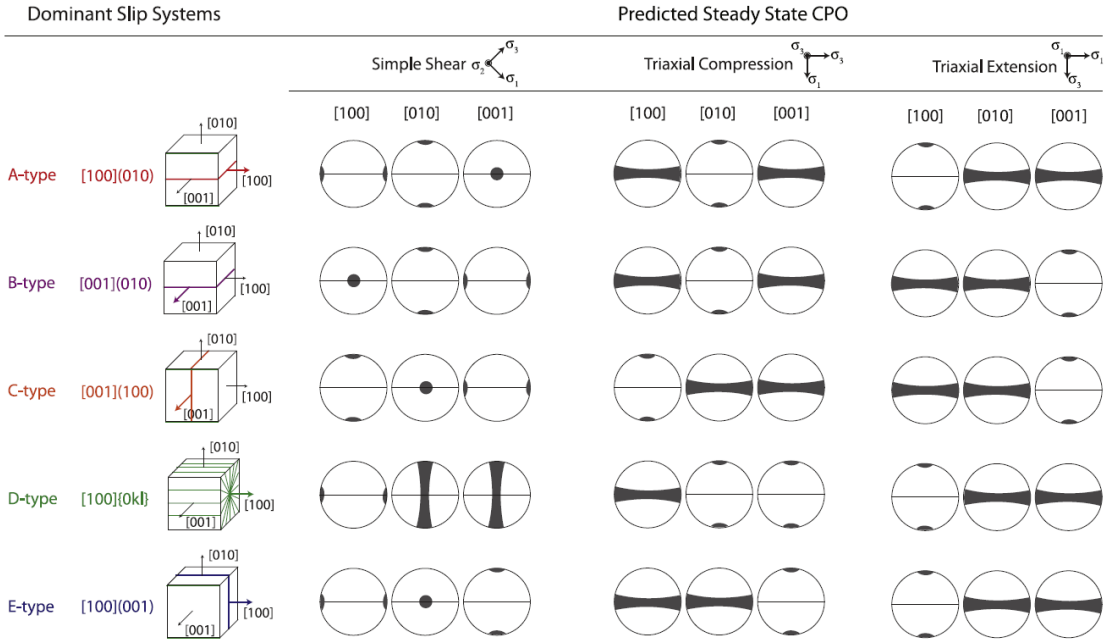

Figure 5-2. Diagram illustrating the spectrum of olivine CPOs expected to form for a range of stress states and slip-system activities. Taken from Skemer and Hansen (2016). Note that AG-type fabric is not represented.

An ideal method to quantify the fabric type is the FIA-index (Michibayashi et al., 2016), which results in a numeric angle value in degrees for each fabric. However, this method requires the x-y-z structural reference frame of the sample (corresponding to the principal axes of the finite strain ellipsoid) to be known, which is, in most cases, difficult for mantle xenoliths. As most thin sections in this study were produced for previous work, the sections were cut in an arbitrary orientation with respect to the structural reference frame. This is a major limitation on the interpretation of fabric types, as discussed above. Alternatively, plotting the alignment of intragrain misorientation axes with misorientation angles between 2^{o} and 10^{o} with respect to [100], [010] and [001] indicates the slip system for grains showing such misorientation axes.

Regardless of these limitations, the presence of D-type and presumably A-type fabrics is typical of continental lithospheric conditions and consistent with the tectonic framework of the Cordilleran interior from which the xenoliths were collected (Michibayashi et al., 2016). These two fabrics are expected to occur in the fore-arc and shallow back-arc mantle lithosphere (Cao et al., 2015 and references therein). This reflects a mostly dry lithospheric mantle, occasionally altered by melt, which may explain the transition to AG fabrics.

5.2 Spatial distribution of fabrics

All suites with xenoliths of the AG-type olivine fabric, also show xenoliths with orthorhombic olivine fabrics (Figure 5-3). AG-type fabric combines the [100] (010) slip system of the dry A-type and the [001] (010) slip system of the B-type. Chin et al. (2020) discuss possible mechanisms for the development of olivine AG-type fabrics from pre-existing A-type fabric. For samples with evidence of rock-melt interaction, they propose an SPO-controlled CPO where olivine grains rotate with their flattest (010) faces aligned with magmatic flow. However, other factors such as the stress geometry (Figure 5-2), static recrystallization and elevated water content in olivine may be responsible (Chin at al., 2020 and references therein). We hypothesize that the AG-type fabrics in our samples developed from A-type xenoliths. In agreement with Chin et al. (2020) we propose that the development of the AG-type in Kostal Lake is caused by melt-rock interaction in localized sections or channels of the lithospheric mantle. In the rest of the suites where the AG-fabric is present but evidence for melt-rock interaction is not, any of the aforementioned mechanisms (or combinations of) could have induced the transition from olivine A- to AG-type.

Except for sample LG14, which displays an orthorhombic fabric; xenoliths in the suites that contain D-type fabric (LG, HF, CR, SL and RR) do not show other fabrics. Relative to the A-type, the D-type is indicative of higher stress with similarly low water contents (Karato et al., 2008). Since calculated temperatures from mantle xenoliths in the Cordillera are inferred to be relatively homogeneous (Greenfield et al., 2013; Prescott, 1983; Shi et al., 1998), this may be indicative of different deformation conditions that are particular to these suites, thus indicating spatial variations

in stress. These higher stress conditions are reflected in a moderate decrease in grain size with respect to that of orthorhombic fabrics (Figure 5-8). Grain-size reduction in D-type fabrics is particularly relevant in Rayleigh River, where all samples are fine-grained, thus trending to mylonitization. The rest of the suites exhibiting D-fabrics display either mosaic equigranular or protogranular textures, indicating annealing. The vast majority of samples in Peri-Laurentian terranes of oceanic origin, present D-type fabrics (Figure 5-3). Suites containing olivine D-type fabric xenoliths include multiple terranes, a wide range of distances to the Cordilleran Deformation Front and almost the entire latitude range of the Canadian Cordillera. In addition to this, Rayfield River is relatively close to Big Timothy and Kostal Lake, which do not have xenoliths with the D-type fabric. While we cannot accurately establish the causes for such spatial variability in the distribution of olivine fabrics, our results indicate heterogeneity in olivine slip systems in the Cordilleran mantle, thus suggesting spatial variations in mantle deformation conditions at the intra and inter suite scales.

Our findings are, for the most part, consistent with previously published results. Most of the 21 olivine CPOs for Summit Lake in Morales and Tommasi (2011) indicate D-type fabrics with the exceptions of sample 01SL24, which is reminiscent of an AG-type fabric and sample 01SL5b, a pyroxenite where the olivine CPO pattern is diffuse. The olivine CPOs of 5 mantle xenoliths from Summit Lake are shown in Saruwatari et al. (2001). Two of these xenoliths display intermediate CPOs between A- and D-types and three xenoliths suggest A-type fabrics. Jacques Lake xenoliths in the same study show AG and A-type olivine fabrics in agreement with our results. Also in agreement with our results, Ji et al. (1994) show D-type olivine patterns for five Castle Rock xenoliths and AG and A-type fabrics for Alligator Lake samples. Our fabric classification of the results published in these studies is based on a visual interpretation of the patterns in their CPO figures. These authors did not aim to classify the olivine fabrics as we did in this study. Consequently, there are no metrics (e.g., BA-index) to confirm these interpretations. Furthermore, the number of represented olivine grains per sample in Ji et al., (1994) and Saruwatari et al., (2001) never exceeds 150. Their data is, therefore, less substantial for CPO characterization than the data in this study.

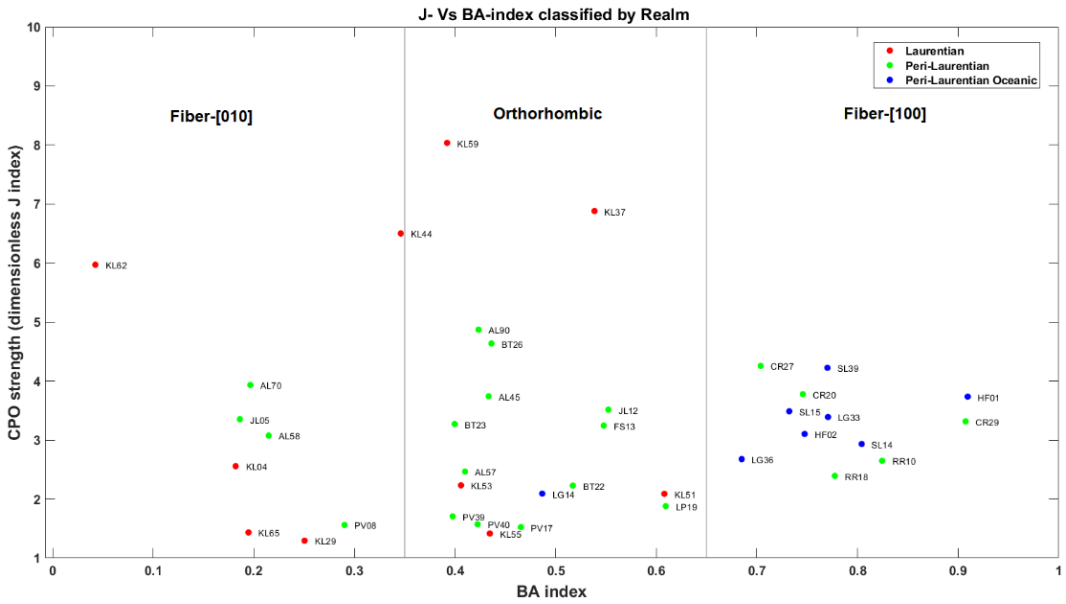

Figure 5-3. J- vs BA-index by Realm. Fiber-[010] field corresponds to AG-type olivine CPO fabric. Orthorhombic field corresponds to A-type olivine CPO fabric. Fiber-[100] corresponds to D-type olivine CPO fabric.

5.3 Spatial-Temporal patterns in the development of microtextures

It is difficult to constrain the timing of the most recent deformation of the studied xenoliths. The elevated temperatures recorded for mantle xenoliths throughout the Cordillera are sufficient for annealing peridotites that are not subject to ongoing deformation (Karato, 1989). Speciale et al. (2020) conducted deformation and grain growth experiments on natural olivine aggregates and proposed that for most tectonic settings with evidence of annealing, the eruption age postdates the timing of the last tectonic event by at least 1 million years. This minimum time estimation for grain growth contrast with faster rates estimated by the olivine grain growth in Karato (1989). Since annealing is a relatively fast process at elevated temperatures of ~1000 ^{o}C, relative to cratonic mantle temperatures of ~450 ^{o}C; we can assume that all mantle xenoliths of the Cordillera exhibiting porphyroclastic, mylonitic and "transitional" textures must record deformation events that occurred less than a million years before their extraction ages (Speciale et al., 2020). Similarly, xenoliths exhibiting annealed textures were last deformed more than a million years before they were transported to the surface by alkaline lavas.

Coarse-grained protogranular and equigranular textures are predominant within the Cordilleran mantle. Figure 4-2 illustrates how equigranular textures are predominant in northern suites followed by coarse, undeformed protogranular and an intermediate texture between

equigranular and protogranular. The evidence of various degrees of annealing in the northern portion of the Cordillera is reflected in abundant ~120°triple junctions, straight to gently curved grain boundaries (low shape factors) and low degree of undulose extinction (low GOS). This suggests the incidence of different processes, conditions, and timing of deformation with respect to the southern suites.

In southern suites, the protogranular texture is the most abundant, being predominant in every suite, except Rayfield River. The porphyroclastic, mylonitic and "transitional" textures, characterized by a marked reduction in grain size, were only observed in the southern suites, particularly in Rayfield River and Kostal Lake. Both suites, together with Summit Lake, contain significant numbers of the Al-augite xenoliths (Francis et al., 2010). These are, for the most part, wehrlites dominated by augite and olivine, which have been interpreted as cumulates formed by the reaction of alkaline melts with a peridotitic lithospheric mantle (Francis et al., 2010; Peslier et al. 2002).

We can infer relative timing of deformation relative to melt-rock interaction based on the pyroxenes grain-shapes and on the correlation (or lack of) of their CPOs with olivine CPOs. The more equilibrated, euhedral pyroxene grains in samples with equigranular textures and, to a lesser extent in some protogranular samples, suggest that annealing occurred after refertilization. This is particularly the case for many mosaic equigranular samples (e.g., PV17, PV40, AL45, AL57), where in addition to their equilibrated pyroxene grain shapes, pyroxene CPOs are correlated/coeval to olivine CPOs. On the other hand, samples with anhedral pyroxenes exhibiting highly sinuous grain boundaries and poor correlation between olivine and pyroxene CPOs (e.g., KL04, KL55) suggest that refertilization succeeded the last main deformation episode. Within individual suites, some samples show equilibrated pyroxene grain shapes and coeval deformation of pyroxenes and olivine while others do not. For example, BT22 shows very sinuous pyroxene grain boundaries with no CPO correlation, whereas orthopyroxene in BT23 displays more euhedral shapes and orthopyroxene CPO correlated to that of olivine. These variations within a suite may indicate either vertical variations in a relatively thin lithospheric mantle (as would be expected for a steeply dipping shear zone that transects a range of temperatures) or different deformation and refertilization events affecting the entire mantle and captured by multiple eruptions.

Evidence of melt-rock interaction in the Cordillera has been reported for SL (Morales and Tommasi, 2011; Peslier et al., 2002), KL (Peslier et al., 2002) and RR (Francis et al., 2010). These three suites present very distinctive textures and deformation sequences. While we cannot propose the exact time of deformation, we can use textural and deformation evidence, together with the eruption ages, to put some constraints on the deformation history of the mantle beneath these suites.

The 13 mantle xenoliths from Summit Lake in this study exhibit protogranular textures. Morales and Tommasi (2011) report predominantly equigranular and protogranular textures and cpx contents ranging from 5 to 37% in Summit Lake xenoliths. Clinopyroxene content recrystallized from melt in SL samples varies from 12% to 18% in our scanned samples and was higher for many SL xenoliths characterized using an optical microscope. Clinopyroxene grains in Summit Lake xenoliths are generally coarse, euhedral, and similar in size and shape to olivine grains, which indicates that the last deformation event affected all phases present. Furthermore, clinopyroxene CPOs in Summit Lake xenoliths are coeval with those of olivine. This indicates that melt-rock interaction precedes a later event that equilibrated/annealed all pre-existing phases in SL, resulting in the dominance of protogranular and equigranular textures. Since all SL samples display equilibrated pyroxene textures, annealing must have occurred after melt ingress, followed by weak deformation as some samples show a weak SPO. The melt ingress observed is not the same melt as that which caused the xenolith transport to the surface as xenoliths transport times by eruption are on the order of a day or two. From these observations, we can infer that melt ingress precedes by more than a million years, the eruption age of 26 Ma for this suite.

All Rayfield River samples exhibit pervasive grain size reduction and various degrees of mylonitization. If melt-rock interaction is the cause for the overall grain size reduction in this suite, it must have modified olivine grains with a pre-existing strong shape-preferred orientation as all samples present a well-defined foliation. In addition to this, coarser grains are slightly elongated conforming to the foliation. As in KL samples showing intact evidence of melt-peridotite interaction (Figure 4-13), these coarser grains also present very cuspate boundaries when in contact with smaller grains resulting from the interaction between olivine and melt. The LPOs of both recrystallized and relict grains show similar, well-defined D-type fabrics. Since rock-melt

interaction tends to weaken and shift the pre-existing CPO towards AG-type, it is not likely that melt-rock interaction was the last deformation event.

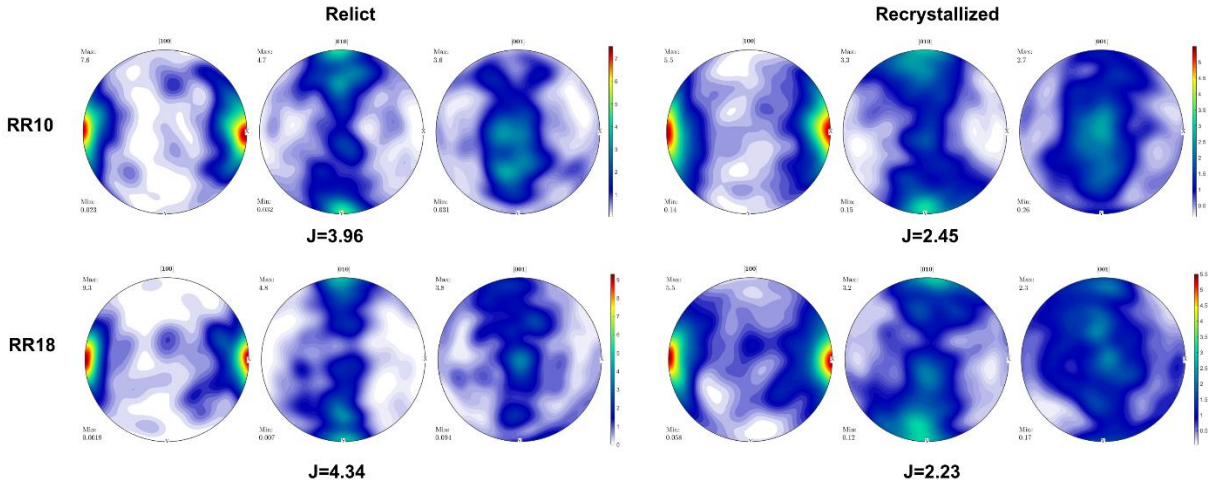

Figure 5-4. *Olivine CPOs of relict and recrystallized grains of scanned Rayfield river samples*.

An alternative sequence requires a relatively undeformed initial texture first affected by melt rock interaction leading to grain size reduction and followed by increased strain in a second deformation event, thus explaining the observed LPO. A third possibility, where rock-melt interaction is absent, would require anomalously high strain levels relative to the observed textures in the rest of suites, thus explaining the prevailing mylonitic textures. In both cases, it is difficult to explain the highly irregular grain boundaries and shapes of small grains, as dynamically recrystallized grains tend to be equant and have smoothly curved boundaries. If increased strain leading to dynamic recrystallization and thus mylonitization was the last event, it was not sufficient to delete the inherited CPO fabric in recrystallized grains or smooth the highly irregular appearance of grain boundaries. In any case, Rayfield river samples were deformed not long before the eruption age of 6-10 Ma as evidenced by the lack of annealed grains.

The best-preserved microstructural evidence of melt-rock interaction in Cordilleran xenoliths comes from Kostal Lake. This suite is exceptional in displaying a wide range of textures in the peridotite deformation cycle. This range of textures contrasts with that observed in xenoliths from other volcanic suites in the Canadian Cordillera, which are generally limited to one or two microtextures. We follow the interpretations of Chin et al. (2020) to propose that, in addition to strain and static recrystallization, rock-melt interactions induced changes in grain size, foliation,

deformation mechanism and strength of the CPO, leading to the development of porphyroclastic, mylonitic and transitional textures in this suite.

Kostal Lake exhibits different CPO strength parameters relative to the other 11 suites in this study, which suggest the influence of local processes and possibly, a distinct deformation history with respect to Peri-Laurentian suites in the Cordillera. Two distinct groups of samples were observed in this suite based on the strength of the CPO (Figure 5-3):

Group 1: Includes samples KL04, KL29, KL51, KL53, KL55 and KL65. These samples present a high proportion of small, recrystallized olivine grains and some of the weakest CPOs among our samples of Cordilleran xenoliths (J-index<3.0). In samples KL04, KL29 and KL55, the overall reduction in grain size clearly results from the contact of olivine with percolating melt (Figures 4-13 and 7-3).

Group 2: Includes samples KL37, KL44, KL59 and KL62. These samples present a unimodal, medium to coarse grain size distribution and the highest J-index values among all the Cordilleran xenoliths investigated in this study (J>5.0). While the cpx content in the two lherzolites (KL37 and KL44) is approximately 8%, cpx grains are coarse, equant and appear in equilibrium with olivine and opx. If cpx in these samples is the product of melt percolation, a second annealing event, possibly followed by deformation by weak strain, must have equilibrated the grain sizes and microstructures towards a more protogranular texture. Further evidence of this comes from the coeval CPOs of both opx and cpx in samples KL37 and KL44.

Based on the observed textures in KL, many of which record recent deformation events, and the calculated eruption age of ~7750 BP (Peslier et al., 2002), we interpret the textures exhibiting melt-rock interactions to be recent relative to eruption. On the other hand, samples with evidence of annealing (e.g., KL59, KL62) were last deformed at least one million years prior to entrainment. Since xenoliths of different textures were erupted at the same time, we can infer a high degree of spatial variability in the mantle underlying KL. Sample KL55 clearly demonstrates that there are spatial variations in the distribution of melt that are pronounced over the scale of a single xenolith (a few cm). This is in agreement with Peslier et al., (2002) who proposed a lithospheric mantle for SL and KL characterized by "Cr-diopside peridotite crosscut by discordant veins of dunite, wehrlite, pyroxenite and opx-poor lherzolite". Peslier et al. (2002) also suggest that the higher proportion of augite xenoliths in this location can be explained by the higher circulation of melts

in the transition zone between the Cordilleran orogen and the craton. Canil and Russell (2022) proposed a thinner lithosphere for Summit Lake, also proximal to the craton boundary. If this is the case lengthwise along the craton edge, focused heat during edge convection would be expected to result in a hot, weak lithosphere favouring melt percolation.

5.4 Proposed modifications to peridotite deformation cycle

In chapter 1 we discussed the peridotite deformation cycle as proposed by Chin et al., (2021) developed after Mercier and Nicholas, (1975). Based on our observations on the processes influencing the development of the described textures, we propose a new diagram that incorporates the mylonitic texture, the distinction between tabular equigranular and mosaic equigranular and the addition of melt-rock interaction as a texture-modifying mechanism (Figure 5-5).

The transitions between textures conditioned by increased strain (blue arrows) and annealing (green arrows) have been well documented by Chin et al. (2021). However, there is no distinction in the proposed cycle between the tabular and the mosaic equigranular textures. We propose that the development of the tabular equigranular texture precedes the mosaic equigranular, based on the abundance of inherited sub grain boundaries indicative of high dislocation densities at high angle to the SPO in the tablets. We interpret these dislocations to result from previously existing ones in relict grains and different orientations of recrystallized grains in preceding textures. As the rock continues to anneal, grain boundaries change to more equant shapes, thus minimizing the number of dislocations per grain and the free energy of the system (Passchier & Trouw, 2005).

In our model, melt interaction can modify the pre-existing textures as follows:

(1) Interaction with protogranular leading to protogranular and mylonitic textures: Interaction of olivine with melt will lead to a progressive reduction in grain size around the boundaries of coarse grains. If the pre-existing protogranular texture has no foliation, both relict and recrystallized grains will lack a shape preferred orientation (e.g., left side of KL55). If the protogranular texture had a weak defined foliation and/or melt infiltrates through preferentially oriented channels, melt percolation may enhance the pre-existing SPO/foliation, more typical of porphyroclastic textures (e.g., KL65, KL29). If grain size

reduction in a preferred orientation persists, porphyroclastic textures transition into mylonitic.

(2) Interaction with tabular equigranular texture: If olivine grain size reduction is mild, a protogranular texture, with very irregular grain boundaries results. If grain size reduction is pervasive and melts circulates favoured by the orientation of the SPO, a mylonitic texture can result.

(3) Interaction with the transitional tablet texture: melt in contact with the tablet would alter the straight grain boundaries, making them more cuspate. The grain size of tablets and relict porphyroclast will be considerably reduced, resulting in a fine-grained protogranular texture.

(4) Interaction with mosaic equigranular texture: results in more variation in grain size and more irregular grain boundaries, thus erasing the 120^{o} triple junctions.

The transitional-tablet texture was only observed in this study in two samples from Kostal Lake (KL51 and KL53). This texture has mostly been reported in cratonic kimberlites (Chin et al., 2021 and references therein), except for one xenolith from the Pannonian Basin where tablet formation has been attributed to the presence of a grain boundary fluid or melt (Falus et al., 2003). KL is a young cinder cone located in the Laurentian realm, proximal to the cratonic edge (http://gsc.nrcan.gc.ca/volcanoes/cat/volcano_e.php?id=wcb_kcn_004). The discovery in this study of two samples exhibiting this texture in an orogenic setting confirms that the transitional-tablet texture is not exclusive to cratonic mantle. Furthermore, we believe that the tablets are relatively short lived as olivine continues to anneal. The presence of this texture in mantle xenoliths, regardless of the tectonic environment, depends on if the timing of entrainment coincides with the short presence of this texture in the lithospheric mantle.

In this study we had the opportunity to study xenoliths from three suites exhibiting evidence of melt-peridotite interaction. The sequences and of deformation varied greatly between suites and we also interpreted spatial variations within the same suite (KL). We conclude that chemical processes, namely melt-rock interaction, can alter peridotite textures as much as mechanical processes. The interplay of different intensities of mechanical deformation and melt-rock interaction can potentially result in multiple microtextures including intermediate textures.

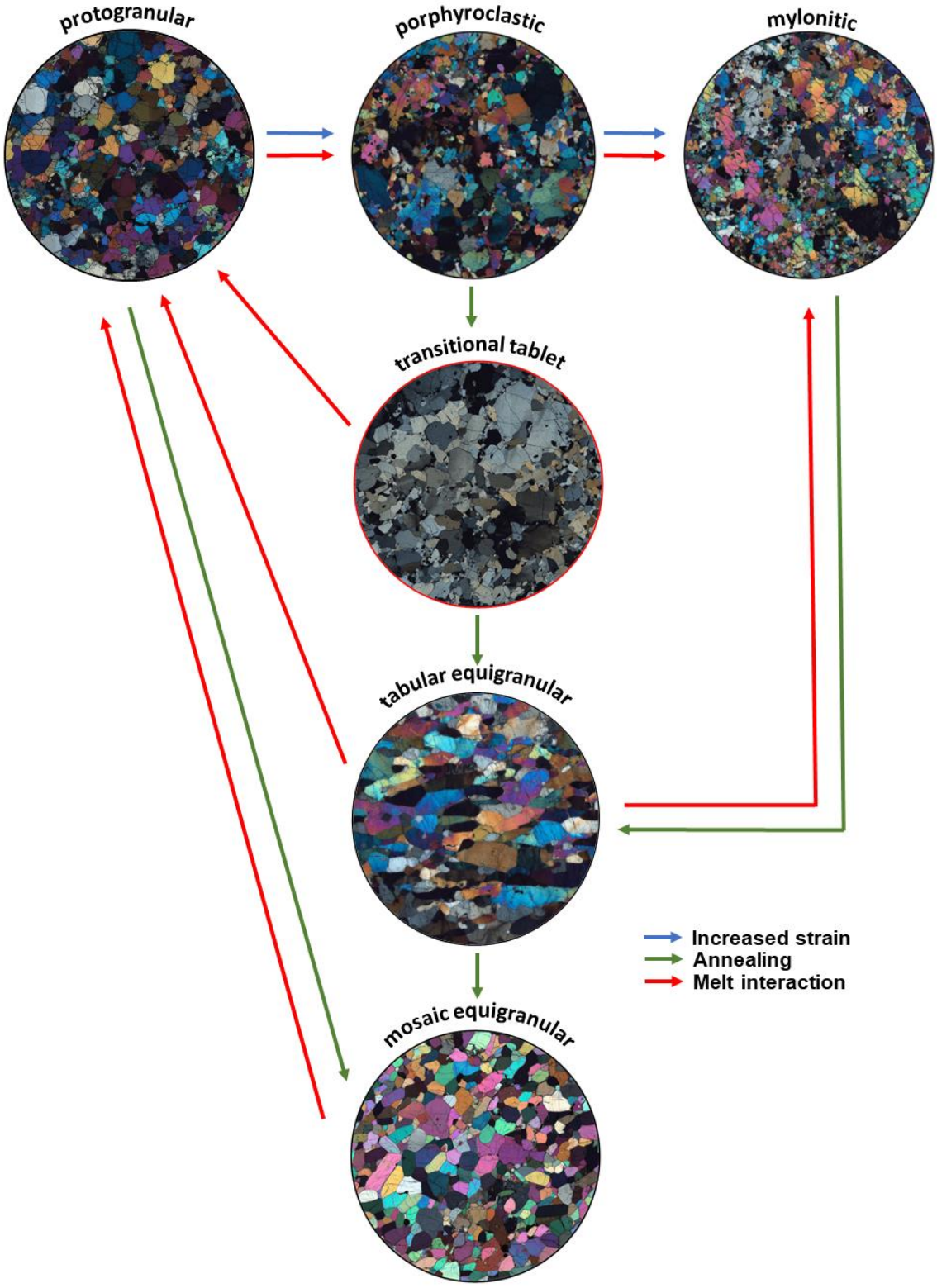

Figure 5-5. Proposed modifications to the peridotite deformation cycle in Chin et al., (2021).

5.5 Spatial patterns in seismic anisotropy and comparison to published geophysical data

Peridotitic xenoliths in this study represent accidental pieces of the lithospheric mantle with unknown spatial position and orientation at the time of entrainment in the eruptive melt. It is, therefore, impossible to know the geographical direction of anisotropy from the study of xenoliths and, by extension, its relationship to structural features and modern constraints on mantle flow. Similarly, extrapolating anisotropic properties from xenoliths to characterize the whole mantle is too difficult and/or not sufficient to test for other observed patterns in regional seismic studies, such as mechanical coupling between the crust and the mantle at the time of deformation in certain areas of the cordillera, mostly near large transform faults (Estève et al., 2021; McLellan et al., 2018). Our results, however, are direct measurements and provide important constraints on the magnitudes and patterns of seismic anisotropy along the Cordillera as well as the factors that influence changes both intra and inter localities. Under the assumption that the orientation of mantle xenoliths results in the same direction of the anisotropy as in geophysical studies, we can compare the magnitudes of seismic anisotropy between the two methods, to better understand the factor that contribute to spatial variations of seismic anisotropy along the cordillera.

The suites with the lowest values of seismic anisotropy correspond to the northernmost (PV) and the southernmost suites (LP), in accordance with their low calculated J-indexes. The range of values for the northern localities (A(Vp)= 2.6-10.5 %; A(Vs)=2.1-7.5 %) approximates that of the southern localities (A(Vp) =1.7-12.5; A(Vs)=1.5–9.0 %). Magnitudes per suite of both A(Vp) and A(Vs) peak at ~54^{o}N (SL) and progressively decrease in the north and south directions (Figure 5-6). The decrease in anisotropic properties from Summit Lake to higher latitudes shows a clear pattern for both A(Vp) and A(Vs). The pattern south of Summit Lake is slightly more complex. Spatially cluttered suites JL, KL and BT display a wide range of A(Vp) and A(Vs) values resulting from variations in fabric, CPO strength and the fact that at the intra-suite level, some xenoliths display coeval pyroxene deformation, thus strengthening the anisotropy and contributing to the variability.

a)

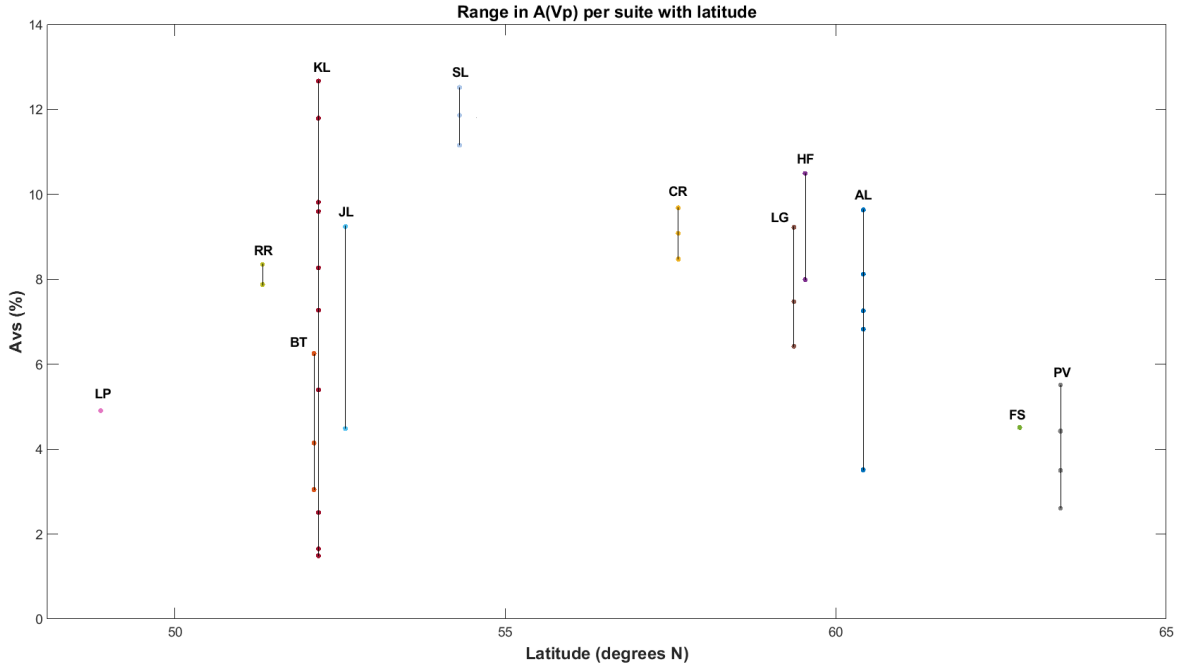

b)

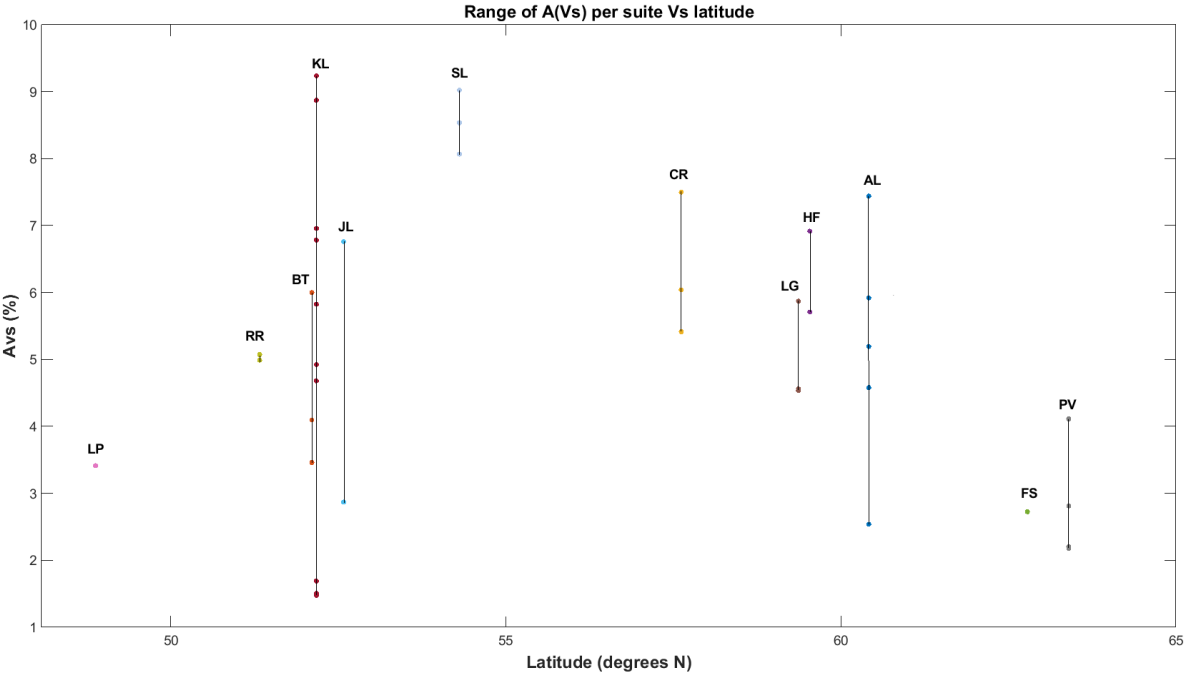

Figure 5-6. (a) Anisotropy (Vp) range per suite Vs latitude. (b) Anisotropy (Vs) range per suite Vs latitude.

Xenoliths displaying the most anisotropic properties are found in Summit Lake and Kostal Lake, the two localities that are closest to the cordillera-craton boundary. In addition to very anisotropic xenoliths, Kostal Lake presents the highest variability in anisotropic properties. Here, statically recrystallized samples (e.g., KL59, KL62) show highly anisotropic properties, whereas

samples with significant grain-size reduction and/or clinopyroxene content (e.g., KL04, KL29, KL51) display the lowest anisotropic values in the cordillera.

Inter-locality spatial variations of seismic anisotropy properties do not display the same patterns as in geophysical studies. For lithospheric mantle depths, Estève et al., (2021) report the highest magnitudes of azimuthal anisotropy in the northern Cordillera for latitudes north of 62^{o} N in a WSW-ENE orientation. Samples from the two suites in this latitude range in this study (PV and FS) display some of the lowest anisotropy values. Despite these differences in spatial distribution, the anisotropy magnitudes of 2-4% for the ~62-64^{o}N latitudes are consistent. Figure 4 in Estève et al., (2021) shows a decrease in anisotropy south of 62^{o} N; and a progressive clockwise change in orientations to NW-SE. Anisotropy values decrease from the cordillera interior to the cordillera-craton boundary (Estève et al., 2020; Estève et al., 2021; Tarayoun et al., 2017), opposite to what our results show. While geophysical studies quantifying seismic anisotropy in the Canadian Cordillera south of 56^{o}N are not readily available, studies focusing on higher latitudes show a well-defined reduction in magnitudes in the interval between 60^{o}N-56^{o}N marked by the presence of the Liard transfer zone and oriented concordantly with the absolute plate motion of the North American plate (Audet et al., 2016; Estève et al., 2020; Tarayoun et al., 2017). Unfortunately, instrumentation deployment for geophysical studies in the southern cordillera is less adequate. Bostock and Cassidy (1995) show a relatively uniform ENE-WSW orientation for SKS splitting measurement but marked spatial differences in arrival times for stations between 46^{o}N and 54^{o}N. This is consistent with the large variations in A(Vp) in the JL, KL, BT, RR cluster. The difference in orientation is mostly attributed to less prevalent influence of dextral faults in the Southern Cordillera and a strong asthenospheric flow signal caused by compressive stresses in the lithosphere. Spatial variations in arrival times are attributed to the possible presence of more than one underlying anisotropic layer at lithospheric and asthenospheric levels. This heterogeneity in lithology is adopted as the preferred interpretation in Saruwatari et al., (2001) to explain the difference between highly anisotropic xenoliths and regional scale isotropy. Overall, our results point towards a discrepancy in spatial variations in anisotropy with respect to geophysical studies for both the northern and the southern Cordillera.

Multiple geophysical studies remark the relevance of the Tintina fault as a structural control for seismic anisotropy in the mantle (Estève et al., 2021; McLellan et al., 2018; Tarayoun et al., 2017). The Tintina fault is a large right-lateral transform fault responsible for ~430 km of horizontal displacement between 65 and 37 Ma that reaches lithospheric mantle depths (Cook et al., 2004; Monger & Price, 2002). Orientation of azimuthal fast-axis is largely sub-parallel to the orientation of the Tintina fault at latitudes between 58 to 65 degrees north and magnitudes are larger in the proximity of the fault (McLellan et al., 2018). Summit Lake is the only suite in this study located relatively close to the Tintina fault. This suite presents the highest average values in anisotropy, which may be the result of a shear-fabric induced by fault motion. If the strong anisotropy of this suite was indeed acquired during dextral motion of the Tintina fault, we can further constrain the last deformation event at Summit Lake between 65 and 37 Ma.

Fort Selkirk is located near to the trace of the Teslin fault. This fault, unlike Tintina, is limited to crustal scale. This may explain the low to average anisotropy recorded in this suite. However, due to the very coarse-grained textures in xenoliths this suite, only one thin section was eligible for EBSD analysis. Furthermore, the current location of this suite coincided with a strongly negative Vp anomaly both prior to and after the 430 km displacement by dextral motion along the Tintina fault (Figure 2 in Estève et al., 2020.). If abnormally high mantle temperatures were the cause for this negative anomaly, they may have been enough to weaken the anisotropy strength of the mantle in this area.

Using observed delay times due to shear wave splitting, Bolton et al. (2021) estimated an anisotropic layer thickness of about 90 km using under the assumption of a 4% anisotropic upper mantle. Our results, however, yield higher average anisotropy (A(Vp) ~ 7.1 %, A(Vs) ~ 5.2 %) than was assumed by Bolton et al. (2021), which indicates the thickness of the anisotropic layer may be ~50 km if we use 7% anisotropy. This result is more consistent with a the seismically imaged shallow LAB, but still requires a substantial component of crustal anisotropy to account for the observed delay times.

While none of the proposed geophysical interpretations fully explain our observations of spatial variations of seismic anisotropy in the cordillera; our calculated anisotropic properties per scanned sample are in accordance with published data for xenoliths in both the northern and southern Canadian Cordillera (Ji et al., 1994; Morales and Tommasi, 2011; Saruwatari et al.,

2001). Anisotropic values and patterns in our samples directly depend on the CPO strength and fabric type. Anisotropy increases with olivine modal content and consequently decreases with increasing pyroxene percentage. Melt-rock interactions are therefore likely to have a profound impact on the interpretation of the geophysical results. We also found that coeval deformation of olivine and pyroxenes results in stronger anisotropic properties for samples with similar olivine content and CPO strength. In this study we present a robust characterization of seismic anisotropy from 39 xenoliths from 12 volcanic suites in the Canadian Cordillera and Alaska. The strength of the anisotropy varies from weak in the north and south most suites to moderate and strong in the 52^{o}N to 62^{o}N latitude range, peaking at 54^{o}N. The discordant spatial distributions with respect to geophysical studies may be indicative of a heterogeneous lithospheric mantle both at the inter and intra locality scales. Our results also suggest a spatial pattern different to that observed at crustal levels, suggesting mechanical de-coupling between the mantle and the crust. The fact that the suites most proximal to the craton are the most anisotropic may be attributed to enhanced edge-driven convection at the cordillera-craton boundary (Bao et al., 2014; Hardebol et al., 2012). While the higher temperatures of upwelling at the cordillera-craton step may partially weaken anisotropy, we propose that enhanced flow is redirected in a strike parallel orientation consistent with geophysical studies (Tarayoun et al., 2017 and references therein) and thus contributing to higher anisotropic values.

5.6 Implications for tectonic history

The crustal architecture of the Canadian Cordillera is particularly complex as it reflects episodes of compression, extension, subduction as well as terrane accretion and collision. Many of the cordilleran terranes developed far away from the craton's edge as volcanic arcs. Table one classifies the tectonic units in which the volcanic centers are located based on surface geology and the classification in Nelson et al. (2013). However, the lithospheric mantle from which the xenoliths were entrained is, in most cases, unknown in relation to the terrane history. Cook et al. (2004) use Lithoprobe seismic reflection profiling to show the main characteristics and units at crustal depths in the cordillera (Figure 5-7). With the possible exception of Stikinia, the terranes on which the volcanic centers in our study are located, are restricted to upper crustal levels. Yukon-Tanana, Slide Mountain, Quesnellia, and Cache Creek terranes represent thin crustal

slivers detached from their lithospheres that were thrust over North American strata from hundreds of kilometers to the west (Cook et al., 2004). These terranes are underlain by a seismically imaged lower crustal layered sequence (LCLS) of Proterozoic strata and their basement of North American affinity. The LCLS extends to the western edge of Stikinia, where it's wedged under the eastern-most Stikinian rocks. Rocks affiliated with Stikinia, therefore, are inferred to occupy most of the crust, possibly implying that a Stikinian lithospheric mantle is still attached and accreted to North American mantle to the east. Alternatively, a rheologically weak thin layer of North American strata, possibly an extension of the LCLS, may underlay Stikinia, over which the Stikinia block was thrust during collision, thus allowing detachment from its original mantle.

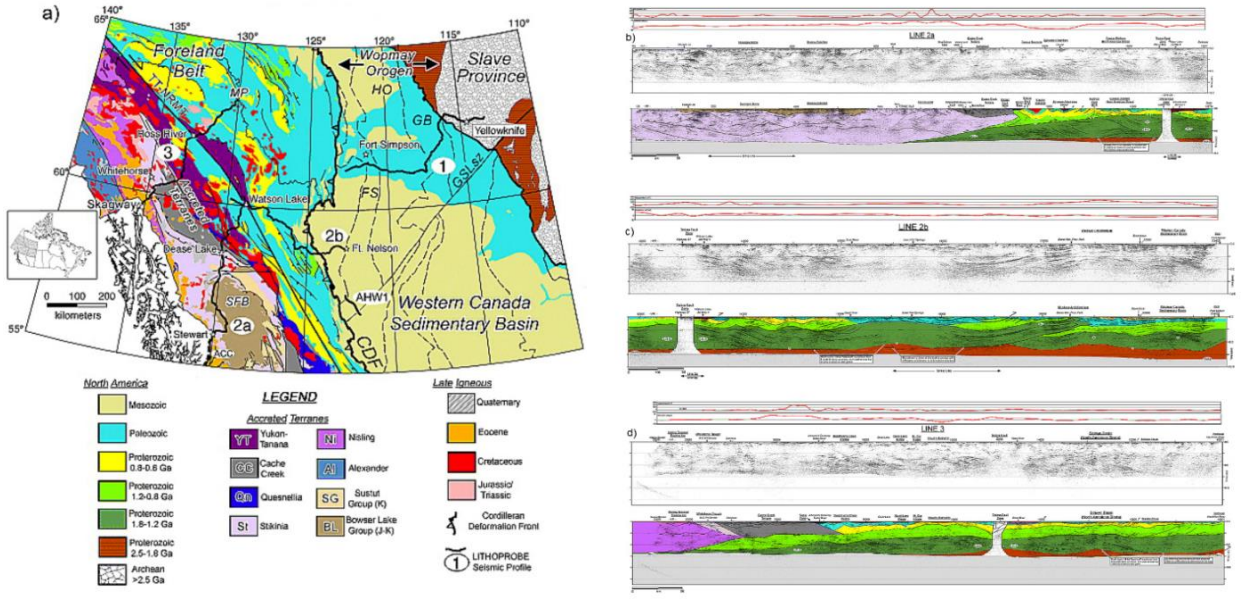

Figure 5-7. Map of terranes showing Lithoprobe transects (a) in Cook et al., (2004). Seismic reflection profiles and interpretations of transects 2a, 2b and 3 represented as (b), (c) and (d), respectively. LCLZ is represented in dark green and underlays Yukon-Tanana, Cache-Creek and Quesnellia. Stikinia (light fuchsia), is interpreted to occupy the entire crustal depth range. Taken from Cook et al., (2004).

Geophysical, petrological and heat flow observations suggest a generally homogeneous lithospheric mantle in the Canadian Cordillera (Hyndman and Canil, 2021 and references therein). Most of the Cordillera is uniformly hot with a flat, shallow Moho and thin lithosphere, in spite of numerous terranes with diverse and complex tectonic histories (Audet et al., 2019; Coney et al., 1980; Tarayoun et al., 2017). Heat flow in the northern cordillera is unusually high, consistent with a shallower LAB of ~50 km with respect to the rest of the North American Cordillera, where LAB

depths average ~65 km (Flück et al., 2003; Lewis et al., 2003). The predominance of relatively fertile lherzolites, reflecting 8% to 10% melting of primitive mantle (Francis et al., 2010; Peslier et al., 2002), uniform model ages with long term melt depletion at about 1.1 Ga (Peslier et al., 2000a) further indicate homogeneity of the lithospheric mantle. Based on the observation, any differences in the mantle composition may therefore be subtle.

Cratonic and island arc mantle lithosphere have several distinguishing characteristics, which could be used to test the origin of the xenoliths erupted through the Stikinia terrane. Relative to cratonic mantle, the lithospheric mantle under volcanic arcs is characterized by higher water content. Peslier et al. (2017) report mostly low water contents in olivine for most cratonic environments of less than 10 ppm, regardless of spatial variabilities horizontally and with depth. The Cordilleran Lithospheric mantle is similarly strong and dry, <50 ppm H_2O (Hyndman and Canil, 2021). Further evidence for low water content comes from the presence of hydrous minerals (amphibole phlogopite) in less than five peridotite xenoliths in the entire Cordilleran region (Canil & Scarfe, 1989; Hyndman & Canil, 2021). The Mg# in mantle peridotites reflects the degree of melt depletion or enrichment in iron (Pearson et al., 2014). The Mg# of on-craton peridotitic olivine is between 91–94, reflecting its generally more iron-depleted nature and 88–92 for off-craton mantle xenoliths (Bernstein et al., 2007; Boyd, 1989). Olivine Mg-numbers for 25 xenoliths in five Stikinian (Castle Rock) and non-Stikinian Cordilleran suites (Nunivak Island, Prindle Volcano, Fort Selkirk, and Jacques Lake) range between 86.7 and 91.6, consistent with off-craton xenoliths (Prescott, 1983). Depleted xenoliths from cratonic mantle are poor in Al and Ca compared to off-cratonic mantle (Bernstein et al., 2007). Peslier et al. (2002) determined that Al_2O_3 contents vary from site to site in the southern Canadian Cordillera. They found that Al_2O_3 content was highest (~4.8 wt %) in lherzolites at Lightning Peak and Kettle River (not in this study) and lowest (~1.4 wt %) in lherzolites at Kostal Lake.

Based on the possible cratonic character of the mantle beneath Yukon-Tanana, Slide Mountain, Quesnellia, and Cache Creek terranes and the possible difference in mantle genesis for Stikinia, we compared the EBSD results xenoliths sourced from Stikinian suites with xenoliths the rest of the volcanic suites. Only two volcanic centers are located on Stikinia (AL, 60.4^{o}N and CR, 57.6^{o}N). Using teleseismic travel-time inversion, Frederiksen et al. (1998) detected a low-velocity seismic anomaly extending to 500-km depth under Alligator Lake, Hirschfeld Creek and Llangorse

Mountain, which has been attributed to high heat flow related to the opening of a slab window ~50 Ma (Kilgore et al., 2018; Madsen et al., 2006; Shi et al., 1998; Thorkelson et al., 2011). The anomalously hot asthenospheric mantle has been interpreted as the cause of the bimodal character of these suites (Kilgore et al., 2018; Shi et al., 1998). The local character of this anomaly, 200 km wide and 500 km deep, supports the conclusion that the mantle and overlying crust are not genetically linked. We found no significant differences in CPO strength, fabric, grain size and textures between Stikinian and non-Stikinian samples. Our results suggest that while these metrics vary at the inter and intra suite level in the cordillera, the mantle under Stikinia is not different from North American mantle under the rest of the terranes. This suggests that (1) the mantle under Stikinia is also of North American origin or (2) if Stikinian mantle was attached to the crust and imported at the time of accretion, a later event altered and homogenized the mantle under the cordillera. These conclusions are also supported by similar Os-model ages (Peslier et al., 2000a) and olivine Mg-numbers (Prescott, 1983)

One clear outcome arising from the EBSD analyses is the prevalence of D-type fabrics in Peri-Laurentian samples as the fiber-100 symmetry is unique to the D-type fabric. Xenoliths from the volcanic suites that that exhibit D-type fabrics, exclusively display this fabric (except for sample LG14). Furthermore, suites in the Peri-Laurentian realm with oceanic genesis only show D-type fabrics. D-type fabrics are indicative of relatively low water content and high stress (Figure 1-3). In this study, we could not measure water content in xenoliths. However, the van der Waal piezometer establishes that smaller olivine grain sizes are indicative of higher stress, regardless of water content (Van der Wal et al., 1993). To test for stress variability strictly with respect to orthorhombic fabrics, we plotted the grain size with respect to BA index (Figure 5-8). Overall, the population of samples exhibiting D-type fabrics shows smaller average grain size than orthorhombic samples, thus suggesting spatial variability in stress magnitudes along the Cordillera. Note that grain size reduction in samples KL51, KL53 and KL65, which exhibit orthorhombic fabrics, is inferred to be a consequence of melt-rock interaction instead of increased strain.

As discussed in previous sections, spatial variability in the Cordilleran mantle is also indicated by the presence of textures indicating melt-rock. Evidence for melt-rock interaction has

only been observed in three southern suites: SL, KL and RR. While edge-driven convection in the proximity to the cordillera-craton boundary has been proposed as the mechanism that facilitates melt ingress in SL and KL, it does not explain melt in RR and its absence in BT. Consequently, another mechanism must be locally responsible for melt ingress, at least in RR. Temporally, we established differences in the relative timing for melt-rock interaction between these suites. Since the eruption times for SL (26 Ma), KL (7750 BP) and RR (6-10 Ma) are relatively far apart, it is difficult to establish if such melt-ingress events affect the three suites in unison or if they represent local, isolated events.

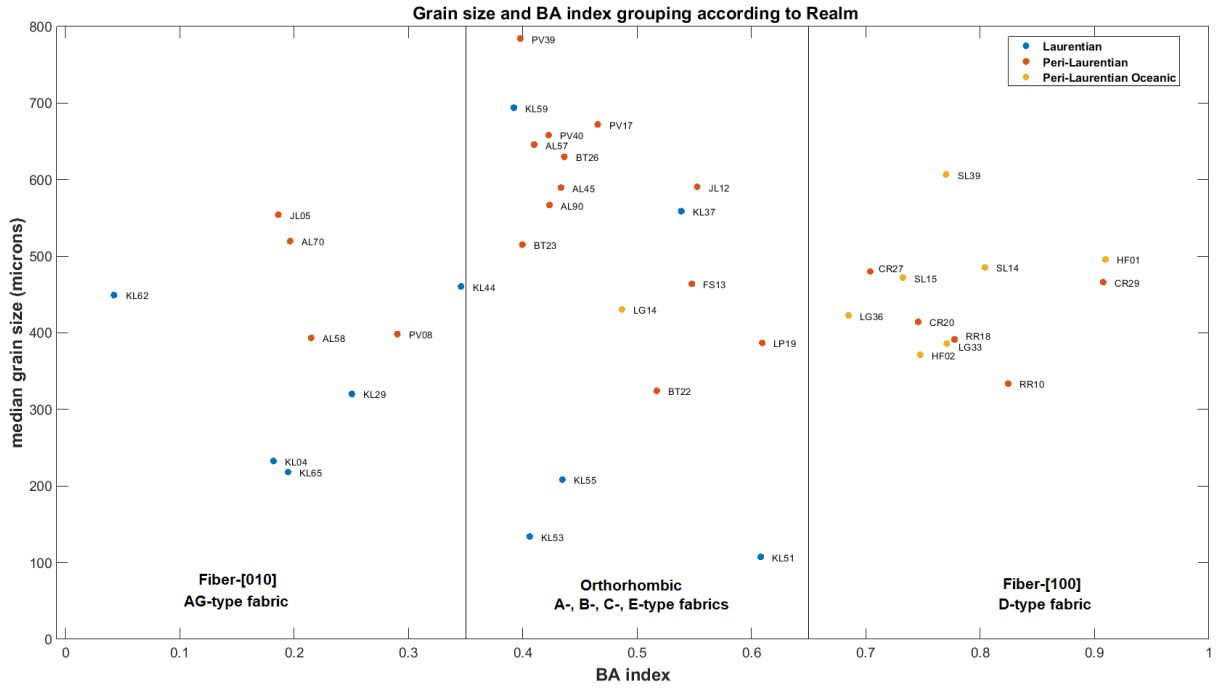

Figure 5-8. Plot of median grain size vs BA-index showing overall smaller grain size of D-type fabrics relative to orthorhombic fabrics as an indicator of higher stress magnitudes in D-type samples. Fine-grained sizes in samples KL51, KL53 and KL55 are inferred to result from rock-melt interaction instead of increased stress.

Aside from the inferred higher stress magnitudes in suites with prevalent D-type fabrics and the localized changes in texture and CPO pattern induced by melt-rock interaction in SL, KL and RR, we found no other clearly defined patterns that differentiate xenoliths from a particular terrane or realm. This is consistent with other factors, such as model ages of ~1.1 Ga inferred throughout the Canadian Cordillera (Peslier et al., 2000a), high temperatures of ~1000 ºC (Table 1-1), coarse grain sizes, and the prevalence of lherzolites (Francis et al., 2010), which point toward a relative

homogeneity (or at least similar degree of variability) for most of Cordilleran mantle and a distinct geochemical signature of the cordilleran mantle with respect to cratonic mantle (Kroner, 2019). A recent study by Canil et al. (2021) used Geothermometry on coexisting ortho- and clinopyroxene using Ca-Mg-Fe (TBKN) and REE (TREE) exchange. From the small differences in TREE and TBKN ($\Delta T_{REE\text{-}BKN}$) they calculated a cooling rate $< 10^5$ ◦C /Myr for the xenoliths and implying an old lithospheric mantle, consistent with Os-model ages of 1.1 Ga in Peslier et al. (2002). The moderate strength of the CPOs and seismic anisotropy of xenoliths in this study, together with previous characterizations of cordilleran xenoliths, suggest an overall annealed to weakly deformed cordilleran mantle, sporadically affected by the incidence of local processes leading to the development of more deformed porphyroclastic and mylonitic textures. The influence of local processes can also be observed at the intra-suite level, as evidenced in the presence of more than one texture in individual volcanic suites, indicative of changes with depth in the ~15km of lithospheric mantle. A hot, weakly deformed mantle is consistent with the "orogenic float model" proposed by Mazzotti and Hyndman (2002). implying that compressional stresses related to the orogeny are accommodated at weak lower crust levels. It also helps explain the difference in magnitudes and orientations of seismic anisotropy between the mantle and crustal levels away from the structural control of the Denali and Tintina faults as seen in Tarayoun et al. (2017).

Of the various models that have been proposed to explain a flat, shallow Moho and a thin lithospheric mantle for the Cordillera, lithospheric delamination is the most consistent with our observations (Bao et al., 2014; Audet et al., 2019 and references therein). Here, the lowermost crust and lithospheric mantle detach due to negative buoyancy (Bao et al., 2014; Audet et al., 2019 and references therein). As the detached lithosphere gradually subsides, asthenospheric mantle rises and new lithosphere is formed from decompression melting and conductive cooling. Constant heat from small-scale asthenospheric convection cells prevents further lithospheric thickening (Bao et al., 2014; Audet et al., 2019). Such a delamination event is inferred to have occurred between 55 Ma and 40Ma in Bao et al., (2014). Audet at al. (2019) estimate that it occurred between ~25 Ma and 5 Ma. If the latter is more accurate, at least the xenoliths from SL precede delamination as they were erupted ~26 Ma. While Bao et al. (2014) interpret the top of a high-velocity layer at a depth of ~150 km as the delaminated Cordilleran lithosphere; it is hard to reconcile a recently rejuvenated lithosphere with the model ages of ~1.1-1.26 Ga calculated by

Peslier et al. (2000a). Similarly, the cooling rates estimated by Canil et al. (2021) imply that the mantle lithosphere in the Cordillera is hundreds of millions of years old. While this doesn't exclude the possibility of a delamination event, it limits its occurrence to: (1) a much older event at ~1.1 Ga or (2) a recent event in which only the lower part of the lithospheric mantle detached along a shear zone.

A rejuvenated lithosphere, regardless of age, is consistent with the relative homogeneity in mantle xenolith along the latitude range of our study area. "Tertiary to Recent" eruption ages (Francis et al., 2010) are later relative to delamination and formation of new lithosphere. In agreement with Peslier at al. (2002) and geophysical studies that image a sharp contrast in depth at the cordillera-craton boundary (e.g., Bao et al., 2014; Audet et al., 2019), we believe that edge-driven convection enhances melt circulation and ingress in SL and KL, thus explaining the compositional and microstructural differences in these localities. An alternative, or possibly coexisting mechanism, was proposed by Hyndman and Canil (2021). In their model, melt ascending through a damp asthenosphere accumulates at the base of the strong dry lithosphere, where it geochemically equilibrates. If buoyant melt becomes gravitationally unstable, it locally ascends to the surface. This mechanism may explain localized melt ingress at Rayfield River.

While characterizing the deformation and anisotropy of mantle xenoliths reveals important constraints on regional and local patterns in the Cordilleran mantle, it is insufficient to test the many hypotheses that have been formulated to explain the origin and evolution of the lithospheric mantle in the Cordillera. Further geophysical evidence is required to test for defining features that will help determine the validity of the models thus far proposed. These include, but are not limited to, resolving the orientation of sutures, variability of structures along the cordillera-craton boundary and better characterization of seismic anisotropy for latitudes south of 56 ^{o}N.

CHAPTER 6

Conclusions

Analyses of microstructures in mantle xenoliths from twelve volcanic centers along the latitude range of the Canadian Cordillera show a relatively homogeneous and weakly deformed lithospheric mantle. Annealed equigranular textures are predominant in northern suites, whereas protogranular textures are most abundant in southern suites. Despite these general trends, changes in textures and deformation parameters are observed at the intra and inter-locality level, suggesting spatio-temporal variations in deformation conditioned by local processes. In particular, evidence for peridotite-melt interaction was observed to induce significant modifications in texture, CPO and seismic properties through an overall decrease in grain size, weakening of the CPO and a shift toward the olivine AG-fabric.

Seismic anisotropy magnitudes obtained from the direct study of mantle xenoliths peak at latitudes between 52 and 54 ^{o}N and decrease as we progress to higher and lower latitudes. This spatial behavior contrasts with patterns resulting from regional geophysical studies, which show weak seismic anisotropy south of 56 ^{o}N. Such results may indicate that geophysical results for seismic anisotropy at depth of approximately ~30 km may have a strong signal from the lower crust. This together with the marked differences with anisotropy at shallower crustal level and the microtextural evidence of weak to moderate deformation support the "orogenic float" proposed by Mazzotti and Hyndman (2002) for the northern Canadian Cordillera.

As a technique, EBSD is a time-consuming process that presents numerous technical challenges. However, it's a powerful tool to understand deformation mechanisms and the evolution of microtextures. While our results are insufficient to test for the many models proposed for the origin and evolution of the lithospheric mantle under the Cordillera, they contribute to a better characterization of the processes at work in such a complex tectonic environment. Further studies are required for a better understanding of the role of the mantle in orogenic settings.

REFERENCES

Abraham, A.-C., Francis, D., & Polvé, M. (2001). Recent alkaline basalts as probes of the lithospheric mantle roots of the Northern Canadian Cordillera. *Chemical Geology*, *175*(3), 361-386. https://doi.org/10.1016/S0009-2541(00)00330-2

Abramson, E., Brown, J., Slutsky, L., & Zaug, J. (1997). The elastic constants of San Carlos olivine to 17 GPa. *Journal of Geophysical Research: Solid Earth*, *102*(B6), 12253-12263.

Arndt, N. T., Guitreau, M., Boullier, A. M., Le Roex, A., Tommasi, A., Cordier, P., & Sobolev, A. (2010). Olivine, and the Origin of Kimberlite. *Journal of Petrology*, *51*(3), 573-602. https://doi.org/10.1093/petrology/egp080

Audet, P., Currie, C. A., Schaeffer, A. J., & Hill, A. M. (2019). Seismic Evidence for Lithospheric Thinning and Heat in the northern Canadian Cordillera. *Geophysical Research Letters*, *46*(8), 4249-4257. https://doi.org/10.1029/2019GL082406

Audet, P., & Mareschal, J.-C. (2007). Wavelet analysis of the coherence between Bouguer gravity and topography: application to the elastic thickness anisotropy in the Canadian Shield. *Geophysical Journal International*, *168*(1), 287-298. https://doi.org/10.1111/j.1365-246X.2006.03231.x

Audet, P., Sole, C., & Schaeffer, A. J. (2016). Control of lithospheric inheritance on neotectonic activity in northwestern Canada? *Geology*, *44*(10), 807-810. https://doi.org/10.1130/G38118.1

Bachmann, F., Hielscher, R., Jupp, P. E., Pantleon, W., Schaeben, H., & Wegert, E. (2010). Inferential statistics of electron backscatter diffraction data from within individual crystalline grains. *Journal of Applied Crystallography*, *43*(6), 1338-1355.

Bachmann, F., Hielscher, R., & Schaeben, H. (2011). Grain detection from 2d and 3d EBSD data—Specification of the MTEX algorithm. *Ultramicroscopy*, *111*(12), 1720-1733.

Bao, X., Eaton, D. W., & Guest, B. (2014). Plateau uplift in western Canada caused by lithospheric delamination along a craton edge. *Nature Geoscience*, *7*(11), 830-833. https://doi.org/10.1038/ngeo2270

Baptiste, V., & Tommasi, A. (2014). Petrophysical constraints on the seismic properties of the Kaapvaal craton mantle root. *Solid Earth*, *5*(1), 45-63.

Behr, W. M., & Hirth, G. (2014). Rheological properties of the mantle lid beneath the Mojave region in southern California. *Earth and Planetary Science Letters*, *393*, 60-72. https://doi.org/https://doi.org/10.1016/j.epsl.2014.02.039

Ben Ismail, W., & Mainprice, D. (1998). An olivine fabric database: an overview of upper mantle fabrics and seismic anisotropy. *Tectonophysics*, *296*, 145-157.

Bernard, R. E., & Behr, W. M. (2017). Fabric heterogeneity in the Mojave lower crust and lithospheric mantle in Southern California. *Journal of Geophysical Research: Solid Earth*, *122*(7), 5000-5025. https://doi.org/10.1002/2017JB014280

Bernard, R. E., Behr, W. M., Becker, T. W., & Young, D. J. (2019). Relationships Between Olivine CPO and Deformation Parameters in Naturally Deformed Rocks and Implications for Mantle Seismic Anisotropy. *Geochemistry, Geophysics, Geosystems*, *20*(7), 3469-3494. https://doi.org/10.1029/2019GC008289

Bernard, R. E., Schulte-Pelkum, V., & Behr, W. M. (2021). The competing effects of olivine and orthopyroxene CPO on seismic anisotropy. *Tectonophysics, 814*. https://doi.org/10.1016/j.tecto.2021.228954

Bernstein, S., Kelemen, P. B., & Hanghøj, K. (2007). Consistent olivine Mg# in cratonic mantle reflects Archean mantle melting to the exhaustion of orthopyroxene. *Geology*, *35*(5), 459-462. https://doi.org/10.1130/g23336a.1

Bolton, A. R., Schutt, D. L., Aster, R. C., Audet, P., Schaeffer, A. J., Estève, C., Freymueller, J. T., & Cubley, J. F. (2021). Evidence for asthenospheric flow rotation in northwest Canada: insights from shear wave splitting. *Geophysical Journal International*, *228*(3), 1780-1792. https://doi.org/10.1093/gji/ggab396

Boneh, Y., Chin, E. J., Chilson-Parks, B. H., Saal, A. E., Hauri, E. H., Carter Hearn, B., & Hirth, G. (2021). Microstructural Shift due to Post-Deformation Annealing in the Upper Mantle. *Geochemistry, Geophysics, Geosystems*, *22*(3). https://doi.org/10.1029/2020GC009377

Boneh, Y., Morales, L. F. G., Kaminski, E., & Skemer, P. (2015). Modeling olivine CPO evolution with complex deformation histories: Implications for the interpretation of seismic anisotropy in the mantle. *Geochemistry, Geophysics, Geosystems*, *16*(10), 3436-3455. https://doi.org/10.1002/2015GC005964

Boneh, Y., Wallis, D., Hansen, L., Krawczynski, M., & Skemer, P. (2017). Oriented grain growth and modification of 'frozen anisotropy' in the lithospheric mantle. *Earth and Planetary Science Letters*, *474*. https://doi.org/10.1016/j.epsl.2017.06.050

Bostock, M. G., & Cassidy, J. F. (1995). Variations in SKS splitting across western Canada. *Geophysical Research Letters*, *22*(1), 5-8. https://doi.org/10.1029/94GL02789

Boullier, A. M., & Nicolas, A. (1975). Classification of textures and fabrics of peridotite xenoliths from South African kimberlites. *Physics and Chemistry of the Earth*, *9*, 467-475. https://doi.org/https://doi.org/10.1016/0079-1946(75)90034-8

Boyd, F. (1989). Compositional distinction between oceanic and cratonic lithosphere. *Earth and Planetary Science Letters*, *96*(1-2), 15-26.

Brearley, M., Scarfe, C. M., & Fujii, T. (1984). The petrology of ultramafic xenoliths from Summit Lake, near Prince George, British Columbia. *Contributions to Mineralogy and Petrology*, *88*(1-2), 53-63. https://doi.org/10.1007/BF00371411

Bunge, H. J. (1982). *Texture analysis in materials science : mathematical methods* (English ed.). Butterworths. http://books.google.com/books?id=ODdRAAAAMAAJ

http://catalog.hathitrust.org/api/volumes/oclc/5219058.html

https://www.sciencedirect.com/science/book/9780408106429

Canil, D., Hyndman, R. D., & Fode, D. (2021). Hygrometric Control on the Lithosphere-Asthenosphere Boundary: A 28 Million Year Record From the Canadian Cordillera. *Geophysical Research Letters*, *48*(9). https://doi.org/10.1029/2020GL091957

Canil, D., & Russell, J. K. (2022). Xenoliths reveal a hot Moho and thin lithosphere at the Cordillera-craton boundary of western Canada. *Geology*. https://doi.org/10.1130/G50151.1

Canil, D., & Scarfe, C. M. (1989). Origin of Phlogopite in Mantle Xenoliths from Kostal Lake, Wells Gray Park, British Columbia. *Journal of Petrology*, *30*(5), 1159-1179. https://doi.org/10.1093/petrology/30.5.1159

Cao, Y., Jung, H., & Song, S. (2017). Olivine fabrics and tectonic evolution of fore-arc mantles: A natural perspective from the Songshugou dunite and harzburgite in the Qinling orogenic belt, central China. *Geochemistry, Geophysics, Geosystems*, *18*(3), 907-934. https://doi.org/10.1002/2016GC006614

Cao, Y., Jung, H., Song, S., Park, M., Jung, S., & Lee, J. (2015). Plastic Deformation and Seismic Properties in Fore-arc Mantles: A Petrofabric Analysis of the Yushigou Harzburgites, North Qilian Suture Zone, NW China. *Journal of Petrology*, *56*(10), 1897-1944. https://doi.org/10.1093/petrology/egv053

Chen, Y., Gu, Y. J., Currie, C. A., Johnston, S. T., Hung, S.-H., Schaeffer, A. J., & Audet, P. (2019). Seismic evidence for a mantle suture and implications for the origin of the Canadian Cordillera. *Nature Communications*, *10*(1), 1-10. https://doi.org/10.1038/s41467-019-09804-8

Chin, E. J., Chilson-Parks, B., Boneh, Y., Hirth, G., Saal, A. E., Hearn, B. C., & Hauri, E. H. (2021). The peridotite deformation cycle in cratons and the deep impact of subduction. *Tectonophysics*, *817*. https://doi.org/10.1016/j.tecto.2021.229029

Chin, E. J., Soustelle, V., Hirth, G., Saal, A. E., Kruckenberg, S. C., & Eiler, J. M. (2016). Microstructural and geochemical constraints on the evolution of deep arc lithosphere. *Geochemistry, Geophysics, Geosystems*, *17*(7), 2497-2521. https://doi.org/10.1002/2015GC006156

Chin, E. J., Soustelle, V., & Liu, Y. (2020). An SPO-induced CPO in composite mantle xenoliths correlated with increasing melt-rock interaction. *Geochimica Et Cosmochimica Acta*, *278*, 199-218. https://doi.org/10.1016/j.gca.2019.10.002

Colpron, M., Logan, J. M., & Mortensen, J. K. (2002). U–Pb zircon age constraint for late Neoproterozoic rifting and initiation of the lower Paleozoic passive margin of western Laurentia. *Canadian Journal of Earth Sciences*, *39*(2), 133-143.

Coney, P. J., Jones, D. L., & Monger, J. W. H. (1980). Cordilleran suspect terranes. *Nature*, *288*(5789), 329-333. https://doi.org/10.1038/288329a0

Cook, F. A., Clowes, R. M., Snyder, D. B., van der Velden, A. J., Hall, K. W., Erdmer, P., & Evenchick, C. A. (2004). Precambrian crust beneath the Mesozoic northern Canadian Cordillera discovered by Lithoprobe seismic reflection profiling PRECAMBRIAN CRUST BENEATH NORTHERN CANADIAN CORDILLERA. *Tectonics*, *23*(2), n/a. https://doi.org/10.1029/2002TC001412

Cross, A. J., Prior, D. J., Stipp, M., & Kidder, S. (2017). The recrystallized grain size piezometer for quartz: An EBSD-based calibration. *Geophysical Research Letters*, *44*(13), 6667-6674. https://doi.org/10.1002/2017GL073836

Currie, C. A., & Hyndman, R. D. (2006). The thermal structure of subduction zone back arcs. *Journal of Geophysical Research: Solid Earth*, *111*(B8). https://doi.org/https://doi.org/10.1029/2005JB004024

Dijkstra, A. H., Drury, M. R., Vissers, R. L. M., & Newman, J. (2002). On the role of melt-rock reaction in mantle shear zone formation in the Othris Peridotite Massif (Greece). *Journal of Structural Geology*, *24*(9), 1431-1450. https://doi.org/https://doi.org/10.1016/S0191-8141(01)00142-0

Drury, M. R., & Roermund, H. L. M. V. (1989). Fluid Assisted Recrystallization in Upper Mantle Peridotite Xenoliths from Kimberlites. *Journal of Petrology*, *30*(1), 133-152. https://doi.org/10.1093/petrology/30.1.133

Edwards, B. R., & Russell, J. K. (2000). Distribution, nature, and origin of Neogene-Quaternary magmatism in the northern Cordilleran volcanic province, Canada. *Geological Society of America Bulletin*, *112*(8), 1280-1295. https://doi.org/10.1130/0016-7606(2000)112<1280:DNAOON>2.0.CO;2

Eiché, G. E., Francis, D. M., & Ludden, J. N. (1987). Primary alkaline magmas associated with the Quaternary Alligator Lake volcanic complex, Yukon Territory, Canada. *Contributions to Mineralogy and Petrology*, *95*(2), 191-201. https://doi.org/10.1007/BF00381268

Estève, C., Audet, P., Schaeffer, A. J., Schutt, D., Aster, R. C., & Cubley, J. (2020). The Upper Mantle Structure of Northwestern Canada From Teleseismic Body Wave Tomography. *Journal of Geophysical Research: Solid Earth*, *125*(2). https://doi.org/10.1029/2019JB018837

Estève, C., Gosselin, J. M., Audet, P., Schaeffer, A. J., Schutt, D. L., & Aster, R. C. (2021). Surface-Wave Tomography of the Northern Canadian Cordillera Using Earthquake Rayleigh Wave Group Velocities. *Journal of Geophysical Research: Solid Earth*, *126*(8). https://doi.org/10.1029/2021JB021960

Falus, G., Drury, M. R., van Roermund, H. L. M., & Szabo, C. (2003). Magmatism-related localized deformation in the mantle: a case study. *Contributions to mineralogy and petrology. Beiträge zur Mineralogie und Petrologie.*, *146*(4), 493.

Flück, P., Hyndman, R. D., & Lowe, C. (2003). Effective elastic thickness Te of the lithosphere in western Canada. *Journal of Geophysical Research: Solid Earth*, *108*(B9). https://doi.org/10.1029/2002JB002201

Francis, D. (1987). Mantle-Melt Interaction Recorded in Spinel Lherzolite Xenoliths from the Alligator Lake Volcanic Complex, Yukon, Canada. *Journal of Petrology*, *28*(3), 569-597. https://doi.org/10.1093/petrology/28.3.569

Francis, D., Minarik, W., Proenza, Y., & Shi, L. (2010). An overview of the Canadian Cordilleran lithospheric mantle. *Canadian Journal of Earth Sciences = Revue Canadienne des Sciences de la Terre*, *47*(4), 353-368. https://doi.org/10.1139/E09-072

Frederiksen, A. W., Bostock, M. G., VanDecar, J. C., & Cassidy, J. F. (1998). Seismic structure of the upper mantle beneath the northern Canadian Cordillera from teleseismic travel-time inversion. *Tectonophysics.*, *294*(1-2), 43.

Gabrielse, H. (1985). Major dextral transcurrent displacements along the Northern Rocky Mountain Trench and related lineaments in north-central British Columbia. *GSA Bulletin*, *96*(1), 1-14. https://doi.org/10.1130/0016-7606(1985)96<1:Mdtdat>2.0.Co;2

Greenfield, A. M. R., Ghent, E. D., Russell, J. K., & Murphy, B. (2013). Geothermobarometry of spinel peridotites from southern British Columbia: implications for the thermal conditions in the upper mantle. *Canadian Journal of Earth Sciences*, *50*(10), 1019-1032. https://doi.org/10.1139/cjes-2013-0037

Hardebol, N. J., Pysklywec, R. N., & Stephenson, R. (2012). Small-scale convection at a continental back-arc to craton transition: Application to the southern Canadian Cordillera. *Journal of Geophysical Research: Solid Earth*, *117*(B1). https://doi.org/10.1029/2011JB008431

Hielscher, R., & Schaeben, H. (2008). A novel pole figure inversion method: Specification of the MTEX algorithm. *Journal of Applied Crystallography - J APPL CRYST*, *41*, 1024-1037. https://doi.org/10.1107/S0021889808030112

Higgie, K., & Tommasi, A. (2012). Feedbacks between deformation and melt distribution in the crust–mantle transition zone of the Oman ophiolite. *Earth and Planetary Science Letters*, *359-360*, 61-72. https://doi.org/https://doi.org/10.1016/j.epsl.2012.10.003

Holtzman, B. K., Kohlstedt, D. L., Zimmerman, M. E., Heidelbach, F., Hiraga, T., & Hustoft, J. (2003). Melt Segregation and Strain Partitioning: Implications for Seismic Anisotropy and Mantle Flow. *Science*, *301*(5637), 1227-1230.

Höy, T. (1989). The age, chemistry, and tectonic setting of the Middle Proterozoic Moyie sills, Purcell Supergroup, southeastern British Columbia. *Canadian Journal of Earth Sciences*, *26*(11), 2305-2317.

Hyndman, R. D., & Canil, D. (2021). Geophysical and Geochemical Constraints on Neogene-Recent Volcanism in the North American Cordillera. *Geochemistry, Geophysics, Geosystems*, *22*(5). https://doi.org/10.1029/2021GC009637

Hyndman, R. D., & Currie, C. A. (2011). Why is the North America Cordillera high? Hot backarcs, thermal isostasy, and mountain belts. *Geology (Boulder)*, *39*(8), 783-786. https://doi.org/10.1130/G31998.1

Hyndman, R. D., Flück, P., Mazzotti, S., Lewis, T. J., Ristau, J., & Leonard, L. (2005). Current tectonics of the northern Canadian Cordillera. *Canadian Journal of Earth Sciences = Revue Canadienne des Sciences de la Terre*, *42*(6), 1117-1136. https://doi.org/10.1139/e05-023

Hyndman, R. D., & Lewis, T. J. (1999). Geophysical consequences of the Cordillera–Craton thermal transition in southwestern Canada. *Tectonophysics*, *306*(3), 397-422. https://doi.org/https://doi.org/10.1016/S0040-1951(99)00068-2

Irving, E., Wynne, P., Thorkelson, D., & Schiarizza, P. (1996). Large (1000 to 4000 km) northward movements of tectonic domains in the northern Cordillera, 83 to 45 Ma. *Journal of Geophysical Research: Solid Earth*, *101*(B8), 17901-17916.

Ji, S. C., Zhao, X. O., & Francis, D. (1994). Calibration of shear-wave splitting in the subcontinental upper-mantle beneath active orogenic belts using ultramafic xenoliths from the Canadian Cordillera and Alaska. *Tectonophysics*, *239*(1-4), 1-27. <Go to ISI>://WOS:A1994PY81300001

Johnston, S. T. (2008). The Cordilleran Ribbon Continent of North America. *ANNUAL REVIEW OF EARTH AND PLANETARY SCIENCES*, *36*(1), 495-530. https://doi.org/10.1146/annurev.earth.36.031207.124331

Jung, H., Katayama, I., Jiang, Z., Hiraga, T., & Karato, S. (2006). Effect of water and stress on the lattice-preferred orientation of olivine. *421*(1-2), 1-22. https://doi.org/10.1016/j.tecto.2006.02.011

Karato, S. (1989). Grain growth kinetics in olivine aggregates. *Tectonophysics*, *168*(4), 255-273. https://doi.org/10.1016/0040-1951(89)90221-7

Karato, S. I. (2008). Deformation of Earth Materials: An Introduction to the Rheology of Solid Earth. *Deformation of Earth Materials: an Introduction to the Rheology of Solid Earth*, 1-463. https://doi.org/10.1017/cbo9780511804892

Karato, S. i., Jung, H., Katayama, I., & Skemer, P. (2008). Geodynamic Significance of Seismic Anisotropy of the Upper Mantle: New Insights from Laboratory Studies. *ANNUAL REVIEW OF EARTH AND PLANETARY SCIENCES*, *36*, 59-96.

Katayama, I., Jung, H., & Karato, S.-i. (2004). New type of olivine fabric from deformation experiments at modest water content and low stress. *Geology*, *32*(12), 1045-1048. https://doi.org/10.1130/g20805.1

Katayama, I., Karato, S.-i., & Brandon, M. (2005). Evidence of high water content in the deep upper mantle inferred from deformation microstructures. *Geology*, *33*(7), 613-616.

Kelemen, P. B., Dick, H. J. B., & Quick, J. E. (1992). Formation of harzburgite by pervasive melt/rock reaction in the upper mantle [Article]. *Nature*, *358*(6388), 635-641. https://doi.org/10.1038/358635a0

Kelemen, P. B., Shimizu, N., & Salters, V. J. M. (1995). Extraction of mid-ocean-ridge basalt from the upwelling mantle by focused flow of melt in dunite channels. *Nature*, *375*(6534), 747-753. https://doi.org/10.1038/375747a0

Kilgore, M. L., Peslier, A. H., Brandon, A. D., & Lamb, W. M. (2018). Water and Oxygen Fugacity in the Lithospheric Mantle Wedge beneath the Northern Canadian Cordillera (Alligator Lake). *Geochemistry Geophysics Geosystems*, *19*(10), 3844-3869. https://doi.org/10.1029/2018gc007700

Kroner, R. K. (2019). *The Cordilleran lithosphere beneath south-central British Columbia : insights from two xenolith suites* [Text, https://open.library.ubc.ca/collections/24/items/1.0379760

Le Roux, V., Tommasi, A., & Vauchez, A. (2008). Feedback between melt percolation and deformation in an exhumed lithosphere-asthenosphere boundary. *Earth and Planetary Science Letters*, *274*(3-4), 401-413. https://doi.org/10.1016/j.epsl.2008.07.053

LeCheminant, A. N., Heaman, L.M., van Breemen, O., Ernst, R.E., Baragar, W.R.A., and Buchan, K.L. (1996). Mafic magmatism, mantle roots and kimberlites in the Slave craton. In *Searching for diamonds in Canada* (Vol. Open File 3228, pp. 161–168). Geological Survey of Canada.

Ledo, J., Jones, A. G., Ferguson, I. J., & Wolynec, L. (2004). Lithospheric structure of the Yukon, northern Canadian Cordillera, obtained from magnetotelluric data. *Journal of Geophysical Research-Solid Earth*, *109*(B4), Article B04410. https://doi.org/10.1029/2003jb002516

Lewis, T. J., Hyndman, R. D., & Flück, P. (2003). Heat flow, heat generation, and crustal temperatures in the northern Canadian Cordillera: Thermal control of tectonics HEAT FLOW IN NORTHERN CANADIAN CORDILLERA. *Journal of Geophysical Research: Solid Earth*, *108*(B6). https://doi.org/10.1029/2002JB002090

Littlejohn, A. L., & Greenwood, H. J. (1974). Lherzolite Nodules in Basalts from British Columbia, Canada. *Canadian Journal of Earth Sciences*, *11*(9), 1288-1308.

Madsen, J. K., Thorkelson, D. J., Friedman, R. M., & Marshall, D. D. (2006). Cenozoic to Recent plate configurations in the Pacific Basin: Ridge subduction and slab window magmatism in western North America. *Geosphere*, *2*(1), 11. https://doi.org/10.1130/GES00020.1

Mainprice, D., Bachmann, F., Hielscher, R., & Schaeben, H. (2014). Descriptive tools for the analysis of texture projects with large datasets using MTEX: Strength, symmetry and components. *Geological Society, London, Special Publications*, *409*. https://doi.org/10.1144/SP409.8

Mainprice, D., Hielscher, R., & Schaeben, H. (2011). Calculating anisotropic physical properties from texture data using the MTEX open-source package.

Mainprice, D., & Silver, P. G. (1993). Interpretation of SKS-waves using samples from the subcontinental lithosphere. *Physics of the Earth and Planetary Interiors*, *78*(3), 257-280. https://doi.org/https://doi.org/10.1016/0031-9201(93)90160-B

Maitland, T., & Sitzman, S. (2007). Electron backscatter diffraction (EBSD) technique and materials characterization examples. *Scanning microscopy for nanotechnology: techniques and applications*, 41-75.

Marechal, A. s., Mazzotti, S., Elliott, J. L., Freymueller, J. T., & Schmidt, M. (2015). Indentor-corner tectonics in the Yakutat-St. Elias collision constrained by GPS. *Journal of Geophysical Research: Solid Earth*, *120*(5), 3897-3908. https://doi.org/10.1002/2014JB011842

Mazzotti, S., & Hyndman, R. D. (2002). Yakutat collision and strain transfer across the northern Canadian Cordillera. *Geology*, *30*(6). https://doi.org/10.1130/0091-7613(2002)030<0495:YCASTA>2.0.CO;2

McLellan, M., Schaeffer, A. J., & Audet, P. (2018). Structure and fabric of the crust and uppermost mantle in the northern Canadian Cordillera from Rayleigh-wave tomography. *Tectonophysics*, *724-725*, 28-41. https://doi.org/10.1016/j.tecto.2018.01.011

Mercier, J. C. C., & Nicolas, A. (1975). Textures and Fabrics of Upper-Mantle Peridotites as Illustrated by Xenoliths from Basalts. *Journal of Petrology*, *16*(2), 454-487. https://doi.org/10.1093/petrology/16.2.454

Michibayashi, K., Mainprice, D., Fujii, A., Uehara, S., Shinkai, Y., Kondo, Y., Ohara, Y., Ishii, T., Fryer, P., Bloomer, S. H., Ishiwatari, A., Hawkins, J. W., & Ji, S. (2016). Natural olivine crystal-fabrics in the western Pacific convergence region: A new method to identify fabric type. *Earth and Planetary Science Letters*, *443*, 70-80. https://doi.org/10.1016/j.epsl.2016.03.019

Minehan, K. (1989). *Paleotectonic setting of Takla Group volcano-sedimentary rocks Quesnellia, North Central British Columbia* McGill University].

Monger, J., Price, R., & Tempelman-Kluit, D. (1982). Tectonic accretion and the origin of the two major metamorphic and plutonic welts in the Canadian Cordillera. *Geology*, *10*(2), 70-75.

Monger, J. W. H., & Price, R. A. (2002). THE CANADIAN CORDILLERA: Geology and Tectonic Evolution.

Morales, L. F. G., & Tommasi, A. (2011). Composition, textures, seismic and thermal anisotropies of xenoliths from a thin and hot lithospheric mantle (Summit Lake, southern

Canadian Cordillera). *Tectonophysics*, *507*(1-4), 1-15. https://doi.org/10.1016/j.tecto.2011.04.014

Nelson, J. L., Colpron, M., Israel, S., Colpron, M., Bissig, T., Rusk, B. G., & Thompson, J. F. H. (2013). The Cordillera of British Columbia, Yukon, and Alaska: Tectonics and Metallogeny. In *Tectonics, Metallogeny, and Discovery: The North American Cordillera and Similar Accretionary Settings* (Vol. 17, pp. 0). Society of Economic Geologists. https://doi.org/10.5382/sp.17.03

Oldow, J. S., Bally, A. W., & Ave Lallemant, H. G. (1990). Transpression, orogenic float, and lithospheric balance. *Geology; (USA)*, *18*(10), 991-994. https://doi.org/10.1130/0091-7613(1990)018<0991:TOFALB>2.3.CO;2

Passchier, C. W., & Trouw, R. A. J. (2005). *Microtectonics* (2nd, rev. and enl. / ed.). Springer. https://doi.org/10.1007/3-540-29359-0

Pearson, D. G., Canil, D., & Shirey, S. B. (2014). 3.5 - Mantle Samples Included in Volcanic Rocks: Xenoliths and Diamonds. In H. D. Holland & K. K. Turekian (Eds.), *Treatise on Geochemistry (Second Edition)* (pp. 169-253). Elsevier. https://doi.org/https://doi.org/10.1016/B978-0-08-095975-7.00216-3

Peslier, A. H., Francis, D., & Ludden, J. (2002). The Lithospheric Mantle beneath Continental Margins: Melting and Melt-Rock Reaction in Canadian Cordillera Xenoliths. *Journal of Petrology*, *43*(11), 2013-2047.

Peslier, A. H., Reisberg, L., Ludden, J., & Francis, D. (2000a). Os isotopic systematics in mantle xenoliths; age constraints on the Canadian Cordillera lithosphere. *Chemical Geology*, *166*(1), 85-101. https://doi.org/10.1016/S0009-2541(99)00187-4

Peslier, A. H., Reisberg, L., Ludden, J., & Francis, D. (2000b). Re–Os constraints on harzburgite and lherzolite formation in the lithospheric mantle: a study of northern Canadian Cordillera xenoliths. *Geochimica Et Cosmochimica Acta*, *64*(17), 3061-3071.

Peslier, A. H., Schönbächler, M., Busemann, H., & Karato, S.-I. (2017). Water in the Earth's Interior: Distribution and Origin. *Space Science Reviews*, *212*(1), 743-810. https://doi.org/10.1007/s11214-017-0387-z

Powell, C. M., Li, Z.-X., McElhinny, M., Meert, J., & Park, J. (1993). Paleomagnetic constraints on timing of the Neoproterozoic breakup of Rodinia and the Cambrian formation of Gondwana. *Geology*, *21*(10), 889-892.

Prescott, J. W. (1983). *Petrogenesis of ultramafic xenoliths from the Canadian Cordillera and Alaska* WorldCat.org. http://gateway.proquest.com/openurl?url_ver=Z39.88-2004&rft_val_fmt=info:ofi/fmt:kev:mtx:dissertation&res_dat=xri:pqm&rft_dat=xri:pqdiss:ML27330

Price, R. A. (1994). Cordilleran tectonics and the evolution of the Western Canada sedimentary basin. In *Geological Atlas of Western Canada: Calgary* (pp. 13-24). Canadian Society of Petroleum Geologists/Alberta Research Counci.

Qi, C., Hansen, L. N., Wallis, D., Holtzman, B. K., Kohlstedt, D. L., & non, U. U. o. o. U. U. A. W. m. (2018). Crystallographic preferred orientation of olivine in sheared partially molten rocks: the source of the "a-c switch". *Geochemistry, Geophysics, Geosystems*, *19*(2).

Rasendra, N., Bonnin, M., Mazzotti, S., & Tiberi, C. (2014). Crustal and upper-mantle anisotropy related to fossilized transpression fabric along the Denali Fault, northern Canadian Cordillera. *Bulletin of the Seismological Society of America*, *104*(4), 1964-1975. https://doi.org/10.1785/0120130233

Roback, R. C., Sevigny, J. H., & Walker, N. W. (1994). Tectonic setting of the Slide Mountain terrane, southern British Columbia. *Tectonics*, *13*(5), 1242-1258. https://doi.org/10.1029/94TC01032

Saruwatari, K., Ji, S., Long, C., & Salisbury, M. H. (2001). Seismic anisotropy of mantle xenoliths and constraints on upper mantle structure beneath the southern Canadian Cordillera. *Tectonophysics*, *339*(3), 403-426. https://doi.org/10.1016/S0040-1951(01)00136-6

Shi, L., Francis, D., Ludden, J., Frederiksen, A., & Bostock, M. (1998). Xenolith evidence for lithospheric melting above anomalously hot mantle under the northern Canadian Cordillera. *Contributions to Mineralogy and Petrology*, *131*(1), 39-53. https://doi.org/10.1007/s004100050377

Skemer, P., & Hansen, L. N. (2016). Inferring upper-mantle flow from seismic anisotropy: An experimental perspective. *Tectonophysics*, *668-669*, 1-14. https://doi.org/10.1016/j.tecto.2015.12.003

Skemer, P., Katayama, I., Jiang, Z., & Karato, S.-i. (2005). The misorientation index: Development of a new method for calculating the strength of lattice-preferred orientation. *Tectonophysics*, *411*(1), 157-167. https://doi.org/10.1016/j.tecto.2005.08.023

Smale, J. (2020). *Understanding Canadian Cordillera crustal and upper-mantle structure with joint Bayesian inversion of receiver functions and surface-wave dispersion curves* [master thesis, University of Calgary, Calgary, AB.].

Snyder, D. B., Clowes, R. M., Cook, F. A., Erdmer, P., Evenchick, C. A., van der Velden, A. J., & Hall, K. W. (2002). Proterozoic Prism Arrests Suspect Terranes: Insights into the Ancient Cordilleran Margin from Seismic Reflection Data. *GSA Today*, *12*(10), 4. https://doi.org/10.1130/1052-5173(2002)012<0004:PPASTI>2.0.CO;2

Soustelle, V., Tommasi, A., Demouchy, S., & Ionov, D. A. (2010). Deformation and Fluid-Rock Interaction in the Supra-subduction Mantle: Microstructures and Water Contents in Peridotite Xenoliths from the Avacha Volcano, Kamchatka. *Journal of Petrology*, *51*(1-2), 363-394.

Speciale, P. A., Behr, W. M., Hirth, G., & Tokle, L. (2020). Rates of Olivine Grain Growth During Dynamic Recrystallization and Postdeformation Annealing. *Journal of Geophysical Research: Solid Earth*, *125*(11). https://doi.org/10.1029/2020JB020415

Tarayoun, A., Audet, P., Mazzotti, S., & Ashoori, A. (2017). Architecture of the crust and uppermost mantle in the northern Canadian Cordillera from receiver functions. *Journal of Geophysical Research-Solid Earth*, *122*(7), 5268-5287. https://doi.org/10.1002/2017jb014284

Thorkelson, D. J., Madsen, J. K., & Sluggett, C. L. (2011). Mantle flow through the northern Cordilleran slab window revealed by volcanic geochemistry. *Geology (Boulder)*, *39*(3), 267-270. https://doi.org/10.1130/G31522.1

Tommasi, A., Vauchez, A., Godard, M., & Belley, F. (2006). Deformation and melt transport in a highly depleted peridotite massif from the Canadian Cordillera: Implications to seismic anisotropy above subduction zones. *Earth and Planetary Science Letters*, *252*(3), 245-259. https://doi.org/https://doi.org/10.1016/j.epsl.2006.09.042

Tommasi, A. a., & Vauchez, A. (2015). Heterogeneity and anisotropy in the lithospheric mantle. *Tectonophysics*, *661*, 11-37. https://doi.org/10.1016/j.tecto.2015.07.026

Van der Wal, D., Chopra, P., Drury, M., & Gerald, J. F. (1993). Relationships between dynamically recrystallized grain size and deformation conditions in experimentally deformed olivine rocks. *Geophysical Research Letters*, *20*(14), 1479-1482. https://doi.org/10.1029/93GL01382

Vauchez, A., & Garrido, C. J. (2001). Seismic properties of an asthenospherized lithospheric mantle: constraints from lattice preferred orientations in peridotite from the Ronda massif. *Earth and Planetary Science Letters*, *192*(2), 235-249. https://doi.org/https://doi.org/10.1016/S0012-821X(01)00448-4

Wingate, M. T., & Giddings, J. W. (2000). Age and palaeomagnetism of the Mundine Well dyke swarm, Western Australia: implications for an Australia–Laurentia connection at 755 Ma. *Precambrian Research*, *100*(1-3), 335-357.

APPENDICES

								Texture									CPO type		
Suite	**Lat (ºN)**	**Lon (ºW)**	**Mantle Age (Ga)[1]**	**Eruption Age**	**Ave. T (ºC)**	**Terrane**	**Realm**	Mosaic Equigranular	Tabular Equigranular	Equigranular-protogranular	Protogranular	Protogranular-porphyroclastic	Protogranular-mylonitic	Porphyroclastic	Transitional Tablet	Mylonitic	AG-type	A-type	D-type
Prindle Volcano (PV)	63.400	141.400	1.1 ± 0.26	6.26 and 3.57 Ma[3]	908[5]	Yukon-Tanana	Peri-Laurentian	18									1	3	0
Fort Selkirk (FS)	62.783	137.400	1.1 + 0.26	1.08 Ma[3]	962[5]	Quesnellia	Peri-Laurentian			3	8						0	1	0
Alligator Lake (AL)	60.416	135.426	1.1 + 0.26	3.3-3.1 Ma[3]	998[6]	Stikinia	Peri-Laurentian	2	4	2	3						2	3	0
Hirchfield Creek (HC)	59.537	132.942	1.1 + 0.26	Tertiary to recent[2]	910[7]	Cache Creek	Peri-Laurentian oceanic	16		5							0	0	2
Llangorse Mountain (LG)	59.367	132.792	1.1 + 0.26	Tertiary to recent[2]	905[7]	Cache Creek	Peri-Laurentian oceanic	35									0	1	2
Castle Rock (CR)	57.617	130.667	1.1 ± 0.26	Tertiary to recent[2]	981[5]	Stikinia	Peri-Laurentian	2		4	13						0	0	3
Summit Lake (SL)	54.307	122.367	1.1 + 0.26	26 Ma[4]	1090[8]	Slide Mountain	Peri-Laurentian				13						0	0	3
Jacques Lake (JL)	52.580	121.050	1.1 + 0.26	Tertiary to recent[2]	988[5]	Quesnellia	Peri-Laurentian			5	8						1	1	0
Big Timothy (BT)	52.105	120.930	1.1 + 0.26	0.4 Ma[4]	959[9]	Quesnellia	Peri-Laurentian				7		1				0	3	0
Kostal Lake (KL)	52.173	119.947	1.1 + 0.26	7750 BP[4]	1002[10]	North American Strata	Laurentian		3	3	14	2	5	1	2		5	5	0
Rayfield River (RR)	51.327	121.108	1.1 ± 0.26	6-10 Ma[4]	912[9]	Quesnellia	Peri-Laurentian									10	0	0	2
Lightning Peak (LP)	48.879	118.530	1.1 + 0.26	2.5 Ma[4]	1000*	Quesnellia	Peri-Laurentian			1	5						0	1	0

*Table 7-1. Characterization of Cordilleran samples: location, average mantle temperature, tectonic context, textures and CPO types. * Average mantle age in Peslier et al., (2000). . (1) Peslier et al., (200x). (2) Francis et al., (2010). (3) Edwards and Russell (2000) . (4) Peslier et al., (2002). (5) Prescott (1983). (6) Francis (1987). (8) Brearly et al., (1984). (9) Greenfield et al., (2013). (10) Canil and Scarfe, (1989). (*) average estimation for the cordillera, data not available.*

						Olivine								OPX		CPX	
Sample	**Rock type**	**Texture**	**Olivine %**	**opx %**	**cpx %**	**n**	**Median grain size (µm)**	**Shape Factor**	**Aspect Ratio**	**Ave GOS (º)**	**J-index**	**M-index**	**BA-index**	**J-index**	**M-index**	**J-index**	**M-index**
AL45	Harzburgite	Equigranular tablet	41.91	55.74	2.35	419	589.62	1.40	2.30	3.95	3.74	0.200	0.43	1.87	0.057	6.97	0.106
AL57	Harzburgite	Equigranular mosaic	80.37	18.82	0.81	327	645.76	1.20	1.60	0.75	2.47	0.083	0.41	2.98	0.075	26.92	0.257
AL58	lherzolite	Protogranular	60.31	25.94	13.75	782	393.46	1.27	1.76	0.76	3.08	0.174	0.21	2.82	0.034	2.24	0.034
AL70	lherzolite	Equigranular-protogranular	78.26	16.04	5.70	258	519.96	1.29	1.91	0.74	3.93	0.191	0.20	4.07	0.080	3.75	0.060
AL90	lherzolite	Equigranular tablet	68.30	20.04	11.66	360	566.83	1.26	1.79	0.53	4.87	0.229	0.42	2.57	0.020	3.67	0.015
BT22	lherzolite	Protogranular	48.90	26.49	24.61	985	324.43	1.28	1.67	1.12	2.23	0.101	0.52	2.60	0.075	1.97	0.015
BT23	lherzolite	Protogranular	67.51	21.70	10.79	310	515.21	1.29	1.70	0.94	3.27	0.102	0.40	3.45	0.070	3.78	0.026
BT26	lherzolite	Protogranular	50.01	32.42	17.57	173	629.86	1.30	1.76	0.80	4.64	0.093	0.44	5.73	0.076	3.38	0.060
CR20	lherzolite	Protogranular	61.68	31.30	7.03	425	414.54	1.24	1.61	1.22	3.78	0.162	0.75	2.08	0.037	3.68	0.032
CR27	lherzolite	Protogranular	58.32	24.42	17.26	353	480.14	1.27	1.62	1.01	4.26	0.203	0.70	4.38	0.156	3.12	0.063
CR29	lherzolite	Protogranular	70.84	19.96	9.19	627	466.13	1.25	1.61	0.89	3.32	0.160	0.91	1.60	0.018	2.84	0.042
FS13	lherzolite	Protogranular	47.76	14.44	37.80	347	464.06	1.30	1.76	1.09	3.25	0.148	0.55	2.30	0.031	3.63	0.022
HF01	lherzolite	Equigranular-protogranular	74.33	18.50	7.17	704	496.01	1.23	1.67	0.61	3.74	0.199	0.91	1.67	0.007	1.95	0.047
HF02	lherzolite	Equigranular-protogranular	69.57	21.07	9.35	343	371.39	1.29	2.09	0.71	3.10	0.142	0.75	2.50	0.016	3.83	0.048
JL05	lherzolite	Protogranular	40.90	41.47	17.63	302	554.32	1.27	1.65	0.55	3.35	0.103	0.19	3.48	0.067	2.29	0.009
JL12	lherzolite	Protogranular	74.81	22.60	2.59	309	590.70	1.28	1.69	1.01	3.52	0.153	0.55	3.27	0.093	17.21	0.140
KL04	wehrlite	protogranular-porphyroclastic	59.11	0.00	40.89	844	232.61	1.28	1.94	0.70	2.56	0.064	0.18			1.91	0.012
KL29	wehrlite	Porphyroclastic	71.11	0.05	28.84	1436	320.31	1.20	1.75	1.04	1.30	0.021	0.25	138.19	0.922	2.13	0.009
KL37	lherzolite	protogranular	73.55	18.56	7.89	604	558.94	1.33	1.87	1.21	6.88	0.322	0.54	3.83	0.142	3.12	0.110
KL44	lherzolite	protomylonitic	71.36	20.94	7.69	1024	460.57	1.33	1.94	1.34	6.50	0.238	0.35	1.59	0.027	1.85	0.023
KL51	wehrlite	transitional	82.62	2.01	15.37	5036	107.42	1.24	1.80	0.92	2.09	0.115	0.61	4.35	0.031	1.74	0.009
KL53	dunite	transitional	99.08	0.33	0.59	4543	134.07	1.26	1.84	0.96	2.23	0.137	0.41	24.90	0.372	2.23	0.011
KL55	dunite	protogranular-porphyroclastic	96.45	0.11	3.44	579	208.54	1.25	1.85	1.02	1.42	0.013	0.43	14.02	0.116	2.77	0.015
KL59	dunite	Equigranular tablet	99.83	0.02	0.15	450	693.89	1.32	1.75	1.24	8.04	0.290	0.39			54.58	0.465
KL62	dunite	Equigranular tablet	94.68	3.42	1.90	539	449.40	1.30	1.76	0.98	5.97	0.277	0.04	7.48	0.195	15.33	0.202
KL65	dunite	protogranular-porphyroclastic	98.82	0.00	1.18	1335	218.28	1.21	1.58	0.66	1.44	0.033	0.19			3.20	0.011
LG14	Harzburgite	Equigranular mosaic	74.89	23.43	1.68	535	430.76	1.17	1.48	0.36	2.09	0.079	0.49	2.23	0.024	4.88	0.041
LG33	lherzolite	Equigranular mosaic	68.97	19.91	11.12	362	386.11	1.22	1.55	0.60	3.39	0.161	0.77	2.01	0.024	3.71	0.034
LG36	lherzolite	Equigranular mosaic	58.41	26.32	15.28	951	422.70	1.23	1.70	0.70	2.68	0.129	0.68	1.48	0.021	2.15	0.035
LP19	lherzolite	Protogranular	61.60	19.82	18.57	586	387.03	1.31	1.70	1.48	1.88	0.051	0.61	1.94	0.023	2.11	0.013
PV08	lherzolite	Equigranular mosaic	61.11	22.36	16.53	1464	398.38	1.26	2.13	0.41	1.56	0.047	0.29	1.41	0.031	1.79	0.022
PV17	lherzolite	Equigranular mosaic	62.48	23.68	13.84	581	672.20	1.29	1.95	0.40	1.53	0.030	0.47	1.75	0.049	2.08	0.016
PV39	lherzolite-cumulate	Equigranular mosaic	86.79	3.67	9.53	484	784.11	1.26	1.60	0.54	1.71	0.040	0.40	2.98	0.026	3.38	0.027
PV40	lherzolite	Equigranular mosaic	63.63	17.80	18.57	735	658.41	1.24	1.68	0.60	1.57	0.035	0.42	1.67	0.047	1.76	0.014
RR10	lherzolite	protomylonitic	67.47	9.49	23.04	1253	333.83	1.29	1.94	1.09	2.65	0.120	0.82	4.15	0.080	4.03	0.114
RR18	lherzolite	protomylonitic	64.31	21.76	13.93	1041	391.31	1.27	1.80	1.20	2.39	0.097	0.78	1.41	0.010	1.79	0.012
SL14	wehrlite	Protogranular	81.33	0.02	18.66	384	485.63	1.28	1.64	0.93	2.93	0.125	0.80	34.18	0.245	2.93	0.031
SL15	wehrlite	Protogranular	82.32	2.26	15.42	481	472.07	1.33	1.64	1.00	3.49	0.169	0.73	8.31	0.056	2.97	0.040
SL39	wehrlite	Protogranular	86.14	0.00	13.86	248	606.74	1.21	1.61	0.57	4.23	0.201	0.77			3.71	0.041

Samples with strongly bimodal grain size distribution																	
						Olivine								OPX		CPX	
Sample	**Rock type**	**Texture**	**Olivine %**	**opx %**	**cpx %**	**n**	**Median grain size (µm)**	**Shape Factor**	**Aspect Ratio**	**Ave GOS (º)**	**J-index**	**M-index**	**BA-index**	**J-index**	**M-index**	**J-index**	**M-index**
KL04 bulk	wehrlite	protogranular-porphyroclastic	56.07	0.00	38.78	844	232.61	1.28	1.94	0.70	2.56	0.064	0.18			1.91	0.012
Relict (76%)						139	886.12	1.44	2.08	1.99	4.87	0.074	0.21				
neoblasts (24%)						644	186.56	1.25	1.92	0.43	2.56	0.062	0.37				
KL29	wehrlite	Porphyroclastic	64.61	0.07	25.55	1436	320.31	1.20	1.75	1.04	1.30	0.021	0.25	138.19	0.922	2.13	0.009
Relict (47%)						217	507.71	1.33	1.88	3.58	1.95	0.015	0.28				
neoblasts (53%)						1047	300.87	1.17	1.73	0.52	1.33	0.023	0.26				
KL51	wehrlite	transitional	78.13	2.10	14.76	5036	107.42	1.24	1.80	0.92	2.09	0.115	0.61	4.35	0.031	1.74	0.009
Relict (47%)						778	184.21	1.49	2.11	3.08	3.10	0.142	0.35				
neoblasts (53%)						4025	97.93	1.19	1.74	0.50	2.02	0.110	0.52				
KL53	wehrlite	transitional	89.75	0.48	0.75	4543	134.07	1.26	1.84	0.96	2.23	0.137	0.41	24.90	0.372	2.23	0.011
Relict (46%)						518	219.14	1.46	2.03	3.29	3.17	0.136	0.59				
neoblasts (54%)						3816	126.13	1.23	1.82	0.64	2.22	0.138	0.36				
KL65	dunite	protogranular-porphyroclastic	98.37	0.00	1.31	1335	218.28	1.21	1.58	0.66	1.44	0.033	0.19			3.20	0.011
Relict (10%)						131	230.47	1.33	1.77	2.21	2.56	0.047	0.22				
neoblasts (90%)						977	213.01	1.19	1.55	0.42	1.44	0.031	0.28				

Table 7-2. Indices resulting from EBSD data post-processing using Mtex 5.7.0 and resulting texture classification. n indicates number of olivine grains.

Sample	T (K)	P (Gpa)	J-index	Avp (km/s)	maxAVs (%)	AVs1 (km/s)	AVs2 (km/s)	Avp/Vs1	Avp/Vs2	Bulk density (g/cm^3)	Olivine (%)	cpx (%)	opx (%)
AL45	1271	1	3.74	3.51	2.54	1.88	1.33	2.01	3.46	3.26	41.90	2.35	55.74
AL57	1271	1	2.47	7.26	5.19	4.42	2.57	5.05	5.49	3.25	79.65	0.81	18.65
AL58	1271	1	3.08	6.83	4.58	3.95	1.53	3.28	6.09	3.24	59.65	13.60	25.65
AL70	1271	1	3.93	8.12	5.92	4.49	2.20	4.30	6.63	3.28	78.17	5.69	16.02
AL90	1271	1	4.87	9.64	7.44	4.11	4.85	5.99	6.37	3.26	67.98	11.60	19.95
BT22	1232	1	2.23	4.15	3.46	1.63	2.90	3.61	1.83	3.21	48.00	24.16	26.01
BT23	1232	1	3.27	6.25	6.00	3.91	2.50	5.06	5.71	3.21	66.04	10.55	21.23
BT26	1232	1	4.64	3.05	4.10	2.53	2.11	3.71	3.50	3.21	49.03	17.22	31.79
CR20	1254	1	3.78	8.48	5.41	3.29	4.88	8.18	4.81	3.25	61.30	6.98	31.10
CR27	1254	1	4.26	9.69	7.50	2.61	6.40	8.38	4.46	3.21	57.16	16.92	23.94
CR29	1254	1	3.32	9.09	6.04	1.94	5.65	9.15	3.81	3.25	70.26	9.12	19.80
FS13	1235	1	3.25	4.51	2.73	2.17	1.78	4.46	3.68	3.24	47.36	37.49	14.32
HF01	1183	1	3.74	10.50	6.92	2.90	6.03	10.29	4.83	3.26	73.71	7.11	18.34
HF02	1183	1	3.10	7.99	5.71	2.81	4.93	6.91	4.16	3.23	68.37	9.19	20.71
JL05	1261	1	3.35	4.49	2.87	2.67	1.47	2.81	3.85	3.21	40.29	17.36	40.85
JL12	1261	1	3.52	9.25	6.76	4.05	4.03	7.92	5.66	3.27	74.48	2.58	22.50
KL04	1275	1	2.56	2.51	1.69	1.38	1.61	2.01	2.34	3.27	59.07	40.86	0.00
KL29	1275	1	1.30	1.49	1.48	0.87	0.88	1.14	2.03	3.27	70.93	28.77	0.05
KL37	1275	1	6.88	9.60	6.96	3.80	4.25	6.84	6.11	3.26	73.09	7.84	18.44
KL44	1275	1	6.50	9.82	6.78	5.27	3.53	5.94	7.60	3.27	71.12	7.67	20.87
KL51	1275	1	2.09	1.65	1.51	0.94	0.96	1.74	1.66	3.28	82.60	15.37	2.01
KL53	1275	1	2.23	7.27	4.92	4.51	2.18	5.12	6.46	3.29	99.07	0.59	0.33
KL55	1275	1	1.42	8.27	5.82	4.33	2.99	6.80	6.41	3.27	95.85	3.42	0.11
KL59	1275	1	8.04	12.67	9.24	6.44	4.43	8.81	9.27	3.28	99.43	0.15	0.02
KL62	1275	1	5.97	11.80	8.87	8.86	2.77	3.67	11.65	3.24	93.30	1.87	3.37
KL65	1275	1	1.44	5.40	4.68	3.87	1.13	3.29	5.21	3.29	98.72	1.18	0.00
LG14	1178	1	2.09	6.42	4.53	1.90	4.12	5.63	3.44	3.28	74.70	1.67	23.37
LG33	1178	1	3.39	9.23	5.87	2.20	5.07	8.83	4.56	3.25	68.26	11.01	19.70
LG36	1178	1	2.68	7.47	4.56	1.95	4.00	6.74	3.98	3.22	57.32	14.99	25.82
LP19	1273	1	1.88	4.91	3.41	2.02	2.81	3.93	3.24	3.20	60.30	18.18	19.40
PV08	1181	1	1.56	4.42	2.81	1.88	1.83	3.11	3.07	3.26	60.75	16.43	22.23
PV17	1181	1	1.53	2.61	2.17	1.00	2.06	2.67	1.35	3.25	61.93	13.72	23.47
PV39	1181	1	1.71	5.51	4.11	2.04	2.54	3.81	3.50	3.14	82.73	9.09	3.50
PV40	1181	1	1.57	3.50	2.20	1.68	1.96	2.93	2.46	3.23	62.64	18.28	17.52
RR10	1185	1	2.65	8.35	5.07	2.70	4.48	7.68	4.35	3.28	67.47	23.04	9.49
RR18	1185	1	2.39	7.88	4.99	2.11	4.67	7.33	3.86	3.24	63.55	13.76	21.51
SL14	1363	1	2.93	11.16	8.07	2.62	6.79	10.34	5.14	3.20	79.49	18.23	0.02
SL15	1363	1	3.49	12.53	8.53	3.59	6.75	10.99	6.57	3.25	81.60	15.29	2.24
SL39	1363	1	4.23	11.87	9.02	2.53	7.55	10.11	5.42	3.25	85.41	13.74	0.00

Table 7-3. Seismic anisotropy parameters in samples selected for EBSD analysis.

Figure 7-1. Photomicrographs of samples selected for EBSD

	plane polarized light	cross-polarized light
PV08 Mosaic Equigranular		
PV17 Tabular Equigranular		
PV39 Mosaic Equigranular		
PV40 Mosaic Equigranular		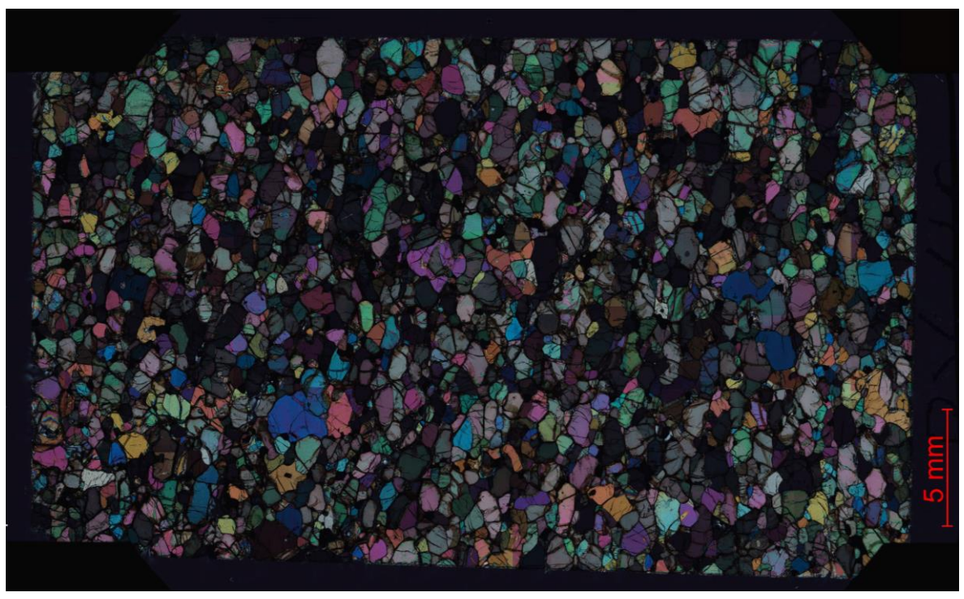
FS13 Protogranular	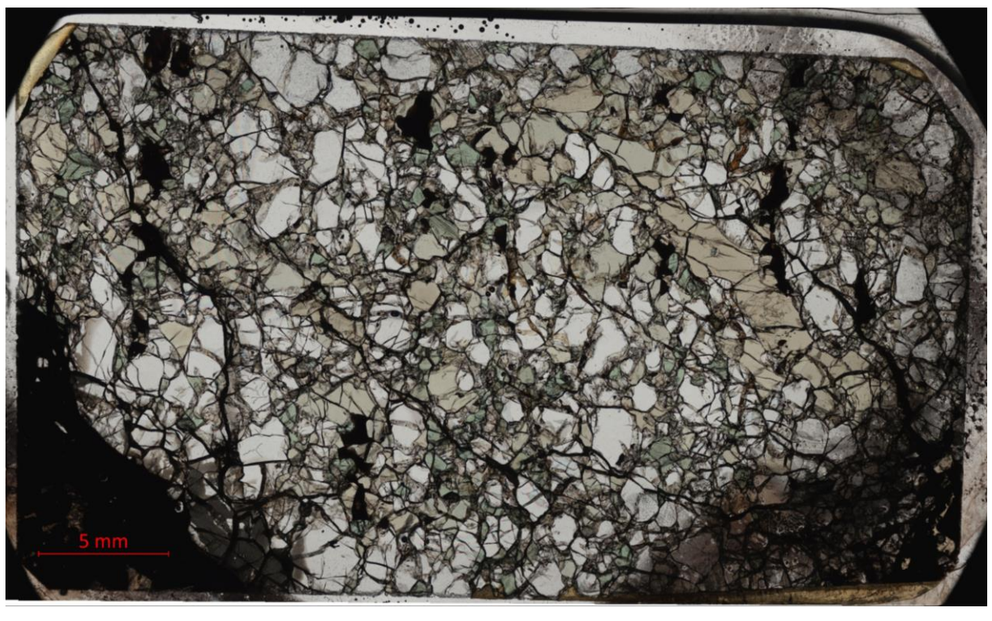	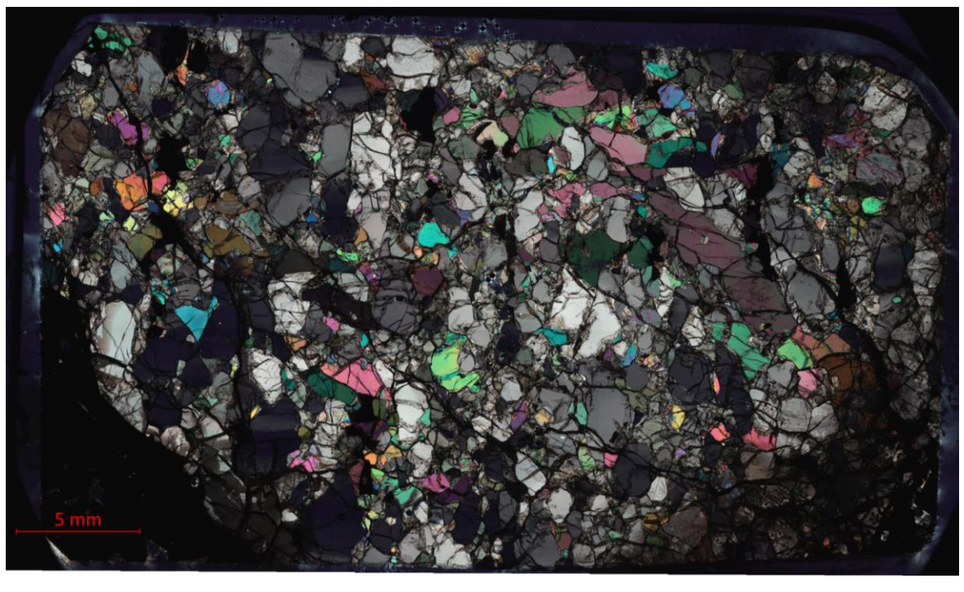

Figure 7-1. continued

plane polarized light

cross-polarized light

AL45
Tabular
Equigranular

AL57
Mosaic
Equigranular

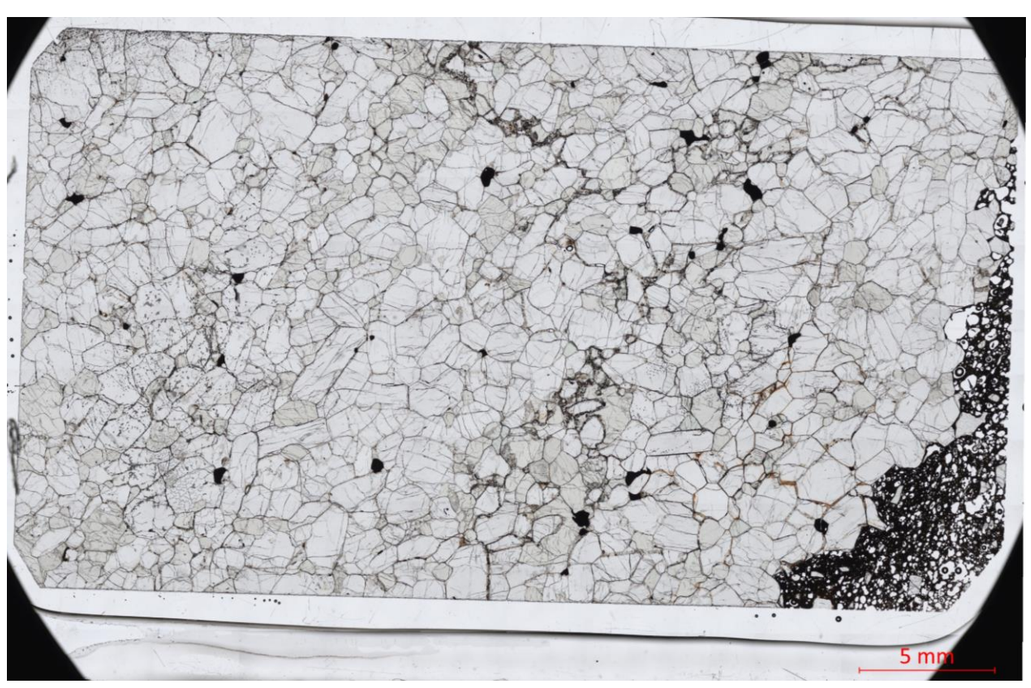

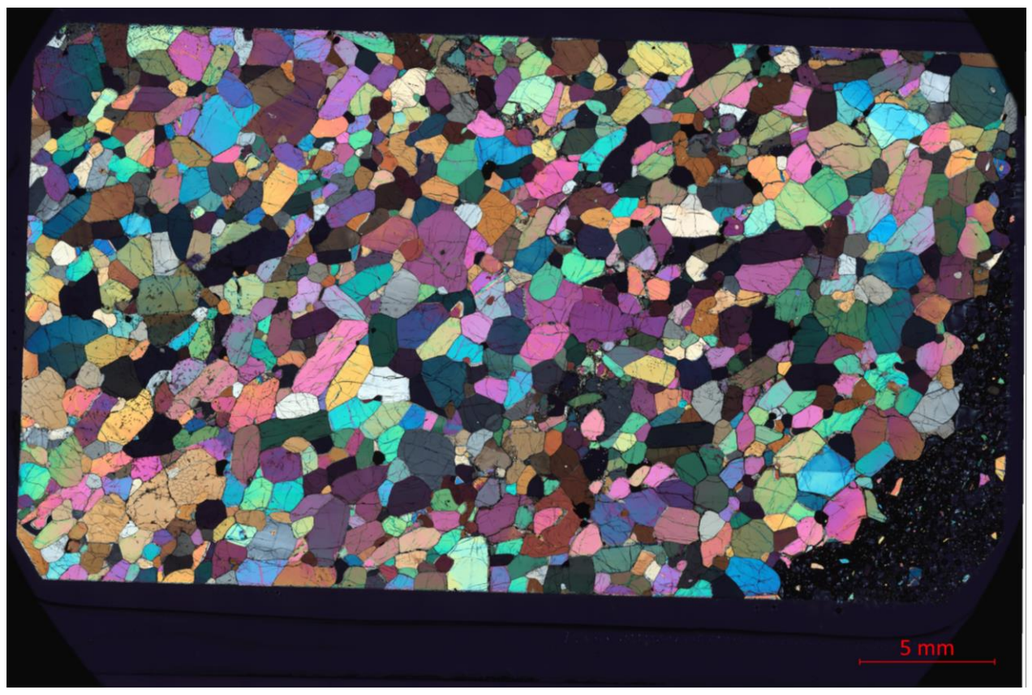

AL58
Protogranular

AL70
Equigranular-
Protogranular

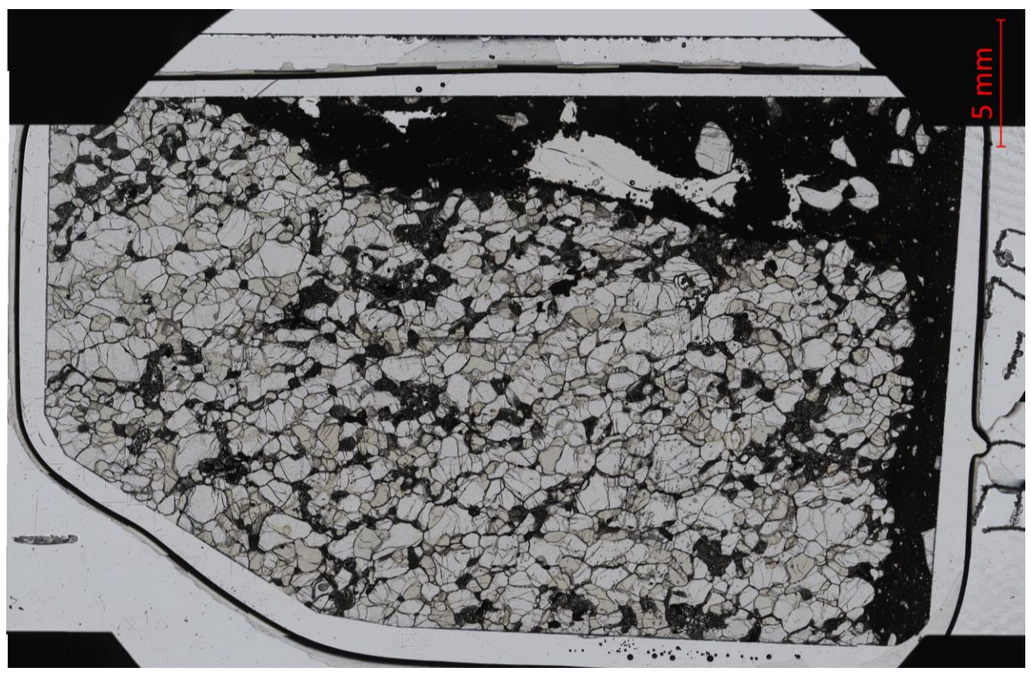

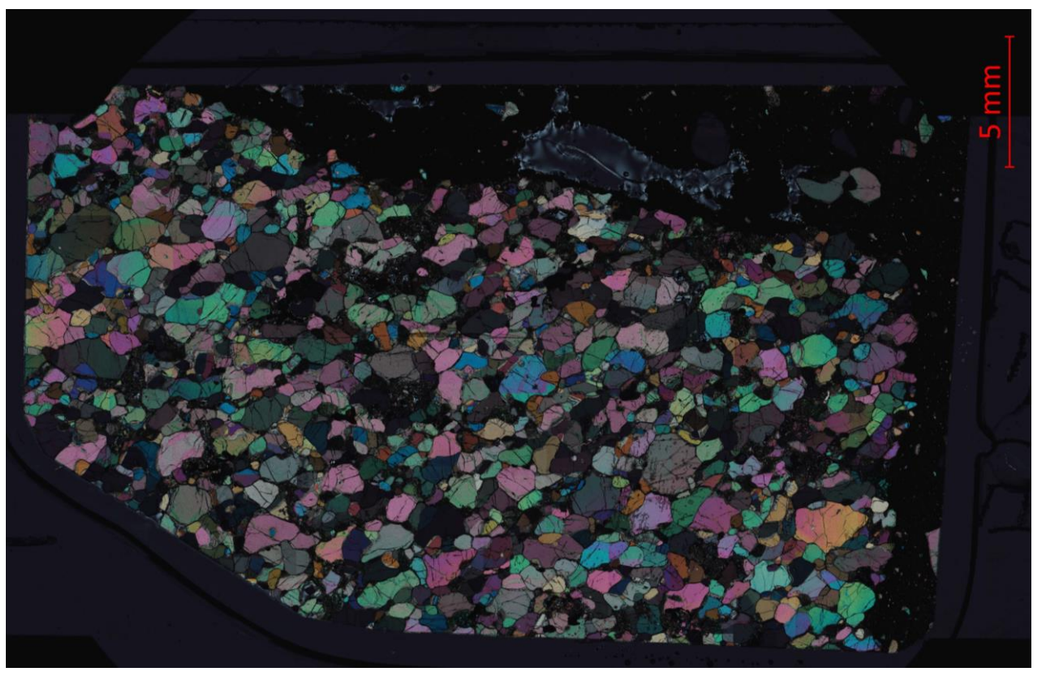

AL90
Equigranular
Tablet

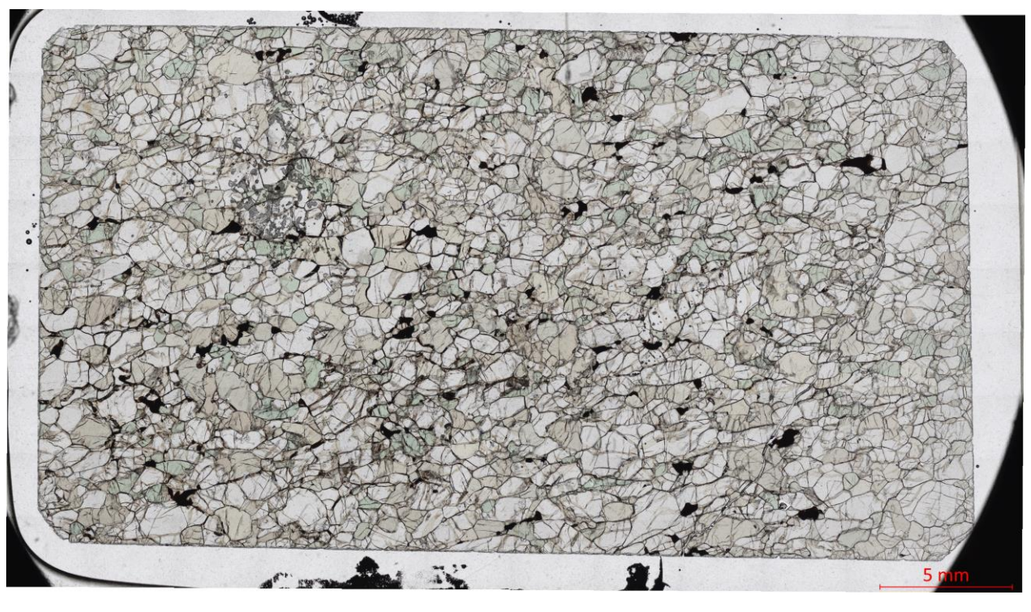

Figure 7-1. continued

	plane polarized light	cross-polarized light
HF01 Equigranular-Protogranular		
HF02 Equigranular-Protogranular		
LG14 Mosaic Equigranular	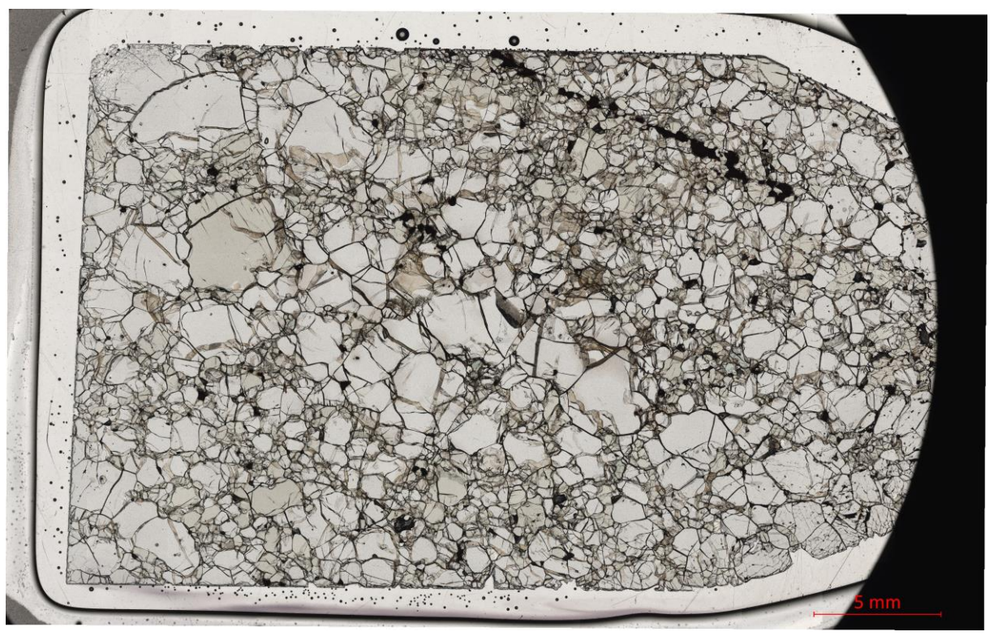	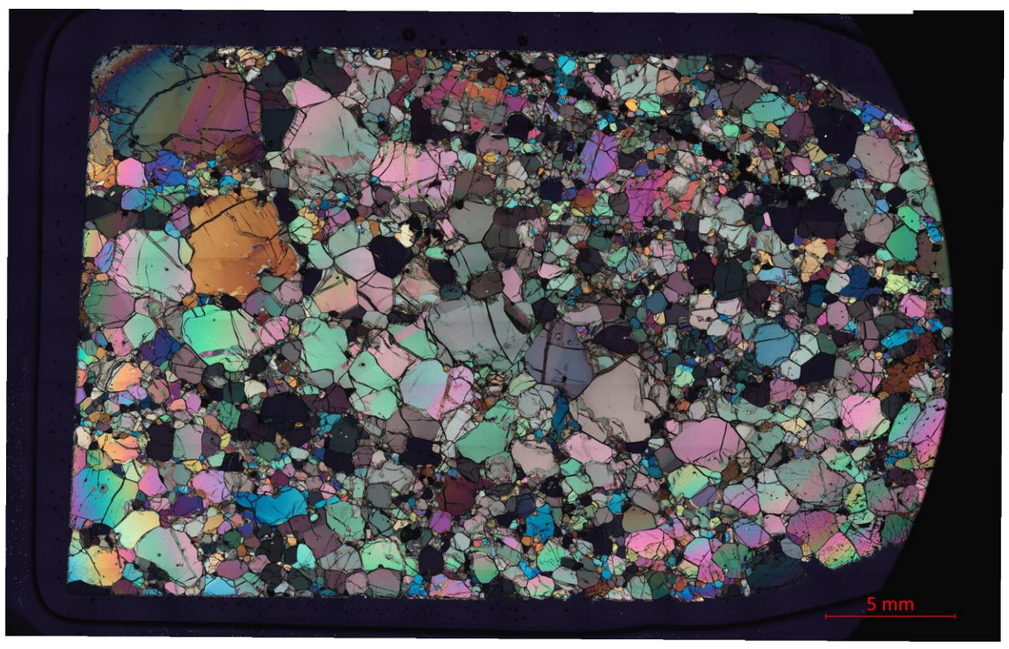
LG33 Mosaic Equigranular	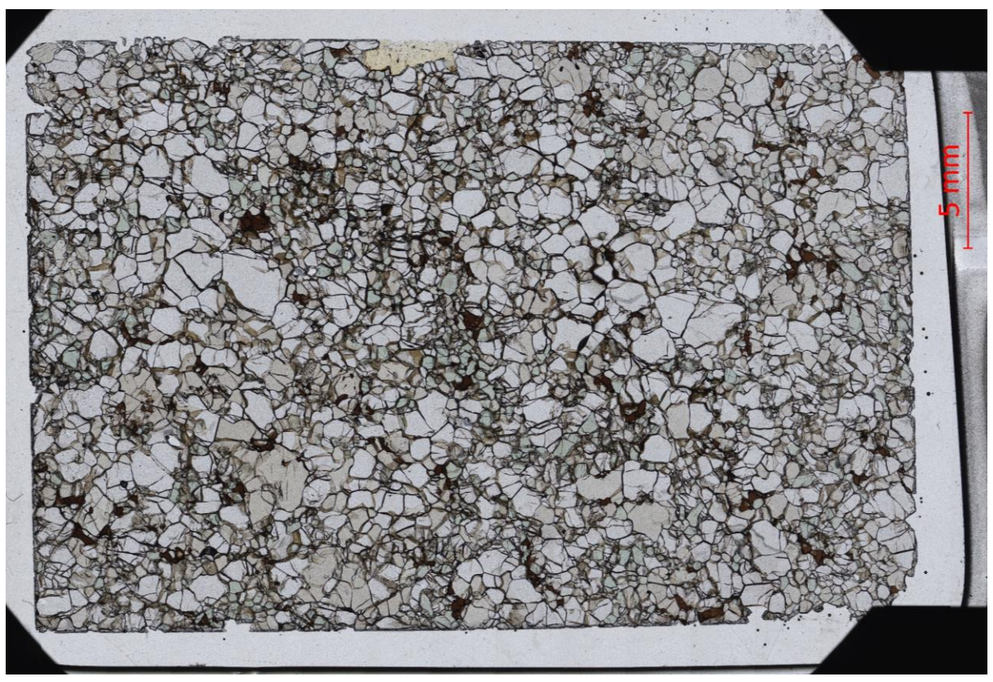	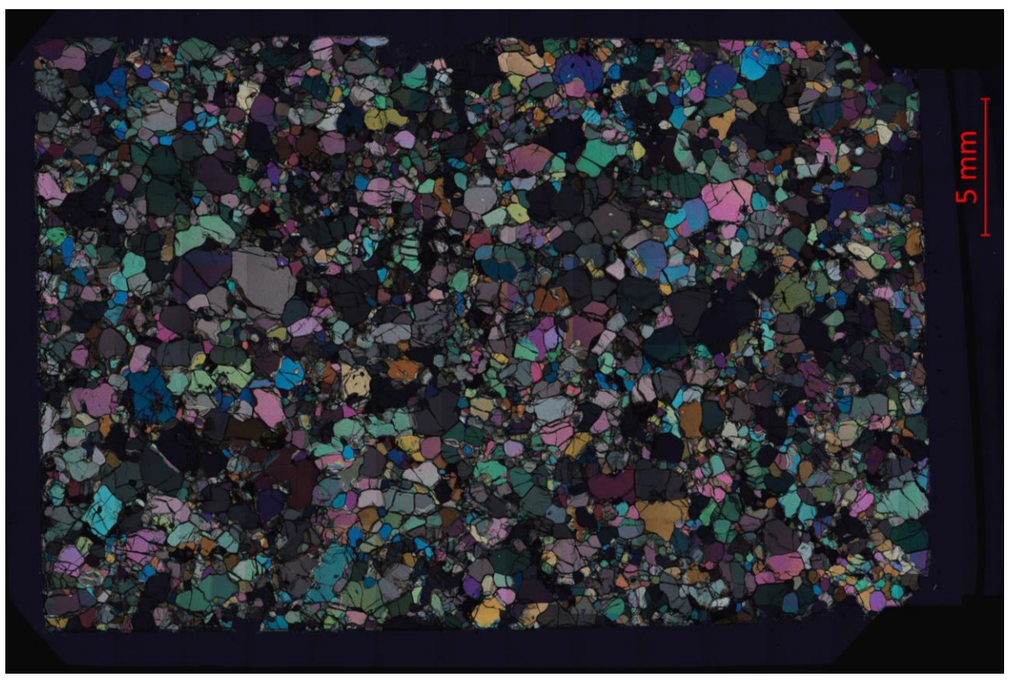
LG36 Mosaic Equigranular		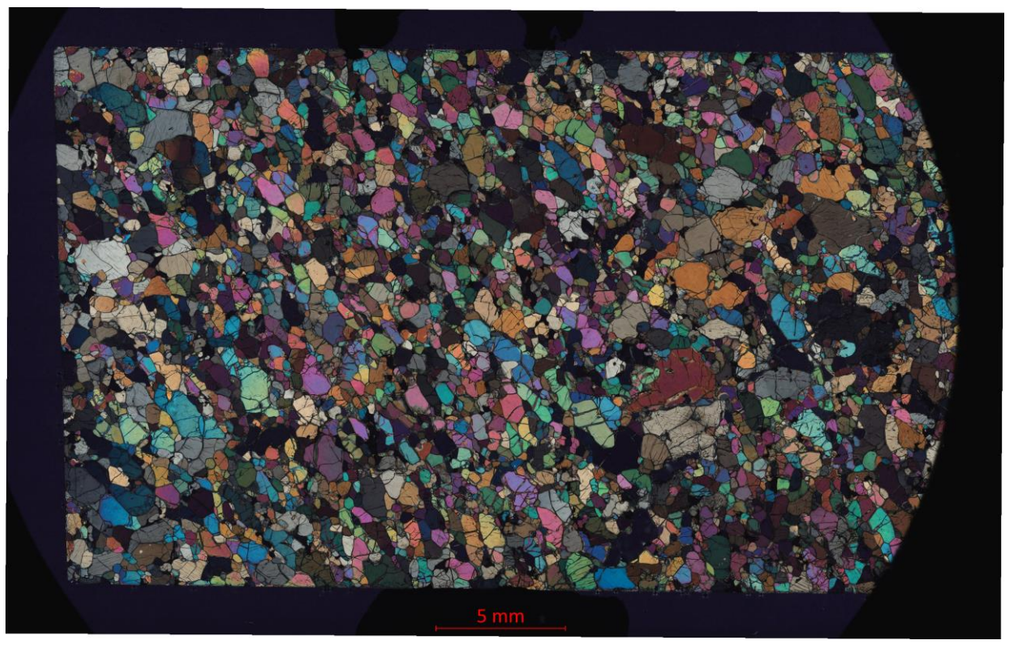

Figure 7-1. continued

plane polarized light

cross-polarized light

CR20
Protogranular

CR27
Protogranular

CR29
Protogranular

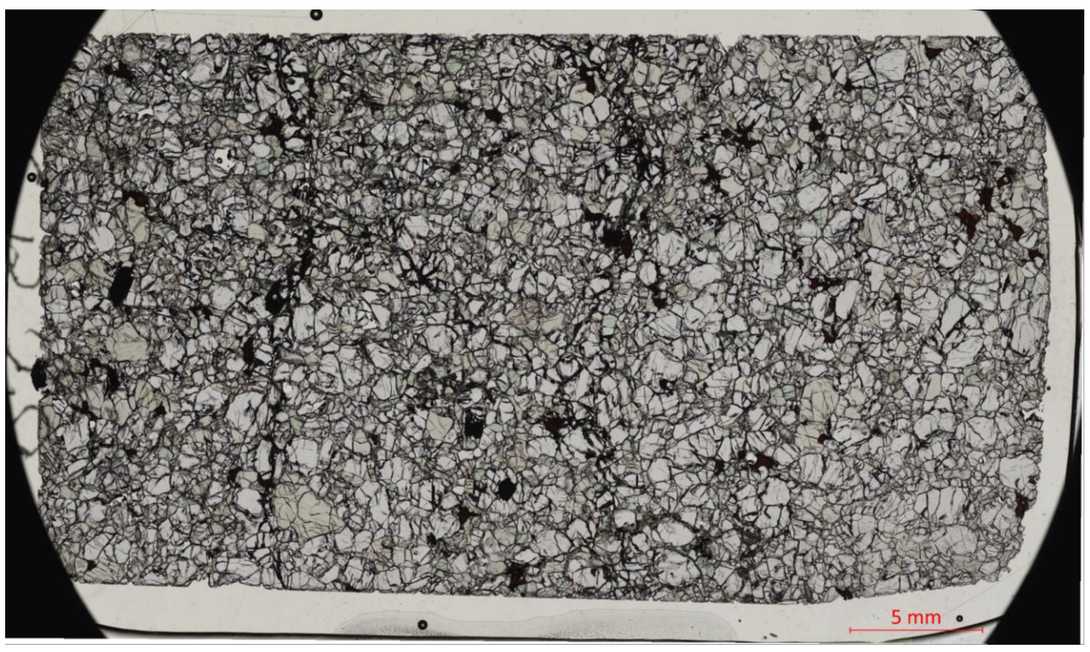

SL14
Protogranular

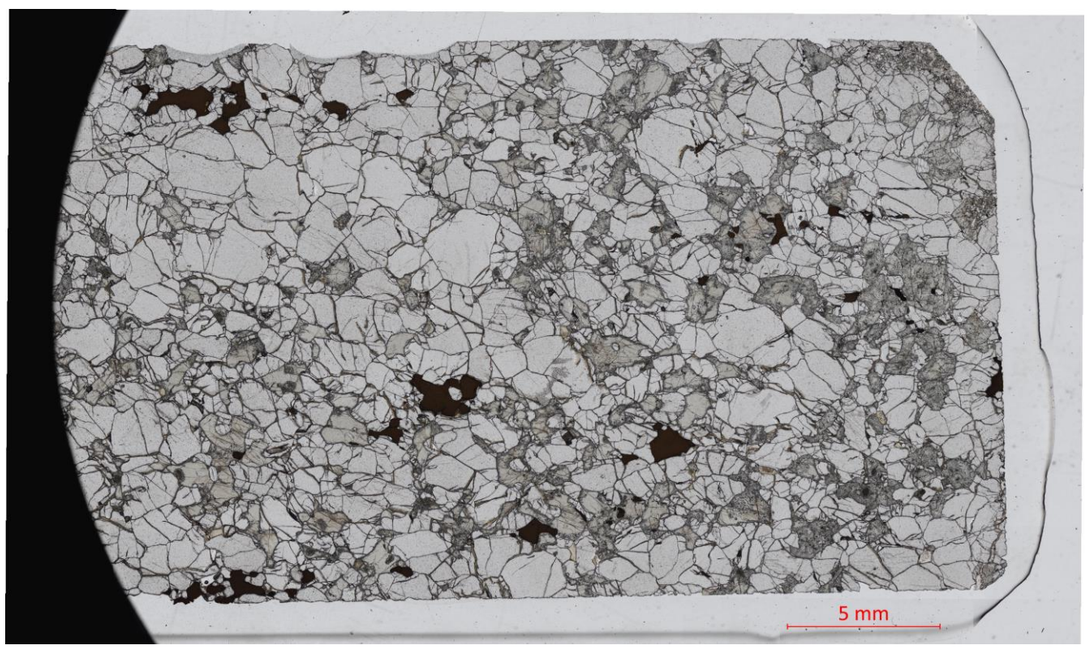

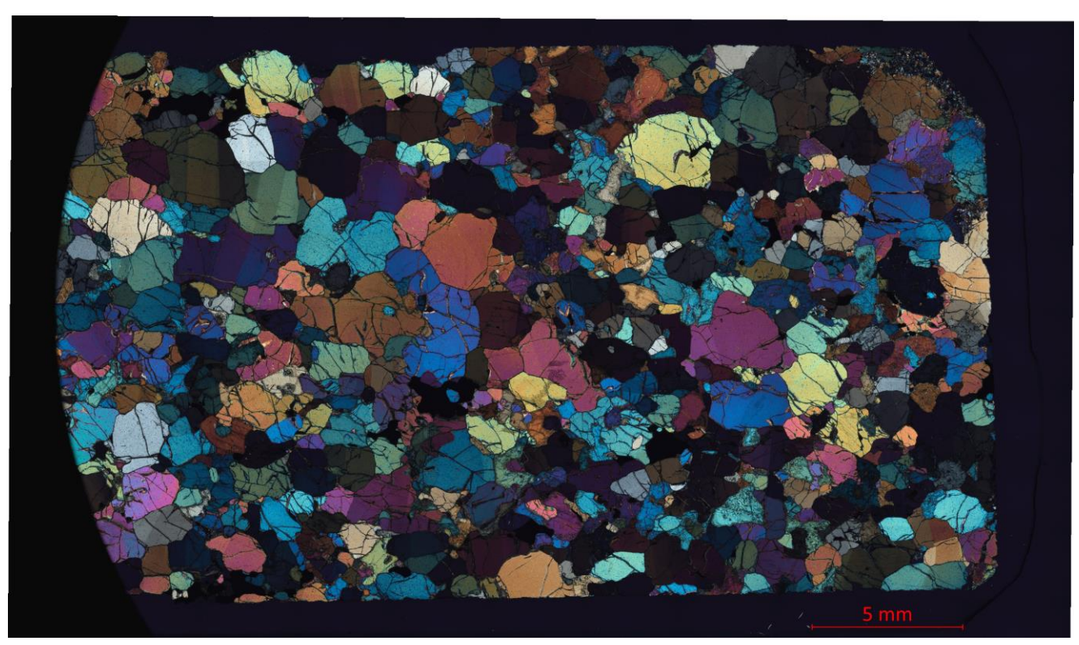

SL15
Protogranular

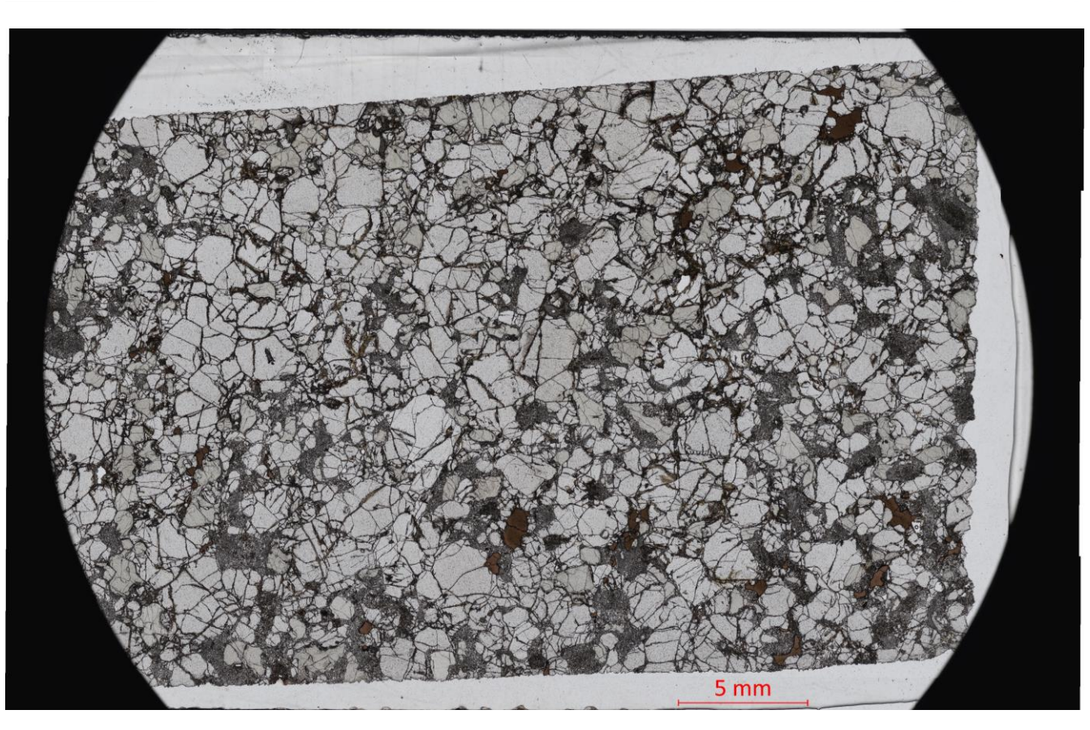

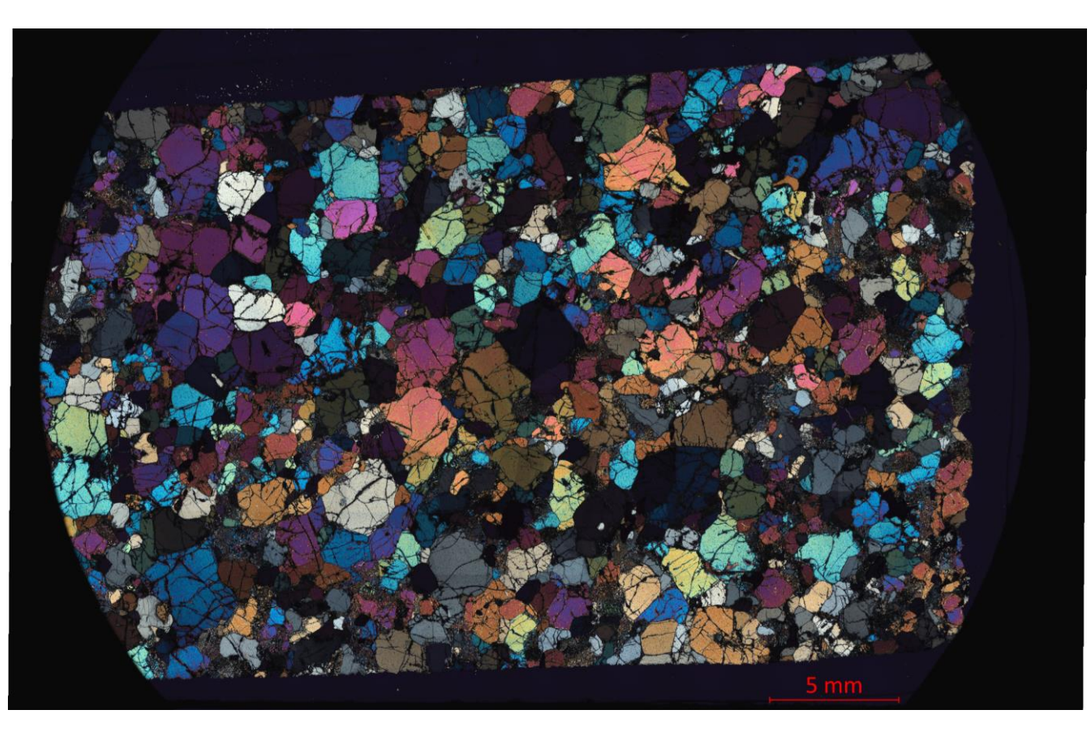

Figure 7-1. continued

	plane polarized light	cross-polarized light
SL39 Protogranular	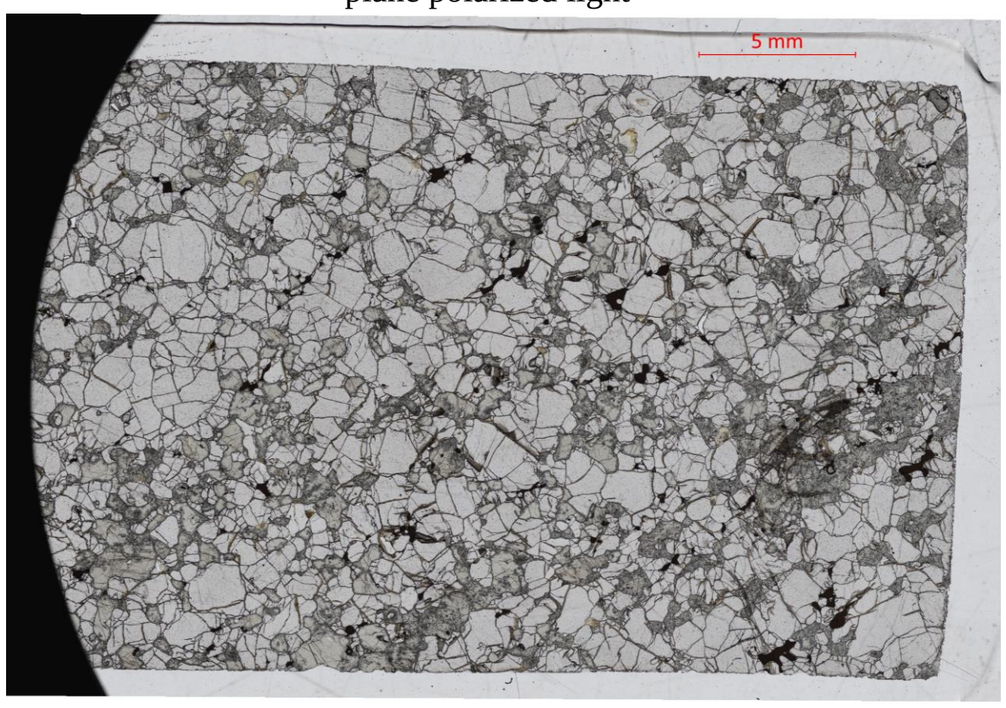	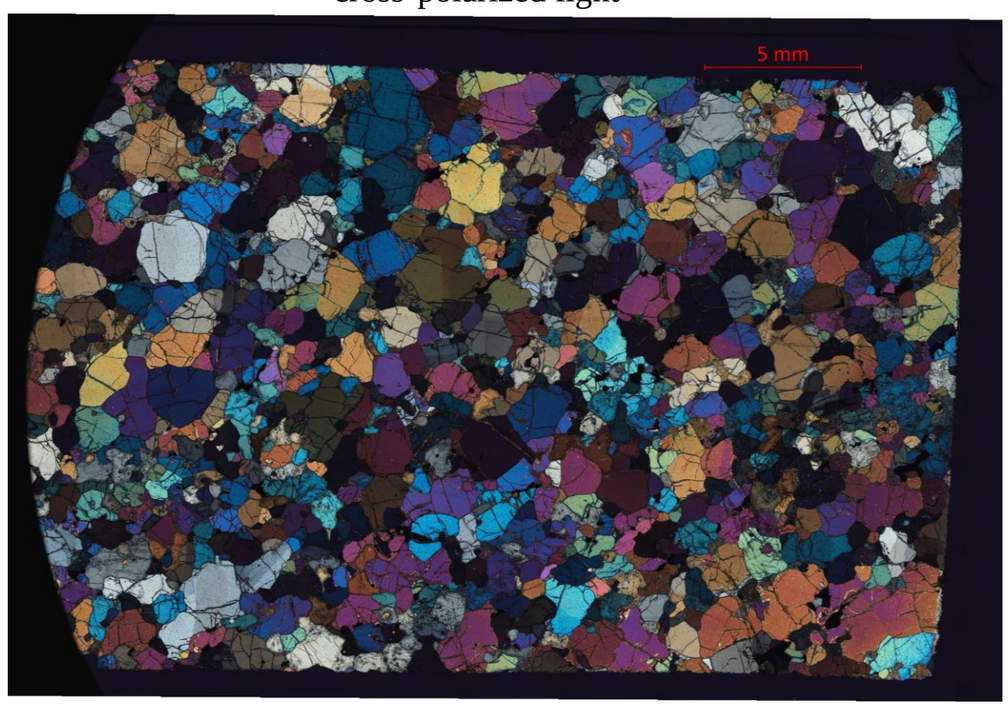
JL05 Protogranular	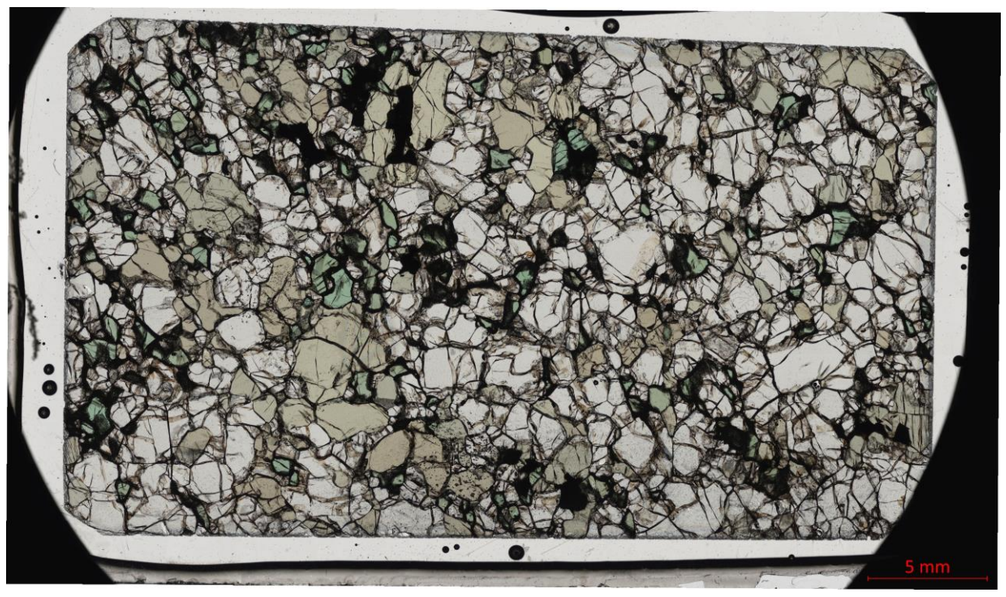	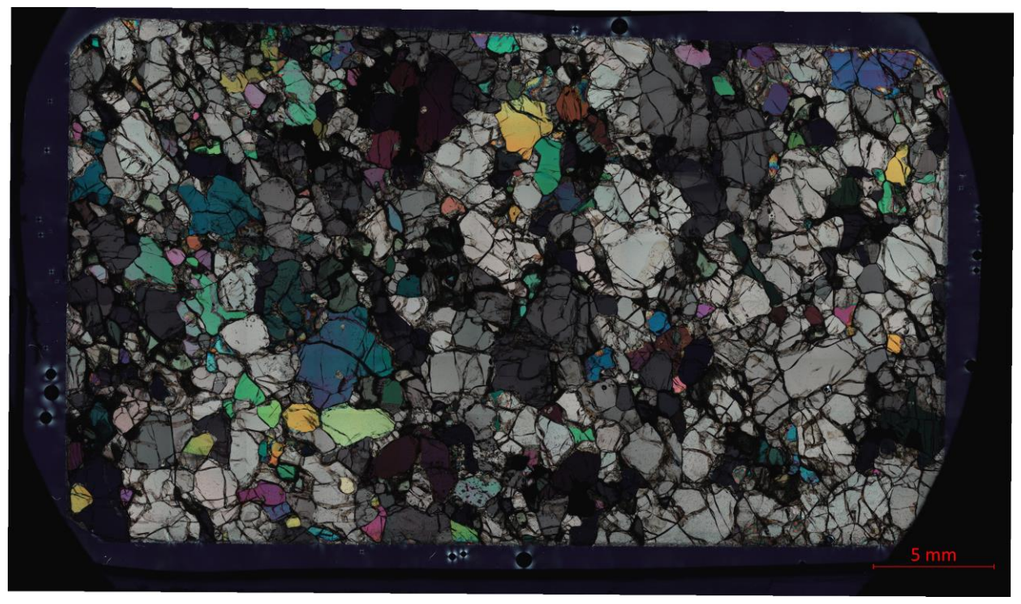
JL12 Protogranular	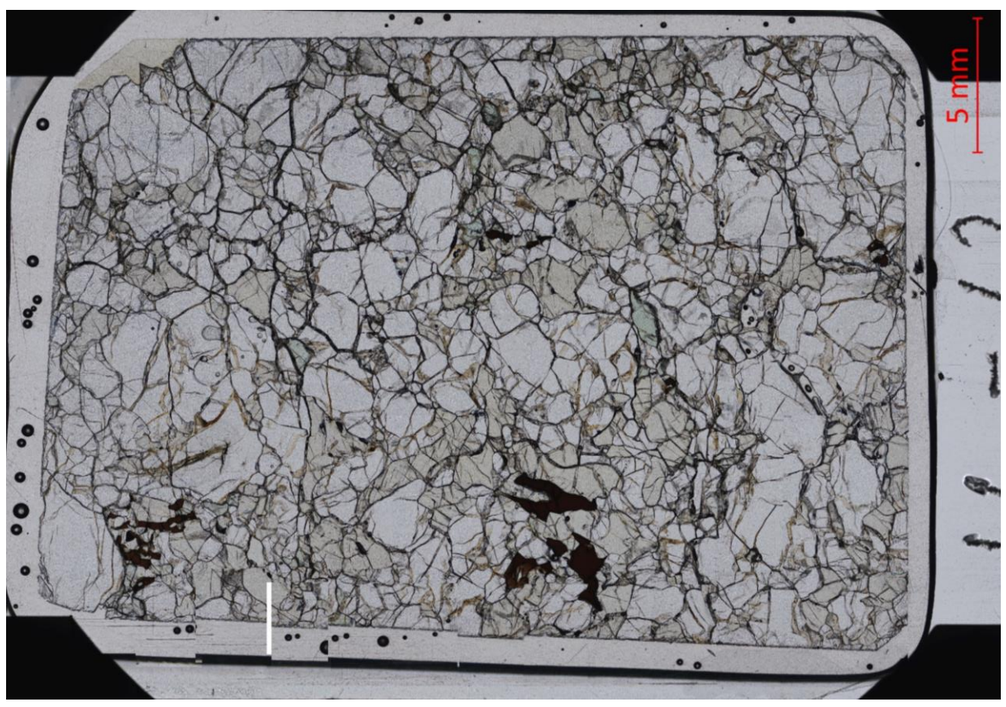	
KL04 Protogranular		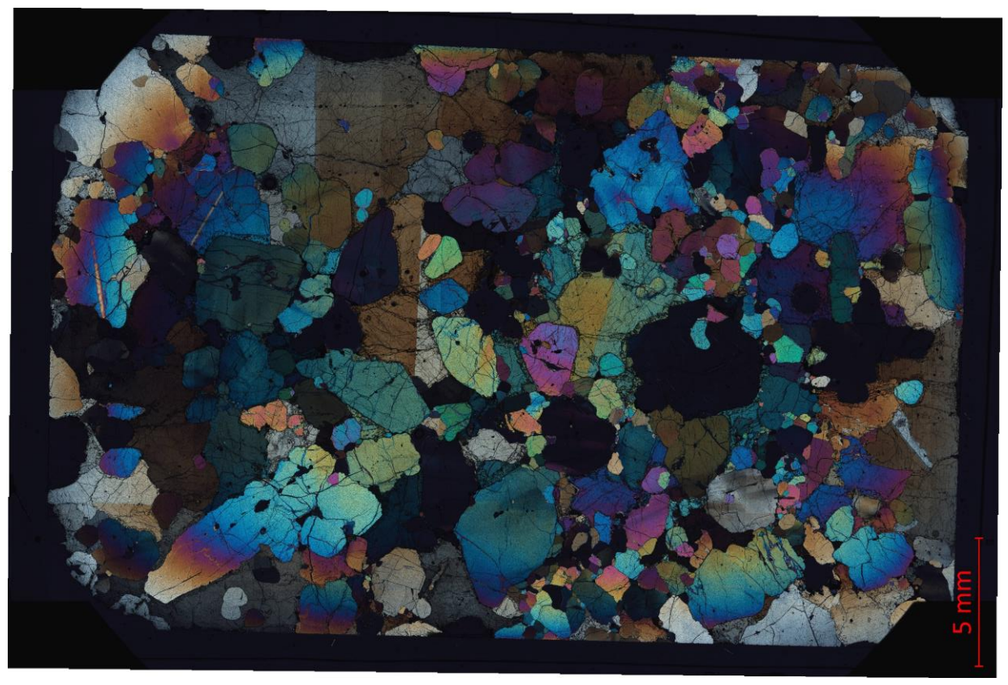
KL29 Porphyroclastic	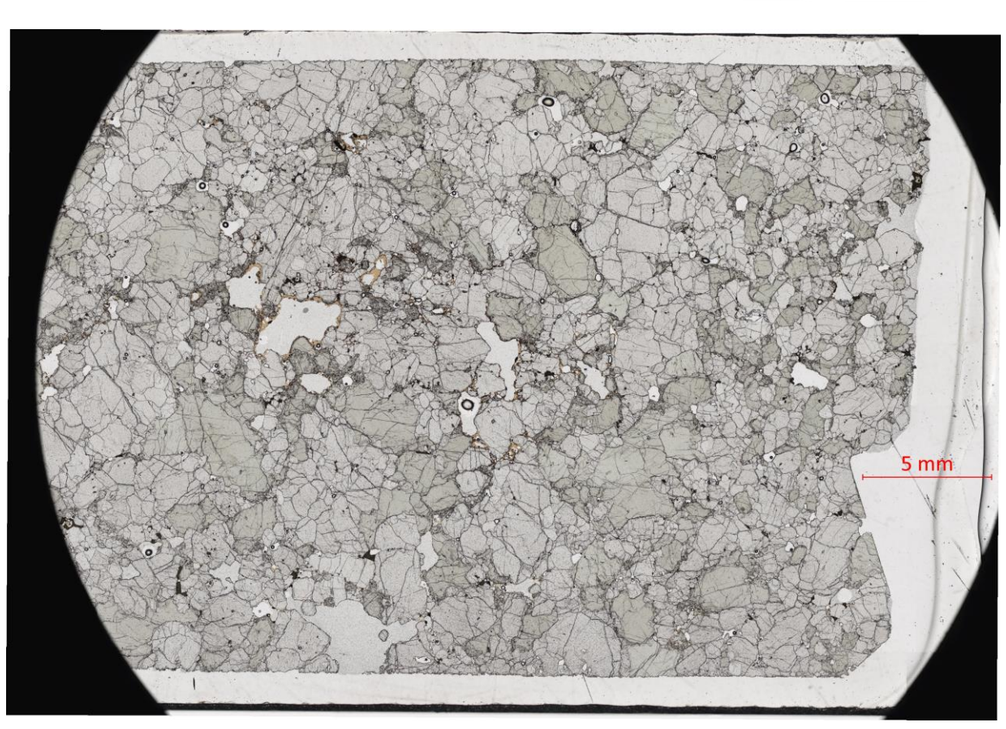	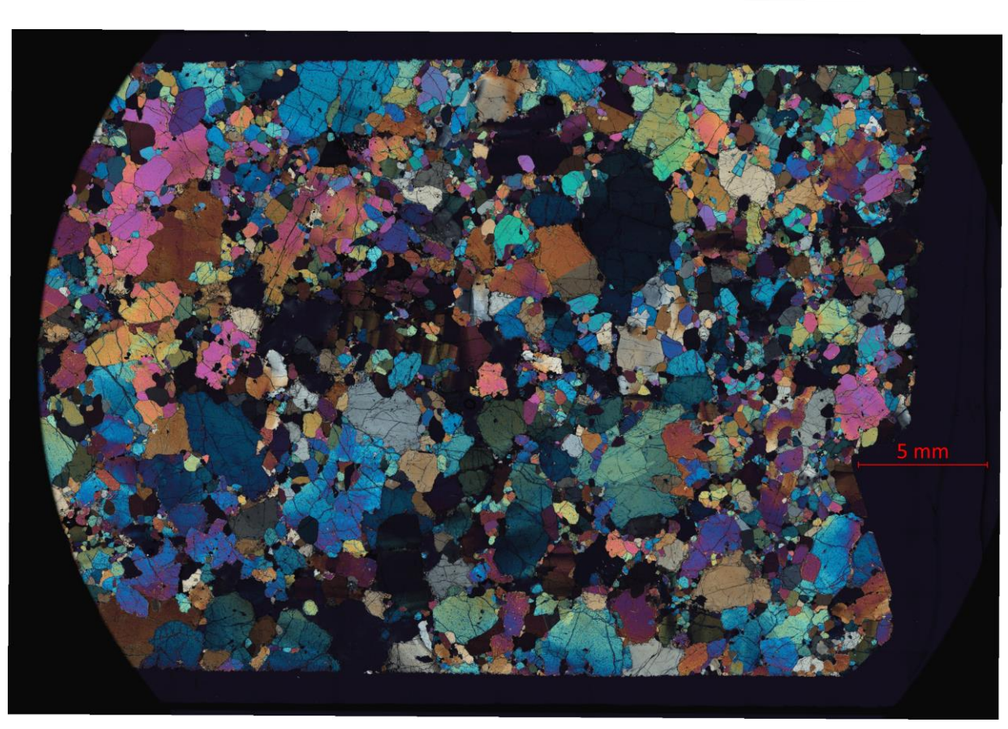

Figure 7-1. continued

plane polarized light

cross-polarized light

KL37
Protogranular
-Mylonitic

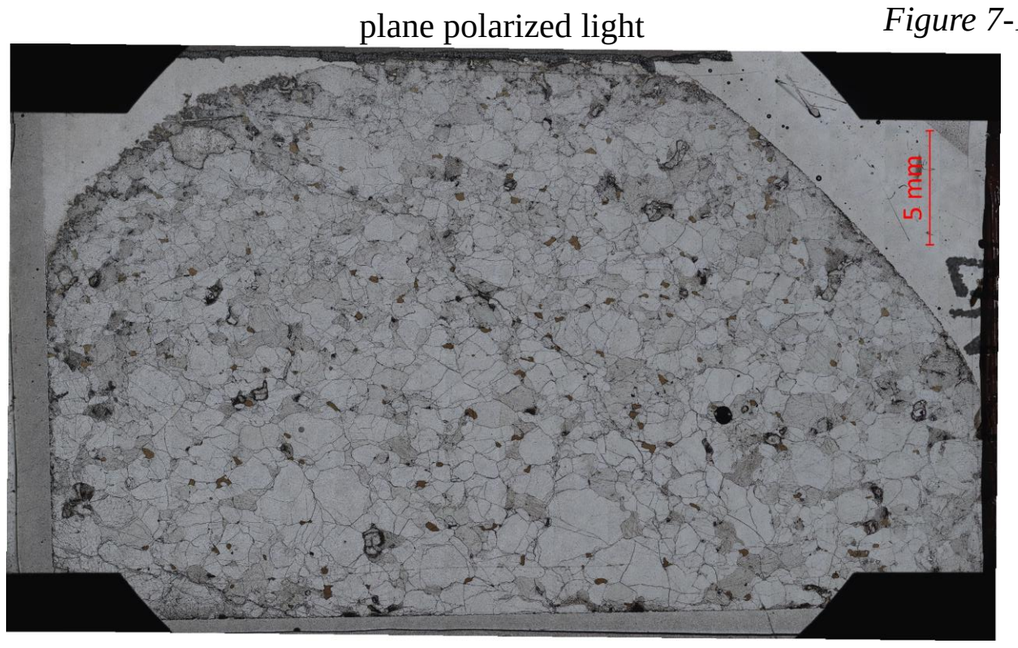

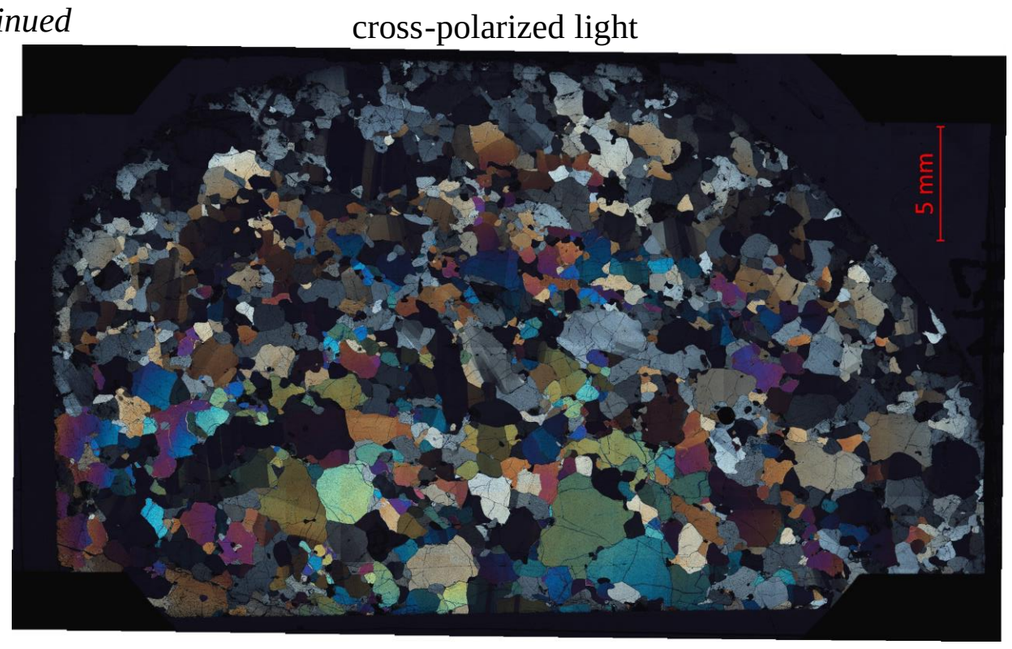

KL44
Protogranular
-Mylonitic

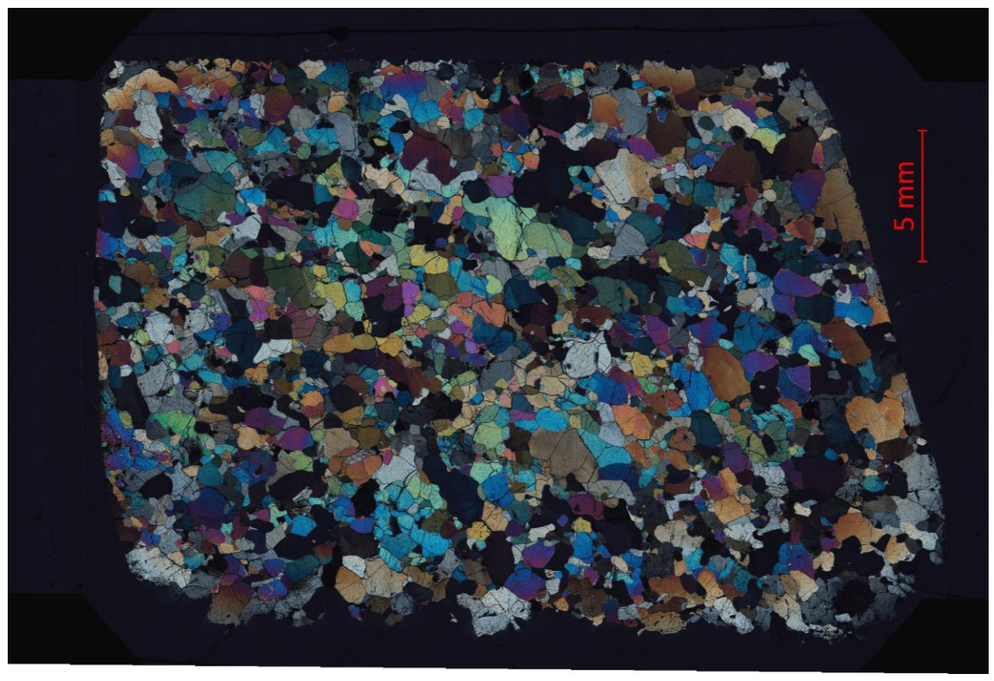

KL51
Transitional
Tablet

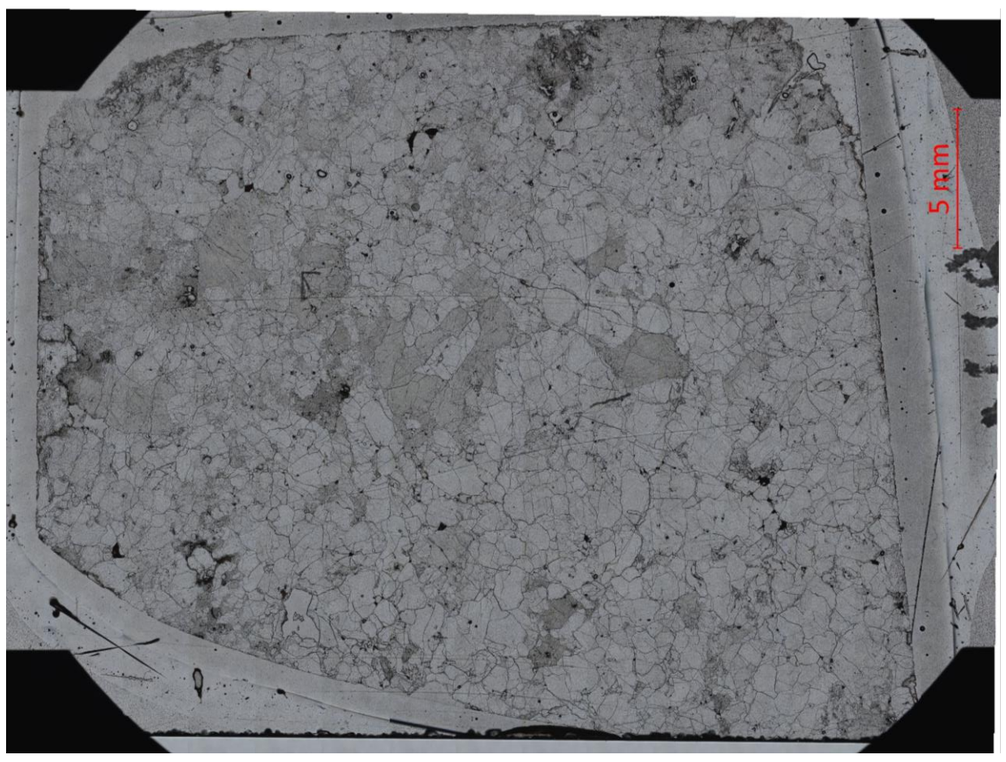

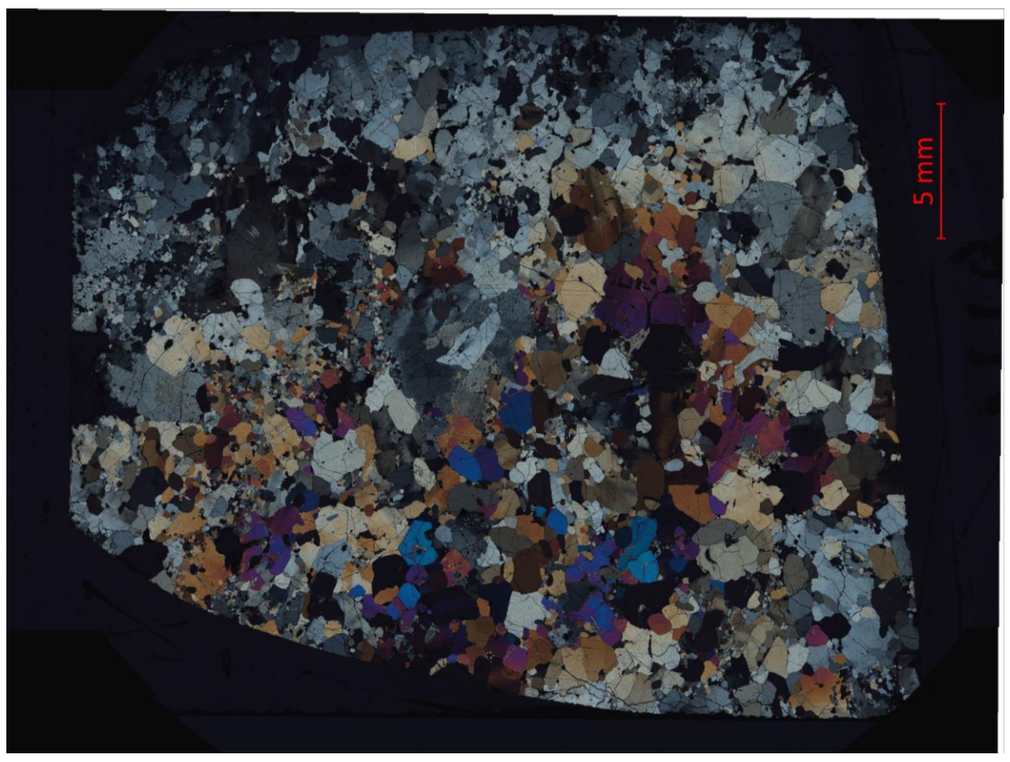

KL53
Transitional
Tablet

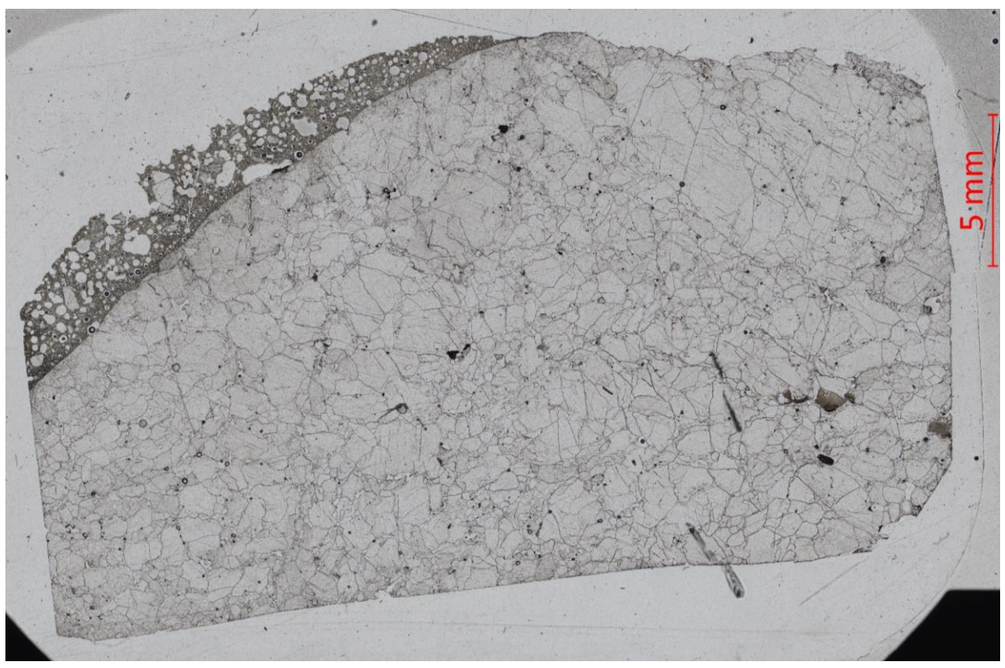

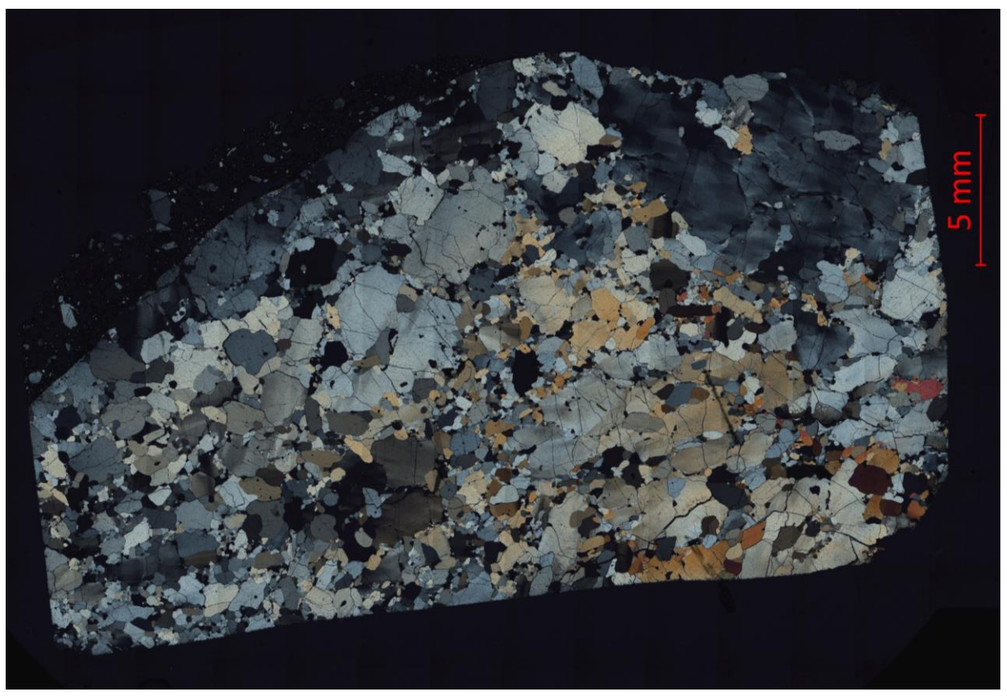

KL55
Protogranular-
Porphyroclastic

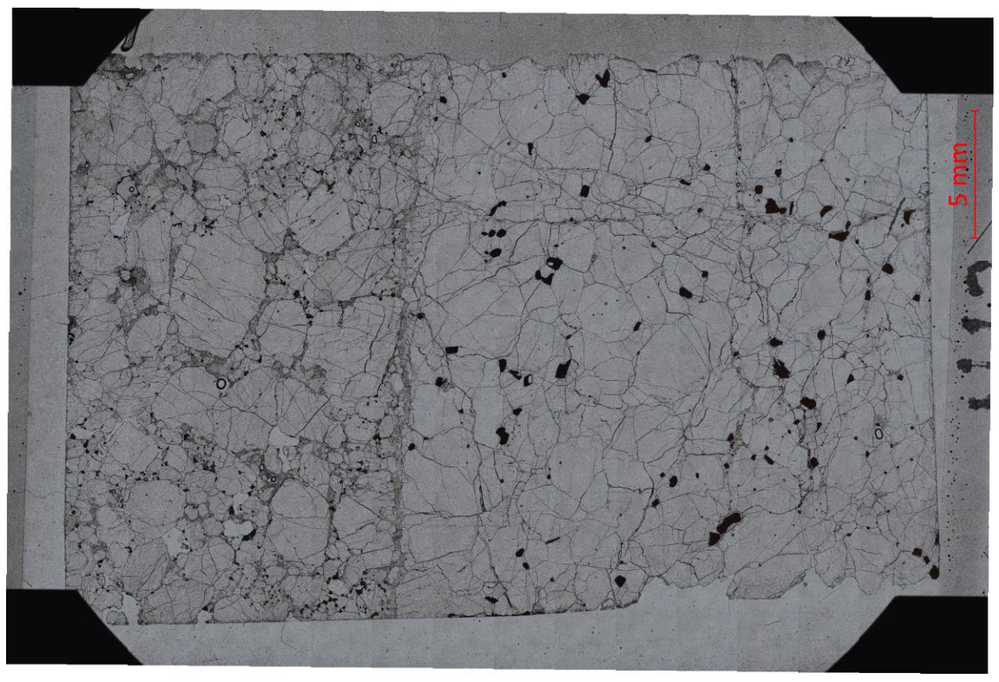

Figure 7-1. continued

plane polarized light

cross-polarized light

KL59
Equigranular
Tabular

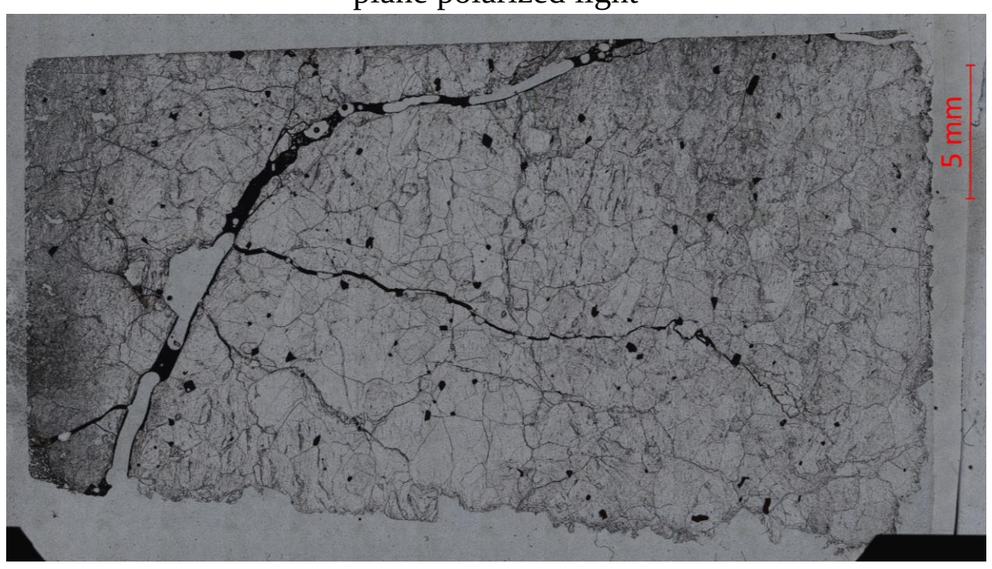

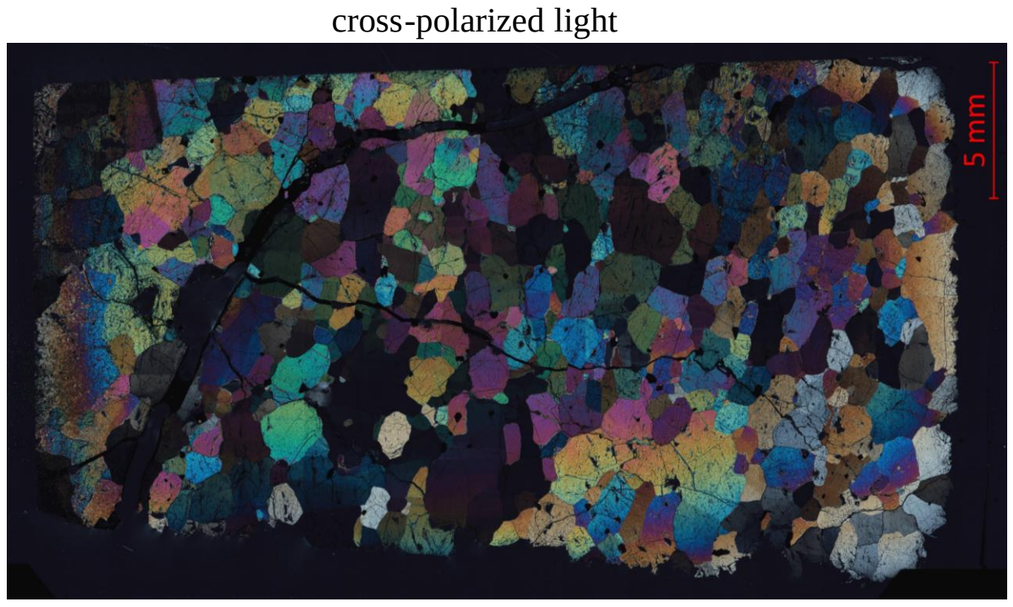

KL62
Equigranular
Tabular

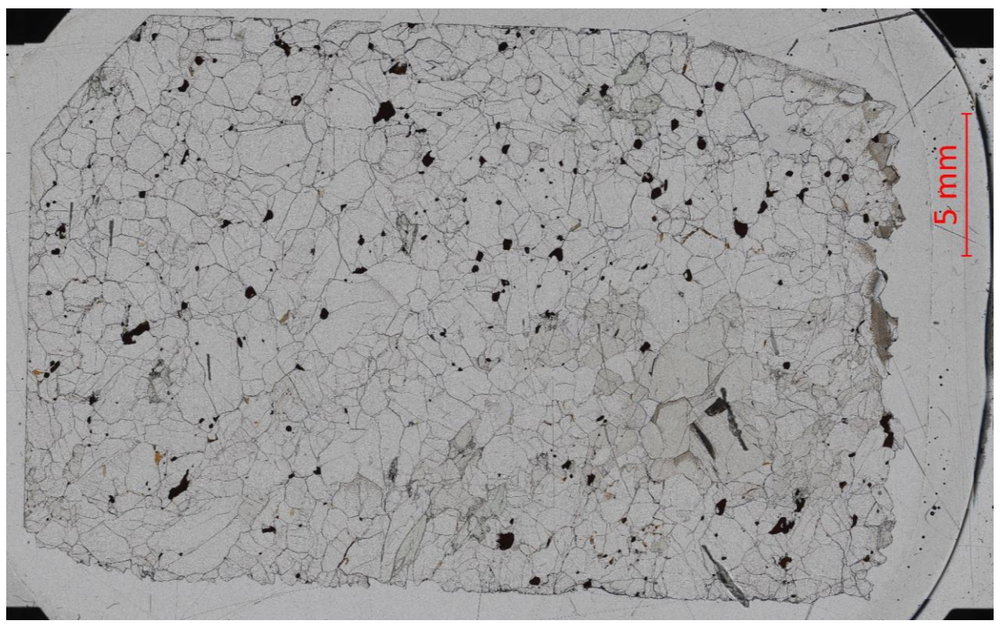

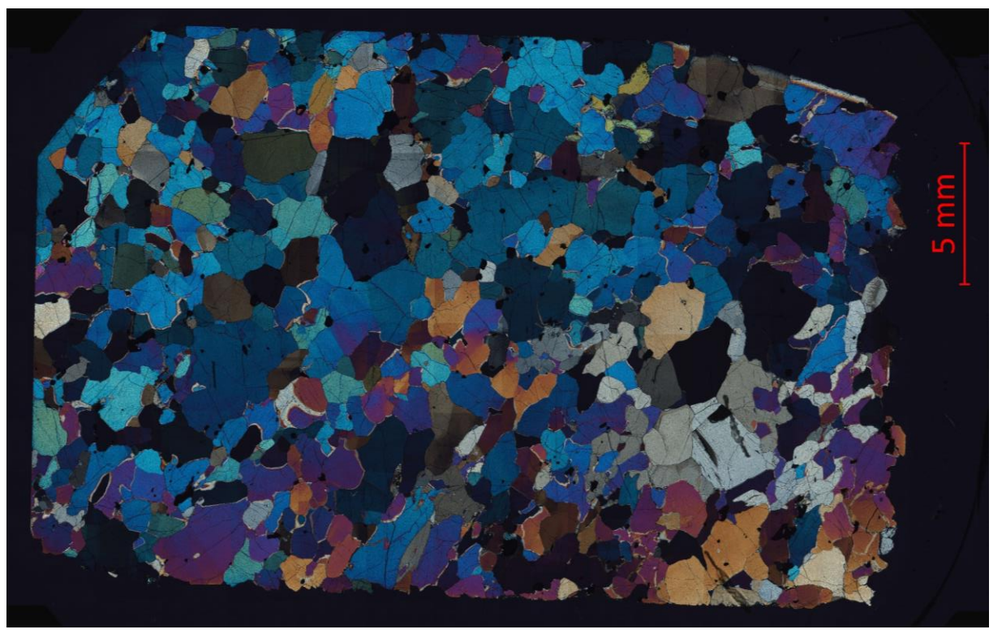

KL65
Protogranular-
Porphyroclastic

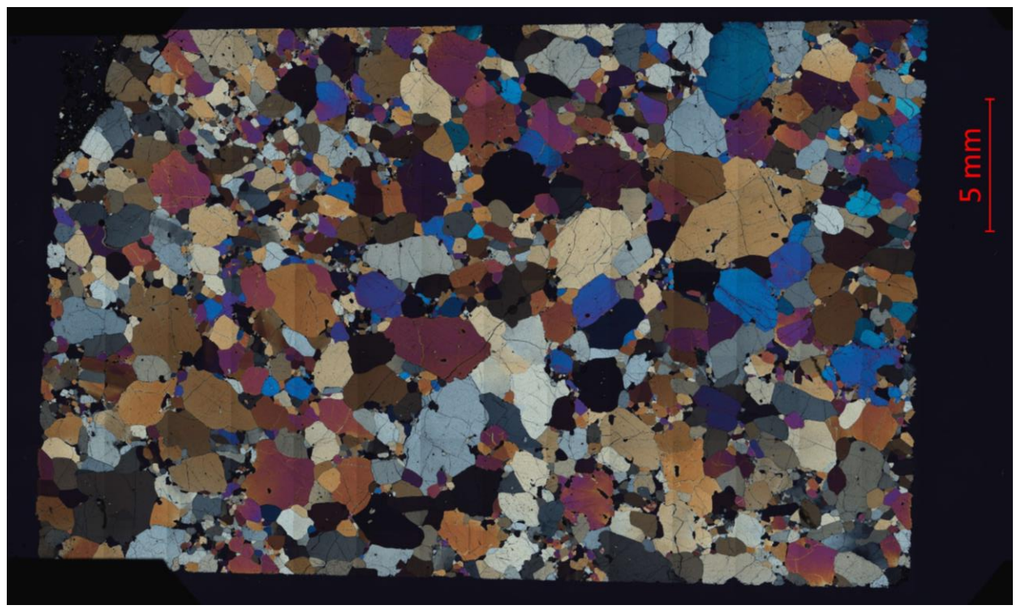

BT22
Protogranular

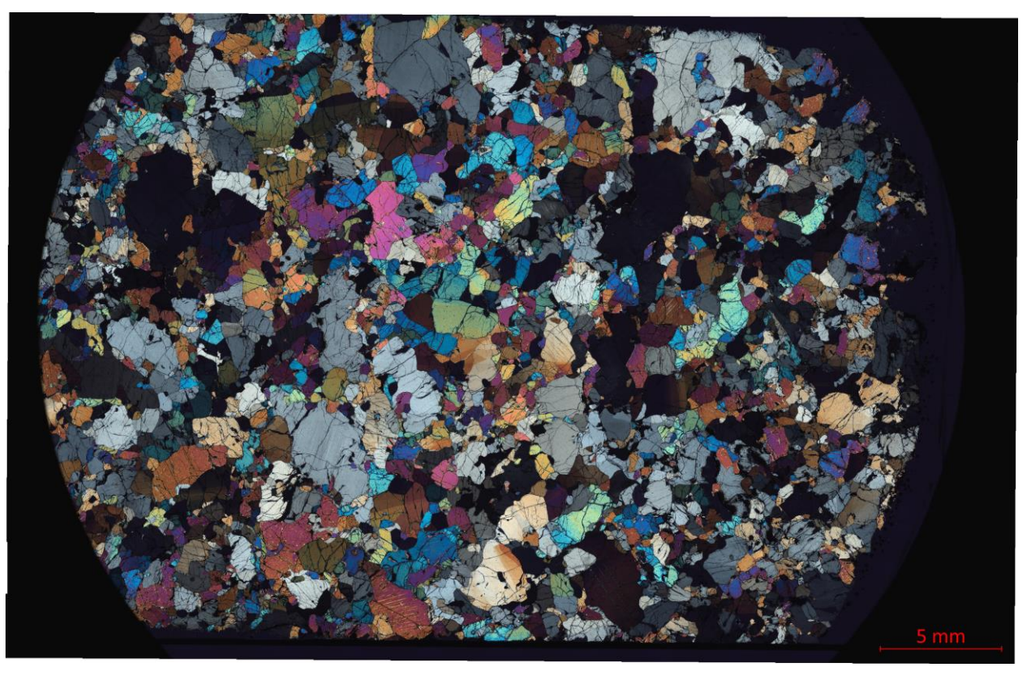

BT23
Protogranular

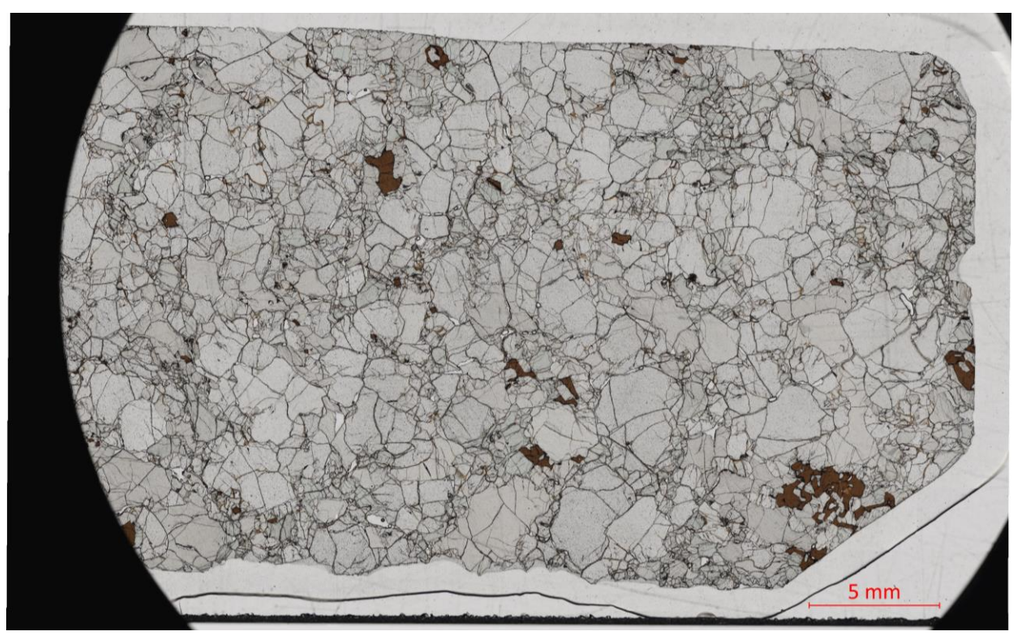

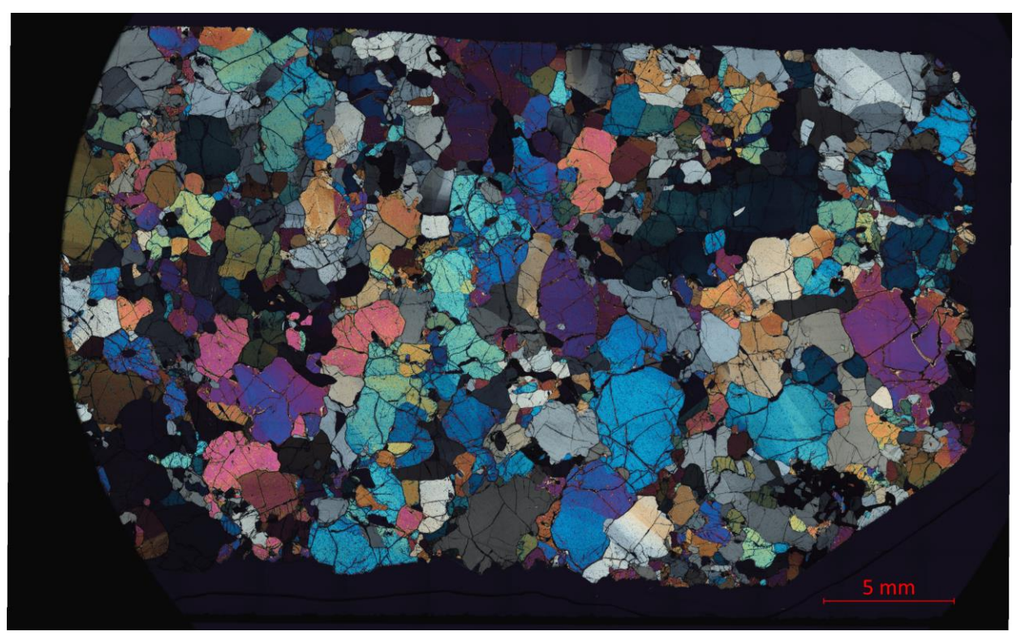

Figure 7-1. continued

plane polarized light

cross-polarized light

BT26
Protogranular

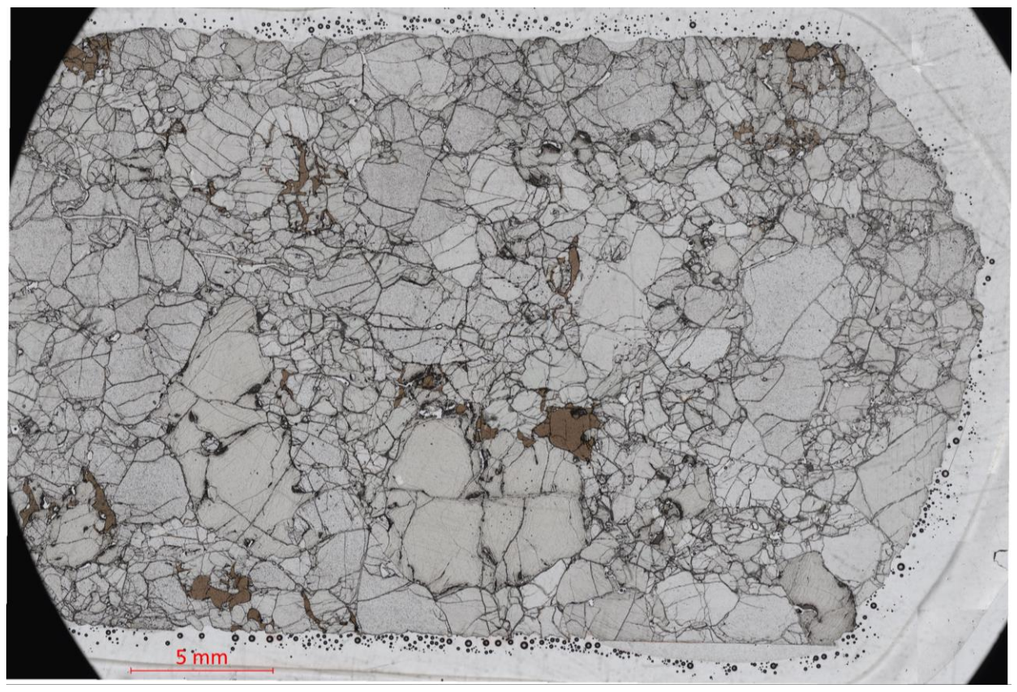

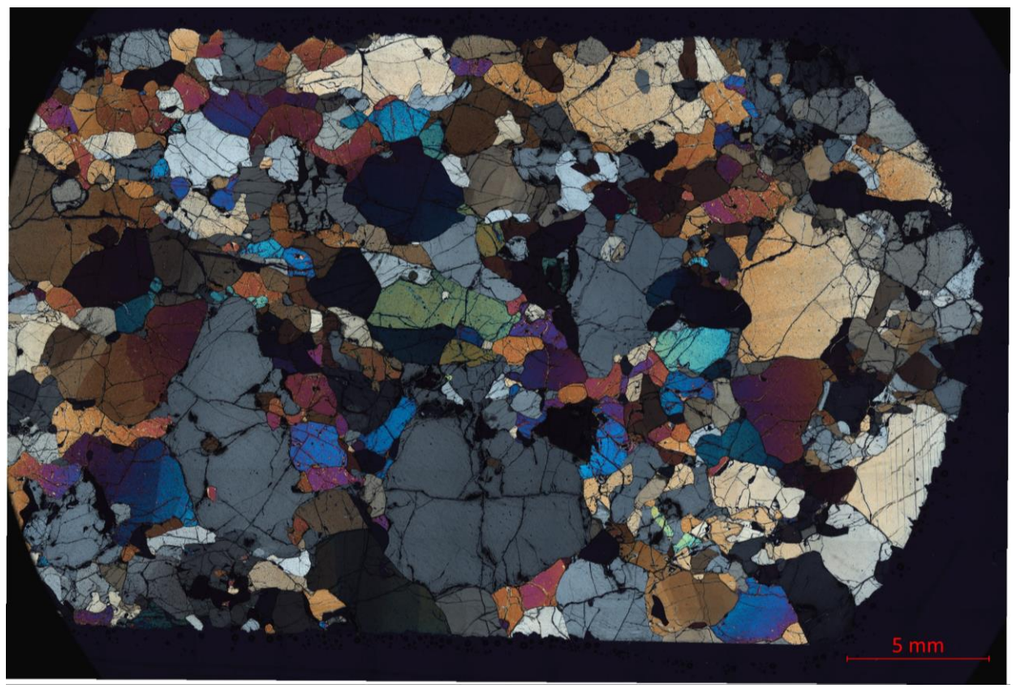

RR10
Mylonitic

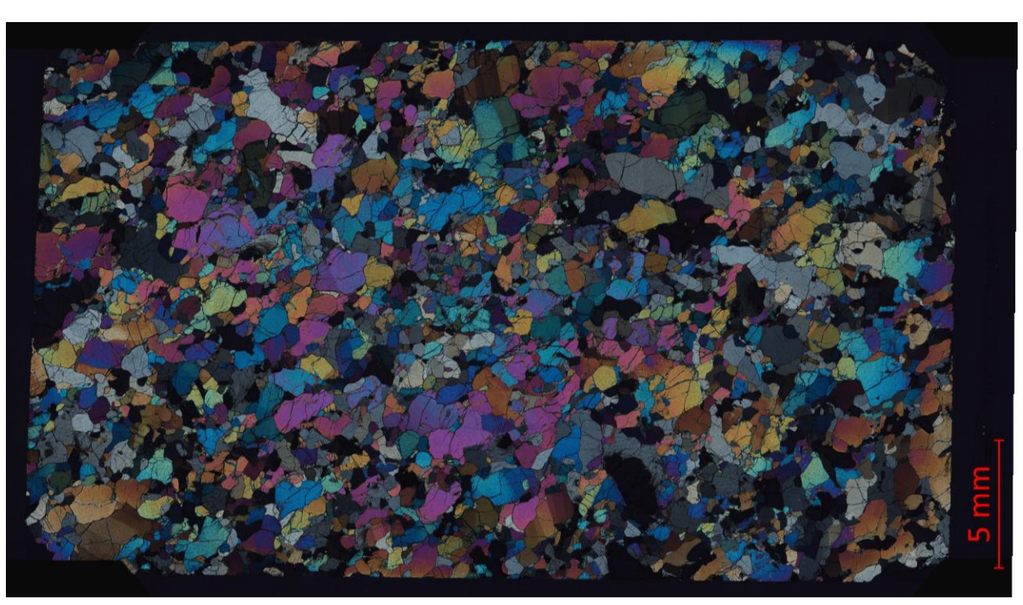

RR18
Mylonitic

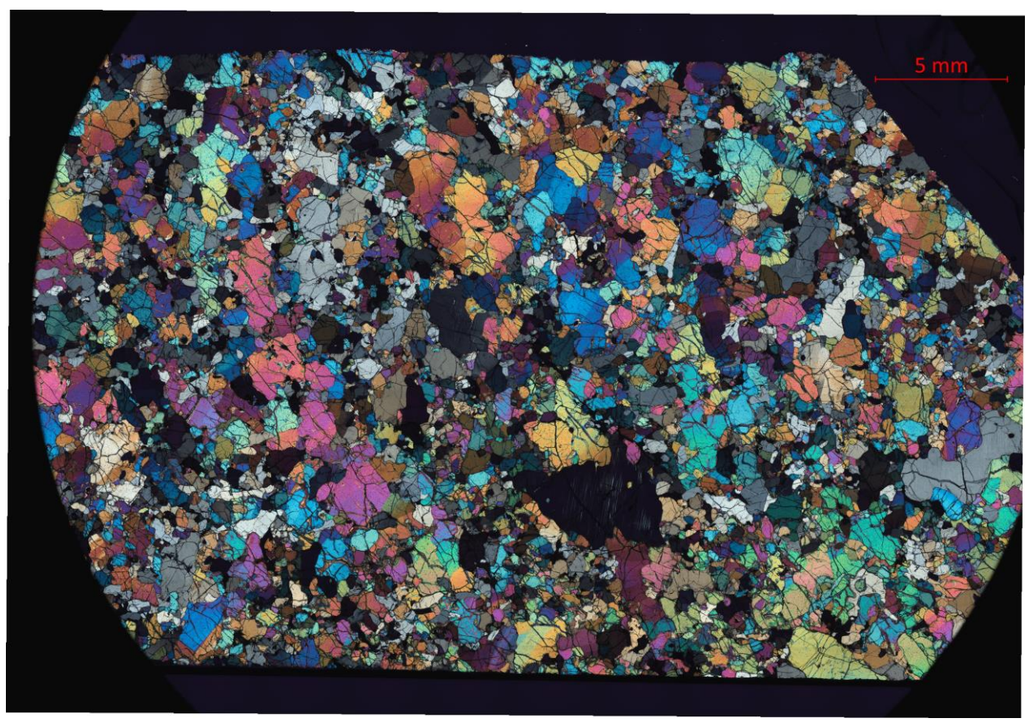

LP19
Protogranular

Figure 7.2. Olivine grain size histograms of EBSD-scanned samples

Prindle Volcano

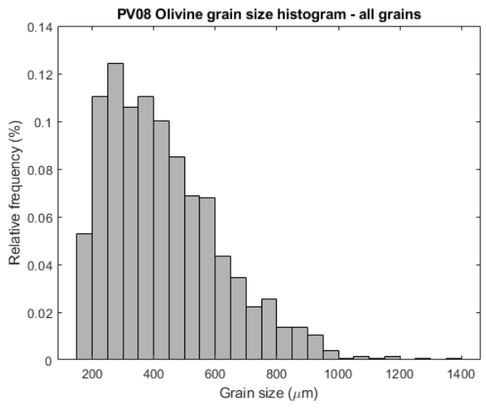

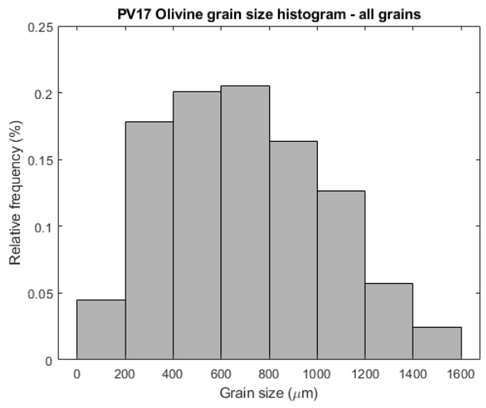

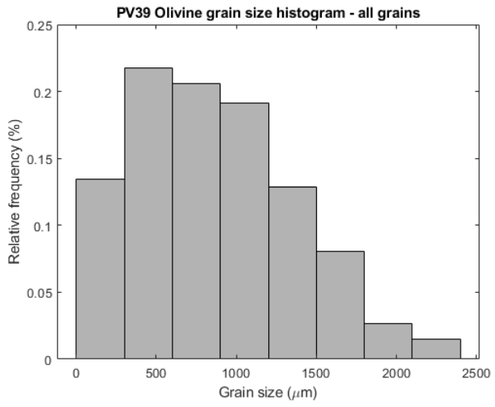

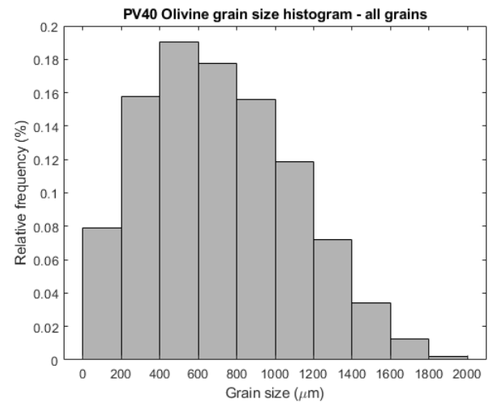

Fort Selkirk

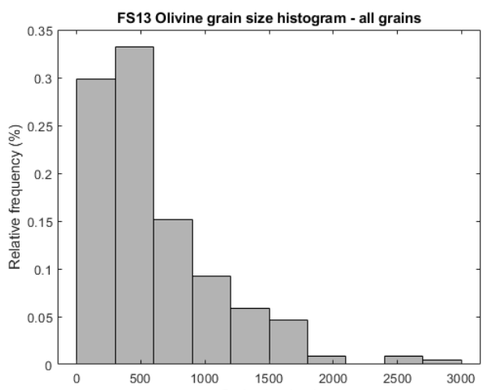

Alligator Lake

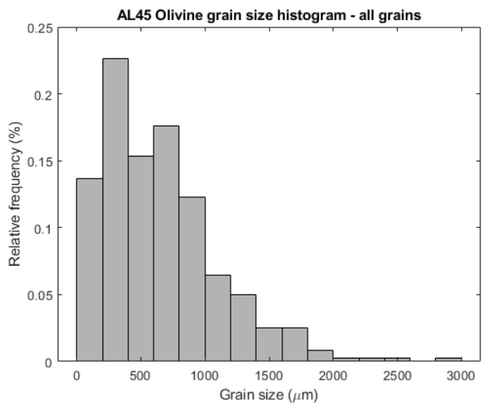

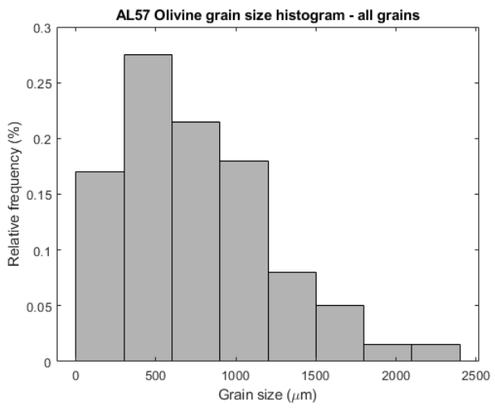

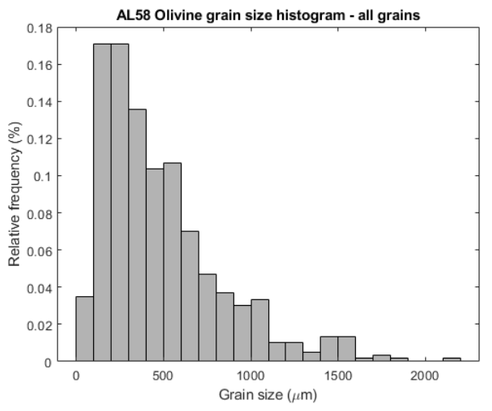

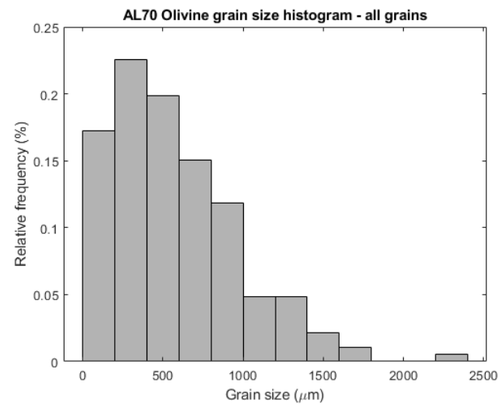

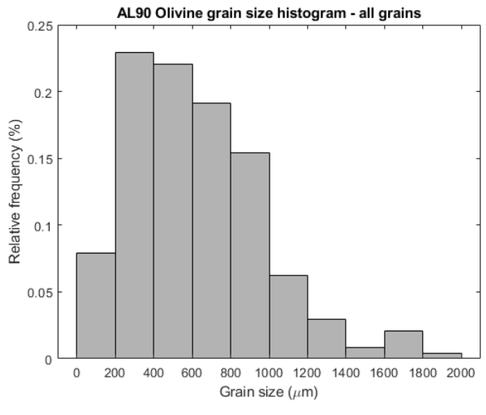

Hirschfield Creek

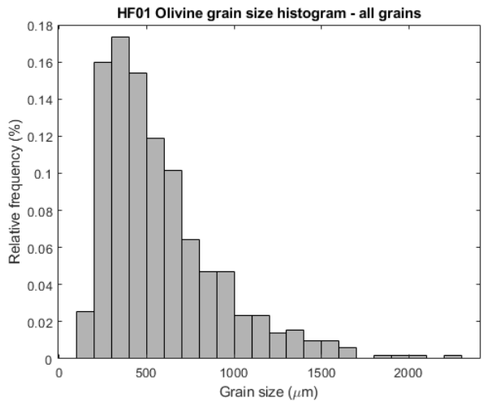

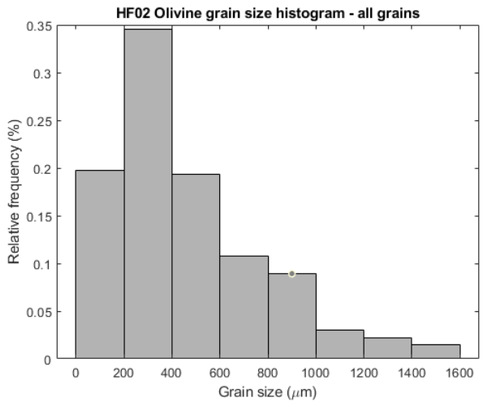

Llangorse Mountain

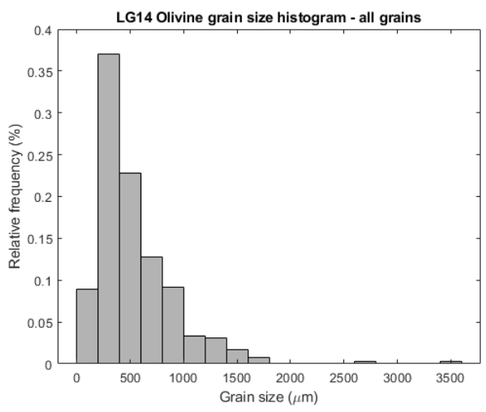

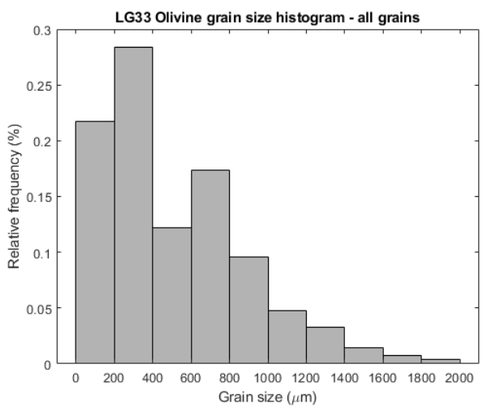

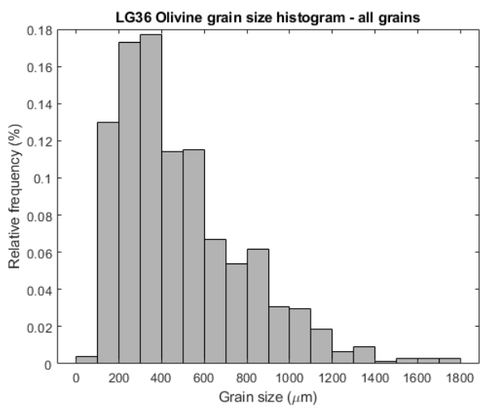

Castle Rock

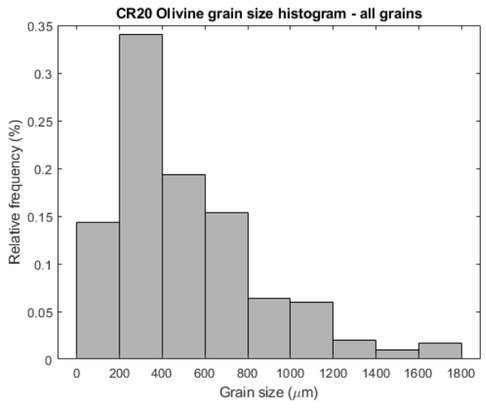

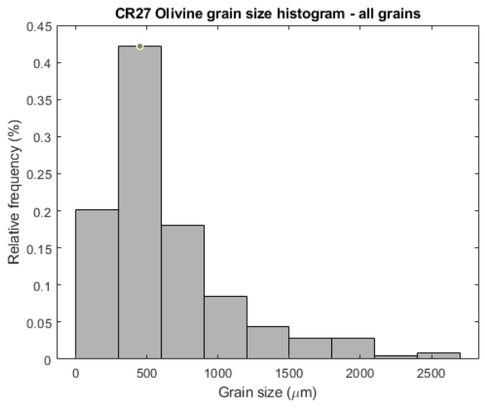

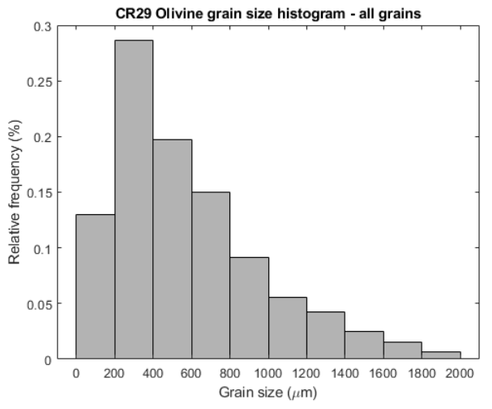

Summit Lake

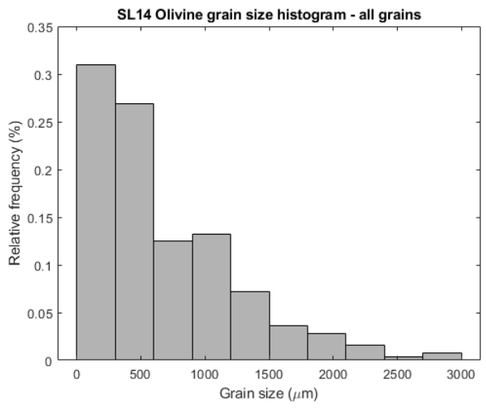

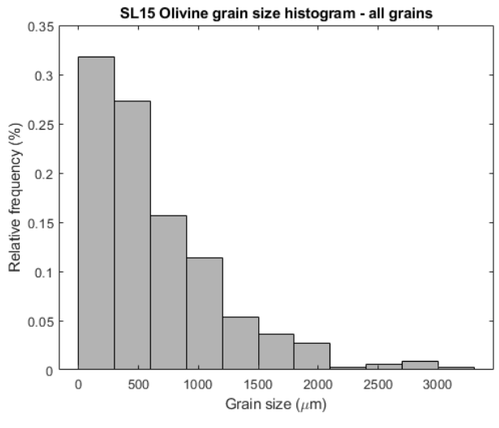

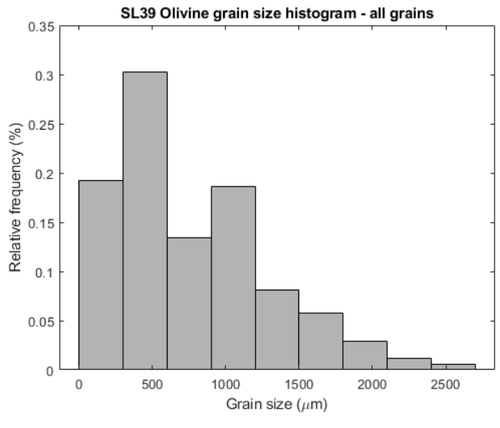

Figure 7.2. continued

Jacques Lake

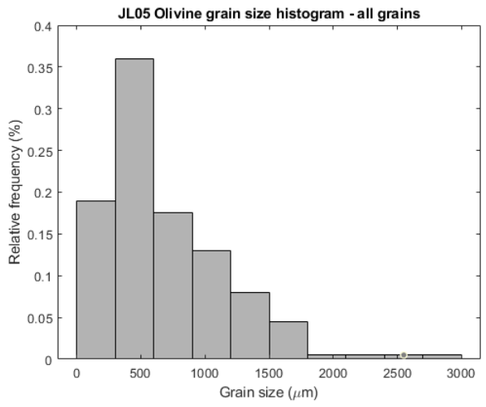

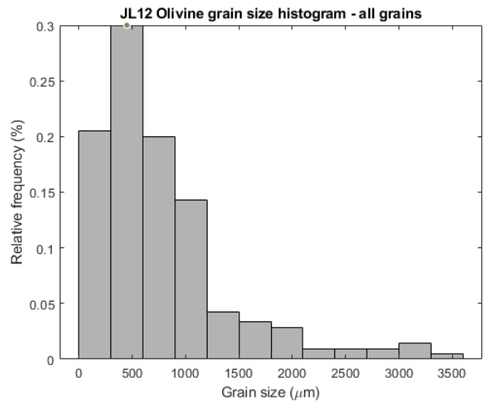

Kostal Lake

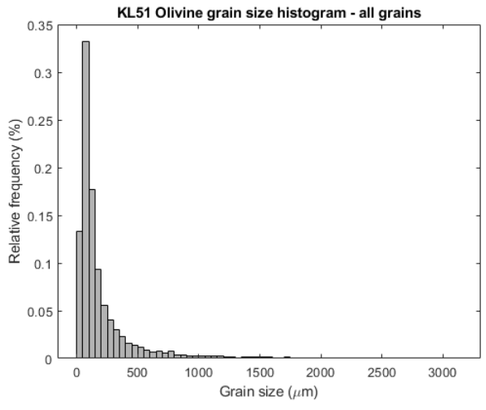

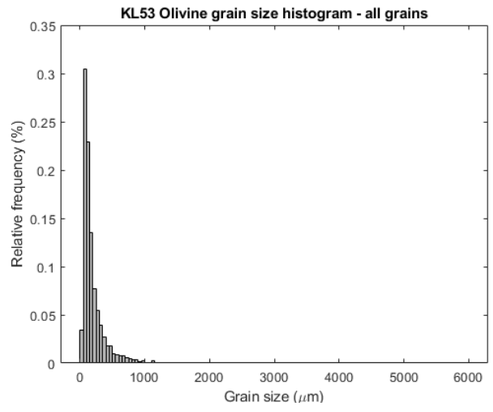

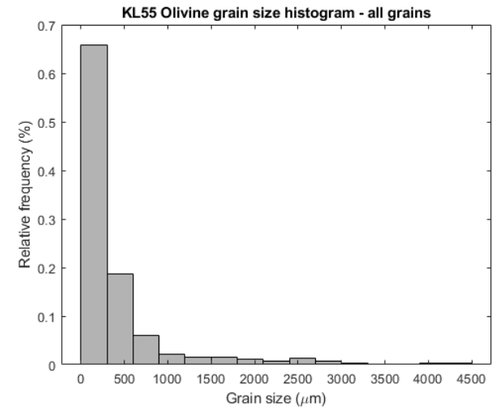

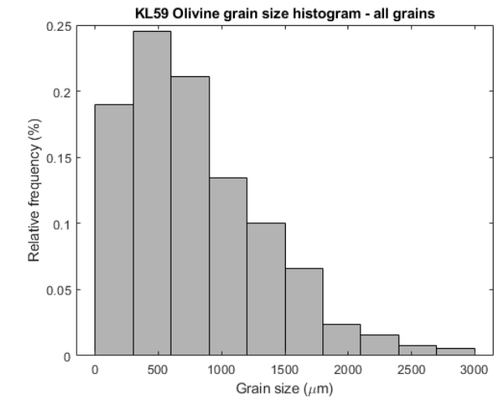

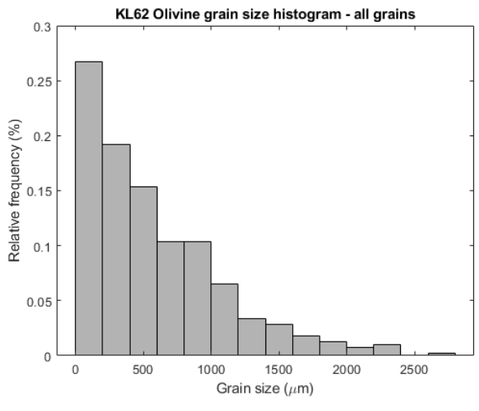

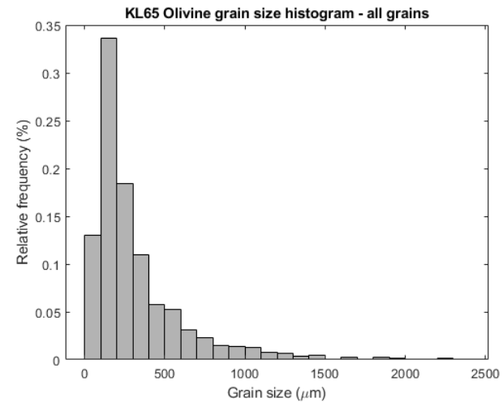

Big Timothy

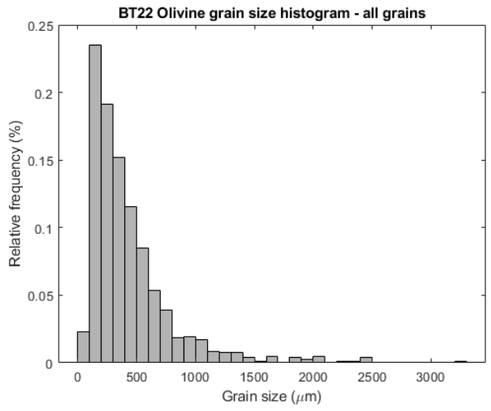

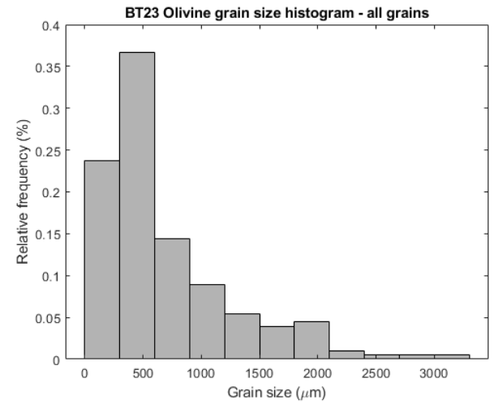

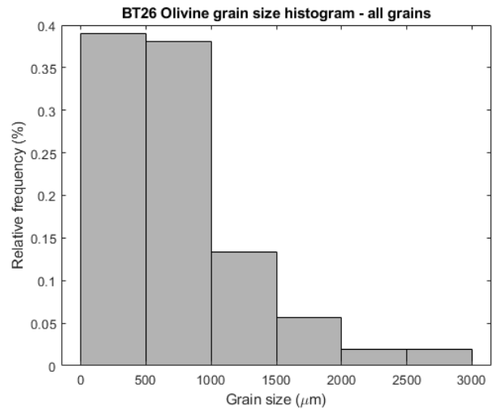

Rayfield River

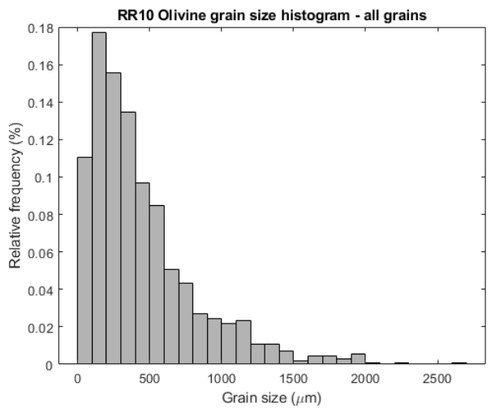

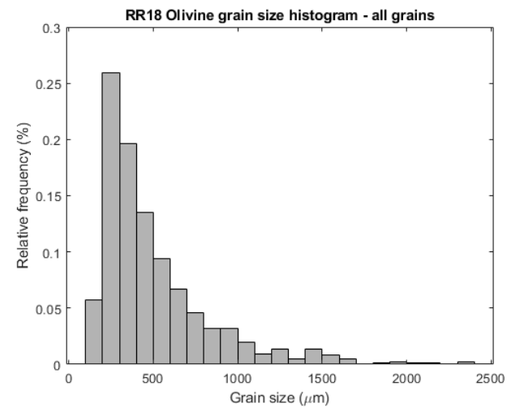

Lightning Peak

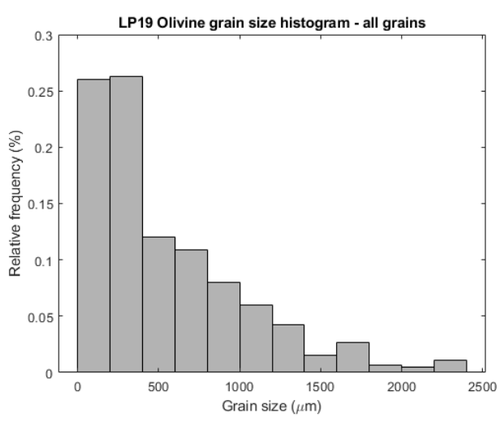

Kostal Lake samples with bimodal grain size distribution

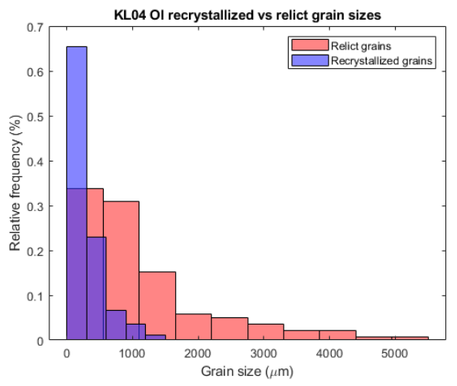

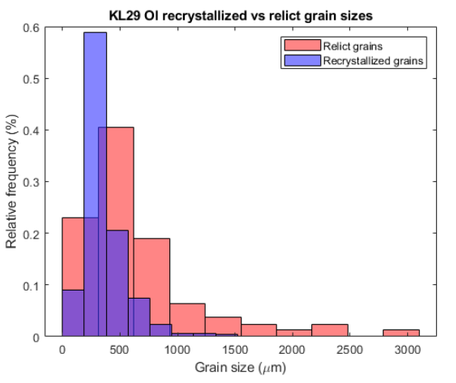

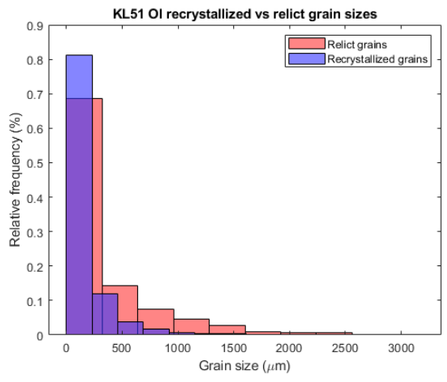

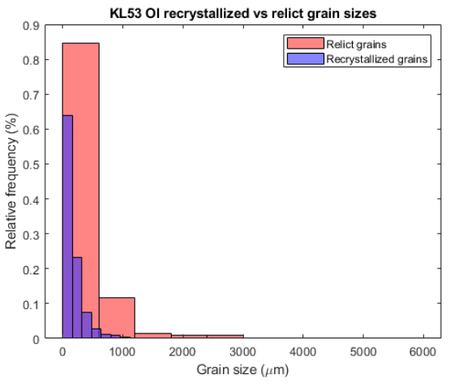

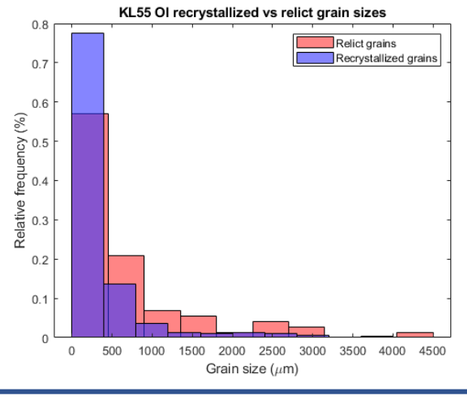

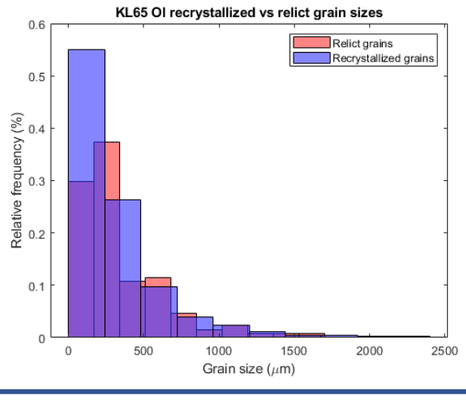

Figure 7.3 Crystallographic Preferred Orientations

Strongly correlated with olivine

Weakly correlated with olivine

Prindle Volcano

	Olivine	Orthopyroxene	Clinopyroxene
PV08 Mosaic Equigranular J=1.56 BA=0.29	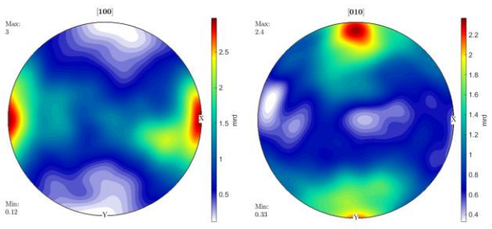	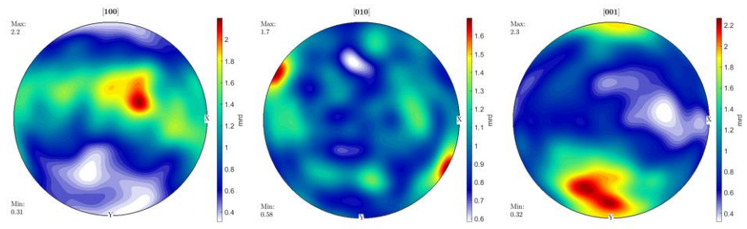	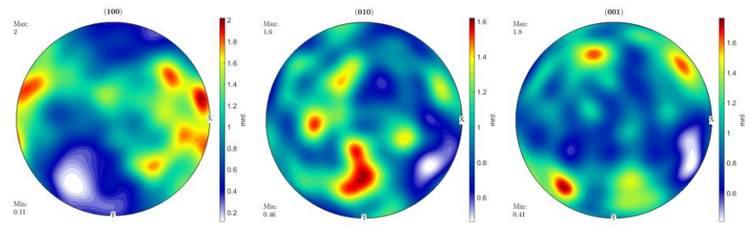
PV17 Mosaic Equigranular J=1.52 BA=0.46	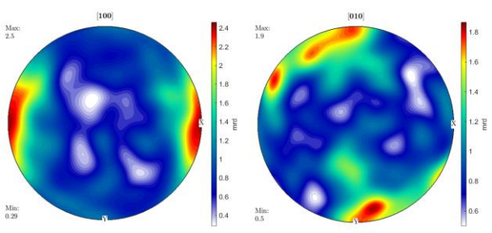	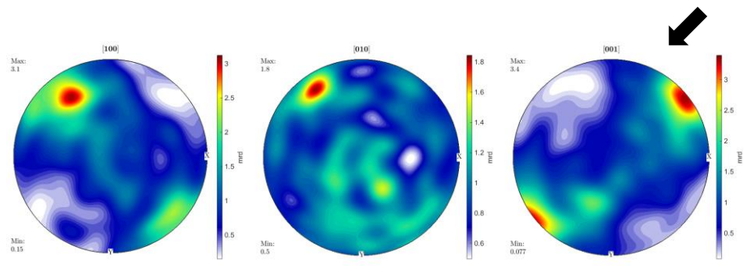	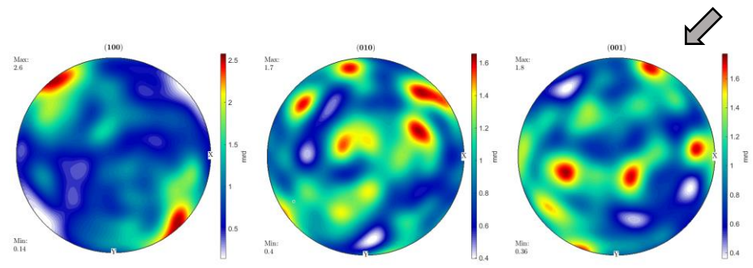
PV39 Mosaic Equigranular J=1.70 BA=0.39	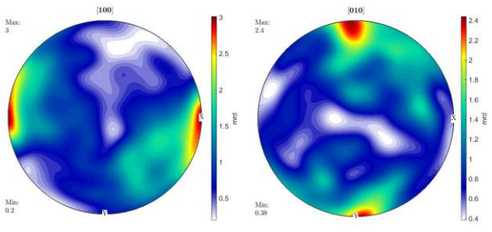	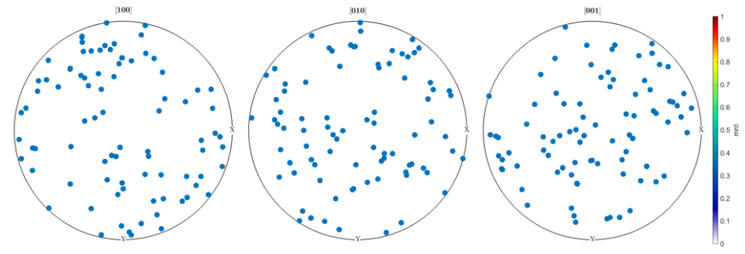	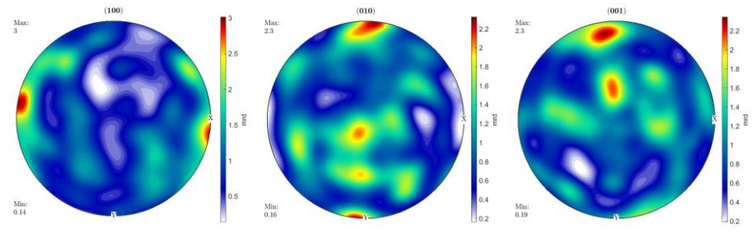
PV40 Mosaic Equigranular J=1.57 BA=0.42	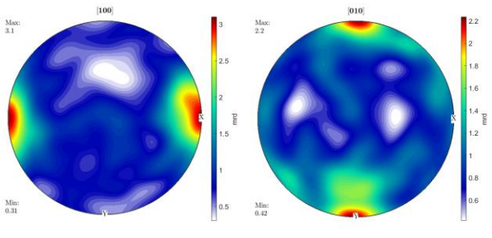	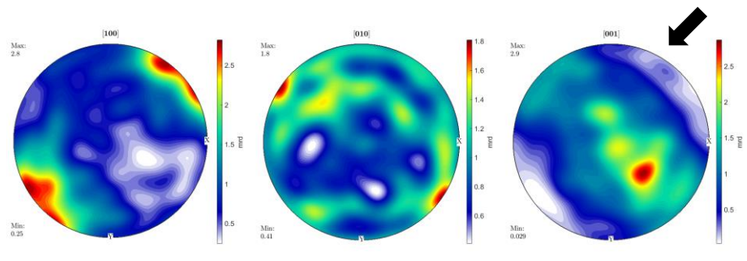	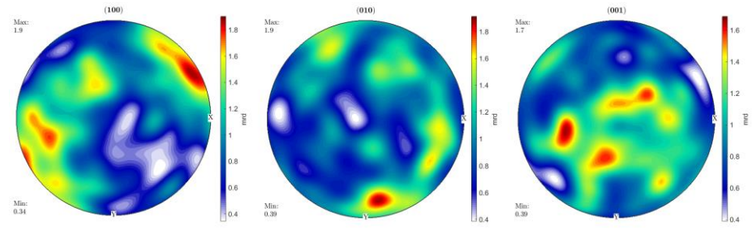

Fort Selkirk

	Olivine	Orthopyroxene	Clinopyroxene
FS13 Protogranular J=3.25 BA=0.55	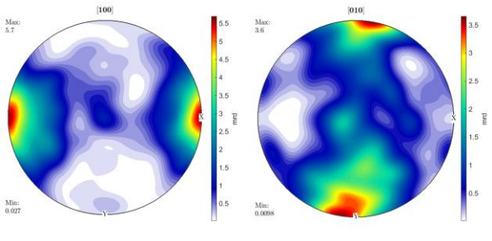	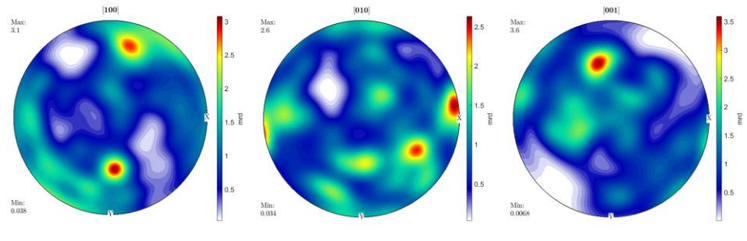	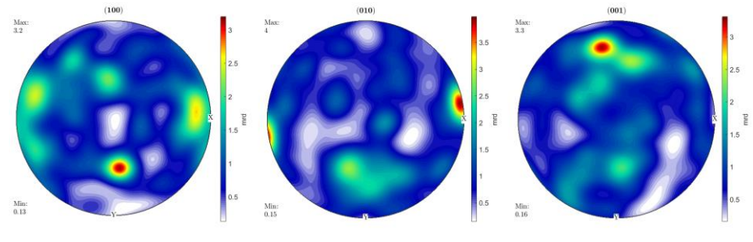

Alligator Lake

	Olivine	Orthopyroxene	Clinopyroxene
AL45 Equigranular J=3.74 BA=0.43	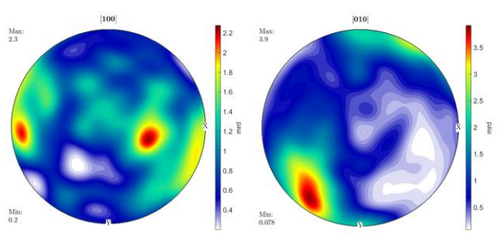	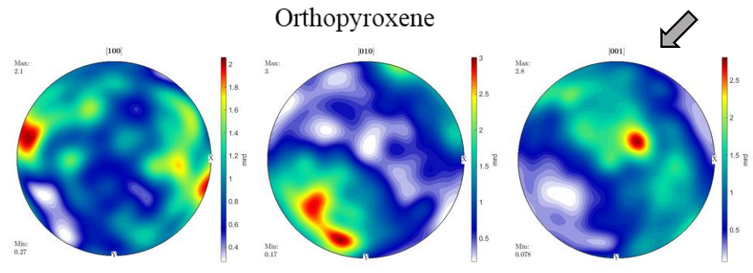	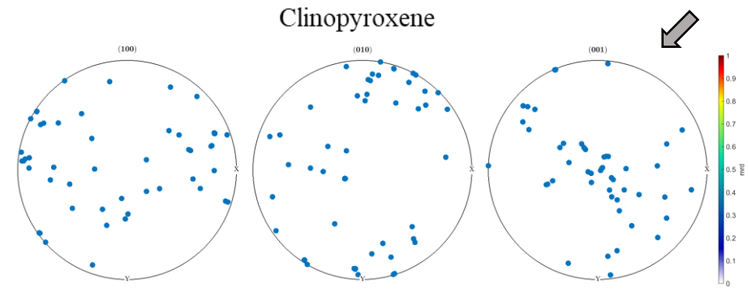
AL57 Equigranular Mosaic J=2.47 BA=0.41	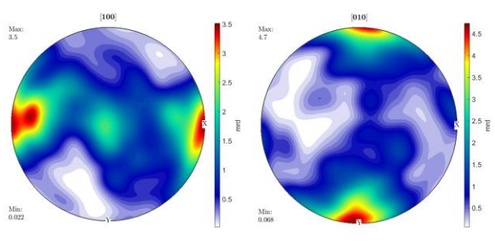	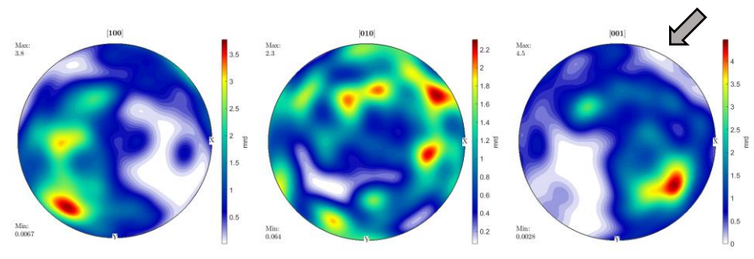	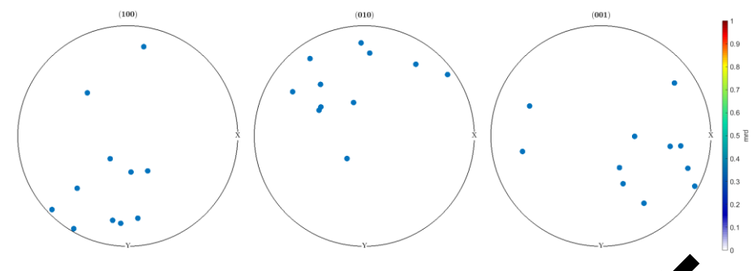
AL58 Protogranular J=3.08 BA=0.21	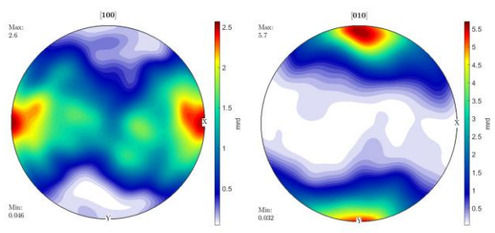	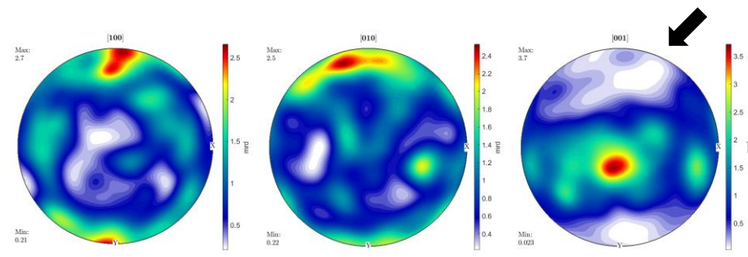	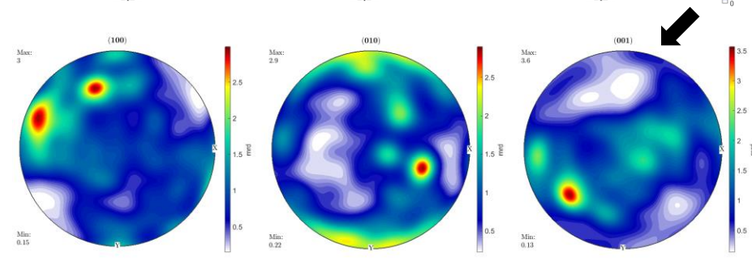
AL70 Equigranular- Protogranular J=3.93 BA=0.20	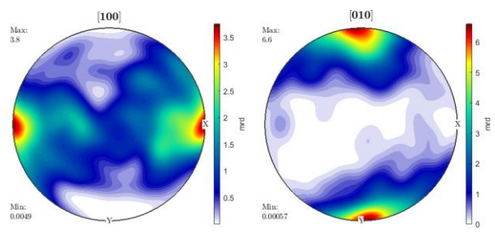	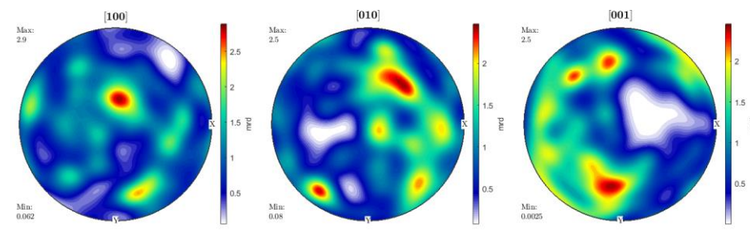	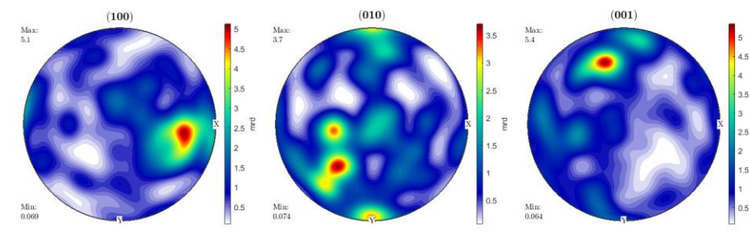
AL90 Tabular Equigranular J=4.87 BA=0.42	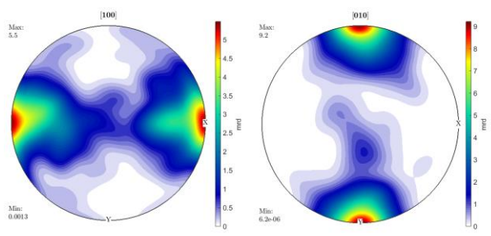	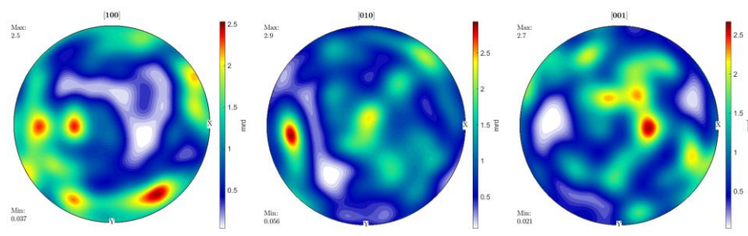	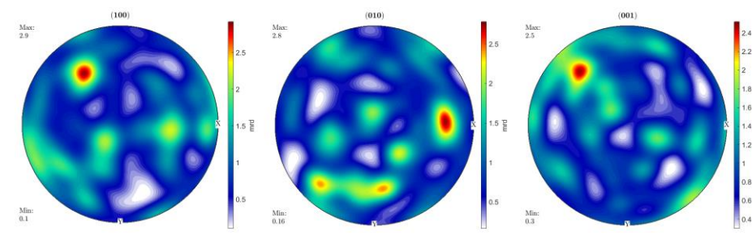

Hirschfield Creek

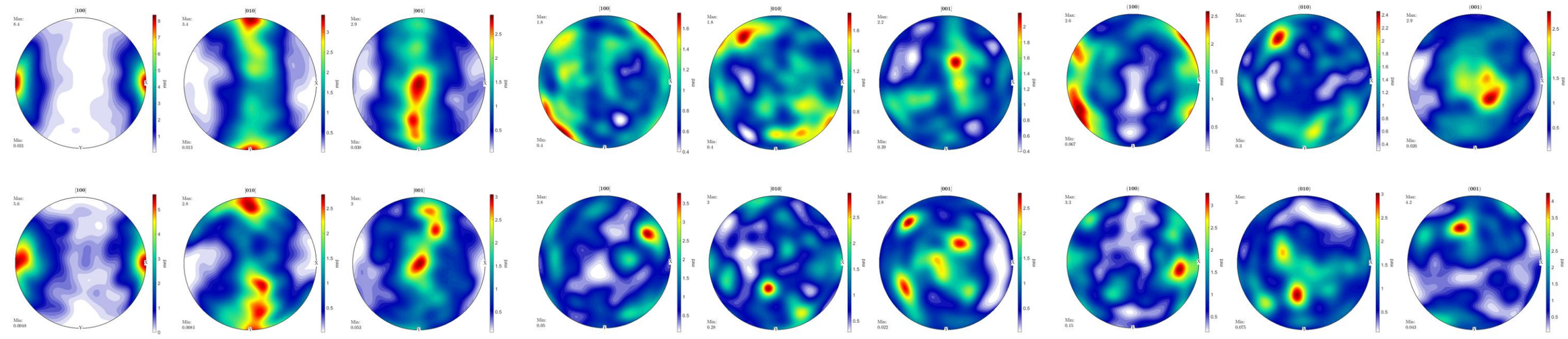

Langorse Mountain

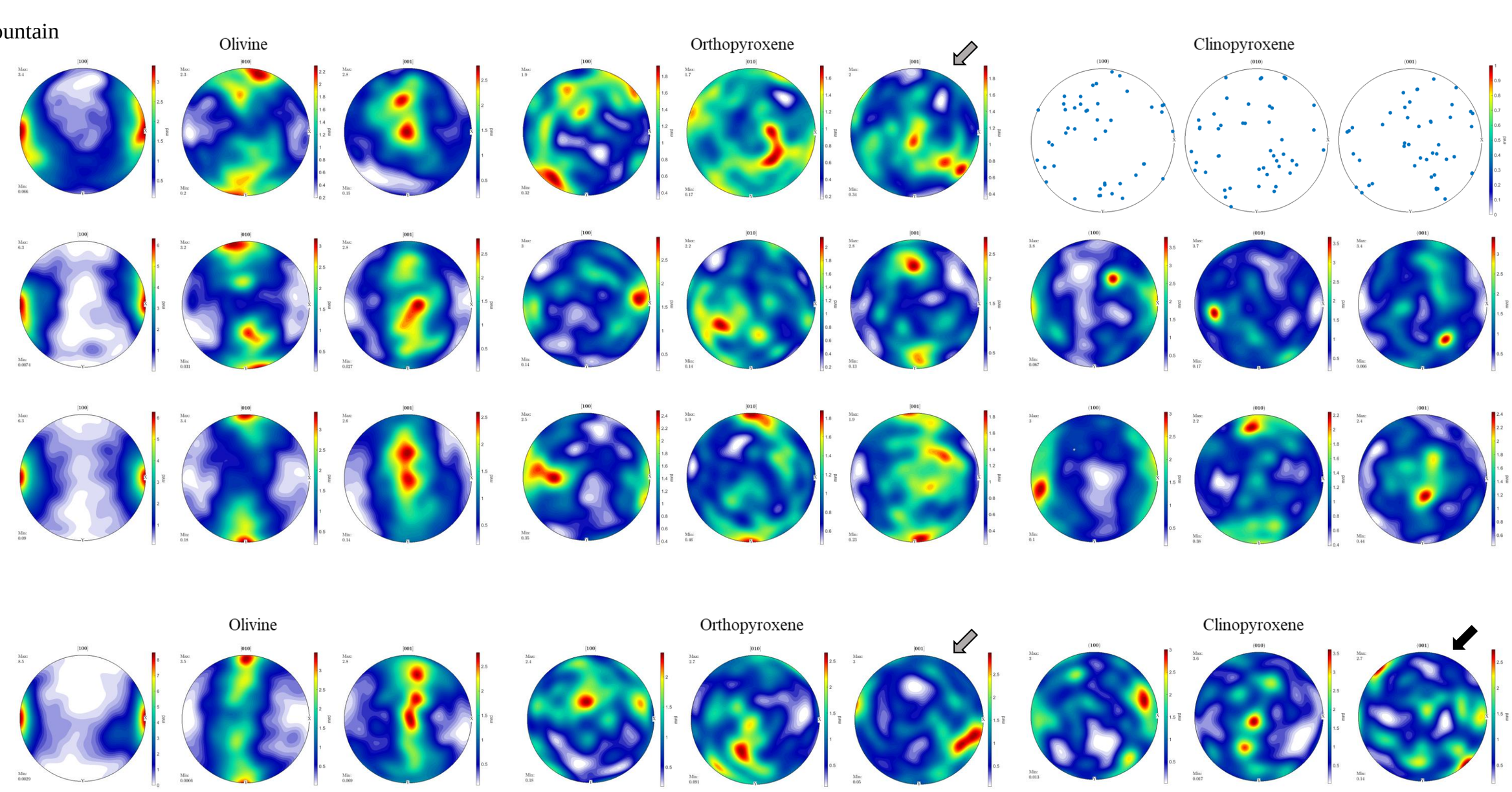

Castle Rock

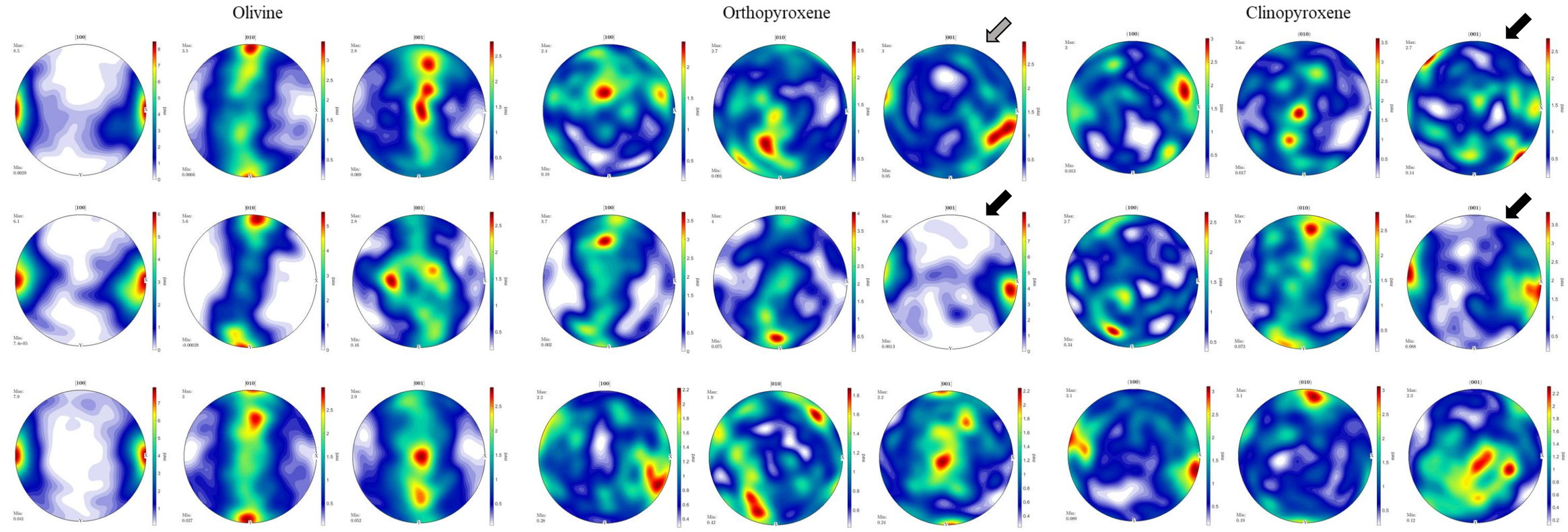

Summit Lake

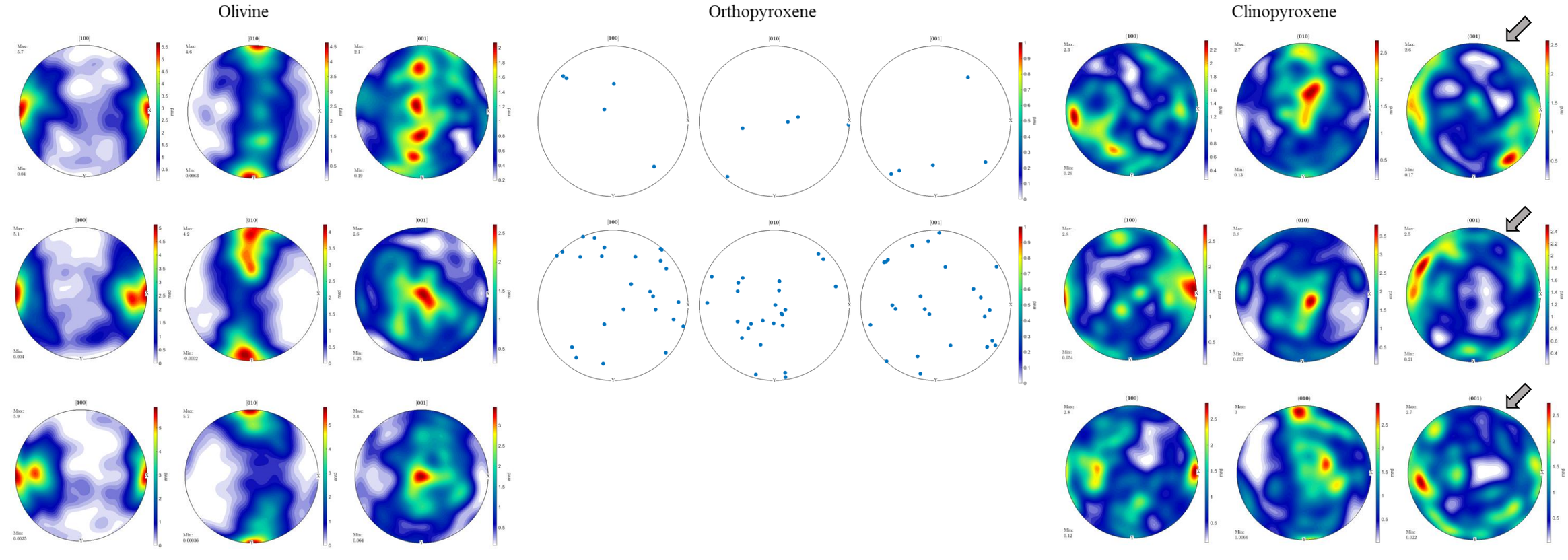

Figure 7-3 continued

Jacques Lake

Olivine | Orthopyroxene | Clinopyroxene

JL05
Protogranular
J=3.35 BA=0.19

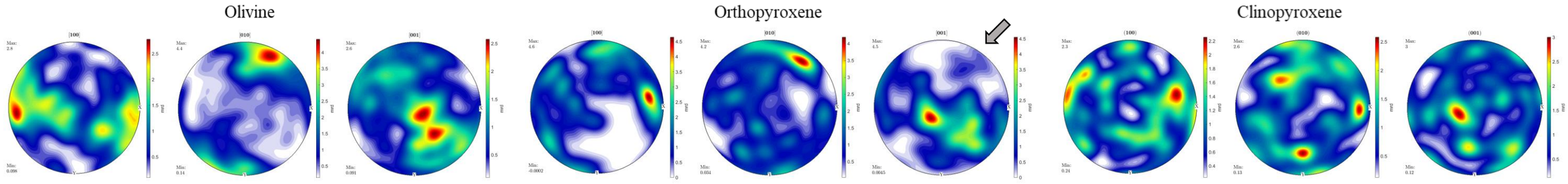

JL12
Protogranular
J=3.52 BA=0.65

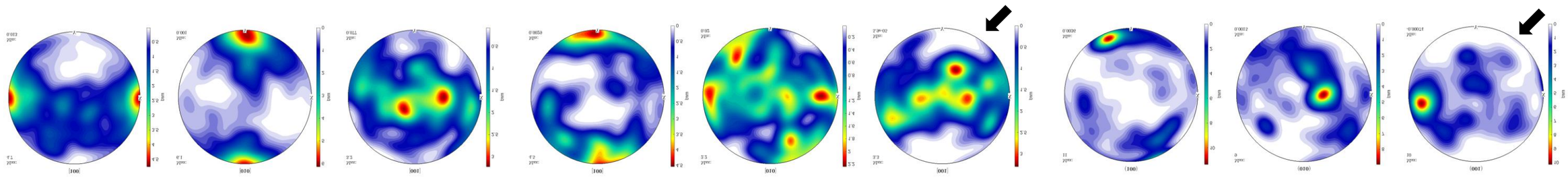

Kostal Lake

Olivine | Orthopyroxene | Clinopyroxene

KL04
Protogranular
J=2.56 BA=0.18

KL29
Porphyroclastic
J=1.30 BA=0.25

KL37
Protogranular
-mylonitic
J=6.88 BA=0.54

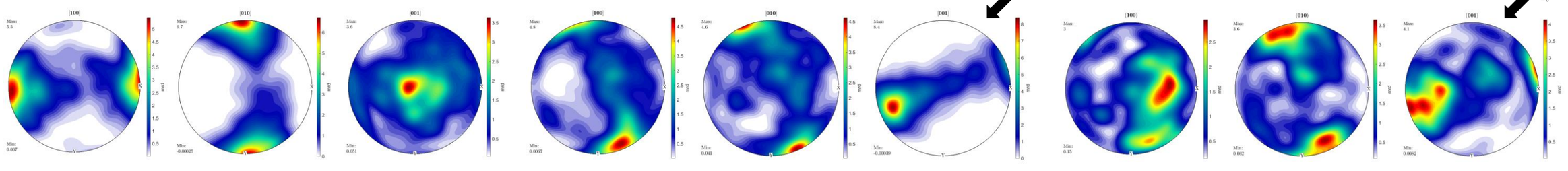

KL44
Protogranular
-mylonitic
J=6.50 BA=0.35

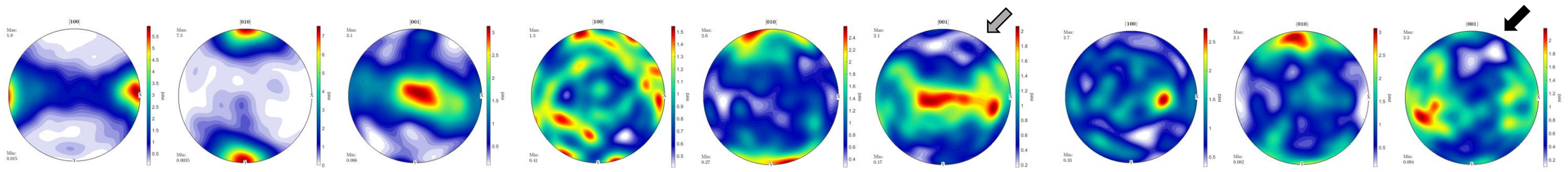

KL51
Transitional
-Tablet
J=2.09 BA=0.61

KL53
Transitional
-Tablet
J=2.23 BA=0.41

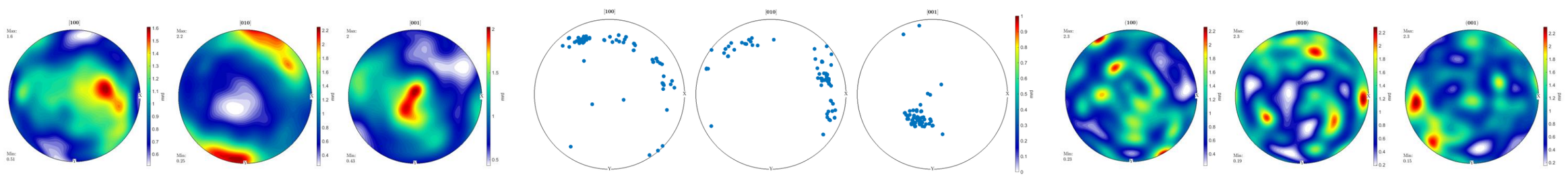

KL55
Protogranular-
Prorphyroclastic
J=1.41 BA=0.43

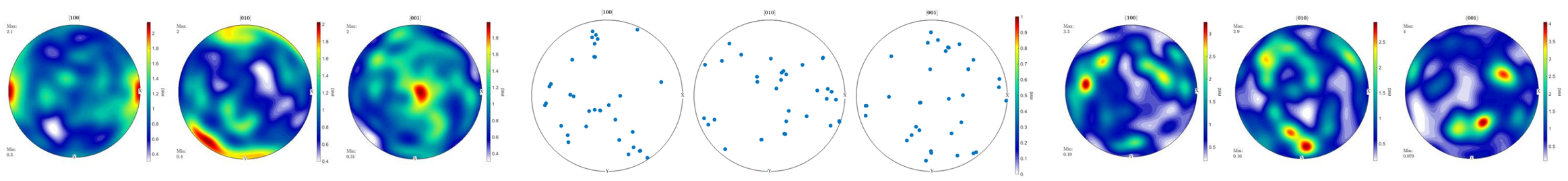

KL59
Tabular
Equigranular
J=8.04 BA=0.39

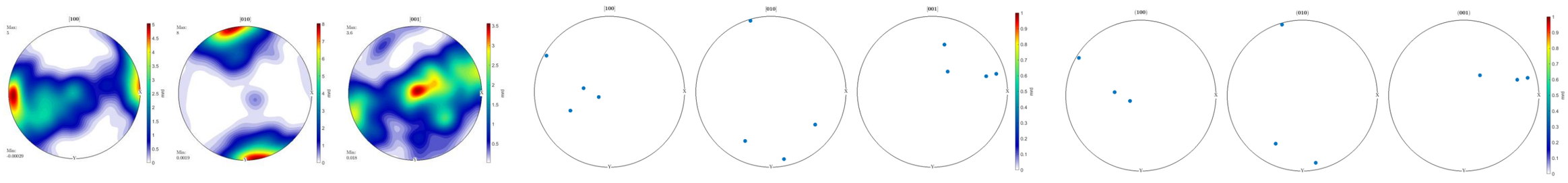

KL62
Tabular
Equigranular
J=5.97 BA=0.04

KL65
Protogranular-
Prorphyroclastic
J=1.44 BA=0.19

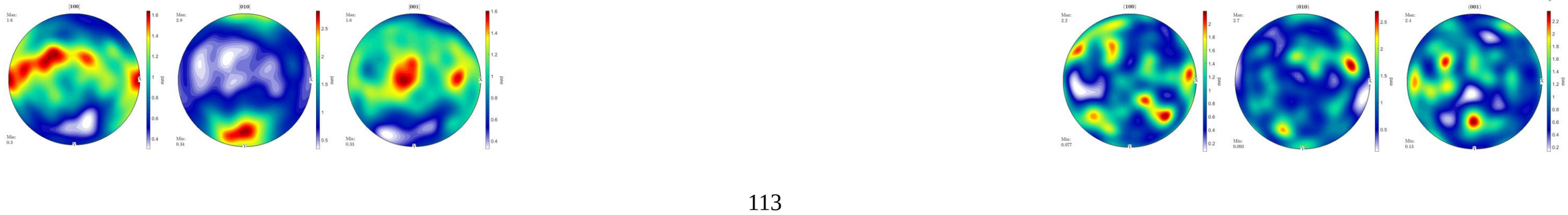

Figure 7-3 continued

Big Timothy

Olivine | Orthopyroxene | Clinopyroxene

BT22
Protogranular
J=2.23 BA=0.52

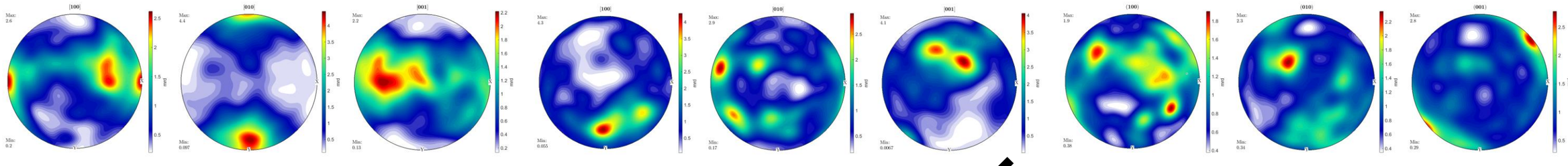

BT23
Protogranular
J=3.27 BA=0.40

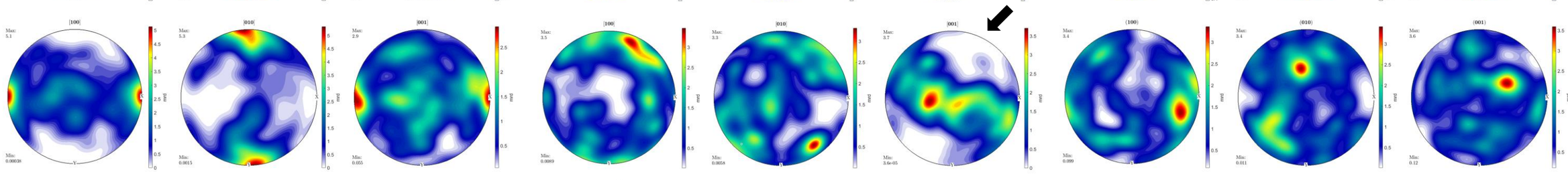

BT26
Protogranular
J=4.64 BA=0.45

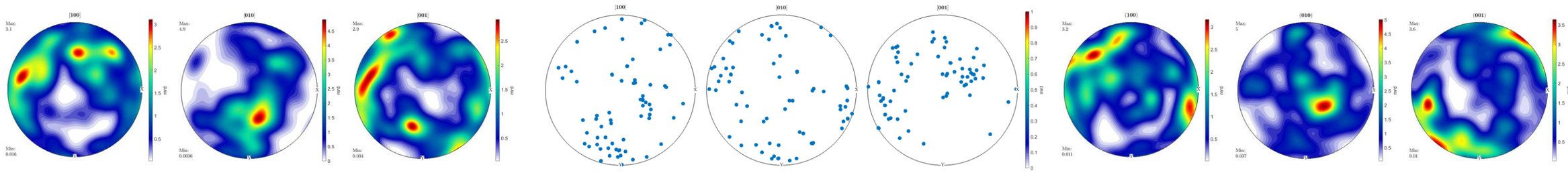

Rayfield River

Olivine | Orthopyroxene | Clinopyroxene

RR10
Mylonitic
J=2.65 BA=0.83

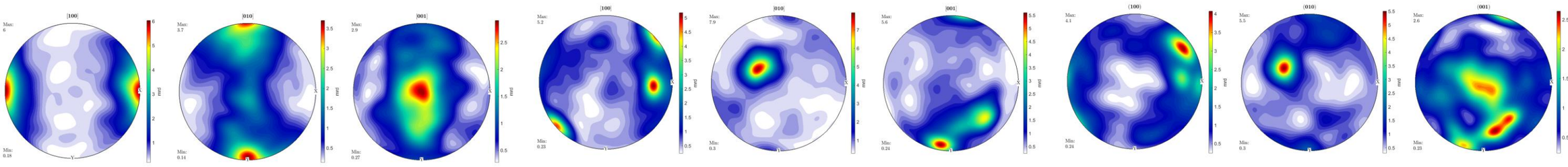

RR18
Mylonitic
J=2.39 BA=0.78

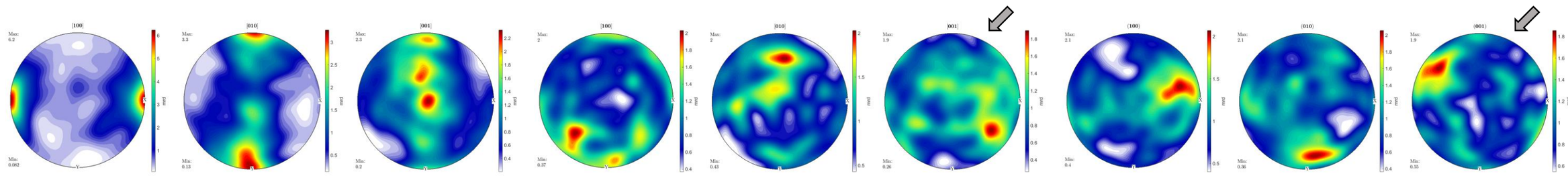

Lightning Peak

Olivine | Orthopyroxene | Clinopyroxene

LP19
Protogranular
J=1.88 BA=0.61

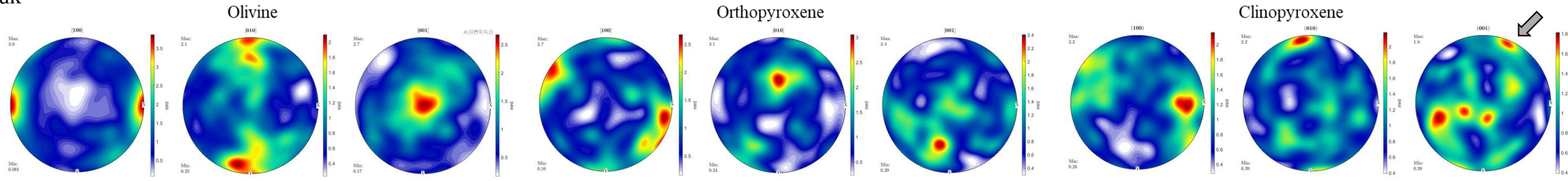

Figure 7-4. Anisotropic properties

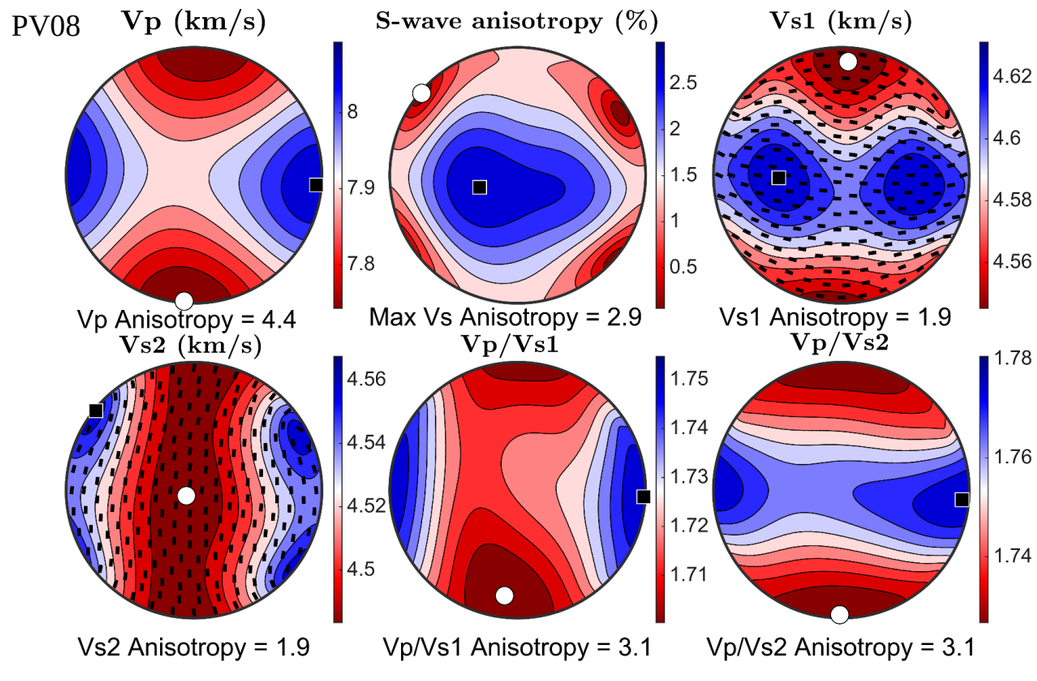

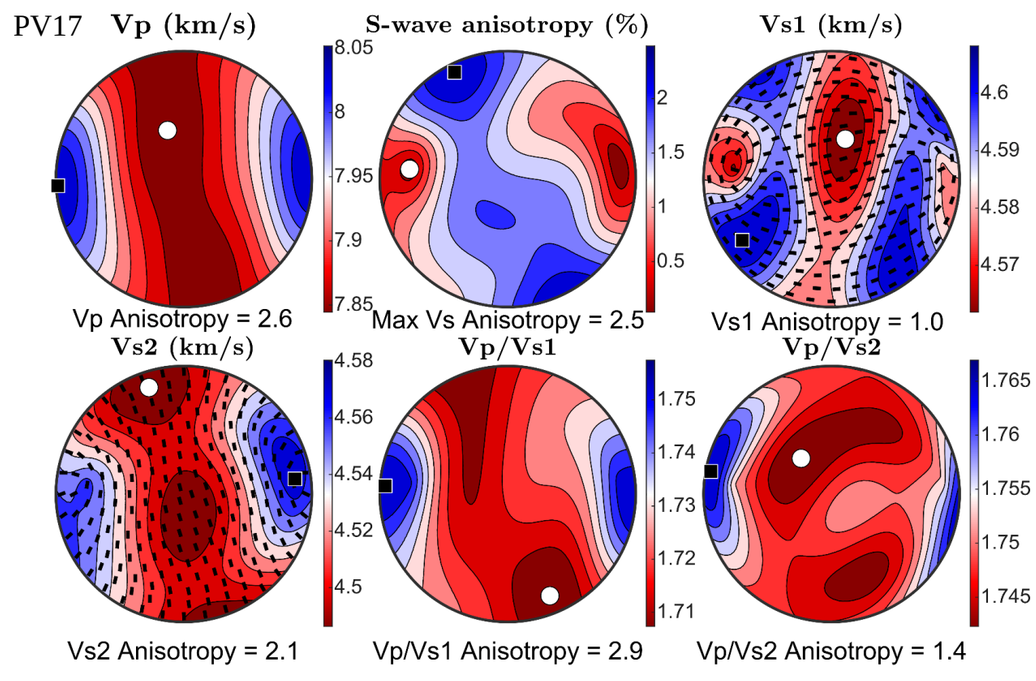

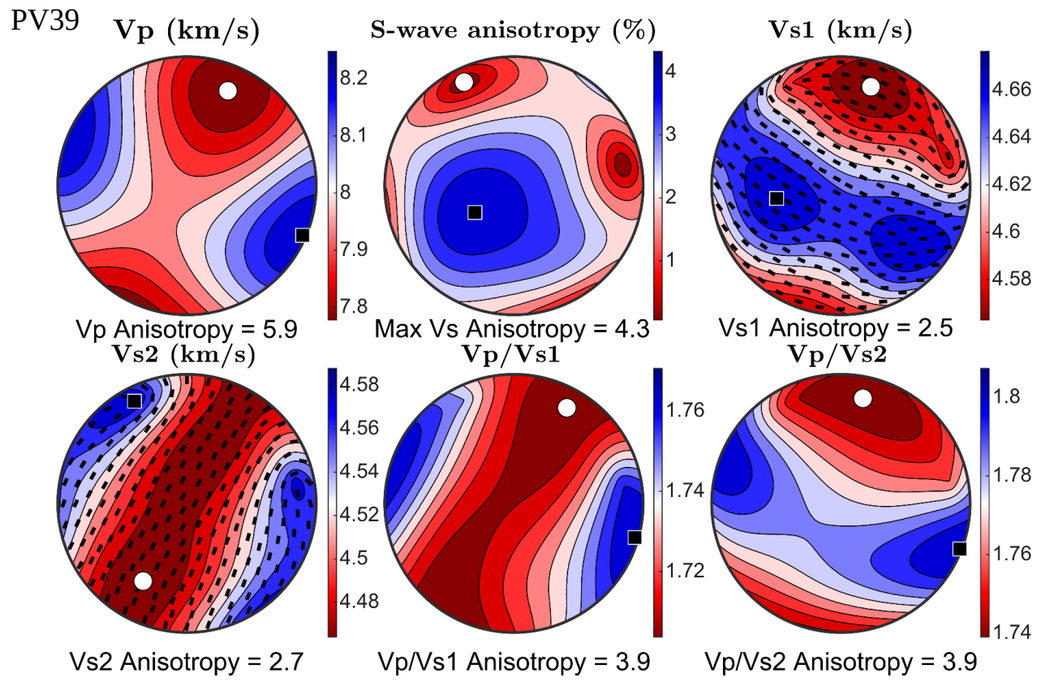

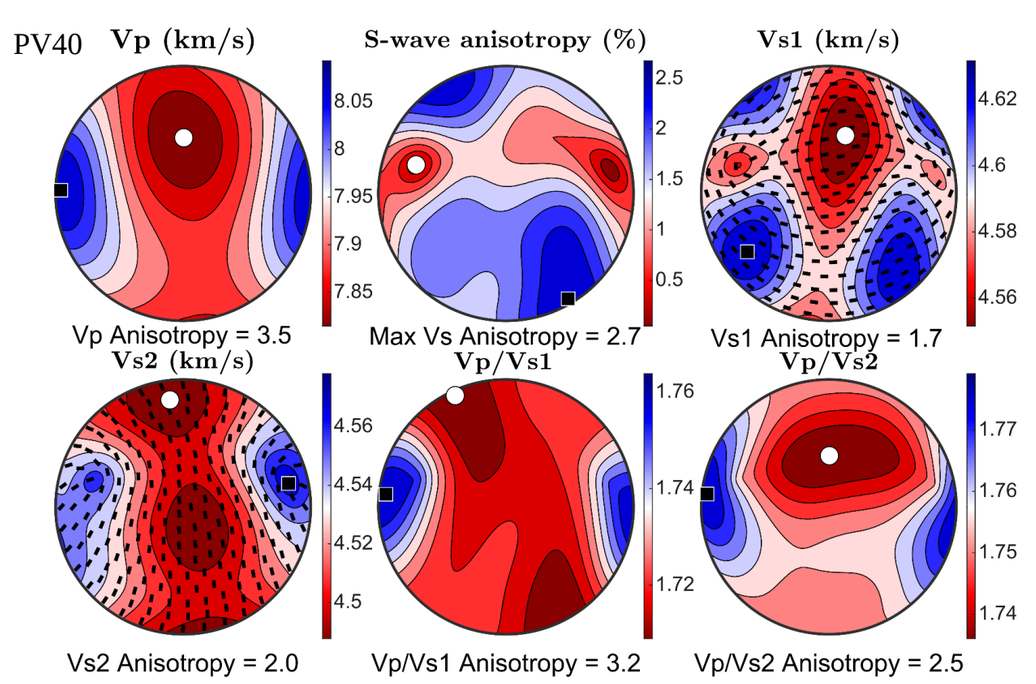

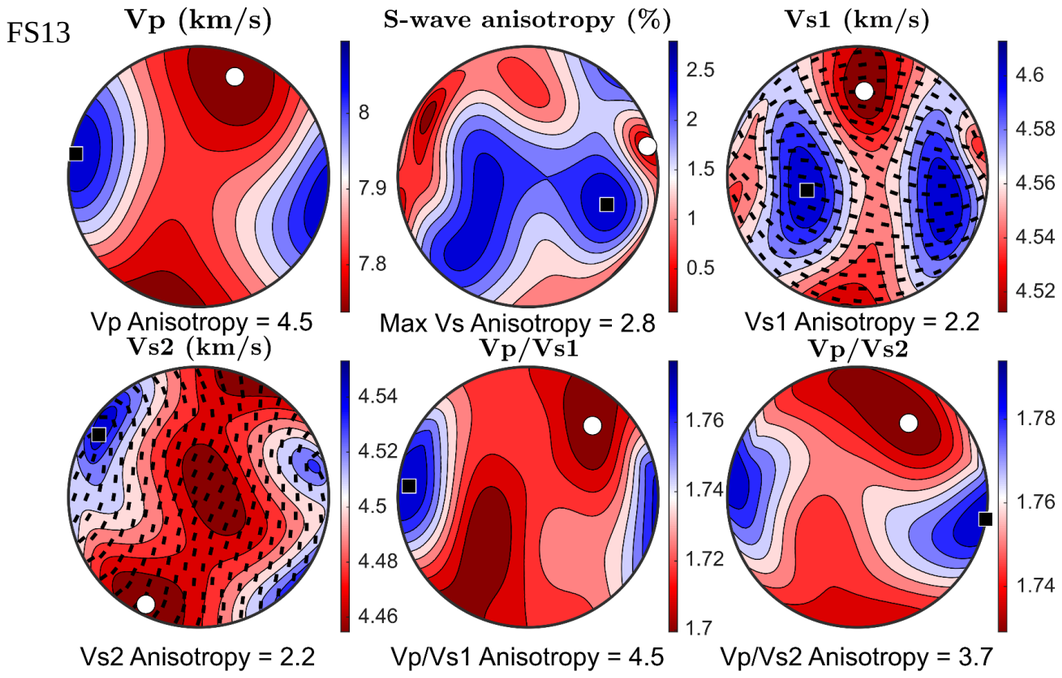

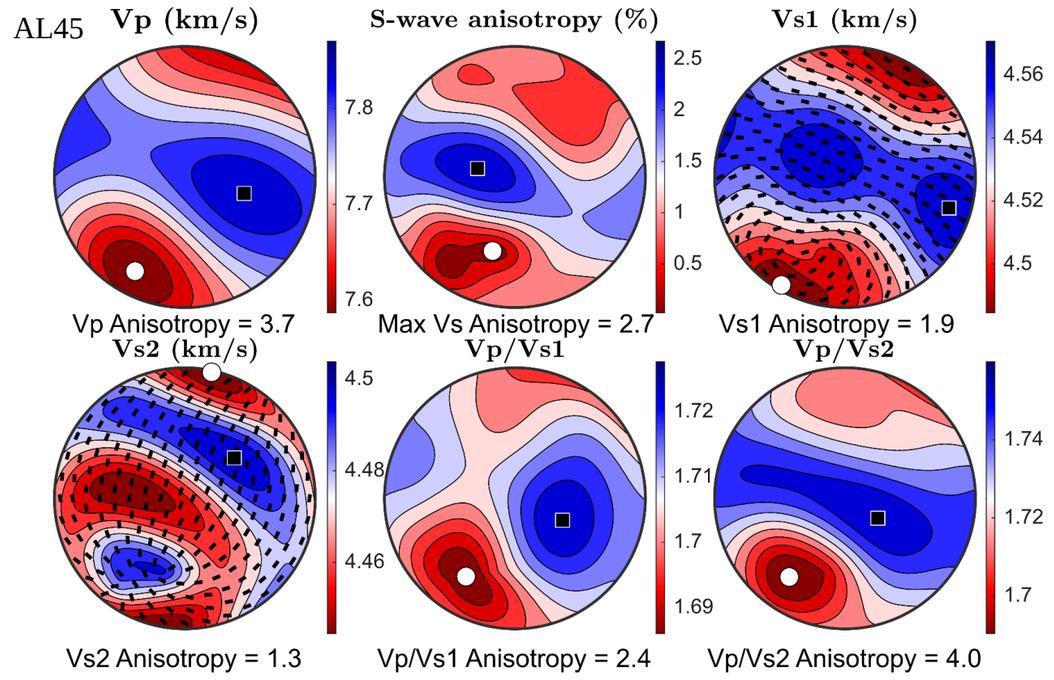

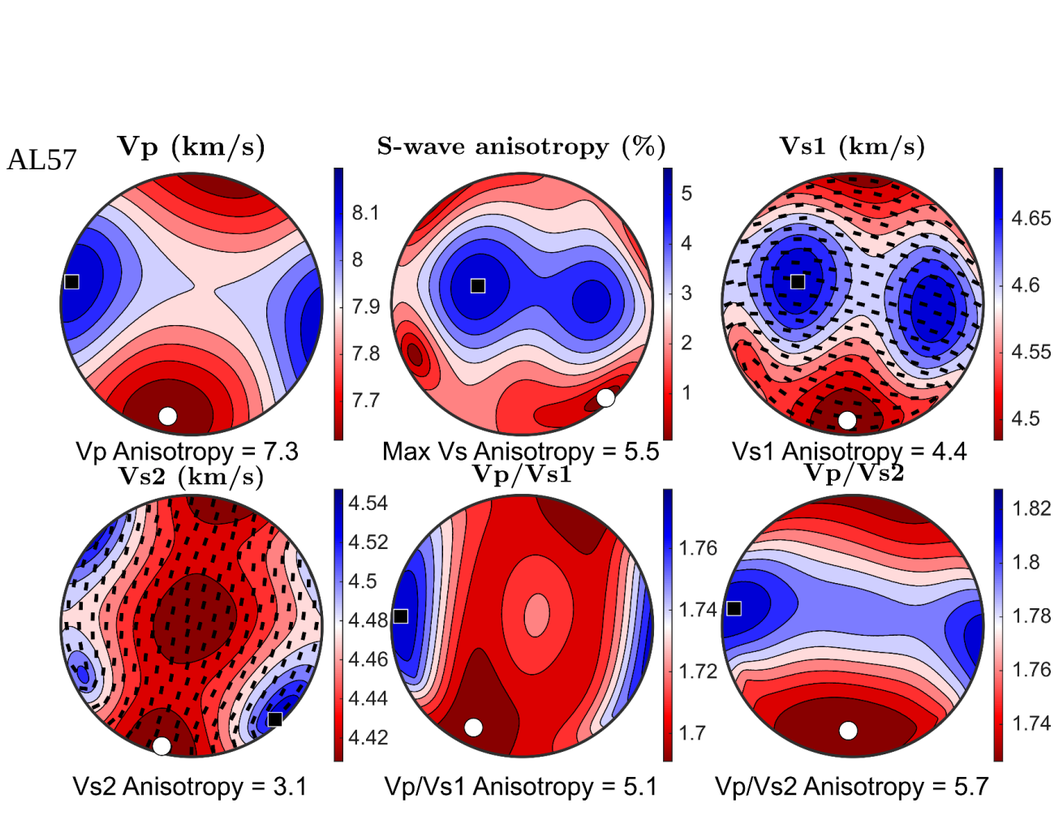

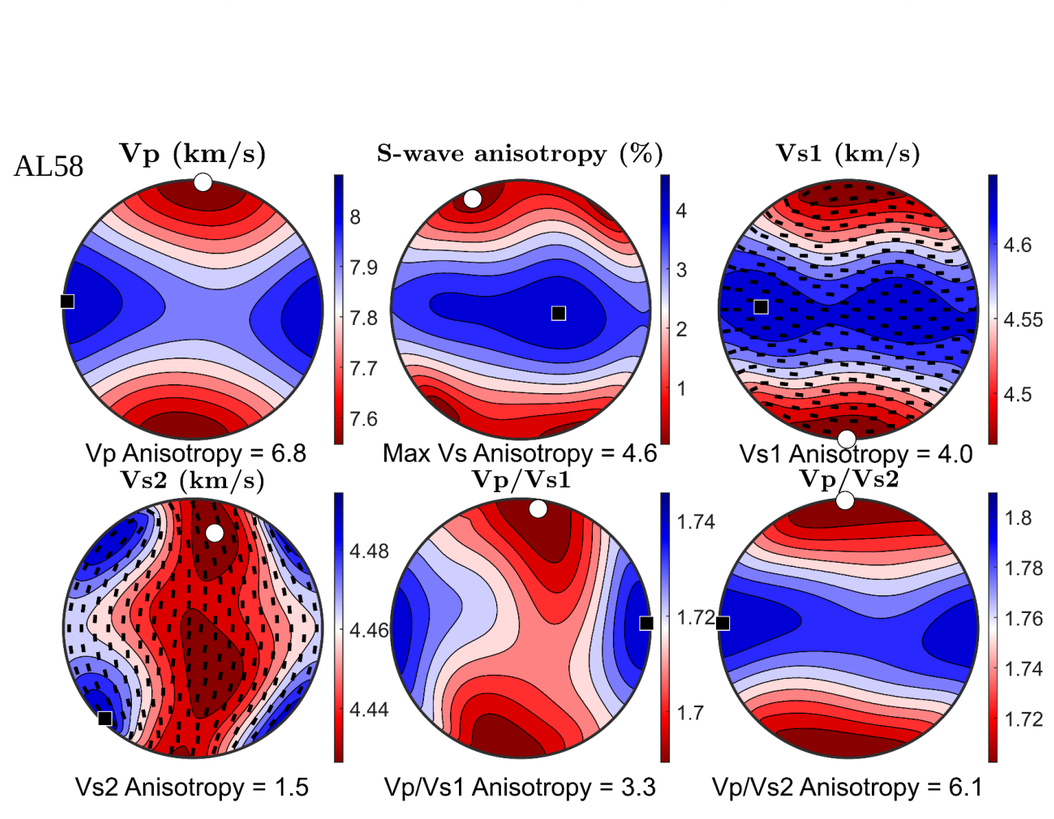

Figure 7-4. continued

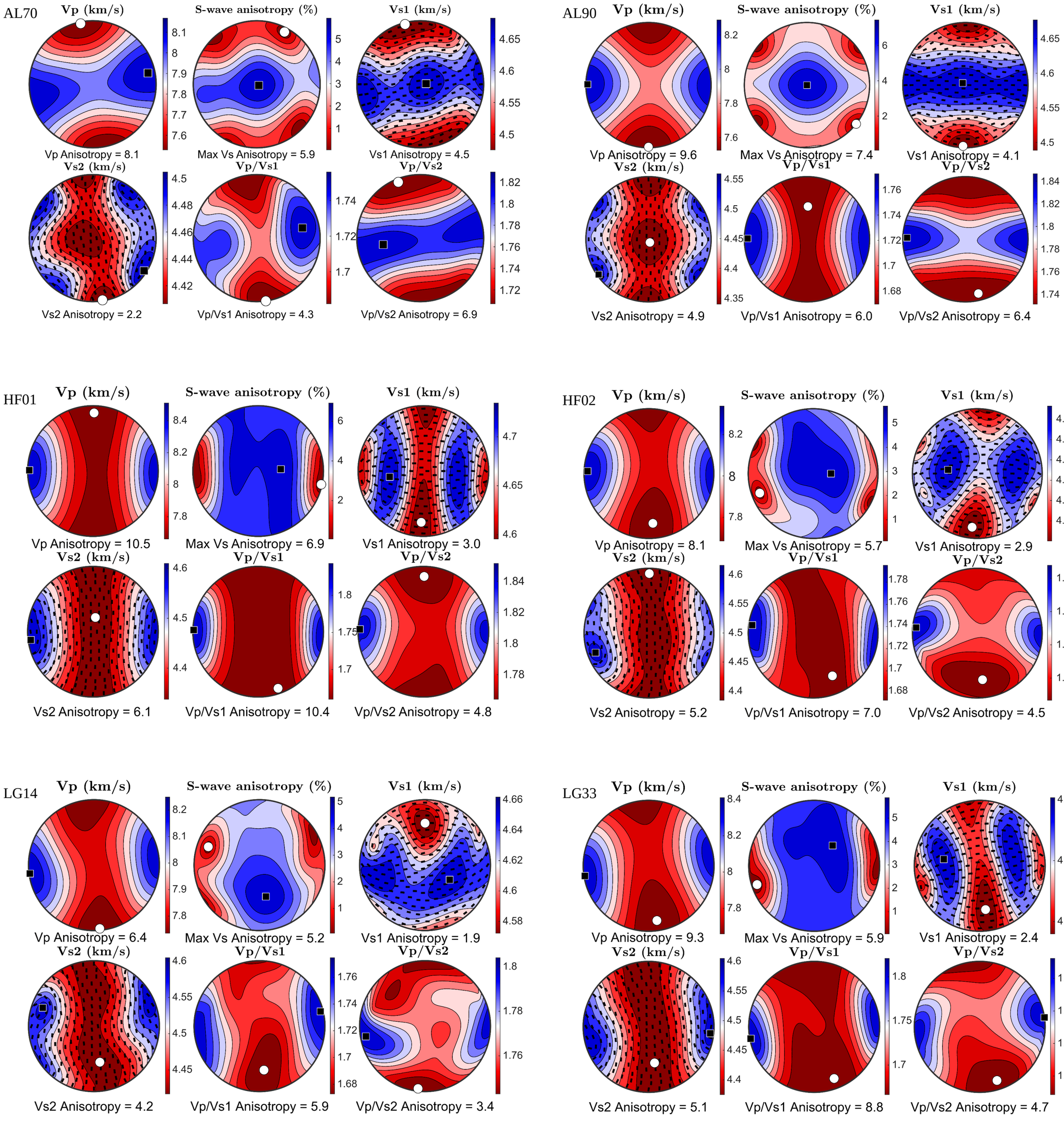

Figure 7-4. continued

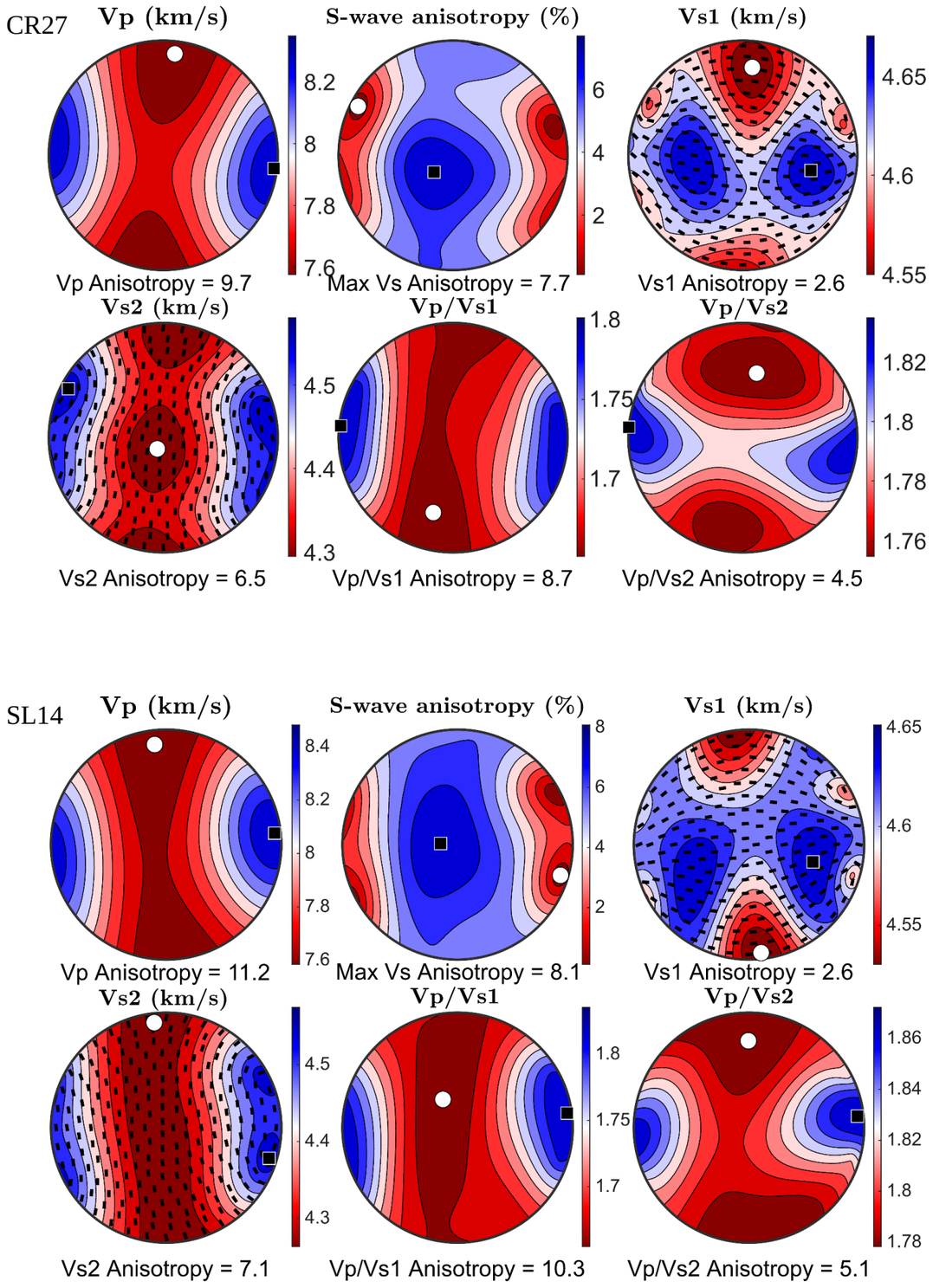

Figure 7-4. continued

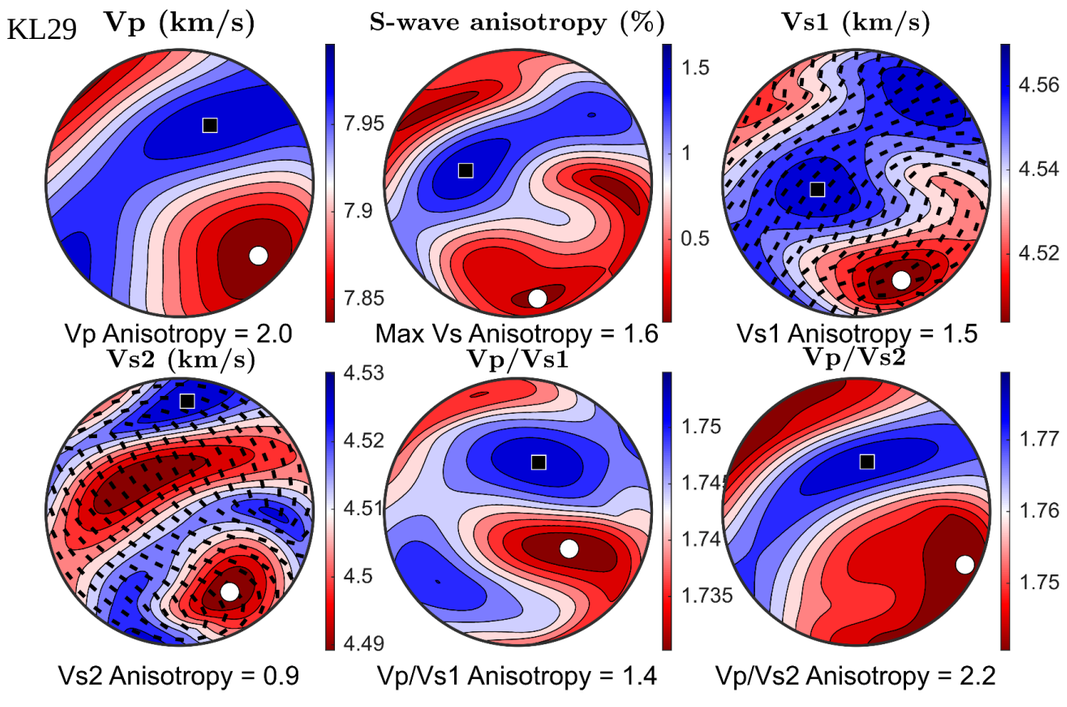

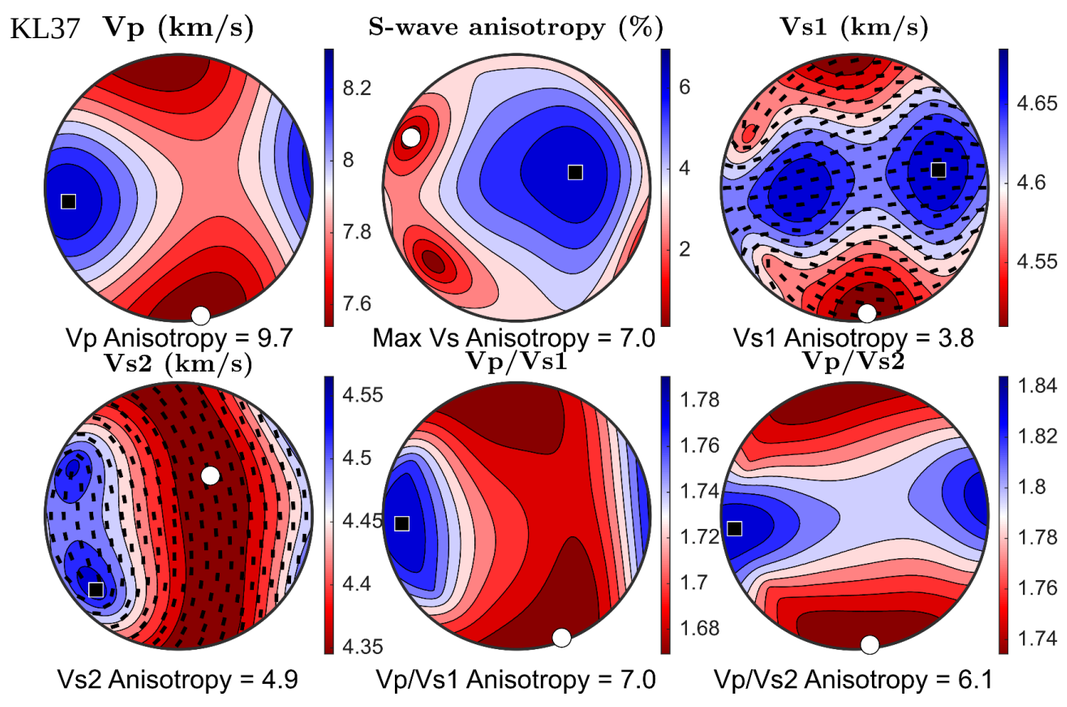

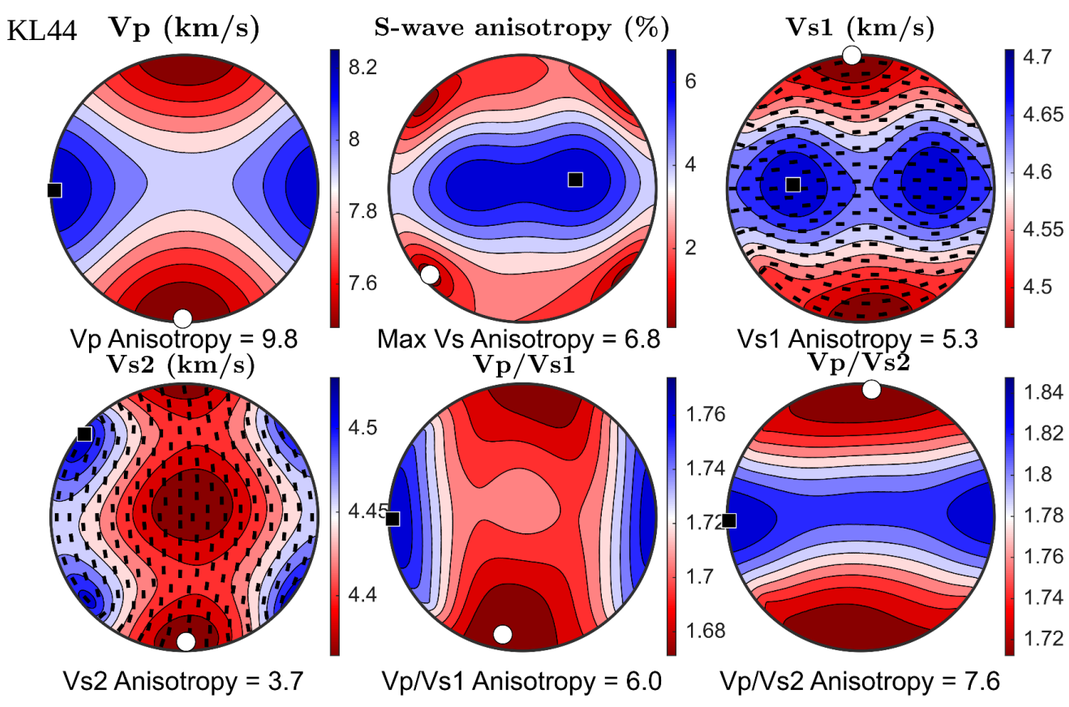

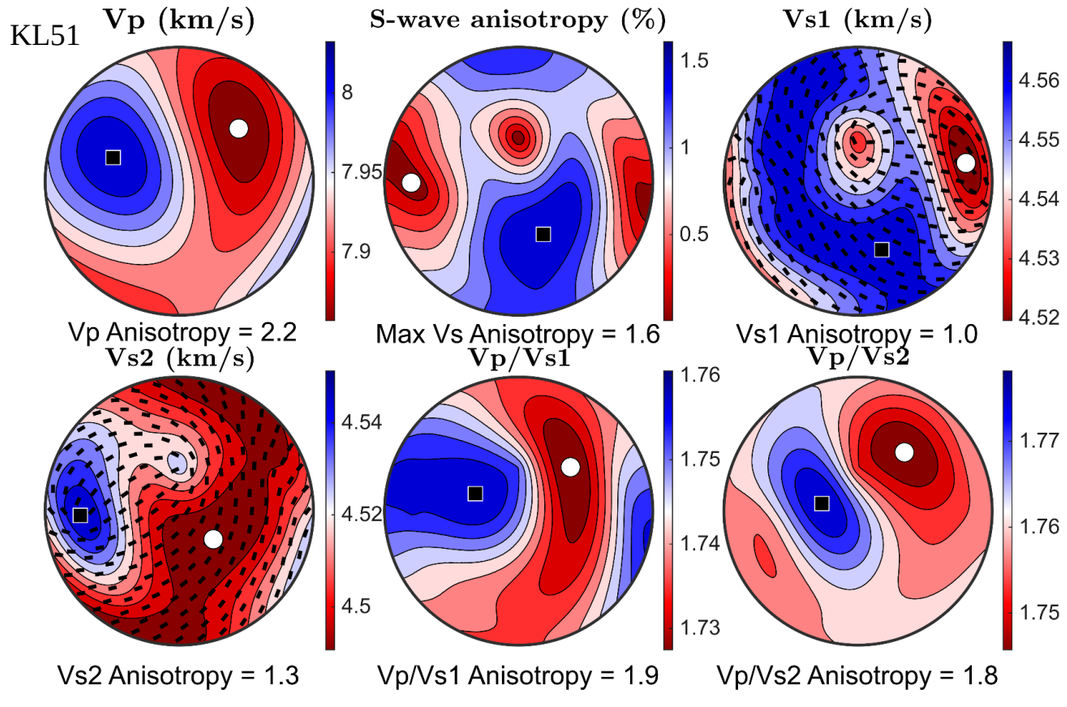

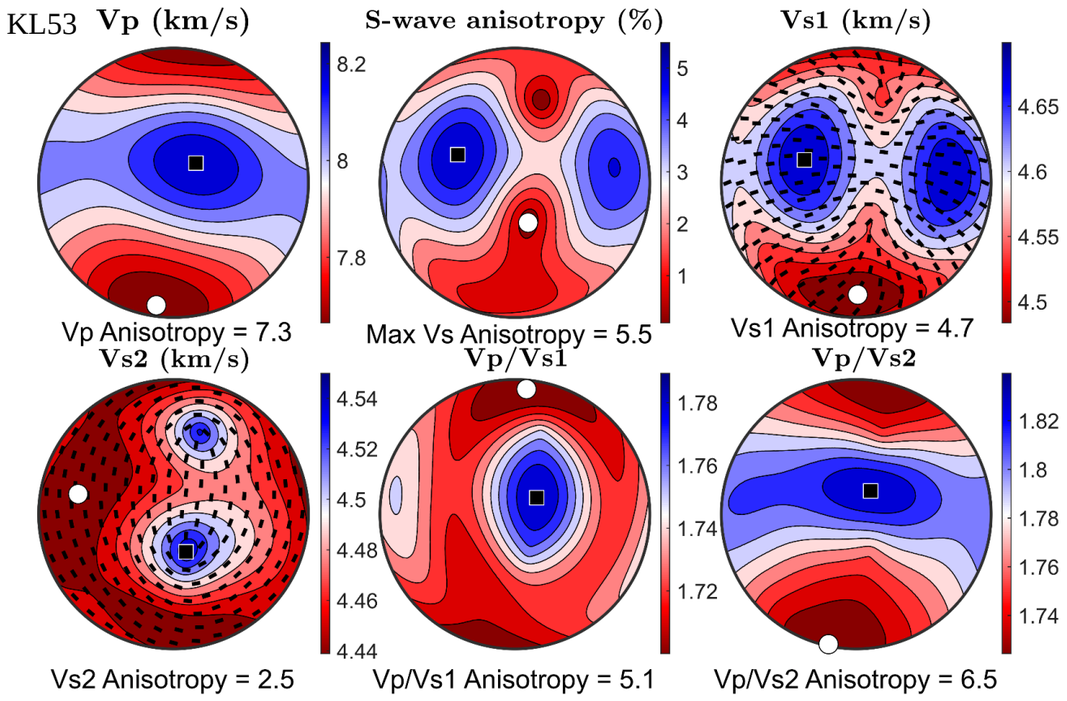

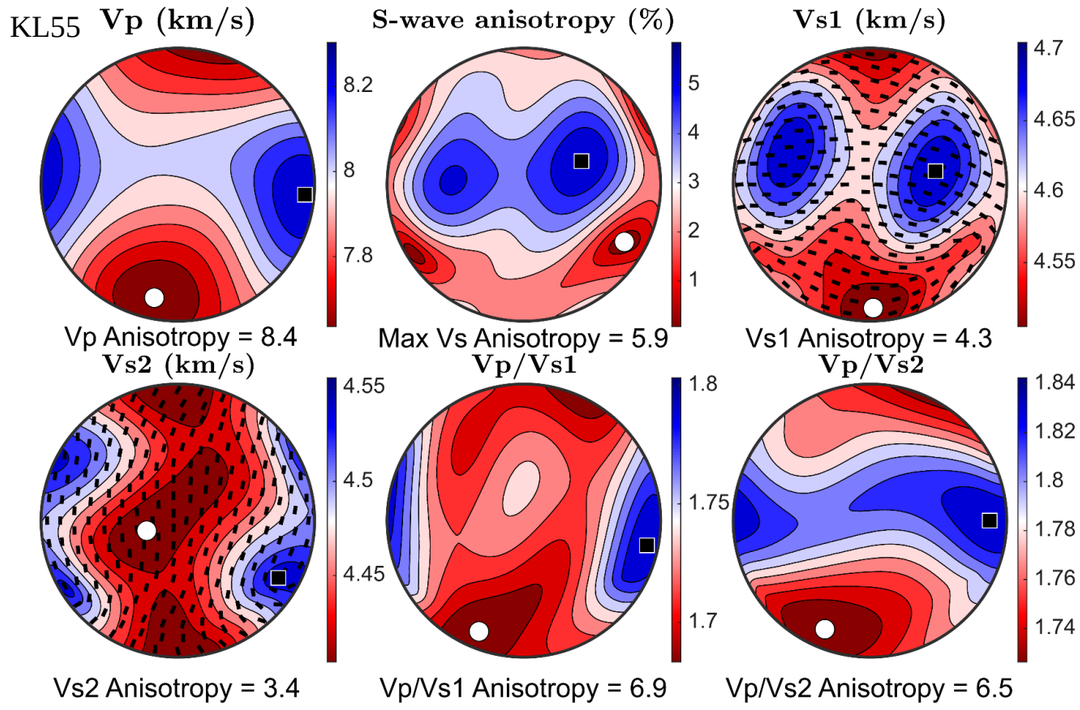

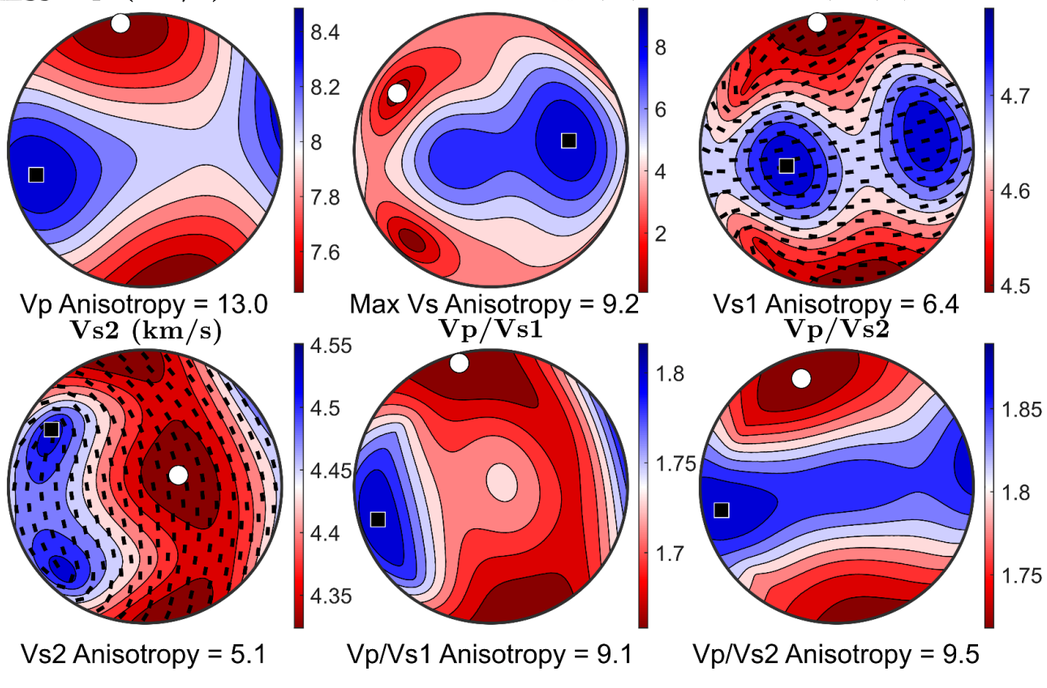

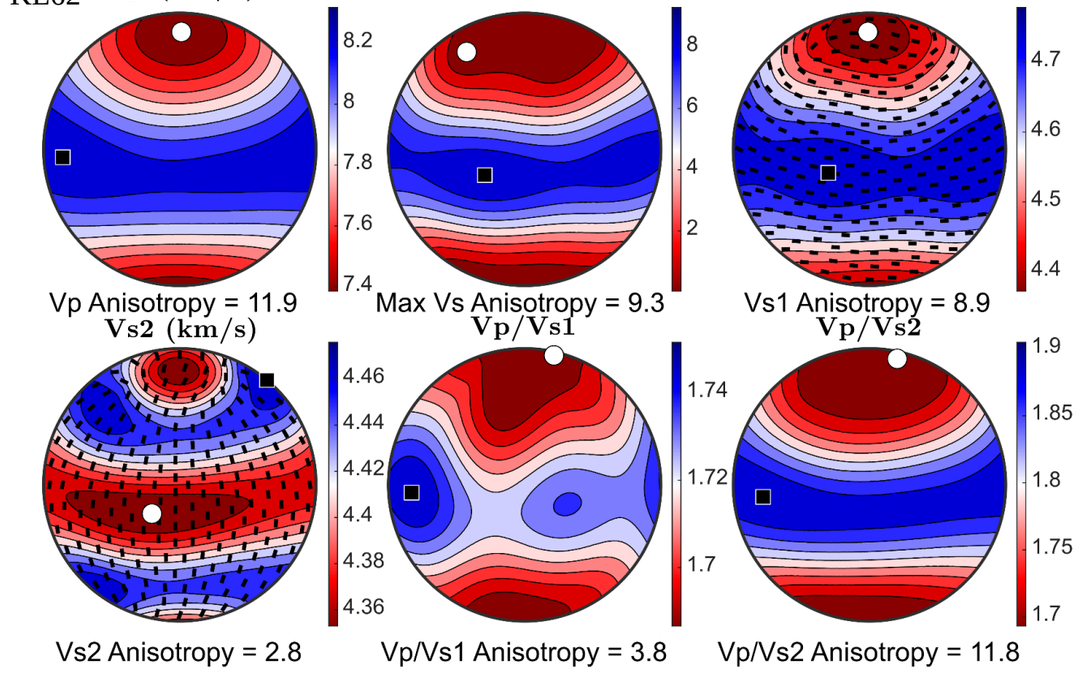

Figure 7-4. continued